THÈSE

en vue de l'obtention du grade de

Docteur de l'Université d'Aix-Marseille

Discipline : **Mécanique et Physique des Fluides**

IRPHE

École Doctorale 353

Présentée et soutenue publiquement le 13 octobre 2020

par Pierre Léard

On the interaction between turbulence and stratification: penetrative convection, internal gravity waves and large-scale flow generation

Geophysical and Astrophysical applications

Mémoire provisoire

Directeurs de Thèse : Michael Le Bars and Patrice Le Gal

Devant la commission d'examen formée de :

M.	Michel Rieutord	*Université de Toulouse*, Professeur	Rapporteur
Mme.	Chantal Staquet	*Université de Grenoble*, Professeure	Rapportrice
M.	Stéphane Mathis	*CEA*, Chercheur	Examinateur
M.	Philippe Odier	*ENS Lyon*, MCF	Examinateur
M.	Antoine Venaille	*CNRS*, CR	Examinateur
M.	Michael Le Bars	*CNRS*, DR	Directeur
M.	Patrice Le Gal	*CNRS*, DR	Directeur

Contents

INTRODUCTION

The internal structure of stars, Earth's atmosphere, oceans and core, or even other celestial objects' atmospheres share similar characteristics. They are all composed of layers with different dynamics. Quite often, among these layers, a convective layer is found to be adjacent to a stably stratified one. Fast chaotic motions animate the convection while the stratification remains much more quiescent. Yet, the flows within the stratified layer are of importance for the global dynamics and must not be overlooked. The coupling between the two layers is a key problem in Geophysics and Astrophysics. However, the very broad range of involved time- and length-scales makes the problem quite challenging. As an example for the very disparate scales existing in these problems, let's consider the Sun. It is aged 4.6 Gy (and will live another 5 or 6 Gy before it turns into a red giant), has activity oscillations with a period of 11 years observed since the early 18th, while oscillations as short as 5 minutes are observed at its surface. Regarding length-scales, convective cell patterns at the Sun surface approximately have the surface of France (circle with diameter ~ 1000 km) while the Sun diameter is 1.4×10^6 km (100 times larger than Earth's diameter). Because of these very wide length and time ranges, the investigation of the long-time evolution of these systems remains inaccessible without modelling and parameterizing the small-scale dynamics, all the more so when parameters (Reynolds, Rayleigh, Prandtl, Ekman numbers) describing these flows reach extreme values. The models describing stars evolution, or predicting the evolution of the climate on Earth depend on our understanding of the diverse mechanisms taking place in those systems. Thus, focalized studies are needed to improve our knowledge and awareness of the global impact that small-scale dynamics may have.

To explore the interaction of coupled convective and stratified layers, the direct integration of the Navier-Stokes equations is prescribed because of the diverse scale ranges. In consequence, it remains the possibility to either address the problem through reduced models capturing its fundamentals, or to model the essential ingredients in an experiment.

This manuscript describes the different studies performed in order to enlighten our understanding of the coupling between a convective layer and a stratified layer. The first chapter details basic knowledge on stratified fluids and associated internal gravity waves, with illustrations coming from observations and laboratory experiments. The Quasi-Biennial Oscillation, a peculiar phenomenon observed in the Earth's stratosphere

is also presented. The information given there will be of interest throughout the whole manuscript.

The second chapter describes a theoretical development and numerical integration of stochastically excited internal gravity waves generating large-scale flows through non-linear interactions. This model mainly concerns the Quasi-Biennial Oscillation, but may apply to similar flows taking place in stars and other planets' atmosphere.

The third chapter introduces an attempt to drive an oscillating large-scale flow, similar to the Quasi-Biennial Oscillation, in a laboratory experiment with stochastic forcing. The experiment has the main advantage to be easily compared to the theoretical model developed. Unfortunately, no oscillating flow was observed.

The fourth chapter concerns our experimental study of penetrative convection in water. Penetrative convection, which refers to the interaction of a convective layer with a stratified layer, is briefly presented. The non-linear equation of state of water allows to study the coupling between the two layers in a stationary configuration. The flow observed is thoroughly described and compared to numerical simulations with comparable parameters.

The fifth and last chapter of this manuscript describes a recently designed experiment focusing on penetrative convection with gases as working fluids. Using gases allows to lower the Prandtl number by one order of magnitude compared to water. Low Prandtl numbers are quite relevant for stellar applications but also in order to see the emergence of large-scale flow from internal gravity wave forcing. This experiment being, at first place, motivated by stellar application, the astrophysics context is described at the beginning of the chapter, especially the importance of the overshooting region in stellar models. The experiment was finalised during the last 6 months of the PhD and only a few test experiments could be performed, but preliminary results are quite promising.

The redaction of the present manuscript has been greatly facilitated by the help of the excellent books written by [Sutherland, 2010] and [Vallis, 2017] which detail anything that need to be known about internal gravity waves and geophysical flows. The recent PhD works of [Renaud, 2018] helpled my comprehension of the Plumb's model, and [Alvan, 2014] introduced me into the astrophysics bibliography.

CHAPTER 1

STRATIFIED FLUIDS, INTERNAL GRAVITY WAVES AND LARGE-SCALE FLOWS

Contents

In this chapter, we introduce the physical concepts of a stratified fluid through basic equations and examples. Internal gravity waves will be introduced using some illustrations of their numerous appearances in geophysical and astrophysical flows. They are driven by buoyancy forces, as surface waves, but propagate in a continuously stratified medium. They are known to transport energy and momentum and are able to drive slowly varying large-scale flows, through non-linear processes. The purpose of this chapter is to give the reader basic but essential concepts about internal gravity waves properties, through

a review of literature.
Note that internal gravity waves are sometimes called “gravity waves” or “internal waves”. The former is avoided due to its confusion with surface waves, which are also driven by gravity forces but are confined to an interface between two fluids with different properties. The oscillations are therefore two dimensional. The latter terminology is often used in the atmospheric community. This may be confusing since “internal wave” only signifies that the wave propagates within a medium (for example inertial waves in rotating fluids are sometimes named internal waves). To avoid any confusion, we will name those waves internal gravity waves, sometimes abbreviated as IGWs.

1.1 Stratified fluids

1.1.1 General description

In Latin, “strata” means layers. One could deduce that a stratified fluid is a fluid composed of several distinct layers. This is sometimes obvious in artificial stratified fluid. A good indicative example would be the colourful cocktails served in bars, divided in several layers of different densities (and colours), as pictured in figure 1.1.

Figure 1.1: Photography of several cocktails. The layers with different colours also have different densities.

Stratifications in nature are generally continuous, with the density evolving continuously with height. If relatively dense fluid is located below relatively light fluid, the fluid is stably stratified. On the contrary, if relatively light fluid is located below relatively dense fluid, the fluid is unstably stratified and convective motions can appear, as it is the case in boiling water.

Examples of stratified environment can easily be found in geophysical flows. The stratification in the ocean starts at few hundreds meters deep and is due to the depth variation of both the temperature and salinity (figure 1.2). Temperature is the most determinant factor, except near estuaries where fresh water comes into the ocean. In the Earth’s atmosphere, most weather events take place in the troposphere, which is weakly stratified in the most part, with local convection occurring during daytime. Convection is triggered by light rays coming from the Sun and heating the ground. As times goes, the convective layer becomes thicker. During night time, the convective motions stop and the troposphere goes back to a stratified state. Located above the troposphere, the stratosphere is strongly stratified. Commercial planes fly in this layer to avoid updraft

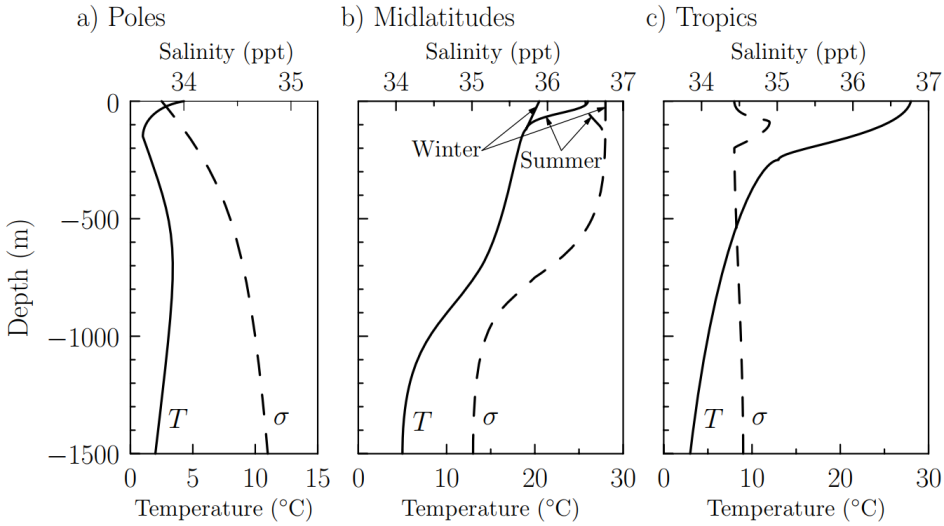

Figure 1.2: Temperature (thick line) and salinity (dash line) profiles in the ocean at different latitudes: poles (a), mid-latitudes (b) and tropics (c). Reproduced from [Sutherland, 2010].

and strong turbulences, which are inhibited by the stratification. The stratosphere is thermally stratified due to the solar radiation absorption by ozone molecules (figure 1.3).

The Earth's internal structure is also divided in layers with different properties. Deep beneath our feet, at $\sim$ 3000 km down, stands the external part of the Earth's core. It is mostly composed of liquid iron and recent evidences [Hirose et al., 2013, Colin and Wong, 2019] suggest that it is partially stratified, either at its inner or outer boundary. The remaining of the outer core is convective and generates the Earth's magnetic field.

Other astronomical objects present stratified environments. Stars are divided in several layers, each characterised by different properties. The Sun, for example, is composed of two main layers (left panel of figure 1.4). The innermost is the radiative core which is stably stratified and where the fusion of hydrogen into helium occurs. Energy in this layer is transported outward radiatively. The outermost layer is convective and energy is also transported outwards. Oppositely, massive stars have a convective core and a radiative outermost layer.

In stably stratified fluids, vertical motions are limited because of the density and pressure evolution with height: it requires energy to move through a stratification since fluid will experience a restoring force acting in the direction opposite to displacement due to buoyancy differences with the environment. Hence, large-scale vertical motions are inhibited. However, one should not infer that vertical displacement cannot occur in a stratification: oscillations involving vertical motions are observed in stratified environments and thus exist in the Earth's atmosphere, oceans, core and in stars.

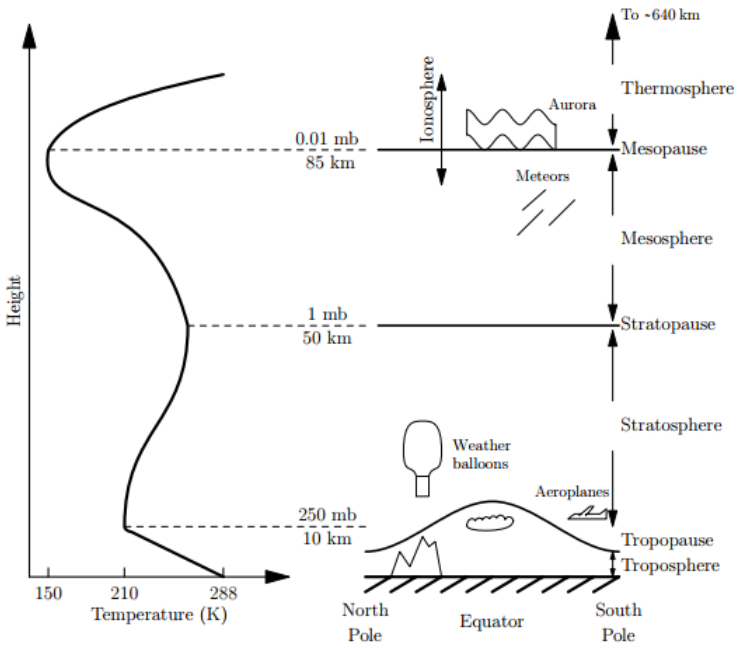

Figure 1.3: Temperature profile in the Earth's atmosphere. The profile is stable in both the troposphere and stratosphere. Yet, instabilities locally appear in the troposphere and convection is triggered. Reproduced from [Sutherland, 2010].

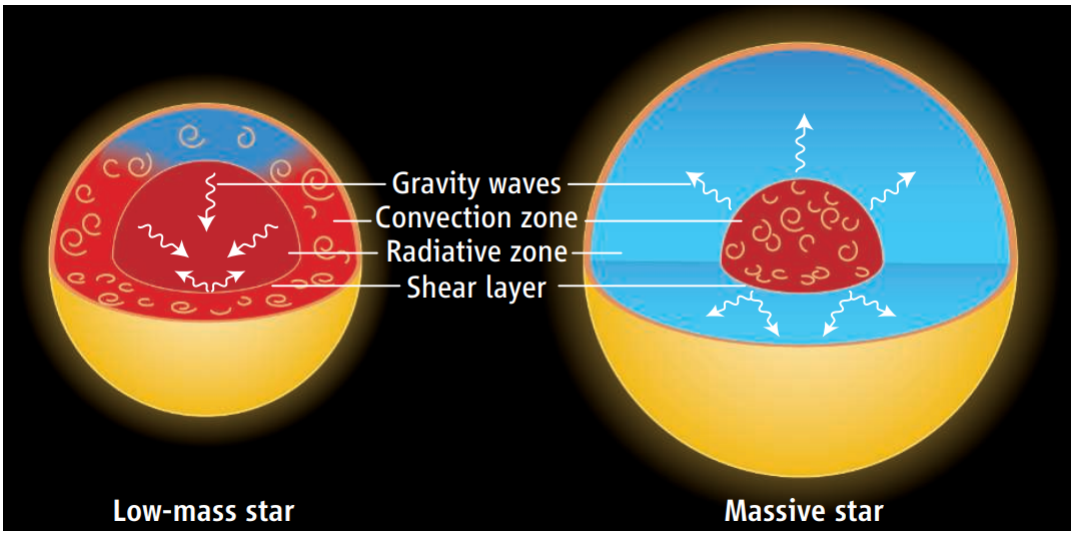

Figure 1.4: Schematic representation of the structure of stars depending on their mass. Reproduced from [Charbonnel and Talon, 2007].

1.1.2 Oscillatory motions in stratified fluid

A gravity wave or surface wave is a gravity-driven wave which propagates at the interface between two fluids. One has inevitably seen the pattern of concentric rings formed by a small rock thrown at a lake, or the surface waves generated in the wake of sailing boats. Surface waves make the free surface move up and down due to buoyancy. Fluid lifted upward is heavier than its surroundings and then falls downward. It overshoots its equilibrium position due to the inertia accumulated and a restoring force lifts the displaced surface upward again. The fluid oscillates in space and time in a spring-like motion.

An internal gravity wave can be pictured as a gravity wave propagating within a fluid (figure 1.5). In a stably stratified fluid, internal gravity waves can propagate vertically and horizontally and are not confined to an interface. Just like surface waves, the mechanism of internal gravity waves can be summed up as follows: in a stably stratified fluid, when a parcel of fluid is lifted above its equilibrium position, it experiences a downward acceleration due to gravity, as it is surrounded by lighter fluid. The parcel falls due to gravity force and overshoots its equilibrium position because of the inertia gained. It becomes surrounded by heavier fluid and experiences an upward acceleration due to buoyancy and moves upward. Inertia makes the parcel overshoots its equilibrium position and so on.

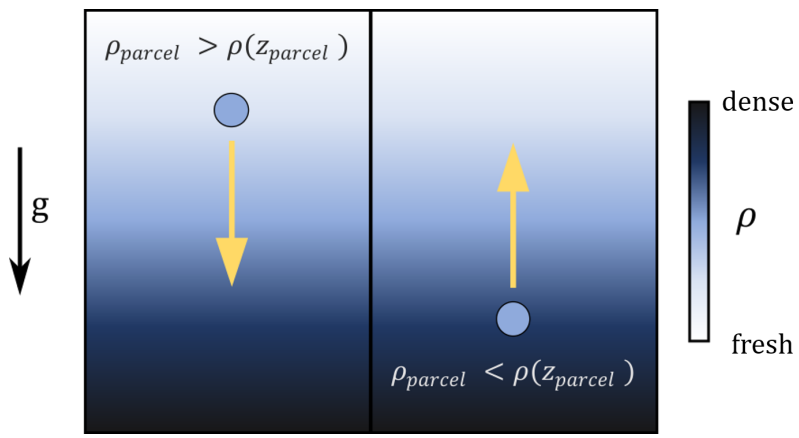

Figure 1.5: Schematic of a fluid particle oscillating around its equilibrium position in a stratified fluid. The restoring forces involved are the buoyancy force and the gravity force.

In an inviscid fluid, a fluid parcel trapped in an internal gravity wave oscillates around its equilibrium position at a frequency given by the buoyancy frequency and the dispersion relation of internal gravity waves (both will be introduced in detail in the next paragraph). Internal gravity waves need a stably stratified medium to propagate since the buoyancy forces are the driving mechanism of the oscillation.

Let us consider a stably stratified fluid with gravity pointing downward. The background density ρ_{bg} decreases with height. We consider a fluid parcel of density ρ_0 located at $z = z_0$. This parcel is moved vertically by a small distance δ_z (figure 1.6). Neglecting dissipative process, Newton's second law gives, along the vertical z axis:

$$\rho_0 \frac{\partial^2 \delta z}{\partial t^2} = -g\,\delta\rho \tag{1.1}$$

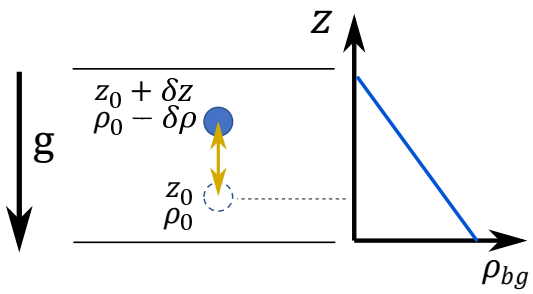

Figure 1.6: Schematic of a fluid parcel, initially at $z = z_0$ and at $\rho = \rho_0$, being displaced by a small distance δz and surrounded by fluid at a density $\rho_0 - \delta\rho$.

Since δ_z is small, we can write:

$$\delta\rho \simeq -\frac{\mathrm{d}\rho_{bg}}{\mathrm{d}z}\delta z \tag{1.2}$$

In a stably stratified fluid, density decreases with height: $\frac{\mathrm{d}\rho_{bg}}{\mathrm{d}z} < 0$. Equation (1.2) indicates the fact that a parcel displaced upward is denser than the surrounding fluid. This leads to:

$$\rho_0 \frac{\partial^2 \delta z}{\partial t^2} - g\frac{\mathrm{d}\rho_{bg}}{\mathrm{d}z}\delta z = 0 \tag{1.3}$$

We introduce the buoyancy frequency N (also known as Brunt-Väisälä[1] frequency):

$$N^2 = -\frac{g}{\rho_0}\frac{\mathrm{d}\rho_{bg}}{\mathrm{d}z} \tag{1.4}$$

Therefore, combining equation (1.3) with the expression of the buoyancy frequency N (1.4), we have:

$$\frac{\partial^2 \delta z}{\partial t^2} + N^2 \delta z = 0 \tag{1.5}$$

Equation (1.5) is the equation of a harmonic oscillator with angular frequency N. Purely vertical motions oscillate at the buoyancy frequency. However, internal gravity waves propagate vertically and horizontally. A fluid parcel would oscillate along a diagonal line l characterised by an angle θ with gravity (see figure 1.7). Newton's law along this line can be written:

$$\rho_0 \frac{\partial^2 \delta l}{\partial t^2} = -g\,\delta\rho\,\cos\theta \tag{1.6}$$

Writing once again the density perturbation as z-derivative of the background density, *i.e.* $\delta\rho = -\frac{\mathrm{d}\rho_{bg}}{\mathrm{d}z}\,\delta l\,\cos\theta$, we have:

$$\frac{\partial^2 \delta l}{\partial t^2} + N^2 \cos^2\theta\;\delta l = 0 \tag{1.7}$$

Consequently, a fluid parcel moving in a stably stratified fluid along a line at an angle θ from the downward gravity oscillates at a frequency given by:

$$\omega = N\cos\theta \tag{1.8}$$

[1]Sir David Brunt (1886–1965) was a Welsh meteorologist, professor at the Imperial College in London. Vilho Väisälä (1889–1969) was a Finnish meteorologist and physicist and a professor at the University of Helsinki.

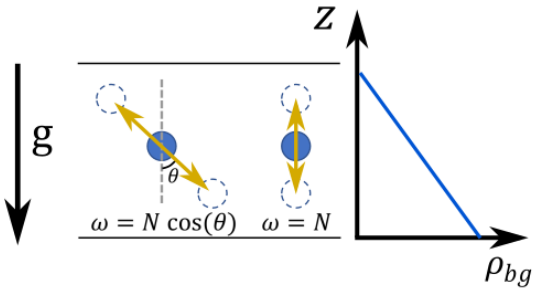

Figure 1.7: Schematic of a fluid particle, oscillating vertically at $\omega = N$ or oscillating at $\omega = N\cos(\theta)$ along a diagonal line.

Equation (1.8) is the dispersion relation of internal gravity waves in an inviscid fluid and links the frequency of the wave with its direction of propagation θ. The implications of this relation will be discussed in section 1.2.1 and a more complete dispersion relation, taking into account dissipative processes, will be derived in chapter 2. Note that if the stratification is linear, meaning that the density ρ_{bg} decreases linearly with height, the buoyancy frequency N is independent of z.

1.2 Internal gravity waves

1.2.1 Propagation properties

The derivation of the dispersion relation by applying Newton's law on a fluid parcel may be intuitive but usually, the dispersion relation is directly derived from the Navier-Stokes equations. In a two-dimensional, diffusionless and incompressible fluid, they write:

$$\rho_0 \frac{\mathrm{D}u}{\mathrm{D}t} = -\frac{\partial P}{\partial x} \tag{1.9a}$$

$$\rho_0 \frac{\mathrm{D}w}{\mathrm{D}t} = -\frac{\partial P}{\partial z} - g\rho \tag{1.9b}$$

$$\frac{\mathrm{D}\rho}{\mathrm{D}t} = -w\frac{\partial \rho_{bg}}{\partial z} \tag{1.9c}$$

$$\nabla \cdot \mathbf{u} = 0 \tag{1.9d}$$

where ρ is the density anomaly compared to the background density ρ_{bg}. In the absence of any mean flow and considering small amplitude waves (*i.e.* small u, w and ρ), advection terms in the material derivatives can be neglected since they are small (they are proportional to the amplitude squared) compared to linear terms (proportional to the amplitude). Thus we can replace each $\frac{\mathrm{D}}{\mathrm{D}t}$ by $\frac{\partial}{\partial t}$.

The four coupled differential equations in (1.9) can be written into a matrix form and solved using matrix algebra. Equations (1.9) can be written:

$$\mathcal{A}\begin{pmatrix} u \\ w \\ \rho \\ P \end{pmatrix} = \mathbf{0} \tag{1.10}$$

with $\mathcal{A} = \begin{pmatrix} \partial_t & 0 & 0 & \frac{1}{\rho_0}\partial_x \\ 0 & \partial_t & \frac{g}{\rho_0} & \frac{1}{\rho_0}\partial_z \\ 0 & -\frac{\rho_0}{g}N^2 & \partial_t & 0 \\ \partial_x & \partial_z & 0 & 0 \end{pmatrix}$.

The fluid is considered linearly stratified. N, as defined in (1.4), is therefore constant. Non trivial solutions are defined by $\det \mathcal{A} = 0$. Consequently, small amplitude internal gravity waves can be described by:

$$\left[\partial_{tt}\nabla^2 + N^2\partial_{xx}\right] b = 0 \tag{1.11}$$

b being one the four fields u, w, ρ or P. In practice, b can be any field linearly related to these four basic fields, such as vorticity or streamfunction. Considering an infinite domain in both x and z directions, solutions can be written:

$$b(x, z, t) = A_b\, e^{i(k_x x + k_z z - \omega t)} \tag{1.12}$$

with A_b being the amplitude at the source of the internal gravity wave, k_x (resp. k_z) the wavenumber in the horizontal (resp. vertical) direction and ω the angular frequency. Thus the matrix $\mathcal{A}$ becomes:

$$\mathcal{A} = \begin{pmatrix} -i\omega & 0 & 0 & \frac{1}{\rho_0}ik_x \\ 0 & -i\omega & \frac{g}{\rho_0} & \frac{1}{\rho_0}ik_z \\ 0 & -\frac{\rho_0}{g}N^2 & -i\omega & 0 \\ ik_x & ik_z & 0 & 0 \end{pmatrix} \tag{1.13}$$

Computing $\det \mathcal{A} = 0$, we obtain the dispersion relation of the internal gravity waves in a xz-plane, for an inviscid fluid:

$$\frac{\omega^2}{N^2} = \frac{k_x^2}{k_x^2 + k_z^2} \tag{1.14}$$

If we write $\theta = \tan^{-1}(k_z/k_x)$, we recover the dispersion relation as written in (1.8): $\omega = N\cos\theta$. A consequence of the dispersion relation is that internal gravity waves cannot oscillate at a frequency higher than the buoyancy frequency (since, at least for real values of k_x and k_z, $k_x^2 + k_z^2 \geqslant k_x^2$). Waves that oscillate at $\omega = N$ have their crests aligned with the z axis, since $\omega = N$ implies that $k_z = 0$. As the wave frequency diminishes, the angle of propagation tilts and becomes parallel with the x axis for very low frequency ω.

The dispersion relation also implies that the direction of phase propagation $\mathbf{k} = (k_x; k_z)$ depends on the frequency of the waves. This means that internal gravity waves which propagate at fixed frequencies have their phase line aligned at a constant angle θ with the vertical.

Figure 1.8 shows a snapshot of the vertical velocity field generated by a vertically oscillating horizontally-aligned cylinder within a linearly stratified fluid. Since the frequency of the internal gravity waves is given by the oscillation frequency of the cylinder, the phase line of generated internal gravity waves must be oriented at constant angle θ given by the dispersion relation. This results in a cross-shaped wave pattern, often referred as St Andrew's cross. The sketch shows the phase and group velocities for each beam. If one takes a closer look at one of the four beams, one shall see that internal gravity waves

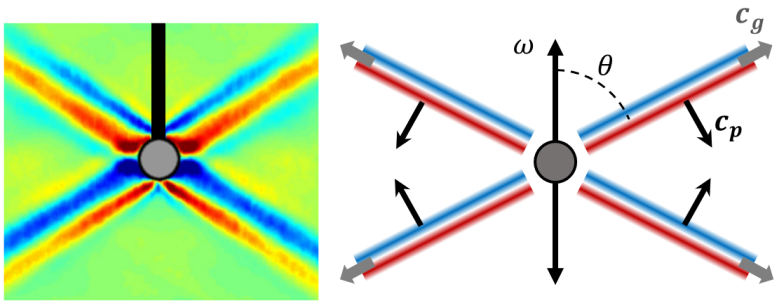

Figure 1.8: (Left) Snapshot of vertical velocity field showing internal gravity waves patterns generated by an oscillating cylinder within stratified water. Because the frequency of oscillations is set by the cylinder, the angle of propagation θ is imposed by the dispersion relation (1.8). The resulting pattern is often refered as St Andrew's cross. Gravity is pointing downward. Reproduced from [Gostiaux, 2006]. (Right) Schematic illustrating the St Andrew's cross pattern and showing the corresponding phase and group velocities.

are characterised by a shear between two crests. Internal gravity waves are also characterised by a phase velocity orthogonal to its group velocity. Moreover, the z-components of phase and group velocities are always of opposite sign: if the group velocity points upward, phase crests will go downward.

These features can be derived mathematically from the definition of phase and group velocities. Phase velocity is by definition:

$$\mathbf{c_p} = \frac{\omega}{|\mathbf{k}|}\mathbf{k} = \frac{\omega}{|\mathbf{k}|}\begin{pmatrix} k_x \\ k_z \end{pmatrix} \tag{1.15}$$

It can pictured as the speed at one would move if one sit on a wave crest.

The group velocity is more delicate to understand. It is yet a quite important concept since it describes the velocity at which energy is transported by the wave. Phase velocity and group velocity do not necessarily point to the same direction, so one cannot infer where energy is transported by looking at crests displacement. Group velocity is given by:

$$\mathbf{c_g} = \nabla_{\mathbf{k}}\,\omega \tag{1.16}$$

where $\nabla_{\mathbf{k}} = (\partial_{k_x}; \partial_{k_z})$.
Using the relation dispersion (1.14), we can write the group velocity as:

$$\mathbf{c_g} = \mathrm{sign}(k_x)\frac{N}{|\mathbf{k}|^3}\begin{pmatrix} k_z^2 \\ -k_x k_z \end{pmatrix} \tag{1.17}$$

It is straightforward that $\mathbf{c_p}.\mathbf{c_g} = 0$. The phase and group velocities are orthogonal. We also see that z-components of phase and group velocities are of opposite sign. Indeed, $-\mathrm{sign}(k_x) \times k_x$ is always negative. Therefore, the z-component of group velocity is always equal to $c_{gz} = -K\,k_z$ with $K = \frac{N}{|\mathbf{k}|^3}|k_x|$ a positive prefactor.

Generally, when a wave encounters a wall, the angle of incidence is equal to the angle of reflection, following the Snell-Descartes law. Due to their dispersion relation, internal

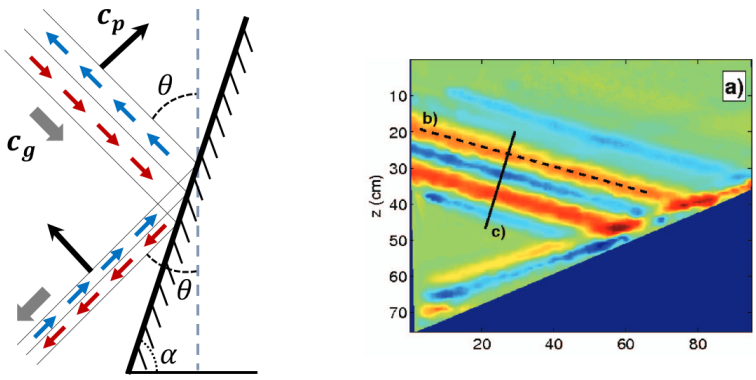

Figure 1.9: (Left) Schematic showing an internal gravity wave propagating towards a wall. The wave is reflected downward, keeping the same angle θ but with opposite sign for the horizontal wavenumber. The values of k_x and k_z may change but still verify the dispersion relation. (Right) Experience showing the reflection of an internal gravity wave at nearly the critical angle $\alpha = \frac{\pi}{2} - |\theta|$. The wave is reflected both upslope and downslope. Figure reproduced from [Gostiaux, 2006].

gravity waves exhibit a peculiar reflection mechanism. Indeed, as frequency ω is conserved, that leaves fixed values of θ for the reflected wave. Left panel of figure 1.9 show a sketch of an internal gravity wave impacting a surface. To conserve its angle of propagation θ (fixed by its frequency ω), the wave can only be reflected downward. Note that the energy is focused after the reflection in this case (crests get closer to each other after the reflection). A critical angle exists ($\alpha = \frac{\pi}{2} - |\theta|$) for which the internal gravity waves is reflected both upslope and downslope. This is shown in right panel of figure 1.9.

1.2.2 Internal gravity waves in geophysical flows

Observation in the atmosphere and oceans

Various mechanisms give birth to the internal gravity waves observed in the atmosphere. They are partly generated at the tropopause by the turbulent convective motions of the troposphere. Figure 1.10 shows satellite observation of an internal gravity wave train generated during a thunderstorm. In the right panel, a characteristic pattern of concentric rings can be seen, with the centre located at the position of thunder activity shown in left panel. During the morning day, the troposphere is stably stratified. It becomes convective as day goes by and as the sun heats the ground, triggering convective motions. Sometimes, in very specific atmospheric conditions, internal gravity waves may form within the troposphere. A quite odd example is the Morning Glory clouds (see figure 1.11) forming regularly in the northern Australia at low altitude such that glider pilots can ride the waves.

Internal gravity waves can be generated by winds impinging on topography. Such waves are named lee waves or orographic waves. They can be observed from satellite observations as they form a pattern of lenticular clouds in the wake of the mountain. Figure 1.12 shows a famous observation of Lee waves by NASA over the Amsterdam island in the Indian ocean.

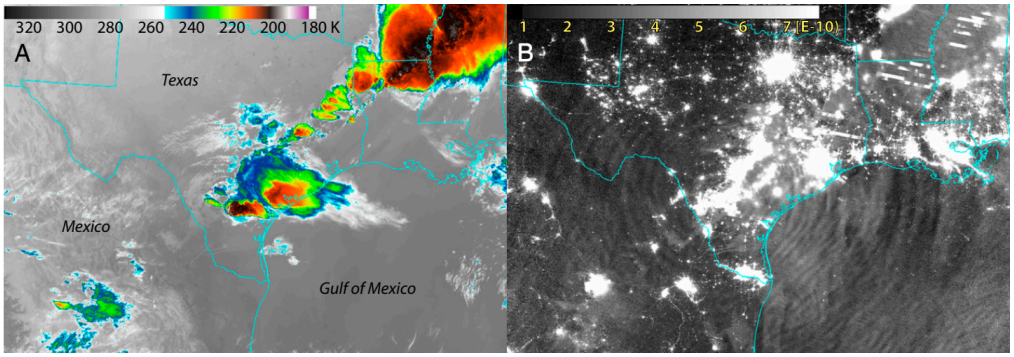

Figure 1.10: Figure reproduced from [Miller et al., 2015]. (Left) Thermal infrared brightness temperature showing a line of thunderstorms in southern Texas. Red and dark patches denotes deep convection overshooting the tropopause. (Right) Night-glow imagery. Bright patches are either light from cities or lightning flashes. A very distinct pattern of concentric rings emerges from the storm, enlightening the internal gravity waves formation. Observations are dated 4 April 2014 at 02:15 AM local time.

Figure 1.11: Photography of the Morning Glory clouds taken from an airplane. The phenomenon occurs at altitude 100 m $< z <$ 2000 m, in a few locations all around the world. The Morning Glory clouds forming over the southern part of the Gulf of Carpentaria are the most frequent. Credits for the photography: Wikimedia - Mick Petroff.

Internal gravity waves are also observed in the ocean, driven either by streams moving above varying bathymetry, or by surface forcing induced by the wind. Internal gravity waves can sometimes be observed at the East of Gibraltar strait (see right panel of figure 1.13). They are generated by Atlantic cold water entering the Mediterranean sea and flowing above the strongly varying bathymetry of the strait (shown on the left panel of figure 1.13).

Note finally that internal gravity waves are also observed in other planets' atmosphere, *e.g.* in Venus [Fukuhara et al., 2017] and Jupiter [Arregi et al., 2009].

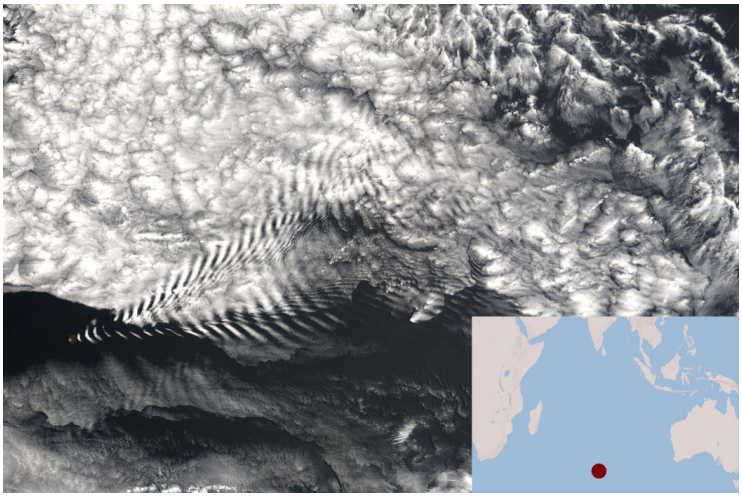

Figure 1.12: Lee waves observed by the Terra satellite in the wake of the Amsterdam island in the south of the Indian ocean, on March 26 2015. The wave are observed thanks to a pattern of lenticular clouds. Source: NASA - https://earthobservatory.nasa.gov/images/6151/wave-clouds-near-amsterdam-island

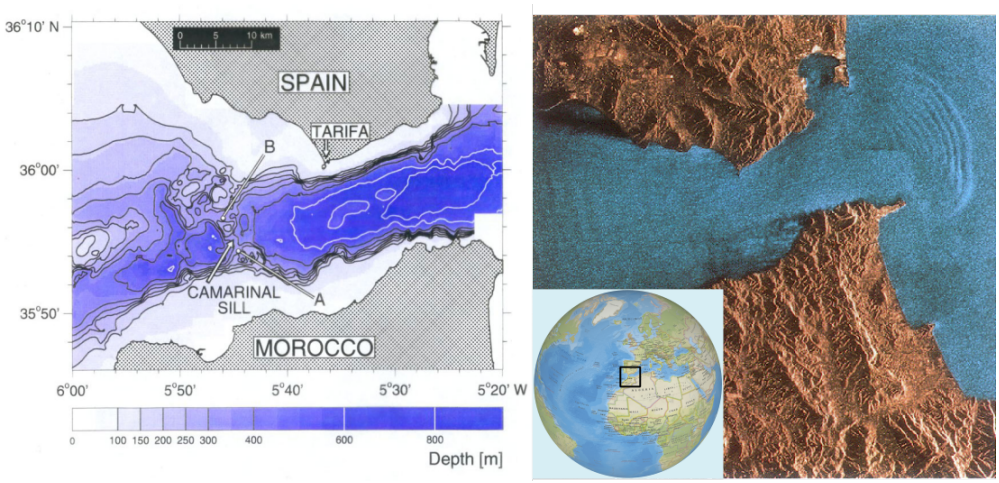

Figure 1.13: Internal gravity waves can be observed in the Gilbraltar strait. (Left) Bathymetry of the Gilbraltar strait. Figure reproduced from [Brandt et al., 1996]. (Right) Observations from the satellite ERS-1, dated from novembre 2006. Credits: ESA - http://www.esa.int/ESA_Multimedia/Images/2006/11/Strait_of_Gibraltar_as_seen_by_ERS-1

Global Circulation Models and internal gravity waves

The global flows in the Earth's atmosphere and oceans are simulated numerically with Global Circulation Models (hereafter GCMs). GCMs are mathematical models which integrate the Navier-Stokes equations to predict the evolution of the associated flow fields (velocity, temperature, pressure, humidity, *etc.*). However, geophysical flows are characterised by very different length- and time-scales. As an example, length-scales for the atmosphere range from less than 1 km (which is called the microscale) to $\geqslant 1000$ km (which is the synoptic scale). Longest wavelengths for planetary waves can reach 10000 km. The separation for time-scales in the atmosphere is also important with scales of a few days for a cyclone and $3-4$ years for El Niño Southern Oscillation (ENSO). Comparatively, small and fast internal gravity waves have horizontal wavelengths around $1-100$ km and associated periods are from fraction of an hour to few hours [Fritts and Alexander, 2003, Alexander, 1996]. For the ocean, the scale separation is also seen with waves having amplitudes between $10-100$ m, periods close to an hour and horizontal wavelengths of several kilometers, and large-scale oceanic motions having periods going up to tens of years and wavelengths of thousands of kilometres [Alford et al., 2015]. Hence, GCMs reproducing the global dynamics over decades have a resolution too coarse to reproduce satisfactorily the dynamics of small-scale events, such as internal gravity waves. Nonetheless, accounting for small-scale dynamics is crucial in order to capture large-scale phenomena adequately (see section 1.3). Therefore, lots of waves are included in GCMs via parametrisation (some are resolved). A big problematic in geophysical fluid dynamics is to parametrise properly the waves in order to create, within the numerical model, realistic phenomena.

1.2.3 Internal gravity waves in stars

Internal gravity waves are present and propagate in the radiative zone of stars. They are a key components of the study of their vibrations. Asteroseismology [2], as it is named, is the study of vibration modes of stars by measuring luminosity and surface radial speed fluctuations. Their internal structure affects wave propagation and, therefore, waves contain information about the medium they travelled through. Thus, by analysing waves and modes, one can deduce the internal structure of stars.

The star at the centre of our planetary system is particularly observed. The study of the Sun started in the 17th century with Galilée and Scheiner, but helioseismology (asteroseismology applied to the Sun - *helios* is greek for Sun) started in the 1960s with the detection of the "5-minutes oscillations" [Leighton et al., 1962] corresponding to small patches of the Sun surface oscillating up and down. Using helioseismology data, [Spiegel and Zahn, 1992] discovered an intermediate layer, located between the convective and radiative zone: the tachocline. *Tachos* can be translated by speed and *kleinen* by gradient. The tachocline is thus a very thin layer characterised by a strong shear in azimuthal speed and it deeply affects internal wave propagation in the Sun [Rogers and Glatzmaier, 2006]. The thickness of this layer is $0.01R_\odot$, $R_\odot$ being the radius of the Sun.

[2] The name "astroseismology" is also used, but is much less frequent

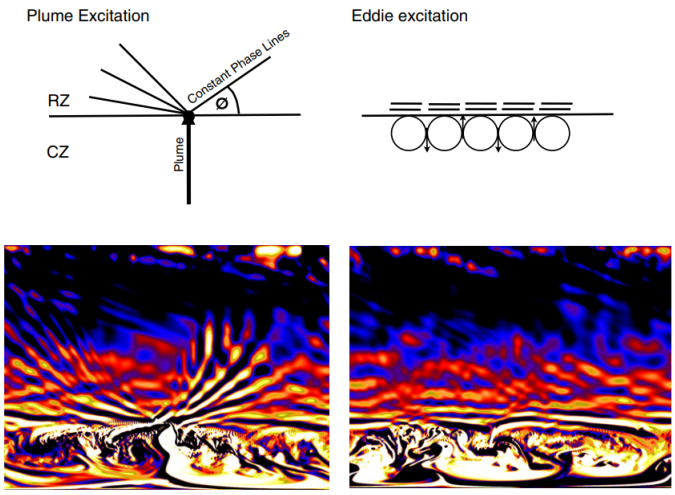

Figure 1.14: The top panels show schematic of the excitation mechanisms: plume excitation (left) and eddy excitation (right). Bottom panels show instantaneous vorticity fields. High frequency waves are generated by plume incursions (constant phase lines are inclined) while the eddy excitation generates mostly low frequency waves (horizontal phase lines). Figure reproduced from [Rogers et al., 2013].

The vibrations measured in stars are generated by different mechanisms:

- a stochastic forcing of internal gravity waves by the convective layer. Two phenomena participate in the wave generation: the fluctuations of the Reynolds stress in the convective layer and the penetration of the convective plumes within the radiative layer. The former results in the generation of low-frequency waves [Rogers et al., 2013]. The latter results in the generation of higher frequency waves (see illustration of the two mechanism in figure 1.14),
- the κ mechanism. It mainly concerns the intermediate and massive stars. Variations in the opacity of the star results in variations of the heat flux, resulting in self-sustaining oscillations,
- the ϵ mechanism. Oscillations are induced by the variations in the energy production rate by the nuclear fusion reaction in the core,

The stochastic forcing strongly relates to this manuscript, since it involves turbulently-generated internal gravity waves.

The vibration modes observed at the surface are a combination of pressure modes (p-mode) and internal gravity wave mode (g-mode). The former have a strong signal and are therefore easy to observe. However, g-modes are evanescent in the convective layer and their signals at the star surface is of same order of magnitude as noise. They are therefore quite difficult to observe. To untangle their signal from background noise is capital to study stellars' interiors. Futhermore, waves are also invoked in chemicals mixing and transport in the Sun. [Charbonnel, 2005, Rogers and McElwaine, 2017]. For these reasons, internal gravity waves are a key ingredient of stars dynamics. Hence, to entirely understand their dynamics and their generation by the stochastic excitation mechanism is crucial in order to improve stellar models.

1.2.4 The effect of rotation: inertial gravity waves

The rotation of planets and stars affect the properties of the waves, especially if the rotation frequency is of same order of greater than the buoyancy frequency. Internal gravity waves, taking into account the rotation, are called inertial gravity waves and their dispersion relation differs from equation 1.8. In a f-plane approximation, it writes:

$$\omega^2 = \frac{N^2 k_x^2 + f^2 k_z^2}{k_x^2 + k_z^2} \tag{1.18}$$

where $f = 2\Omega \sin(\varphi)$ is the Coriolis parameter, Ω being the rotation rate and φ the latitude. The frequency of internal gravity waves affected by the rotation can take values delimited by: $f < \omega < N$. In Earth's atmosphere and oceans, $f \ll N$.

In this manuscript the effect of rotation will not be considered and we therefore only consider internal gravity waves.

1.3 Interactions of internal gravity waves with their environment

As internal gravity waves propagate in a stratified fluid, they interact with the environment via the mixing they generate and the momentum, temperature, chemicals, *etc.* they transport. The striking example of the Quasi-Biennial Oscillation, a phenomenon driven by internal gravity waves will be an important part of this manuscript and will be introduced at the end of this section.

1.3.1 Mixing and breaking

During the internal gravity wave propagation, linear mechanisms damp the wave. Wave attenuation is mostly due to radiative damping in the atmosphere and viscous dissipation in the ocean. As mentioned before, internal gravity waves are shear waves. This shear may create some small-scale mixing along the wave propagation. Since internal gravity waves are often not resolved in models, mixing is modelled by an eddy diffusivity which is orders of magnitude higher than molecular diffusion. Turbulent mixing is invoked to explain why the ocean is stratified. Indeed, considering only thermal diffusivity ($\kappa \sim 10^{-7}$ m$^2 \cdot$ s^{-1}) or salt diffusivity ($D \sim 10^{-9}$ m$^2 \cdot$ s^{-1}) and assuming a global average vertical velocity $w = 10^{-7}$ m $\cdot$ s^{-1} (compute from a global mean of bottom water production), typical length scales for the stratification in the ocean would be ~ 1 m or 10^{-2} m [Wunsch and Ferrari, 2004]. These values are a lot smaller than the actual ocean depth. Another mechanism to transport buoyancy through the ocean is therefore needed: this is the eddy diffusivity, modelling the turbulent mixing, which typical value is $10^{-4} - 10^{-3}$ m$^2 \cdot$ s^{-1} [3].

When non-linearities are involved, waves can become unstable and break or generate secondary waves [Staquet and Sommeria, 2002]. Those mechanisms induce a strong mixing locally and change the stratification. These non-linear behaviours increase hugely the

[3] The eddy diffusivity models mixing coming from different phenomena, including, but not only, internal gravity waves.

local eddy diffusivity. As a result, density gradients are locally smoothed and vertical transport of chemicals is enhanced. Internal gravity waves deeply impact the turbulent mixing in the ocean [Kunze, 2017] and are invoked in the transport of bioelements. [Moore and Lien, 2007] found that whales gather in very specific location in the China sea, where internal gravity waves bring high concentration of plankton.

1.3.2 Internal gravity waves in a shear flow

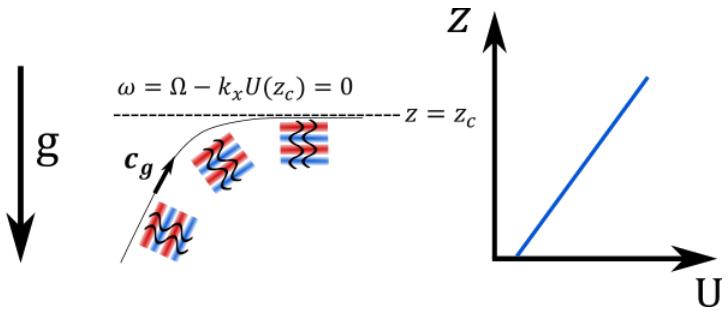

Figure 1.15: Schematic of the mechanism of a critical layer. While propagating in a vertically sheared, horizontal flow, the wave is Doppler-shifted. At a critical level, $\omega = 0$ and the energy is locally deposited.

Internal gravity waves propagating in a flow with an horizontal velocity $\overline{U}$ see their propagation properties altered by the ambient flow. Indeed, the frequency is Doppler shifted towards lower (resp. higher) frequencies for prograde (resp. retrograde) waves [4]. The Doppler-shifted frequency is:

$$\omega = \pm\Omega \mp k_x \overline{U} \tag{1.19}$$

with Ω the absolute frequency of the wave, k_x its horizontal wavenumber. The sign $\pm$ depends on the direction of the waves. One can see that, for a critical value of the ambient flow speed $\overline{U} = \pm\frac{\Omega}{k_x}$, the Doppler-shifted frequency goes to zero $\omega = 0$. Let's consider the example shown in figure 1.15. As the prograde wave propagates upward, the mean-flow increases. Thus the Doppler-shifted frequency lowers and the angle of propagation becomes more and more horizontal. When the wave reaches the altitude at which $\overline{U}$ is equal to the critical value, the frequency is zero and the propagation is purely horizontal. This location is called a critical layer. At the critical layer, the wave is absorbed and the energy is given to the ambient flow, resulting in a significant acceleration [Booker and Bretherton, 1967]. This phenomenon is really primordial for geophysical and astrophysical context [Alvan et al., 2013]. Figure 1.16 shows the phenomenon of the critical layer reproduced in a laboratory experiment [Koop, 1981]. The prograde wave propagate in a shear flow and its trajectory, marked by the shadowgraph photography, illustrates the tilting of the wave propagation towards the horizontal. Additionally, the reflection of the retrograde wave when $\omega = N$ is also visible.

[4] A prograde wave is going in the same direction as the mean flow, while the retrograde wave propagates in the opposite direction as the mean flow.

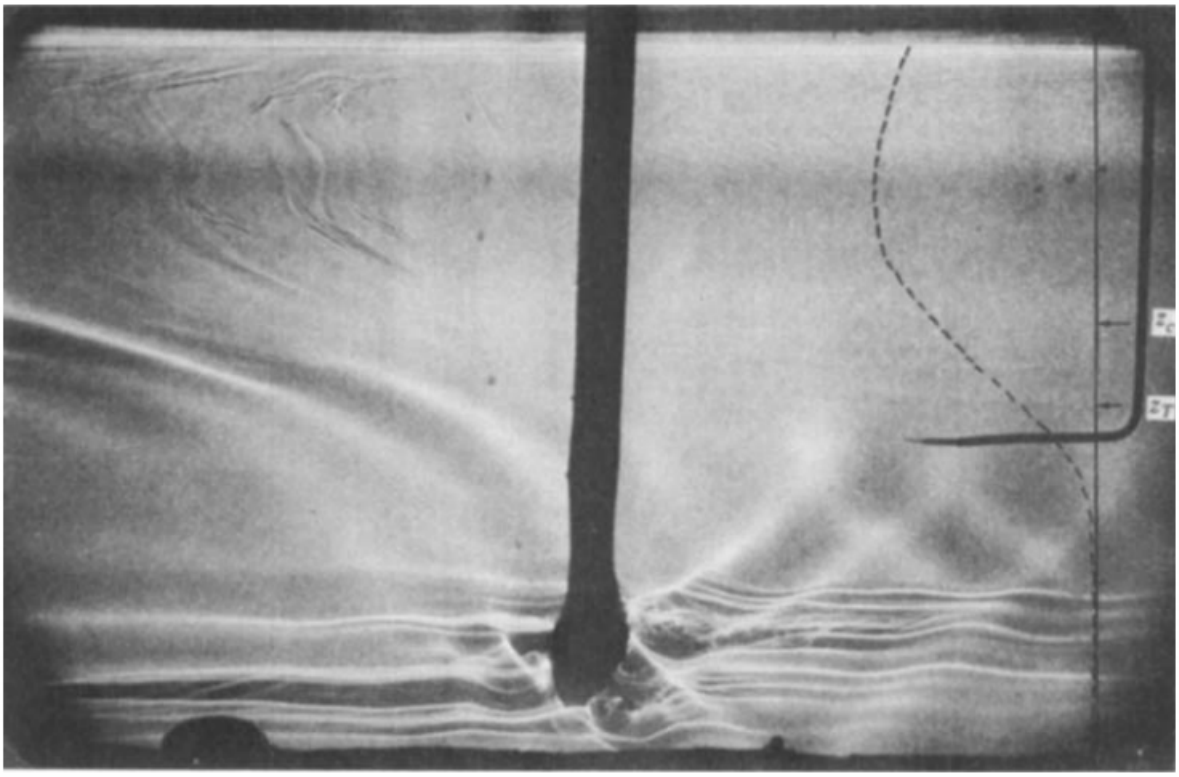

Figure 1.16: Shadowgraph photography of a critical layer visualisation in a shear flow. The cylinder at the centre of the frame is oscillating at a fixed frequency and the vertical profile of the horizontal velocity in the channel is shown by the dashed line at the right side of the photography. At the left of the cylinder, the wave propagation is affected by the shear and tilts horizontally. On the right of the cylinder is also observable the turning point level, at which the wave frequency reaches $\omega = N$ and is thus reflected downward. Reproduced from [Koop, 1981].

Figure 1.17 is reproduced from [Thorpe, 1975] and shows the different mechanisms generating internal gravity waves in the ocean, as well as physical concepts applying to their propagative behaviours such as critical layers and turning point level described in the next paragraph. It gives a good summary of the concepts introduced in this subsection and in section 1.2.

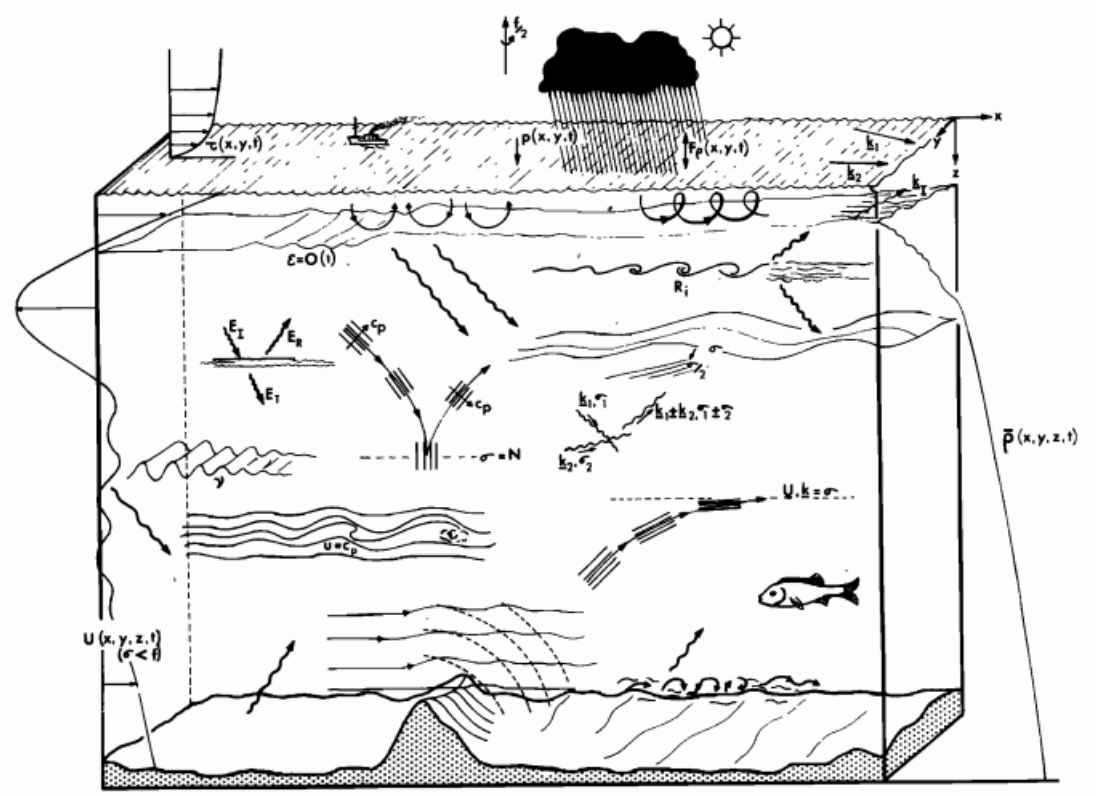

Figure 1.17: This figure from [Thorpe, 1975] sums up generation mechanisms for internal gravity waves in the ocean, and some of their propagating properties (all are applicable to atmospheric and stellar flows). About the generation mechanisms, one can see the turbulent layer at the top of the ocean. The turbulent motions generate internal gravity waves at the interface with the stratified layer. Turbulence also occurs at the bottom of the ocean when water flows over an irregular floor, and internal gravity waves are generated. At the bottom of the ocean, one can also see orographic waves generated by high topography, very similar to the illustration in figure 1.12. Internal gravity waves are also generated from Kelvin-Helmoltz instabilities. About the propagating behaviour, one can see the representation of tunnelling effect when a wave encounter an interface with an unstratified layer. Part of the wave is reflected, and another part can go through the unstratified layer and propagate again in the other side of the unstratified layer. We also see internal gravity wave reflecting when the Doppler-shifted frequency is equal to the buoyancy frequency N. About wave dissipation, one can see the kinematic viscosity ν slowly damping the wave. Internal gravity waves encounter a critical layer when the Doppler shifted frequency goes to 0 (see section 1.3.2). At the critical level, the wave experiences overturning and energy is dissipated locally. Overturning is also represented here.

1.3.3 Large-scale flows driven by waves

Experiments of acoustic streaming

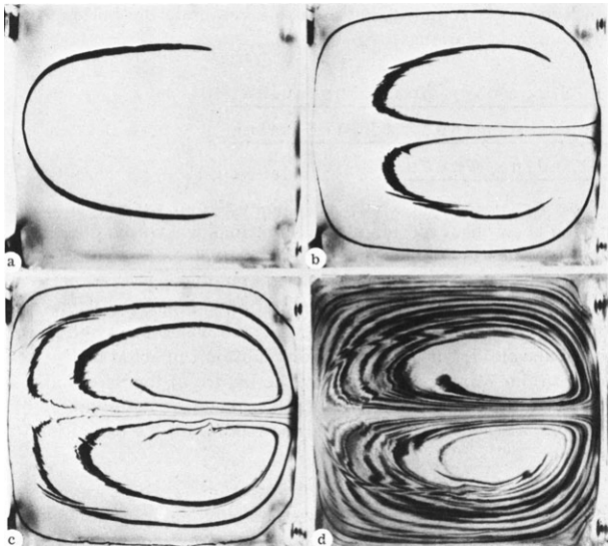

Figure 1.18: Evolution of a large-scale flow induced by acoustic streaming. Snapshots show different times. The visualisation is made at the interface of two immiscible fluids. The quartz generating ultrasound is located at the centre of the right wall. Figure reproduced from [Zarembo, 1971].

During their propagation, waves attenuate and exchange momentum with the ambient flow. Under certain conditions, they can generate and sustain a slowly-evolving large-scale flow. Large means that there is a length-scale separation between the wave and the driven flow. In the same way, slowly implies that the flow evolves at time-scales much larger than the wave time-scale. Very visual illustrations of flows driven by waves can be found in acoustic streaming experiments (see [Lighthill, 1978] for an introduction of the topic). Figure 1.18 shows the time evolution of a large-scale flow driven by a quartz generating ultrasound. Ink is used to mark the streamlines of the two contra-rotating cells generated. A video of a recent experiment on acoustic streaming can also be found here: `https://www.youtube.com/watch?v=ArpclLD4yP8`. The large-scale flow generation comes from the non-linear term of the Navier-Stokes equations. Hence, wave–mean-flow interactions exist with many type of small-scale oscillations, including internal gravity waves, whose specific propagation properties can drive reversing flows.

Internal gravity waves and The Quasi-Biennial Oscillation

In the atmosphere, oscillations of equatorial winds are observed in the stratosphere. This was observed when, in 1883 [Baldwin et al., 2001], a volcano erupted, throwing ashes in the stratosphere. The ash clouds were observed to travel from east to west. In 1908, A. Berson, a German meteorologist, launched balloons and found that winds were blowing in the opposite direction: they were directed eastward [Süring, 2013]. More advanced radiosonde measurements in the 60s from two independant studies [Reed et al., 1961,Ebdon, 1960] led to the first description of the Quasi-Biennial Oscillation (hereafter QBO). At

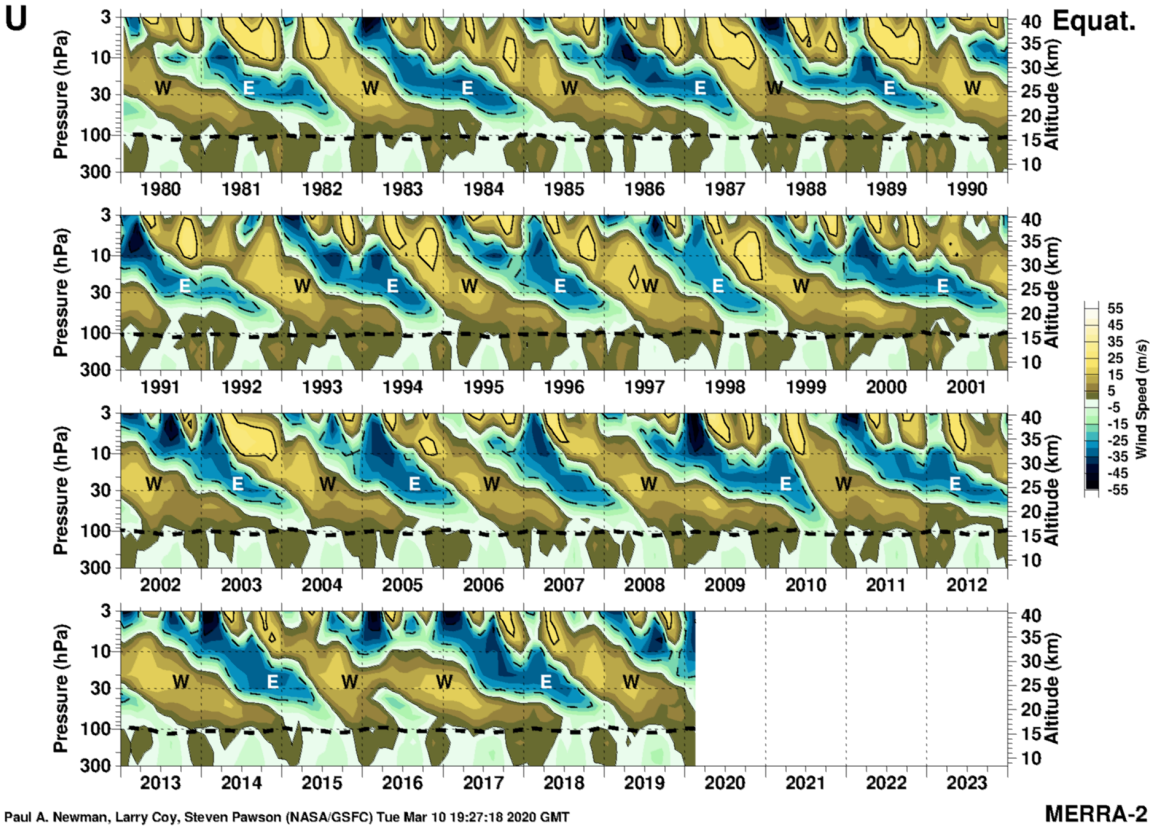

Figure 1.19: Satellite observation of the zonal-mean of azimuthal velocities in the stratosphere along the equator, as a function of time and altitude. Note the disruption in the periodic behaviour in 2016. Figure is from the Merra-2 project.

equatorial latitudes, winds oscillate from westward to eastward, with a period of roughly 28 months. The oscillations extend from 20 km to 40 km in altitude and propagate downward. Wind speeds range is 15–35 $\mathrm{m \cdot s^{-1}}$. Observations of these oscillations by satellite can be seen in figure 1.19. The striking feature of these observations is the downward phase propagation of the oscillation and its regularity.

The QBO can be explained by wave–mean-flow oscillations. Lindzen & Holton [Lindzen and Holton, 1968,Holton and Lindzen, 1972] simulated the oscillation in a one-dimensional model, using gravity waves as forcing. It was first invoked that large-scale equatorial waves drive the QBO: westward propagating Rossby waves generating westward momentum and eastward propagating Kelvin waves generating eastward momentum. However, it was shown years later that these large-scale waves are not energetic enough to drive the QBO by themselves [Dunkerton, 1997, Ern and Preusse, 2009]. Smaller scale gravity waves are therefore needed in order to drive the oscillations at the observed amplitude and period.
In 1977, [Plumb, 1977] simulated QBO with an idealised model, using, as forcing, two contra-propagating internal gravity waves with the same frequency. If the waves have enough energy, they can drive an oscillating flow. The reversing mechanism is shown in figure 1.20. The horizontal axis is a velocity axis, the vertical axis is the z-direction. At the

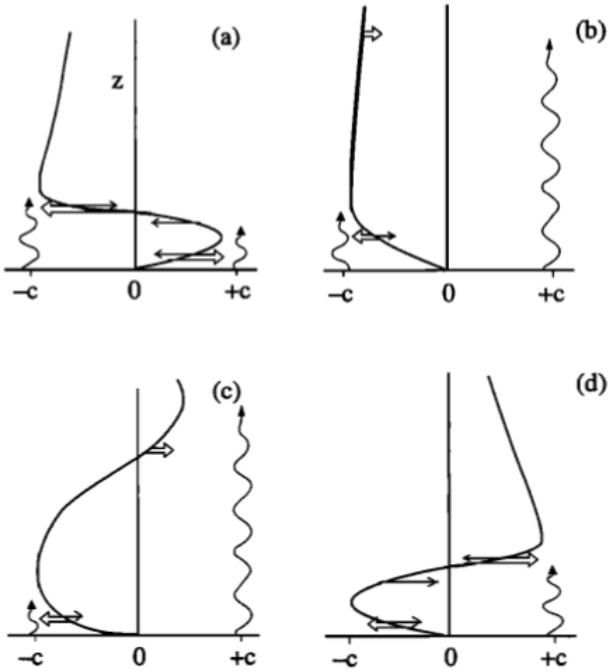

Figure 1.20: Reproduced from [Plumb, 1984]. The different panels show the horizontal flow generated by two contra-propagating internal gravity waves at different times. The flow goes through different stages and reverses from (a) to (d).

bottom, two waves are generated and propagate upward. They have the same frequency but opposite directions of propagation (*i.e.* opposite phase speeds). The key mechanism is that IGWs have an "anti-diffusive effect": they give more energy to the mean flow if they go in the same direction as the mean flow. A prograde wave interacts more with the mean flow than a retrograde wave. This can be understood with the concept introduced in section 1.3.2 and figure 1.15. While approaching its critical altitude, the group velocity of the prograde wave will become more and more horizontal, resulting in an acceleration of the flow, while the group velocity of the retrograde wave will become more and more vertical, resulting in a small exchange of energy and thus a slight deceleration for the flow. The total contribution is an acceleration in the direction of the prograde wave.

In the model, the bottom condition is no-slip: $\overline{u} = 0$ at $z = 0$ and the top condition is free slip: $\frac{\partial \overline{u}}{\partial z}|_{z=1} = 0$. On 1.20a, the initial mean flow $\overline{u}$ is shown. Thick empty arrows represent the energy given to the mean flow $\overline{u}$ by the wave, and narrow filled arrows represent the viscous attenuation of the mean flow $\overline{u}$. On 1.20a, the $+c$ wave gives its energy at the bottom of the stratified layer, where the mean flow is positive. On the opposite, the $-c$ wave goes through the positive mean flow area and deposits its energy just above. At the height z_c where $\overline{u}(z_c) = 0$, the fluid experiences positive viscous entrainment from below and negative viscous entrainment from above. However, the $-c$ wave deposits its energy just above z_c, whereas the $+c$ wave deposits its energy far below. Thus the mean flow $\overline{u}$ will be forced towards negative values at z_c. The height where $\overline{u} = 0$ moves downward through time.

On figure 1.20b, the area where the mean flow was positive has vanished due to vis-

cosity [5] and the mean flow is negative along the whole height. The $-c$ wave is attenuated at the bottom of the stratified layer whereas the $+c$ wave goes through the whole stratification and reaches the top where it gives its energy and thus slows locally the mean flow $\overline{u}$. At the top, the mean flow becomes positive (figure 1.20c), and the point where $\overline{u} = 0$ moves downward due to the interaction of the $+c$ wave with the mean flow (see how the $-c$ wave is "stuck" at the bottom). On figure 1.20d, the mean flow has reversed from its initial condition in 1.20a. This simple model with only two waves as forcing is sufficient to drive mean flow reversals from an initial mean flow and has been verified experimentally by Plumb and McEwan in their experiment [Plumb and McEwan, 1978], later confirmed and extended by [Semin et al., 2018].

These simple and idealistic models, including large-scale planetary waves along with smaller scale internal gravity waves, are able to drive oscillation of the equatorial zonal flow. However, even if it is know that the large-scale flow amplitude is set by the zonal phase speed of the forcing wave, very little is known upon the large-scale flow driven by a stochastic forcing. Yet, as seen in section 1.2.2, the internal gravity waves in the atmosphere are driven by various mechanisms and the properties (frequency, wavenumber) of those waves differ in space and time. This may have an impact on the driven QBO which is not yet understood.

Large-scale flow in other atmospheres and stars

Flows similar to the Earth's QBO are observed in others planets. The quasi-quadriennal (in terrestrial years) oscillation of Jupiter [Leovy et al., 1991] is observed from temperature measurements in the stratosphere. The equatorial winds in Saturn also oscillate with an estimated period of 15 years [Fouchet et al., 2008, Guerlet et al., 2018]. Mean zonal wind profiles from Saturn's atmosphere are shown in figure 1.21.

In stars, internal gravity waves influence the rotation profile and induce some fluctuations at relatively short time-scales compared to others time scales involved [Rogers et al., 2012]. Therefore, the rotation of the surface (and thus observable) layers is not representative of the rotation of the whole star. This phenomenon is invoked to explain why in some hot stars system (where the radiative layer is the outermost layer), exoplanets seem to be spin-misaligned with the host star. A flow somehow similar to the Earth's QBO is also observed in the Sun [Kim and MacGregor, 2001, Charbonnel, 2005].

1.4 The importance of the QBO in the Earth's atmospheric flows

The QBO is one of the most important sources of annual variability in the Earth's atmosphere. The QBO filters propagating waves in the stratosphere, depending on the direction of its phase. In particular, if the QBO is directed westward, Rossby waves, also propagating westward, encounter a critical layer while propagating towards the equator and are hence trapped at high latitudes. They propagate high in the stratosphere and

[5] for some cases *e.g.* if the wave has significant energy, the positive area does not vanish and the flow stays in a steady state, with a shear located at the bottom domain, as illustrated in figure 1.20a.

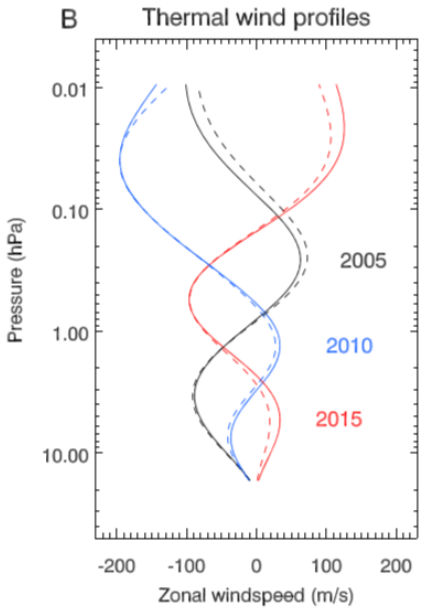

Figure 1.21: Mean zonal wind profile in Saturn's stratosphere from Cassini's temperature measurements. Taken at 7° S (solid lines) and 7° N (dashed line). Reproduced from [Guerlet et al., 2018].

interact with the polar vortex (eastward flow), weaken it and eventually, if the amplitudes of the waves are large enough, a westward flow takes place at the pole and the stratosphere at the pole warms up rapidly [Baldwin et al., 2001]. This is especially verified at the Northern hemisphere, where the Rossby wave activity is strong compared to the Southern hemisphere. The phenomenon is named Sudden Stratospheric Warming (SSW) [Schoeberl, 1978] and temperatures can increase by 50 °C in a few days. This sudden rise of the stratospheric temperature can perturb the jet stream and this results in cold snaps in Europe.

Interactions with the El Niño Southern Oscillation (ENSO) phenomenon are also observed: ENSO influences QBO [Taguchi, 2010] by affecting convective motions in the troposphere and thus affecting wave generation; and QBO affects ENSO [Gray et al., 1992a, Gray et al., 1992b] by influencing the convective activity in the tropical Pacific. ENSO is known to strongly impact the climate locally in the Pacific and Indian oceans as well as landmass nearby. It leads to severe droughts and floods and has tremendous environmental, social and economical impacts. But ENSO is not confined in the Pacific regions and its influence spreads globally [Brönnimann, 2007].

Additionally, QBO interacts with the Madden-Julian Oscillation (MJO) [Madden and Julian, 1971, Zhang, 2005]. The Madden-Julian oscillation is a key feature of the intraseasonal variability (30-90 days) in the tropical troposphere and influences the climate worldwide. It has been found quite recently that boreal winter MJO is stronger than normal when QBO is directed westward at 50 hPa whereas it is weaker than normal when QBO is directed eastward at 50 hPa [Yoo and Son, 2016].

In the 80s, it was thought that QBO had a repercussion on hurricane activity in the North Atlantic ocean [Gray, 1984], with more hurricane activity when the QBO is

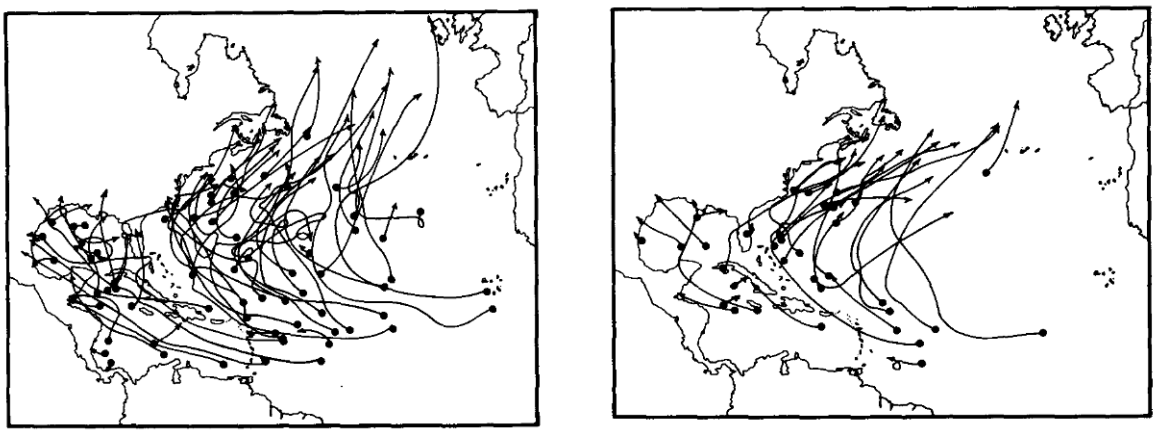

Figure 1.22: Tracks of all hurricane-intensity storm for nine seasons of eastward QBO phase (left) and nine seasons of westward QBO phase. Much more numerous tracks are observed when the QBO phase is eastward. Reproduced from [Gray, 1984].

eastward (figure 1.22). The QBO phase was then used to predict the hurricane activity in the Atlantic. Yet, the mechanism of interaction (an influence of the wind shear in the lower stratosphere) was not clearly convincing. A more recent study, including data recorded after the study of [Gray, 1984] shows that although there is a statistical correlation between QBO and hurricane activity from the 50s to the 80s, this relationship no longer exists for recent data [Camargo and Sobel, 2010]. The influence of QBO on hurricane activity remains unclear.

The interaction of QBO with other atmospheric phenomena is also captured in GCMs, especially the influence of ENSO upon QBO [Schirber, 2015, Serva et al., 2020] as well as the consequences of the QBO phase on the northern polar vortex [Anstey et al., 2010] and thus on the northern hemisphere winter climate [Marshall and Scaife, 2009].

In geophysical and astrophysical frameworks, internal gravity waves take an important place in the global dynamics despite their small length scales and short time scales. They participate in the transport of energy and momentum, induce mixing locally and are able to drive flows at larger scale.

1.5 Conclusion

This introductory chapter summaries basic but essential knowledge on internal gravity waves. The geophysical and astrophysical contexts were briefly presented and two problematics appear:

- The GCMs are currently not able to solve for short and small scales such as internal gravity waves. They are therefore parametrised, while the physics of their interactions with the global flows (induced mixing and exchange of momentum) is only partially understood, especially in the case of stochastic forcing. Yet, internal gravity waves drive the QBO which has strong impacts on the global climate. It is capital that the QBO is well modelled in GCMs.

- The amount of energy that transfers from the turbulent motion of the convective layer into the internal gravity waves is still unknown. Fundamental studies to understand the energy-transfer function are needed.

These two points motivate the necessity to investigate the interaction between a turbulent convective layer, generating stochastically internal gravity waves, and a stably-stratified layer, in order to build better modelisation of flows in atmospheres, oceans and stars. This thesis will bring new elements in order to get a better apprehension of the two problematics above.

The next section will introduce an extension of the Plumb's model [Plumb, 1977], in which the forcing is not monochromatic, but is a superposition of waves at different frequencies, in order to reproduce the stochastic behaviour observed in the atmosphere, and hence, complete our understanding of the QBO generation.

CHAPTER 2

MULTI-MODAL MODEL FOR THE QUASI-BIENNIAL OSCILLATION

Contents

The Quasi-Biennial Oscillation is a striking example of large-scale flow driven by internal gravity wave streaming. The period for the reversing winds is approximately 28 months and has been fairly robust for the past 65 years of observation. This oscillating behaviour has been explained by wave–mean-flow interactions. A comprehensive review of the phenomenon and of its implications can be found in [Baldwin et al., 2001].

[Lindzen and Holton, 1968, Lindzen, 1972] first came with a theoretical model reproducing mean-flow oscillations with planetary waves (Rossby and Kelvin waves) forcing. Based on this preliminary work, [Plumb, 1977] derived a simple model using internal gravity waves as forcing. This model has been studied both numerically [Kim and MacGregor, 2001, Renaud et al., 2019] and experimentally [Plumb and McEwan, 1978, Otobe et al., 1998, Semin et al., 2016, Semin et al., 2018]. It reproduces very well the main features of the QBO. Figure 2.1 shows the experimental results of [Plumb and McEwan, 1978] and

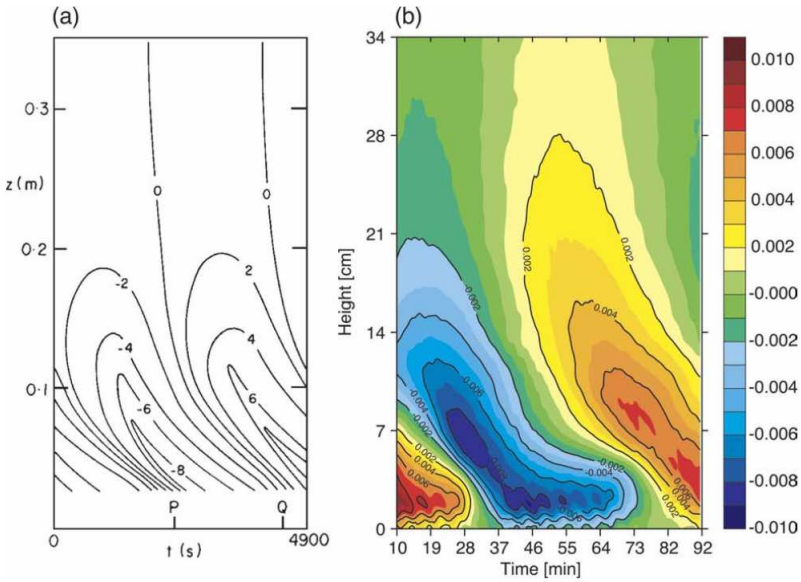

Figure 2.1: (a) Time series of the observed horizontally averaged velocity in the experiment of [Plumb and McEwan, 1978]. Contours are in $\mathrm{mm} \cdot \mathrm{s}^{-1}$. (b) Time series of the horizontally averaged velocity in a 3D DNS. Contours are in $\mathrm{m} \cdot \mathrm{s}^{-1}$. The figure is reproduced from [Wedi and Smolarkiewicz, 2006].

the results of [Wedi and Smolarkiewicz, 2006] reproducing the experimental results in 3D DNS.

However, these models are limited by their idealised approach: the forcing is monochromatic. In Plumb's model, a monochromatic standing internal gravity wave, corresponding to two contra-propagating IGWs, is generated at the bottom boundary of a stratified fluid and propagates upwards. An oscillating large-scale flow then appears if a threshold value for the forcing parameter is overpassed. In the Earth's stratosphere, as mentioned in the previous chapter, the internal gravity waves are generated by various mechanisms. Therefore, they present different frequencies, amplitudes and wavenumbers. This diversity, currently not captured in the models, may play a major role in the generation of a large-scale flow.

In section 2.1, we introduce the Plumb's model equations. Some past studies using this model are presented in section 2.2. Then, section 2.3 will introduce the numerical schemes and the different forcing spectra considered in our study. Finally, section 2.4 will present and discuss our results.

2.1 Plumb's theoretical model

The aim of this section is to introduce the Plumb's model and its equations. The Plumb's model is derived from the two-dimensional Navier-Stokes equations, using the Boussinesq approximation and the Reynolds decomposition. Since dissipative processes are the key ingredient of wave–mean-flow interactions, it is important that they are included in the

equations. In the atmosphere, the attenuation of the waves occurs through critical layers and radiative damping while it happens mostly through eddy diffusivity in the ocean. In the experiments, the attenuation is mostly viscous and/or due to wall friction.

2.1.1 The Navier-Stokes equations

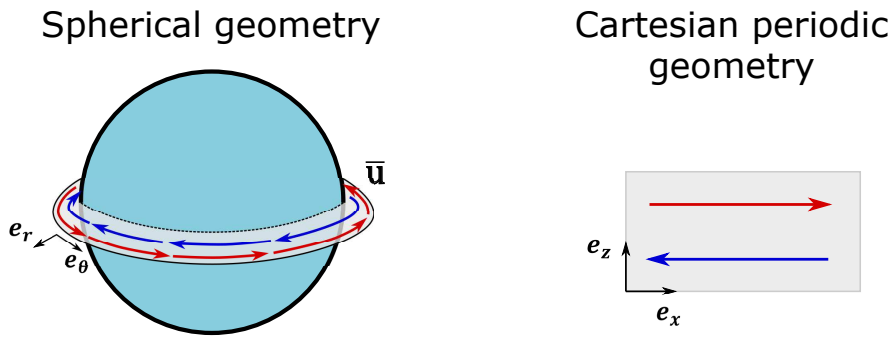

Figure 2.2: Sketch illustrating the analogy between the QBO geometry (left) and the 2D cartesian geometry (right). The Earth's curvature is ignored. Consequently, the equatorial plane $(\mathbf{e}_\theta, \mathbf{e_r})$ is similar to the 2D periodic geometry $(\mathbf{e_x}, \mathbf{e_z})$

Our framework is a two-dimensional domain with Cartesian coordinates $(\mathbf{e_x}, \mathbf{e_z})$ (see figure 2.2). Since QBO occurs at equatorial latitudes, the effect of rotation can be neglected since the Coriolis force effects are weak at the equator and the centrifugal force is included in the gravity force. The Earth's curvature is also ignored, since the height of the stratosphere ($\sim$ 40 km) is small compared to the Earth's radius ($\sim$ 6400 km). Gravity points downward such that $\mathbf{g} = -g\mathbf{e_z}$, with $\mathbf{e_z}$ pointing upward. The fluid is linearly stratified with constant buoyancy frequency N. We will first consider the inviscid equations and the dissipative processes will be added later. The inviscid momentum equations reads:

$$\rho \mathrm{D}_t \mathbf{u} = -\nabla P + \rho \mathbf{g} \tag{2.1}$$

with $\mathrm{D}_t = \partial_t + \mathbf{u} \cdot \nabla$ is the material derivative and $\nabla = (\partial_x; \partial_z)$ is the gradient operator. $\mathbf{u} = (u; w)$ is the velocity vector.

The diffusionless mass equation is:

$$\mathrm{D}_t \rho + \rho \nabla \cdot \mathbf{u} = 0 \tag{2.2}$$

The fluid density is given by its equation of state:

$$\rho = \rho(P, S, T) \tag{2.3}$$

Here, T is the temperature field and S is another field affecting the density, *e.g.* the salinity in the ocean. These fields follow a typical advection equation:

$$\mathrm{D}_t T = 0 \tag{2.4}$$

$$\mathrm{D}_t S = 0 \tag{2.5}$$

The Boussinesq approximation

If the density variations are small relatively to a mean density, the dynamical equations can be greatly simplified using the Boussinesq approximation. This approximation is accurately respected for the oceanic motions.

In the ocean, the variations of the density field $\delta\rho$ are due to three effects:

- the compressibility of water due to the pressure: $\Delta_P\rho = \frac{\Delta P}{c_s^2}$
- the expansion of water due to temperature variations: $\Delta_T\rho = -\alpha_T\rho_0\Delta T$
- the contraction of water due to salinity variations: $\Delta_S\rho = \alpha_S\rho_0\Delta_S$

The equation of state given by (2.3) can be linearised by:

$$\rho = \rho_0\left[1 - \alpha_T(T - T_0) + \alpha_S(S - S_0) + \frac{P}{\rho_0 c_s^2}\right] \tag{2.6}$$

with $c_s = 1500\ \mathrm{m\cdot s^{-1}}$ is the sound speed in water, considered as constant. The pressure variations ΔP are modelled by the hydrostatic approximation: $\Delta P = \rho_0 g H$. If we consider for the different variations realistic values: $H = 10^4$ m, $\Delta T = 20$ K and $\Delta S = 5\ \mathrm{g\cdot kg^{-1}}$ [1], with $g = 10\ \mathrm{m\cdot s^{-2}}$, $\alpha_T = 2\times 10^{-4}\ \mathrm{K^{-1}}$ and $\alpha_S = 10^{-3}\ \mathrm{kg\cdot g^{-1}}$, we deduce that the density variations $\delta\rho$ are small ($\sim 5\%$) compared to the reference density ρ_0.
The Boussinesq approximation is also fully relevant for laboratory experiments, considering thermal or salt stratification. However, it is not applicable to atmospheres and stellar interiors, which are fully compressible. Those will be studied in the next section.

We write the pressure and density vertical profiles as a sum of the background profile plus perturbations:

$$\rho = \rho_0 + \rho_{bg}(z) + \delta\rho(x, y, z, t) \tag{2.7}$$
$$P = p_0(z) + \delta p(x, y, z, t) \tag{2.8}$$

with $|\delta\rho|$,$|\rho_{bg}| \ll \rho_0$ and $|\delta p| \ll p_0$.

Using (2.7) in (2.1), the momentum equation now reads:

$$(\rho_0 + \rho_{bg} + \delta\rho)\,\mathrm{D}_t\mathbf{u} = -\nabla\delta p - \partial_z p_0\mathbf{e_z} - g\,(\rho_0 + \rho_{bg} + \delta\rho)\,\mathrm{e_z} \tag{2.9}$$

Considering the hydrostatic equilibrium:

$$d_z p_0 = -g\rho_0 \tag{2.10}$$

and taking into account $|\delta\rho|$,$|\rho_{bg}| \ll \rho_0$, *i.e.* $\rho_0 + \rho_{bg} + \delta\rho \sim \rho_0$, we have:

$$\rho_0\mathrm{D}_t\mathbf{u} = -\nabla\delta p - g(\rho_{bg} + \delta\rho)\mathrm{e_z} \tag{2.11}$$

[1] $\mathrm{g\cdot kg^{-1}}$ is the typical unit for salinity in water. $1\ \mathrm{g\cdot kg^{-1}}$ meaning 1 g gram of salt for 1 kg of water

The term $g\delta\rho$ is the buoyancy term, responsible for the existence of internal gravity waves in a stratified environment. Writing $\phi = \frac{\delta p + g\int \rho_{bg} \mathrm{d}z'}{\rho_0}$ and $b = -g\delta\rho/\rho_0$, we now have:

$$\mathrm{D}_t \mathbf{u} = -\nabla\phi + b\mathbf{e_z} \tag{2.12}$$

The mass conservation can be written, without any approximation:

$$\mathrm{D}_t \delta\rho + (\rho_0 + \rho_{bg} + \delta\rho)\nabla \cdot \mathbf{u} = 0 \tag{2.13}$$

At first order, we can approximate (2.13) by:

$$\nabla \cdot \mathbf{u} = 0 \tag{2.14}$$

From the linearised equation of state (2.6) and using $p_0 = -\rho_0 g z$, we have:

$$\frac{\rho_{bg}}{\rho_0} + \frac{\delta\rho}{\rho_0} = -\alpha_T(T - T_0) + \alpha_S(S - S_0) + \frac{-\rho_0 g z + \delta p}{\rho_0 c_s^2} \tag{2.15}$$

Considering $g\mathrm{D}_t\times$ (2.15), and writing $b_{bg} = -g\rho_{bg}/\rho_0$, we obtain:

$$\mathrm{D}_t(b_{bg} + b) = \mathrm{D}_t\left(\frac{-\rho_0 g z + \delta p}{\rho_0 c_s^2}\right) \tag{2.16}$$

The right hand side of (2.16) is neglected in the Boussinesq model:

$$\mathrm{D}_t(b_{bg} + b) = 0 \tag{2.17}$$

Using the fact that $\mathrm{D}_t b_{bg} = \partial_t b_{bg} + \mathbf{u} \cdot \nabla b_{bg} = w\partial_z b_{bg} = w\partial_z\left(\frac{-g\rho_{bg}}{\rho_0}\right) = N^2 w$, we can write the buoyancy equation:

$$\mathrm{D}_t b + N^2 w = 0 \tag{2.18}$$

The equations (2.12), (2.14) and (2.18) form the Boussinesq model. It is adapted to study the motions in the ocean, where the density perturbations and the background profile are small compared to the mean density. However, this is not the case in the atmosphere and another set of equations has to be derived.

The anelastic approximation

In the atmosphere and in stellar interiors, the density varies strongly with height and cannot be written as $\rho = \rho_0 + \rho_{bg}(z) + \delta\rho(x, y, z, t)$, *i.e.* as a constant value plus small variations. Still, the dynamical equations can be simplified using the anelastic approximation. This model uses the fact that the relative variations of the potential density are small. The potential density of a particle at a pressure P is the density the particle would have if brought to a reference pressure P_0, in an adiabatic process. The same definition applies for potential temperature. We will very briefly present the major steps of the

derivation and give the final set of equations. For a more detailed derivation, one should read the corresponding section of Vallis' book [Vallis, 2017].

We will consider the potential temperature, assuming that the air is an idealised gas:

$$\theta = \frac{p^{c_v/c_p}}{\rho} \tag{2.19}$$

with c_v and c_p being the constant volume and pressure heat capacity of air. The density, pressure and potential temperature fields are written as a background part plus relatively small perturbations:

$$\rho = \rho_0(z) + \delta\rho(x, y, z, t) \tag{2.20}$$
$$P = p_0(z) + \delta p(x, y, z, t) \tag{2.21}$$
$$\theta = \theta_0 + \delta\theta(x, y, z, t) \tag{2.22}$$

Again the density perturbations $\delta\rho$ are neglected against ρ_0 in the left-hand side of the momentum equation. Using the potential temperature θ, we obtain:

$$\mathrm{D}_t\mathbf{u} = -\nabla\frac{\delta p}{p_0(z)} + b\mathbf{e_z} \tag{2.23}$$

with $b = -g\delta\theta/\theta_0$.

Equation (2.23) is similar to the momentum equation of the Boussinesq model (2.12). The major difference is that the buoyancy term is computed from the potential temperature and not from density itself.

The equation for the buoyancy is:

$$\mathrm{D}_t b + N^2 w = 0 \tag{2.24}$$

The mass conservation reads:

$$\partial_t\delta\rho + \nabla\cdot\left[(\rho_0 + \delta\rho)\,\mathbf{u}\right] = 0 \tag{2.25}$$

Keeping the leading order terms, we have the incompressibility equation:

$$\nabla\cdot(\rho_0(z)\mathbf{u}) = 0 \tag{2.26}$$

Equations (2.23), (2.24) and (2.26) form an equivalent of the Boussinesq model for the atmosphere with the buoyancy being defined by the potential temperature instead of the density. They take into account part of the compressibility effects, but not all: in particular they filter out acoustic waves.

Dissipative processes

To model wave–mean flow interactions, it is crucial to implement dissipative mechanisms in the Boussinesq equations. Indeed, those terms allow the transfer of momentum from the waves to the mean flow.

We first introduce momentum diffusion in the momentum equation:

$$\mathrm{D}_t\mathbf{u} = -\frac{1}{\rho_0}\nabla p + b\mathbf{e_z} + \nu^*\nabla^2\mathbf{u} \tag{2.27}$$

Here, ν^* is the dimensioned kinematic viscosity of the fluid. It affects both the mean flow and the wave field.

The buoyancy field is also affected by diffusive processes (thermal diffusion for example) and also by a linear dissipative process. This linear term can model the radiative damping in the atmosphere [Plumb, 1977] or the friction of a solid wall in experiments [Semin et al., 2018].

$$\mathrm{D}_t b + N^2 w = -\gamma b + \mathcal{D}^*\nabla^2 b \tag{2.28}$$

In the atmosphere, the radiative term is dominant while, in the ocean, the wave dissipation is modelled via the eddy diffusivity discussed in section 1.3, implying that the term $\mathcal{D}^*\nabla^2 b$ will be dominant.

In our study, we will only consider diffusive mechanisms to attenuate the wave. Therefore, the linear term γb will not be considered.

Final set of dimensionless equations

In the typical monochromatic Plumb's model, the length and time scales used to obtain the dimensionless equations are the inverse of the wave frequency ω and its attenuation length l. In our study, as mentioned before, we will consider several waves with different frequencies and attenuation lengths. Therefore, we cannot choose wave properties as scales and the usual dimensionless approach does not fit our needs. We will use the buoyancy frequency N and an arbitrary scale H (we will take the height of the stratified layer) as time and length scale. The dimensionless momentum equation is:

$$\mathrm{D}_t\mathbf{u} = -\nabla p + b\mathbf{e_z} + \nu\nabla^2\mathbf{u} \tag{2.29}$$

with $\nu = \frac{\nu^*}{N\,H^2}$ the dimensionless kinematic viscosity.

The buoyancy equation is:

$$\mathrm{D}_t b + w = \mathcal{D}\nabla^2 b \tag{2.30}$$

with $\mathcal{D} = \frac{\mathcal{D}^*}{N\,H^2}$ a dimensionless diffusion coefficient associated with the buoyancy b.

The incompressibility equation still reads:

$$\nabla\cdot\mathbf{u} = 0 \tag{2.31}$$

2.1.2 Reynolds decomposition

Our interest is to study the interactions of small fluctuations $\mathbf{u}'$, b' and p' with large-scale dynamics $\overline{\mathbf{u}}$, $\overline{b}$ and $\overline{p}$. To do so, we perform a Reynolds decomposition of our fields. It consists in writing the different fields as the sum of a horizontally averaged mean part and a fluctuation part. We have:

$$\begin{cases} \mathbf{u}(x,z,t) = \overline{\mathbf{u}}(z,t) + \mathbf{u}'(x,z,t) \\ b(x,z,t) = \overline{b}(z,t) + b'(x,z,t) \\ p(x,z,t) = \overline{p}(z,t) + p'(x,z,t) \end{cases} \tag{2.32}$$

The mean part of the different fields does not depend on the horizontal direction x. Using the Reynolds decomposition in the equations (2.29), (2.30) and (2.31), we will derive the mean-flow and wave equations.

Mean-flow equations

Horizontally averaging the incompressibility equation (2.31) results in:

$$\partial_z \overline{w} = 0 \tag{2.33}$$

which implies that $\overline{w} = \overline{w}(t)$. In this thesis, we will consider $\overline{w} = 0$, corresponding to no mean penetration at the boundaries. We neglect any large-scale vertical motion.

The horizontal average of the horizontal projection of the momentum equation (2.29) gives the mean-flow equation:

$$\partial_t \overline{u} - \nu \partial_z^2 \overline{u} = -\partial_z \overline{u'w'} \tag{2.34}$$

This equation gives the time evolution of the horizontal mean-flow $\overline{u}$. The right hand side term is the z-derivative of the $\overline{u'w'}$-component of the Reynolds stress. This term represents the wave field forcing on the mean-flow. This equation will be numerically integrated (see section 2.3.2) to solve for the mean-flow. In order to do so, one needs to know the right hand side term of equation (2.34). Another equation is thus needed to obtain an expression of the forcing term $\partial_z \overline{u'w'}$.

The horizontal average of the vertical projection of the momentum equation (2.29) gives the hydrostatic equation for the mean pressure:

$$\partial_z \overline{p} = \overline{(\boldsymbol{u}\boldsymbol{\nabla})\, w} + \overline{b} \tag{2.35}$$

Wave equations

The wave equations are obtained by subtracting the mean-flow equations to the general equations (2.29), (2.30) and (2.31).

$$\partial_t u' + \left[(u'.\nabla)\, u' - \overline{(u'.\nabla)\, u'}\right] + \overline{u}\partial_x u' + w'\partial_z \overline{u} + \partial_x p' = \nu\nabla^2 u' \tag{2.36a}$$

$$\partial_t w' + \left[(u'.\nabla)\, w' - \overline{(u'.\nabla)\, w'}\right] + \overline{u}\partial_x w' + \partial_z p' = \nu\nabla^2 w' + b' \tag{2.36b}$$

$$\partial_t b' + \left[(u'.\nabla)\, b' - \overline{(u'.\nabla)\, b'}\right] + \overline{u}\partial_x b' + w'\partial_z \overline{b} + w' = \mathcal{D}\nabla^2 b' \tag{2.36c}$$

$$\partial_x u' + \partial_z w' = 0 \tag{2.36d}$$

The bracketed terms are neglected: this is the mean-field approximation described by [Plumb, 1975] as follows: "the non-linear effects are neglected except where they represent interactions between waves and the mean-flow". Here the bracketed terms are wave-wave non-linear effects.

We compute ∂_z(2.36a) - ∂_x(2.36b) in order to obtain an equation for the streamfunction ψ ($u' = \psi_z$ and $w' = -\psi_x$).

$$\left(\partial_t + \overline{u}\partial_x - \nu\nabla^2\right)\nabla^2\psi - \overline{u}_{zz}\partial_x\psi = -\partial_x b' \tag{2.37}$$

We consider $(\partial_t + \overline{u}\partial_x - \mathcal{D}\nabla^2) \times$ (2.37). Using the wave equation for buoyancy (2.36c), neglecting any effect of the vertical variation of the mean buoyancy $\partial_z\overline{b}$ (we assume that the stratification profile is dominated at any time by the initial profile, $\partial_z\overline{b} \ll N^2$ with $N^2 = 1$ with our choice of time-scale) and neglecting once again the bracketed terms in (2.36c), we have:

$$\left(\partial_t + \overline{u}\partial_x - \mathcal{D}\nabla^2\right)\left[\left(\partial_t + \overline{u}\partial_x - \nu\nabla^2\right)\nabla^2 - \overline{u}_{zz}\partial_x\right]\psi = \partial_x^2\psi \tag{2.38}$$

We will now derive from the linearised wave equation (2.38) an expression for $-\partial_z\overline{u'w'}$.

2.1.3 Analytical expression for the forcing term

Equation (2.38) gives the evolution of the wave field. We will consider the asymptotic description given by the WKB approximation: the mean-flow $\overline{u}$ evolves slowly compared to the fast wave dynamics and the waves propagate in a flow without vertical shear. Therefore, the time derivative and the z-derivative of the mean-flow are neglected $\partial_{t,z}\overline{u} = 0$ (which is verified for $\frac{c\overline{u}}{N^2H^2} \ll 1$ and for horizontal wavenumber k_x not too large). We consider a plane-wave solution for the expression of the streamfunction:

$$\psi = A(z)e^{i(k_x x - \omega t)} \tag{2.39}$$

with k_x the horizontal wavenumber and $\omega = \Omega - k_x\overline{u}$ the Doppler-shifted frequency.

We introduce the Doppler-shifted phase speed $c = \omega/k_x = \Omega/k_x - \overline{u}$ and we write the order 6 wave equation under the following form:

$$\left[c^2\left(-k_x^2 + \partial_z^2\right) + \frac{ic}{k_x}\left(\mathcal{D} + \nu\right)\left(-k_x^2 + \partial_z^2\right)^2 - \frac{\mathcal{D}\nu}{k_x^2}\left(-k_x^2 + \partial_z^2\right)^3\right]A(z) = -A(z) \tag{2.40}$$

Small dissipation approximation

A final approximation needs to be made to simplify the equations and to get an analytical expression for the forcing term in equation (2.34). This approximation consists in assuming that the dissipative processes are of second order. We write the kinematic viscosity ν as $\epsilon\nu$ and the buoyancy diffusivity $\mathcal{D}$ as $\epsilon\mathcal{D}$, where ϵ is a small parameter. ϵ^2 terms are neglected.

$$c^2\left(-k_x^2+\partial_z^2\right)A(z)+\frac{ic\epsilon}{k_x}\left(\nu+\mathcal{D}\right)\left(-k_x^2+\partial_z^2\right)^2A(z)=-A(z) \tag{2.41}$$

We seek a WKB (Wentzel Kramers Brillouin) solution $A(z)$ of the form:

$$A(z)=A_0\,e^{\int_0^z(ik_z(\epsilon\xi)+\epsilon\chi(\epsilon\xi))\mathrm{d}\xi} \tag{2.42}$$

This solution expresses the slow modulation of the properties of the waves along the vertical direction. The function k_z is the vertical wavenumber and the function χ is the damping due to dissipative processes. The ϵ in front of the χ function expresses the small dissipation assumption.

Leading order solution of 2.41 satisfies:

$$k_z^2=\frac{1-c^2k_x^2}{c^2} \tag{2.43}$$

Equation (2.43) is the inviscid dispersion relation for the internal gravity waves.

At next order, we can have an expression for χ:

$$ic^2\epsilon k_z'+2\epsilon c^2ik_z\chi+\frac{ic\epsilon}{k_x}\left(\nu+\mathcal{D}\right)\left(k_x^4+2k_x^2k_z^2+k_z^4\right)=0 \tag{2.44}$$

That allows to write explicitly an analytical expression for the damping term χ:

$$\chi=\frac{\mathrm{d}}{\mathrm{d}z}\ln k_z^{-1/2}-\frac{(\nu+\mathcal{D})}{2k_x\left(1-k_x^2c^2\right)^{1/2}c^4} \tag{2.45}$$

Finally, we have an expression for the amplitude function $A(z)$:

$$A^{\pm}(z)=\frac{A_0\,K}{\left(\frac{1-k_x^2c^2}{c^2}\right)^{1/4}}e^{\mp i\int\mathrm{d}\xi\left(\frac{1-k_x^2c^2}{c^2}\right)^{1/2}}e^{-\frac{1}{2k_x}\int\mathrm{d}\xi\frac{\nu+\mathcal{D}}{(1-k_x^2c^2)^{1/2}c^4}} \tag{2.46}$$

where $\pm$ is $+$ for prograde $\omega<0$ waves and $-$ for retrograde $\omega>0$ waves. K is the constant from the integration of $e^{\int\mathrm{d}z\frac{\mathrm{d}}{\mathrm{d}z}lnk_z^{-1/2}}$. The bottom condition gives:

$$A^{\pm}(z=0)=\frac{A_0\,K}{k_z(z=0)^{1/2}}=A_0$$

So $K=k_z(z=0)^{1/2}$.

Analytical expression for the forcing term

Now that we have an expression for the streamfunction ψ, we can compute the term $\overline{u'w'}$. We write the streamfunction ψ as:

$$\psi = Ae^{ik_x(x-ct)} + A^* e^{-ik_x(x-ct)} \tag{2.47}$$

Then $\overline{u'w'}$ is:

$$\begin{aligned}\overline{u'w'} &= \overline{\left(\frac{\partial A}{\partial z}e^{ik_x(x-ct)} + \frac{\partial A^*}{\partial z}e^{-i(x-ct)}\right) \times \left(-ik_x A e^{ik_x(x-ct)} + ik_x A^* e^{-ik_x(x-ct)}\right)} \\ &= \overline{-ik_x A\frac{\partial A}{\partial z}e^{2ik_x(x-ct)} + ik_x A^*\frac{\partial A}{\partial z} - ik_x A\frac{\partial A^*}{\partial z} + ik_x A^*\frac{\partial A}{\partial z}e^{-2ik_x(x-ct)}}\end{aligned} \tag{2.48}$$

Finally:

$$\overline{u'w'} = -ik_x\left(-A^*\frac{\partial A}{\partial z} + A\frac{\partial A^*}{\partial z}\right) \tag{2.49}$$

By using the expression for $A(z)$ of equation (2.46), we write:

$$\begin{aligned}\overline{u'w'}^{\pm} &= -ik_x\left(-A^{\pm,*}\partial_z A^{\pm} + A^{\pm}\partial_z A^{\pm,*}\right) \\ &= \pm 2k_x|A_0|^2 k_z(z=0)e^{-\frac{1}{k_x}\int \mathrm{d}\xi \frac{\nu+\mathcal{D}}{\left(1-k_x^2c_\pm^2\right)^{1/2}c_\pm^4}} \\ &= \pm 2k_x|A_0|^2 k_z(z=0)e^{-\int \mathrm{d}\xi l_\pm^{-1}}\end{aligned} \tag{2.50}$$

with $l_\pm^{-1} = \frac{(\nu+\mathcal{D})k_x^3}{\left(1-\omega_\pm^2\right)^{1/2}\omega_\pm^4}$ being the inverse of the attenuation length associated with the wave. The attenuation length is a slowly-varying function of z.

The forcing term writes:

$$\begin{aligned}-\left(\partial_z\overline{u'w'}^{+} + \partial_z\overline{u'w'}^{-}\right) =& 2A_0^2 k_z(z=0)l_+^{-1}k_x e^{-\int \mathrm{d}\xi l_+^{-1}} \\ &- 2A_0^2 k_z(z=0)l_-^{-1}k_x e^{-\int \mathrm{d}\xi l_-^{-1}}\end{aligned} \tag{2.51}$$

with intrinsic prograde frequency $\omega_+ = \omega - k_x\overline{u}$ and retrograde frequency $\omega_- = \omega + k_x\overline{u}$.

With the analytical expression for the Reynold stress in equation (2.51), one can now numerically integrate the mean-flow equation (2.34), which we reproduce below:

$$\partial_t\overline{u} - \nu\partial_z^2\overline{u} = -\partial_z\overline{u'w'}$$

An example of a numerical integration done with the model described in section 2.3 is shown in figure 2.3. Figure 2.3(j) shows the Hovmöller diagram, reproducing the main features of the QBO: the mean-flow $\overline{u}$ reverses periodically, with phases propagating downward. Figures 2.3(a-i) show snapshots of the vertical profile of $\overline{u}$ at different times. They correspond to a full oscillating period and are reminesecent of the sketch from [Plumb, 1984] seen in section 1.3.3.

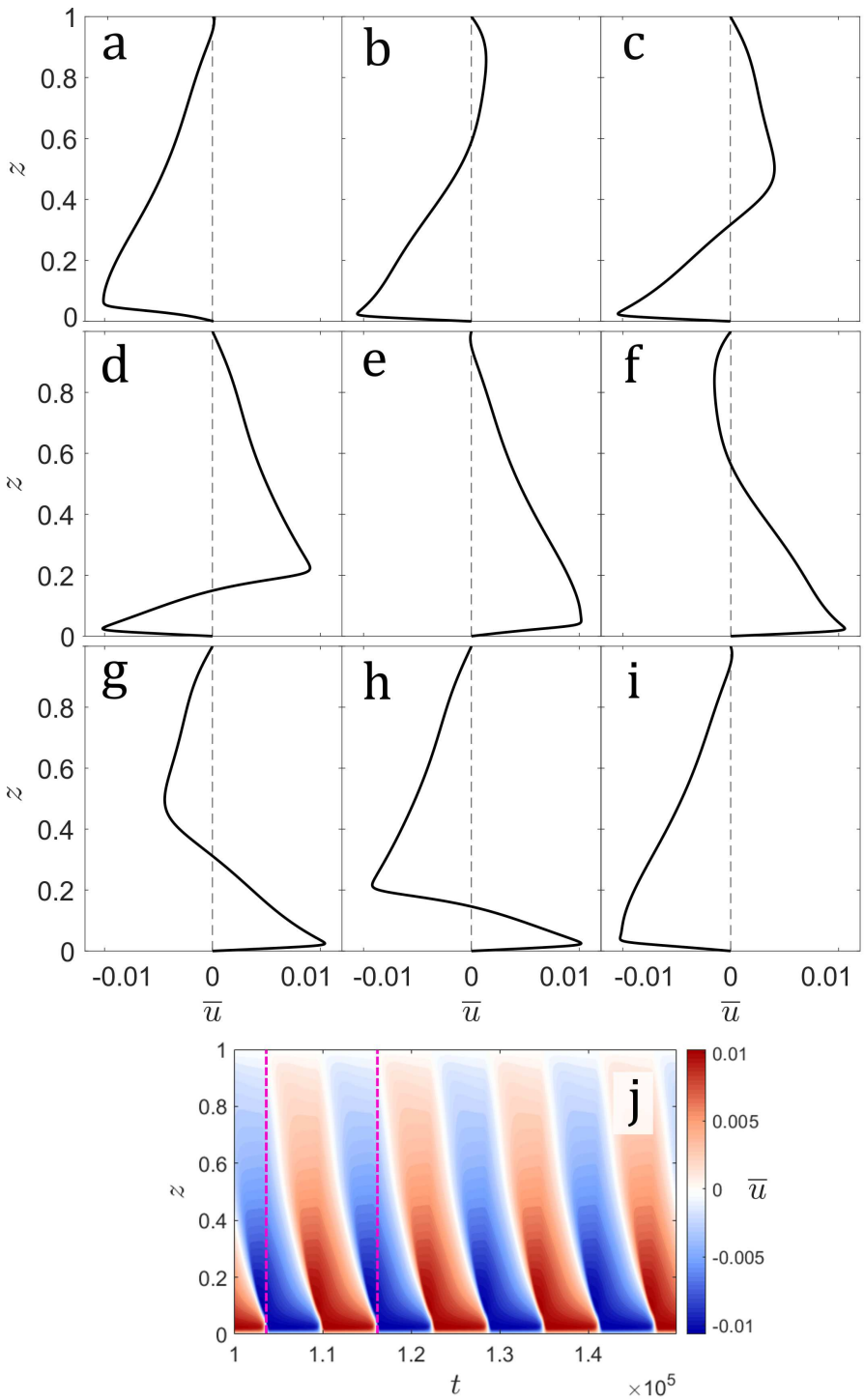

Figure 2.3: (a-i) Snapshots of the vertical profile of the mean-flow $\overline{u}$. One oscillating period is represented. (j) Hovmöller diagram showing a longer time evolution, and several periods.

2.2 Past studies using the Plumb's model

Since the fundamental aspects of the QBO theory developed by [Plumb, 1977], several studies have investigated the model deeply, looking for bifurcations in the dynamics. Other studies have used Plumb-like models in GCMs. This section briefly introduces those studies that are relevant for a better understanding of our own approach developed in section 2.3.

2.2.1 Chaotic behaviour of the Plumb's model

In 2016, the QBO observations exhibit a disruption in the oscillations of the zonal flow [Osprey et al., 2016, Newman et al., 2016] (see the QBO observation in chapter 1 figure 1.19). Similar disruptions were also observed for the Saturn's oscillations [Fletcher et al., 2017] and quite recently in Jupiter's atmosphere [Giles et al., 2020]. For the Earth's QBO, these anomalies are explained by extra-tropical intense Rossby waves (themselves due to an extreme El Niño event) interacting with the westward phase of the QBO [Barton and McCormack, 2017, Li et al., 2020], whereas the contribution of those waves to the QBO forcing is usually secondary [O'Sullivan, 1997]. Yet, another explanation can be advanced to explain this irregularity. Recently, the Plumb's model [Renaud et al., 2019] was systematically explored to look for bifurcations from periodic to non-periodic regimes. By varying the Reynolds number of the waves (*i.e.* changing either the energy of the waves or their dissipation), it was shown that the Plumb's model exhibits a route to chaos with increasing Reynolds number.

Data processing and Poincaré map

In order to visualise the bifurcations from one dynamical regime to another, Poincaré maps (see figure 2.5d) are useful. To plot this kind of diagram, time is given to the dynamical system to reach its attractor. After the attractor is reached, the mean-flow oscillates $[15-20]$ times and the signals of $\overline{u}$ at two different heights are extracted: $\overline{u_1} = \overline{u}(z = 0.1)$ and $\overline{u_3} = \overline{u}(z = 0.5)$. Then, the values of $\overline{u_3}$ every time $\overline{u_1} = 0$ are stored in a set. One set is saved for each simulation performed with a parameter varying from one simulation to another. The Poincaré map then shows the stored values as a function of the varying parameter. The process for our results is illustrated in figure 2.4. Left panel of figure 2.4 shows different Hovmöller diagram corresponding to different dynamical regimes. Middle panel shows the corresponding signals for $\overline{u_1}$ (thick black curve) and $\overline{u_3}$ (red dash curve) and right panel shows phase-space diagram representing $\overline{u_3}$ as a function of $\overline{u_1}$. Each time the curve crosses the axes $\overline{u_1} = 0$, a red dot, indicating the corresponding value of $\overline{u_3}$ is plotted. Those red dots are then reproduced in the Poincaré map (shown in section 2.4 for our results and in figure 2.5 for the results of [Renaud et al., 2019]). The cases visible in figure 2.4 are from our study described in sections 2.3 and 2.4.

Periodic oscillations are characterised by two dots, symmetric about $\overline{u_3} = 0$. Frequency-locked oscillations also exhibit a periodic structure with several frequencies appearing in the reversing signal: they are characterised by a finite number of dots. Finally, for quasi-periodic oscillations, the dots do not superimpose (for a great number of reversals, they would form a continuous line).

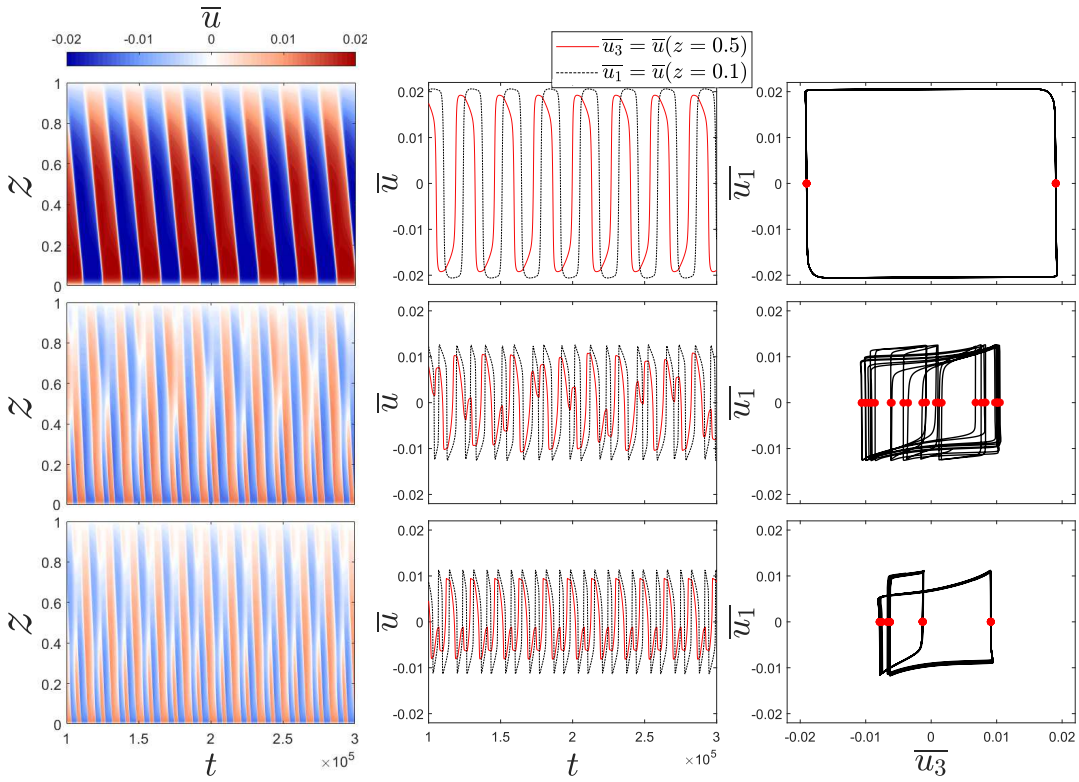

Figure 2.4: (left) Hovmöller diagram for different oscillating behaviours: periodic (top), quasi-periodic (middle) and frequency-locked (bottom). (Middle) Corresponding mean-flow signal for $\overline{u_1} = \overline{u}(z = 0.1)$ (black dashed) and $\overline{u_3} = \overline{u}(z = 0.5)$ (red thick). (Right) 2D phase-space diagram showing $\overline{u_1}$ as a function of $\overline{u_3}$. The red dots enlighten the points $\{\overline{u_3}(t) \mid \overline{u_1}(t) = 0\}$.

A route to chaos in the Plumb's model

Figure 2.5 shows the results of the systematic study of the model in terms of wave Reynolds number [Renaud et al., 2019]. The top panels show Hovmöller diagrams of observation of the QBO (a) and two different dynamical regimes simulated with the Plumb's model (b-c).

The bottom left panel shows the route to chaos observed in the Plumb's model while increasing Re. The oscillations are periodic for $Re^{-1} = 0.06$ and show chaotic behaviour for the lowest Re^{-1} values, with passages into quasi-periodic regime ($Re^{-1} = 0.05$) and frequency-locked regime ($Re^{-1} = 0.025$), where some periodicity is retrieved.

The right panel shows the dynamical regimes as a function of Re^{-1} and a damping parameter α. The parameter α models the competition between two different dissipative mechanisms for the waves: a linear damping term (modelling the radiative cooling of the atmosphere) and a diffusive attenuation (see section 2.1.1 for a discussion on the dissipative mechanisms). When $\alpha \to 0$, the wave attenuation comes from the linear term only. On the opposite, when $\alpha \to 1$, the dissipation is mainly diffusive. The coloured field gives the dynamical regime. Low values of α (in white) correspond to periodic and frequency locked regimes, while high values (in red) are chaotic regimes. This result shows that the bifurcation thresholds are affected by the dissipative mechanism considered, but the

route to chaotic regimes is still observed. These results were confirmed by two dimensional DNS, suggesting that the observed bifurcations are not an artefact of the idealised Plumb's model. The existence of these non-periodic regimes could be an explanation for the QBO periodicity disruption observed in 2016 [Newman et al., 2016,Osprey et al., 2016].

In astrophysics, a model very similar to the Plumb's model was developed to investigate the flow driven by internal gravity waves in the Sun, especially at the tachocline [Kim and MacGregor, 2001]. Results (see figure 2.6) show that this model also exhibits different oscillation regimes, depending on the value of the viscous damping ν. The model was investigated to explain small amplitude periodic variations of the angular velocity observed at the solar tachocline [Howe et al., 2000]. For high value of viscosity, the model drives a stationary shear flow, similarly to the tachocline. However, when the viscosity is decreased, oscillations appear and a route to chaos is observed with decreasing viscosity.

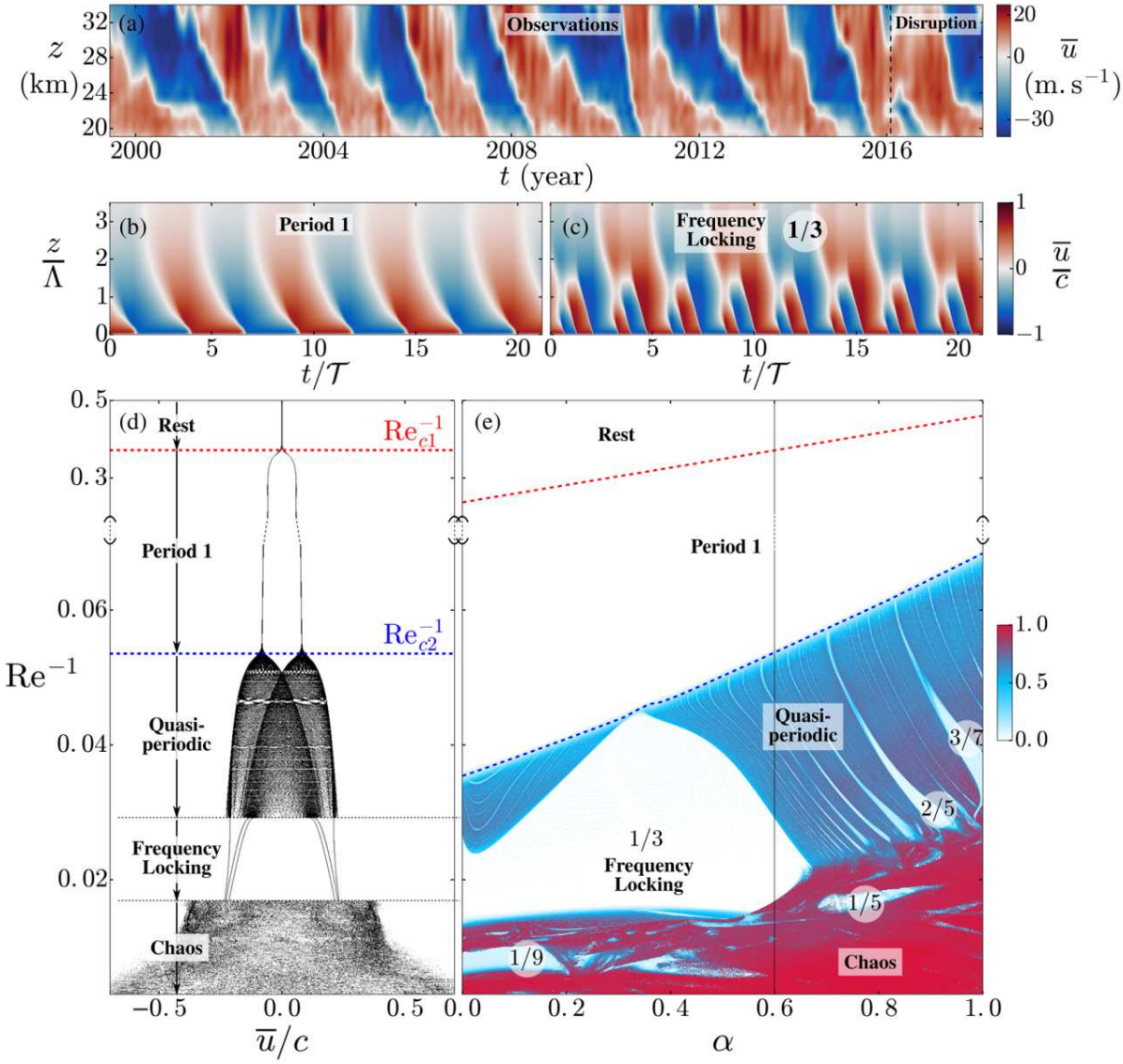

Figure 2.5: (a) Hovmöller diagram of observations of the QBO. The 2016 disruption is enlighten by a dash-line. (b-c) Hovmöller diagrams of the oscillations obtained using the Plumb's model. The oscillations are in a periodic regime (b) and frequency-locked regime (c). Λ is the wave attenuation length and $\mathcal{T}$ is the characteristic timescale of mean-flow reversals. (d) Poincaré map of the systematic exploration in term of Re of the Plumb's model. c is the wave zonal phase speed. (e) 2D Poincaré map showing the exporation in Re and α. The colourfield represents empirically the dynamical regime of the oscillations, with white colour corresponding to periodic and frequency-locked regimes, blue colour is quasi-periodic regimes and red is chaotic regimes. Reproduced from [Renaud et al., 2019].

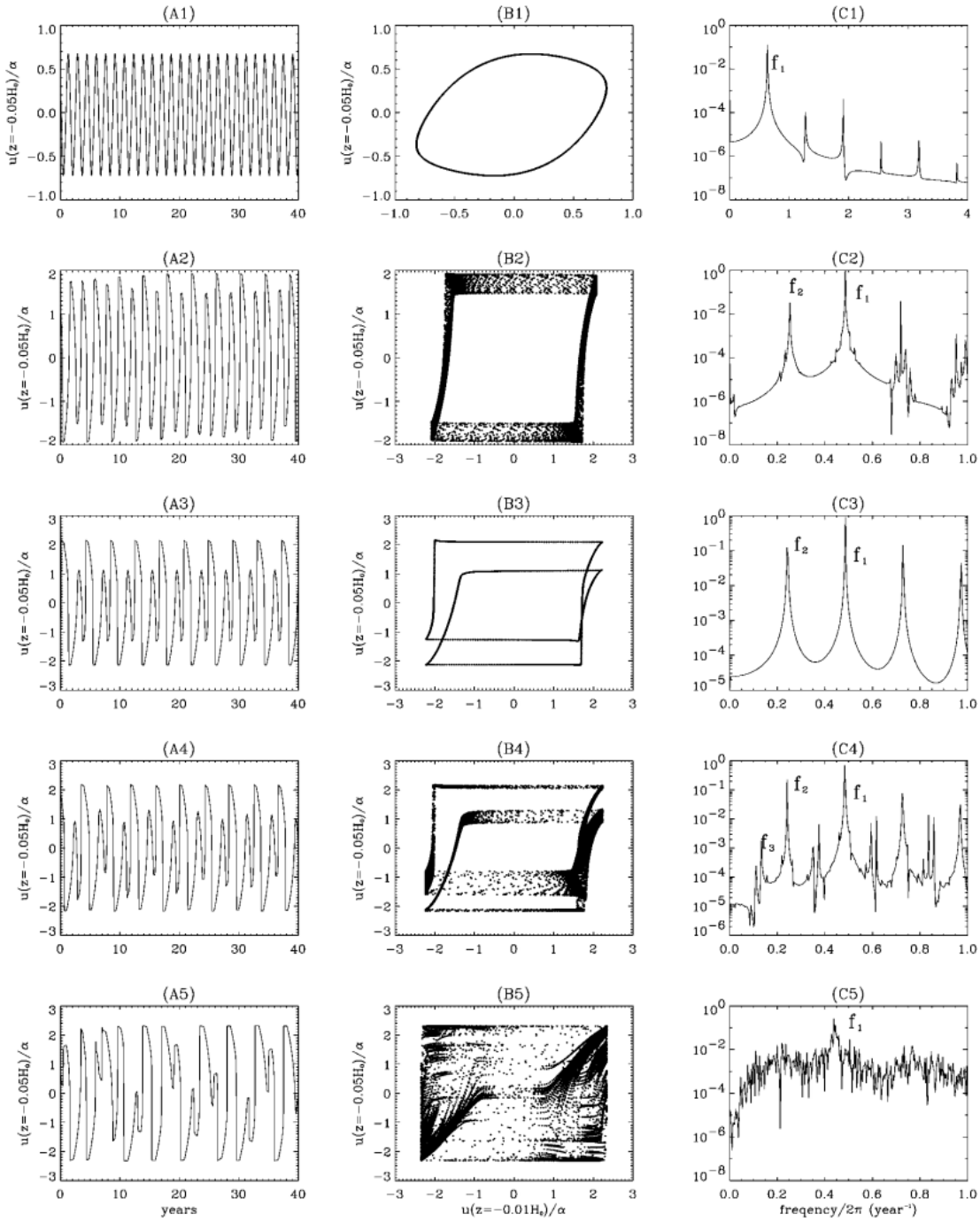

Figure 2.6: (A1-A5) Time evolution of $\overline{u}$ at a given height. (B1-B5) Phase-space diagram with the values of $\overline{u}$ taken at two different heights. (C1-C5) Frequency power spectrum for the signals shown on the first column. The kinematic viscosity ν decreases from the first row ($\nu = 3 \times 10^9$ cm$^2 \cdot$ s^{-1}) to the last row ($\nu = 10^8$ cm$^2 \cdot$ s^{-1}). Reproduced from [Kim and MacGregor, 2001].

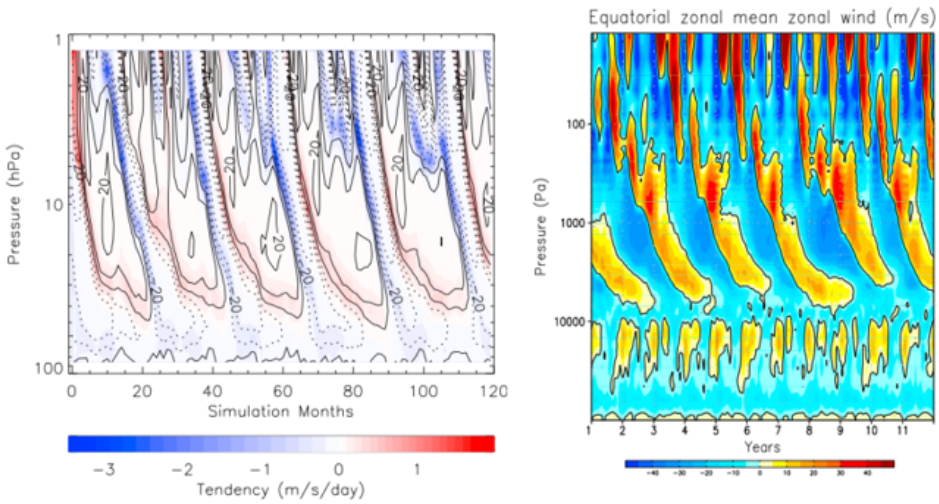

Figure 2.7: (Left) Time-height cross section of the monthly mean zonally averaged zonal winds. Winds are plotted in intervals of 10 $\mathrm{m \cdot s^{-1}}$. Colour field shows the wave forcing. Red (resp. blue) corresponds to eastward (resp. westward) acceleration. The numerical model used is the Whole Atmosphere Community Climate Model (WACCM). 61 waves are launched uniformally spaced in the range $[-c_0; c_0]$, with $c_0 = 30\ \mathrm{m \cdot s^{-1}}$ and $dc = 1\mathrm{m \cdot s^{-1}}$. The horizontal wavenumber $k_x = \frac{2\pi}{1000\ \mathrm{km^{-1}}}$ is constant for each wave. Reproduced from [Xue et al., 2012]. (Right) Time-height cross section of the zonally averaged zonal wind from a stochastic internal gravity waves parameterisation. The numerical model used is the LMDz GCM. Absolute phase speeds are randomly chosen in the range $[1; 50]\ \mathrm{m \cdot s^{-1}}$ and horizontal wavenumbers are chosen in the range $[0.02; 1]\ \mathrm{km^{-1}}$. Reproduced from [Lott et al., 2012].

2.2.2 Plumb-like models in GCMs

The QBO has a significant impact on weather events. As mentioned in chapter 1, it may affect hurricane activity in the Atlantic ocean. It deeply modulates the northern hemisphere winter climate, acts on the MJO and is also connected to ENSO. Additionally, recent studies have used GCMs to model the effects of the QBO on the climate system. It was found that the atmospheric response to sea ice loss is enhanced depending on the phase of the QBO [Labe et al., 2019] and that trace gas levels at the Earth's surface were affected by the QBO [Ray et al., 2020]. Consequently, it is hugely important that the QBO features are well reproduced in GCMs, in order to predict precisely the time evolution of the global dynamics. QBO is also considered as a metronome of atmospheric dynamics, and its presence as a proof of validity of a given model.

However, as mentioned in section 1.2.2, the GCMs resolution is too coarse to resolve small length-scale and short time-scale motions. Therefore, the QBO is generated *via* numerical models which are similar to the Plumb's model (WKB approach to compute a momentum flux associated with the wave field, which gives momentum to the ambient mean-flow). The waves are parametrised in order to drive a QBO which reproduced the actual QBO in terms of amplitude and period. Basically, at each time step, a finite number n of waves are generated. Their properties (amplitude, wavenumber, frequency,

direction) are set randomly and they propagate for certain time Δt given by their the dissipative mechanisms considered. Some results [Lott et al., 2012, Xue et al., 2012] are reproduced in figure 2.7.

Yet, the parameterisation of the waves is not trivial [Song et al., 2007] and the sensitivity of the GCM results regarding the vertical resolution is still discussed [Anstey et al., 2016, Yu et al., 2017]. The Plumb's model needs to be investigated to fully understand the effect of a multi-wave forcing on the QBO properties in order to refine the QBO generation in GCMs. The QBO initiative project (QBOi [Butchart et al., 2018, Bushell et al.,]) compares the QBO generated in 17 different models in order to improve the QBO modelling. Here, we return to the essentials of the problem and investigate the Plumb's model with a multi-modal forcing.

2.3 Our study

In the ocean and atmosphere, internal gravity waves are generated stochastically, with various amplitude, frequencies and wavenumbers. Spectra from observations are reproduced in figure 2.8 for the ocean and in figure 2.9 for the atmosphere. They both show a wide distribution of frequencies. Therefore, the classical monochromatic Plumb's model seems inadequate to study real wave driven flows, such as QBO, or the similar oscillations observed in Saturn or Jupiter.

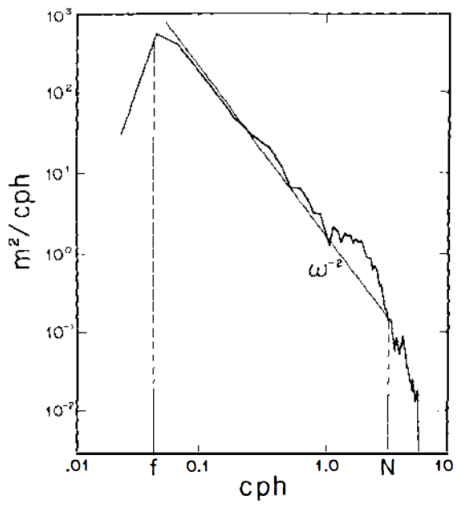

Figure 2.8: Power spectrum of the vertical displacement of an isotherm in the ocean. The line shows a -2 slope for reference. The -2 slope is generally observed and theoretically modelled in [Garrett and Munk, 1971]. Initial study is from [Cairns and Williams, 1976]. The figure is reproduced from [Garrett and Munk, 1979]. The waves are here affected by the rotation and decrease drastically for $\omega < f$ (see chapter 1).

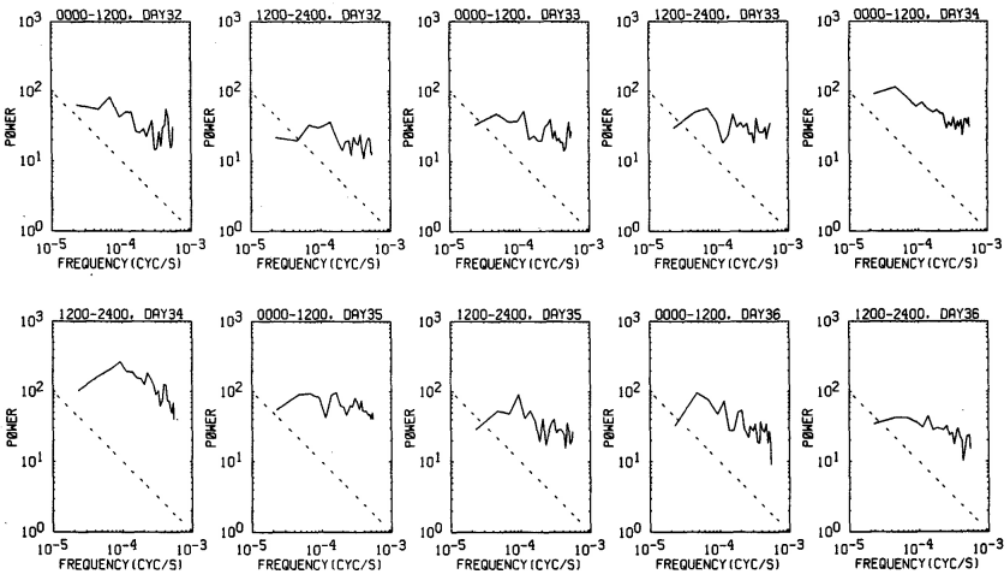

Figure 2.9: Averaged vertical velocity spectra, each mesured for 12 hours in the lower stratosphere. Frequencies are in cycles per second and energies in $(\mathrm{m}^2 \cdot \mathrm{s}^-2)/(\mathrm{cyc} \cdot \mathrm{s}^{-1})$. The dashed lines show a -1 slope for reference. Reproduced from [Fritts and Chou, 1987].

2.3.1 A spectrum as forcing

To account for the stochastic excitation present in nature, we consider a frequency spectrum for the forcing, instead of the usual monochromatic forcing in the Plumb's model. The horizontal wavenumber k_x is constant for all waves and we only consider a spectrum of frequencies in order to limit our study to the influence of ω. Wave amplitudes differ for each wave considered in the forcing spectrum.
Different spectra were considered:

- a Gaussian spectrum (figure 2.10a), characterised by a mean value ω_0 and a standard deviation σ. The total energy of the forcing E_{tot} is distributed among a frequency bandwidth $[\omega_{min} - \omega_{max}]$. Frequencies with $\mathrm{d}E/\mathrm{d}\omega < 10^{-4} \times \max(\mathrm{d}E/\mathrm{d}\omega)$ were not considered in the forcing spectrum. Thus, ω_{min} (resp. ω_{max}) is the lowest (resp. highest) frequency considered, with at least 0.01% energy of the most energetic wave. A small standard deviation is equivalent to a monochromatic forcing. The three parameters ω_0, σ and E_{tot} will be systematically explored in section 2.4.

- Spectra inspired from homogeneous turbulence, with and without rotation (figure 2.10b). Spectrum without rotation is flat from ω_{min} to a cut-off frequency ω_c, then the energy drops as $\omega^{-5/3}$. In the presence of rotation, the energy drops as ω^{-3} after the cut-off frequency.

For all cases considered, only the wave self-interactions are accounted for: all other wave–wave interactions are neglected.

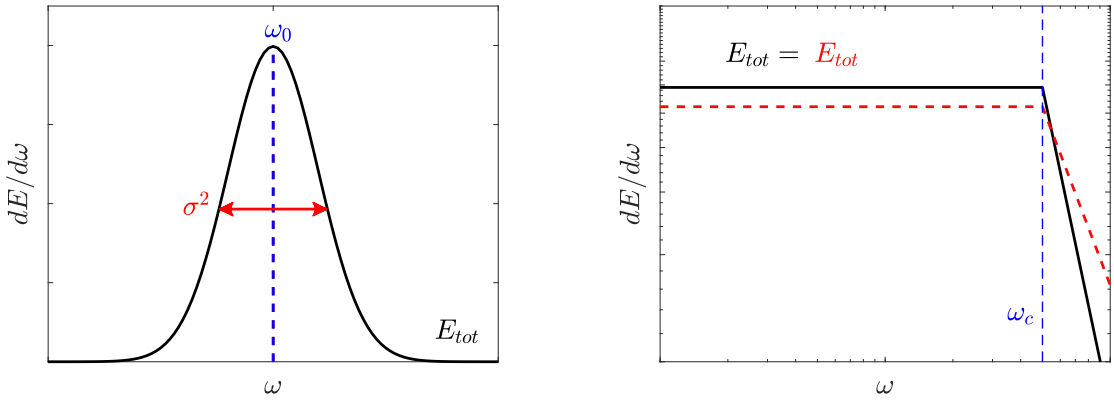

(a) (b)

Figure 2.10: (a) Gaussian spectrum characterised by the mean frequency ω_0, the standard deviation σ and the total energy E_{tot}. (b) Turbulent spectra without rotation (red dashed curve) and with rotation (black thick curve). Both are characterised by their cut-off frequency ω_c and the total energy E_{tot}.

Relation between energy and amplitude

In the equations described in section 2.1, the forcing term depends on the amplitude of the streamfunction ψ. In our study, we want to keep the total energy in the wave spectrum constant from one case to another. Therefore, a relation between wave amplitude and energy is needed.

In a Boussinesq fluid, with no background horizontal flow, the kinetic energy per unit of mass is written $E_k = \frac{1}{2}|\boldsymbol{u}|^2$. If we consider small amplitude waves and horizontally average over one wavelength, we can demonstrate that the mean available potential energy $\langle E_p \rangle$ is equal to the mean kinetic energy $\langle E_k \rangle$.

To compute the available potential energy, we use a fluid parcel argument. Let's consider that the fluid has constant buoyancy frequency at an arbitrary level, denoted $z = 0$. The background density near $z = 0$ is given by $\rho(z) \approx \rho_0(1 - \frac{z}{H})$, where H is a local density scale height. We compute the difference of potential energy when two parcels of fluid at $z = \pm\delta$ exchange their location with each other.

$$\begin{aligned} \Delta E_p &= g\rho_0 \left[(1 - \delta/H)(-\delta) + (1 + \delta/H)\,\delta\right] \\ &\quad - g\rho_0 \left[(1 + \delta/H)(-\delta) + (1 - \delta/H)\,\delta\right] \\ &= 4\rho_0 g \frac{\delta^2}{H} \end{aligned} \tag{2.52}$$

Thus, the available potential energy for **one** fluid parcel is $\Delta E_p/2$. Writing $g/H = N^2$ and $2\delta = \xi$, we write

$$E_p = \frac{1}{2}\rho_0 N^2 \xi^2 \tag{2.53}$$

We compute a horizontal average over a wavelength of the kinetic and available potential energies. The vertical displacement ξ can be written $\xi = A_\xi \cos\varphi$, with $\varphi =$

$k_x x + k_z z + \omega t$. Thus, the horizontal average of available potential energy is:

$$\begin{aligned}\langle E_p \rangle &= \langle \frac{1}{2}\rho_0 N^2 \xi^2 \rangle \\ &= \frac{1}{2}\rho_0 N^2 A_\xi^2 \langle \cos^2\varphi \rangle \\ &= \frac{1}{4}\rho_0 N^2 A_\xi^2\end{aligned} \tag{2.54}$$

The horizontal averaged kinetic energy is $\langle E_k \rangle = \langle \frac{1}{2}\rho_0 (u'^2 + w'^2) \rangle$. Using the fact that $w' = \frac{\partial \xi}{\partial z}$, the polarisation relation $A_{u'} = -\frac{k_z}{k_x} A_{w'}$ and the inviscid dispersion relation $\omega = N\cos(\theta)$ with $\theta = \tan^{-1}(k_z/k_x)$, we can write $u' = -N\sin(\theta) A_\xi \sin(\varphi)$ and $w' = N\cos(\theta) A_\xi \sin(\varphi)$. Then, we write:

$$\begin{aligned}\langle E_k \rangle &= \langle \frac{1}{2}\rho_0 (u'^2 + w'^2) \rangle \\ &= \frac{1}{2}\rho_0 \langle N^2 \sin^2\theta A_\xi^2 \sin^2\varphi + N^2 \cos^2\theta A_\xi^2 \sin^2\varphi \rangle \\ &= \frac{1}{2}\rho_0 N^2 A_\xi^2 \langle \sin^2\varphi \rangle \\ &= \frac{1}{4}\rho_0 N^2 A_\xi^2\end{aligned} \tag{2.55}$$

We see that $\langle E_p \rangle = \langle E_k \rangle$. Thus, the total average energy is:

$$\langle E \rangle = 2\langle E_k \rangle = 2\langle E_p \rangle \tag{2.56}$$

In order to compare the different cases, we need to keep the total energy injected at $z = 0$ equal to the same value. Let's consider the horizontally averaged energy per unit of mass for one frequency:

$$\langle E_\omega \rangle = 2\langle E_k \rangle = \langle |\boldsymbol{u'}|^2 \rangle \tag{2.57}$$

with $\boldsymbol{u'} = (u', w')$, $u' = \frac{\partial \psi}{\partial z}$ and $w' = -\frac{\partial \psi}{\partial x}$. We write $\psi = A_0 \cos(k_x x + k_z z + \omega t) = A_0 \cos(\varphi)$, with A_0 a function of ω. Then:

$$\begin{aligned}\langle E_\omega \rangle &= \langle (u'^2 + w'^2) \rangle \\ &= \langle \left(\frac{\partial \psi}{\partial z}\right)^2 + \left(-\frac{\partial \psi}{\partial x}\right)^2 \rangle \\ &= \langle A_0^2 k_z^2 \sin^2(\varphi) + A_0^2 k_x^2 \sin^2(\varphi) \rangle \\ &= A_0^2 \frac{k_x^2}{\omega^2} \langle \sin^2(\varphi) \rangle \\ &= \frac{1}{2} A_0^2 \frac{k_x^2}{\omega^2}\end{aligned} \tag{2.58}$$

The energy we want to keep constant through studies is the total energy contained in the considered spectrum of waves, *i.e.*:

$$\langle E \rangle = \langle \int E_\omega \mathrm{d}\omega \rangle = \frac{1}{2} \int k_x^2 \frac{A_0^2(\omega)}{\omega^2} \mathrm{d}\omega \tag{2.59}$$

2.3.2 Numerical model

The mean-flow equation (2.34) is numerically integrated with a semi implicit/explicit time scheme using finite differences. Time scheme is an order 1 Euler scheme and the Laplacian term is solved *via* an order 2 centred finite differences scheme. At each time step, the forcing term $\partial_z \overline{u'w'}$ is computed from equation (2.51) at a time t. Then, the mean-flow $\overline{u}(z, t + \delta_t)$ is calculated by adding the effect of the divergence of the Reynolds stress and viscosity. We use a no-slip boundary condition at the bottom, $\overline{u}|_{z=0} = 0$, and a free-slip boundary condition at the top $\left.\frac{\partial \overline{u}}{\partial z}\right|_{z=1} = 0$. The influence of the top-boundary condition will be discussed in section 2.4.

Singularities appear in the forcing term expression (2.51) when $\omega_\pm \to 0$ or $\omega_\pm \to 1$. The former case physically corresponds to a critical layer. Numerically, critical layers are treated as follows: if the mean-flow reaches a value higher than 0.95 ω/k_x at a given height z_c, the momentum contained in the waves is deposited at the grid point below z_c and the forcing terms for $z \geqslant z_c$ are set to 0. The latter case corresponds to a wave whose Doppler-shifted frequency is close to the buoyancy frequency. This is treated as in the critical layer case, with the condition now being $|\omega_\pm| \geqslant 0.95$. The choice of the 0.95 pre-factor allows to have a δ_t reasonably large without affecting the results. A lower value would increase the computation errors. A larger value would impose to consider very small time steps to solve the critical layer precisely.

Viscosity and diffusivity are set to experimental values for salty water, as in experiments [Semin et al., 2018]. Using the laboratory experiment parameters of [Semin et al., 2018], we have $H = 0.41$ m (the height of the stratified layer) and $N = 2.16$ s^{-1}. The dimensionless dissipation constants are $\nu = 2.8 \times 10^{-6}$ and $\mathcal{D} = \nu/700$. Thus, viscosity is the main dissipative mechanism for both the large-scale flow and the waves.

Note that $\mathcal{D}$ only appears in the wave attenuation while ν appears in both the wave attenuation and the mean-flow dissipation.

There are three main numerical parameters in our simulations: the time step δ_t, the grid spacing δ_z and the number of frequencies in the forcing spectrum N_ω. We ran convergence studies to choose the values of these parameters. We ran simulations with $E_{tot} = 10^{-5}$ or $E_{tot} = 2 \times 10^{-6}$ and for two standard deviations $\sigma = 10^{-4}$ and $\sigma = 10^{-1}$. Simulations are run for ~ 15 reversal times. The results for these convergence calculations are presented in appendix.

We use $\delta_z = 1/2000$ for all simulations. A total number of frequencies $N_\omega = 20$ was found to be satisfactory for all cases. These frequencies were separated by $\Delta\omega = (\omega_{max} - \omega_{min})/N_\omega$. δ_t was adjusted for each study: we chose $\delta_t = 1$ for the σ and ω_0 systematic studies, while δ_t was set to either 0.1, 0.5 or 1 depending on the value of E_{tot} for the energy systematic study.

2.4 Multi-modal model for the QBO

This article, currently in review for *Physical Review Letters*, sums up the results of our study of the Plumb's model using a stochastic forcing. The article gives the reader a reminder of the context and introduces the essentials of the model. Then the results showing the systematic exploration of the Gaussian forcing, and comparison with "turbulent spectra" forcings, are presented and discussed.

Multi-modal excitation to model the Quasi-Biennial Oscillation

P. Léard[1,†], D. Lecoanet[2], and M. Le Bars[1]
[1] *Aix Marseille Université, CNRS, Centrale Marseille, IRPHE, Marseille, France*
[2] *Department of Astrophysical Sciences, Princeton, USA*
[†] *corresponding author: leard@irphe.univ-mrs.fr*
(Dated: June 30, 2020)

The Quasi-Biennial Oscillation (QBO) of stratospheric winds is the most striking example of mean-flow generation and reversal by the non-linear interactions of internal waves. Previous studies have used an idealized monochromatic forcing to investigate the QBO. Here we instead force a more realistic continuous wave spectrum. Unexpectedly, spreading the wave energy across a wide frequency range leads to more regular oscillations. We also find that different forcing spectra can yield the same QBO. Multi-modal wave forcing is thus essential for understanding wave—mean-flow interactions in nature.

Internal gravity waves (IGWs) are ubiquitous in geophysical and astrophysical flows, *e.g.* in Earth's oceans [1], atmosphere [2, 3] and core [4], as well as in stellar interiors [5–7]. IGWs extract momentum from where they are excited and transport it to where they are damped [8]. In the Earth's stratosphere, these waves are known to drive oscillations of the zonal winds at equatorial latitudes, with a period of nearly 28 months. This phenomenon, known as Quasi-Biennial Oscillation (QBO), affects, e.g., hurricane activity in the Atlantic ocean [9], and the winter climate in Europe [10, 11]. Similar reversals are observed in the atmosphere of other planets of the Solar system [12, 13]. The QBO is a striking example of order spontaneously emerging from a chaotic system [14], similar to magnetic field reversals in dynamo experiments [15] or large-scale, mean flow reversals in Rayleigh-Bénard convection [16].

Atmospheric waves are excited by turbulent motions in the troposphere and propagate in the stratosphere, leading to zonal wind reversals. Lindzen and Holton [17, 18] first proposed the QBO is due to wave–mean-flow interactions, which Plumb [19] used to construct an idealized model. The model considers the interaction of two counter-propagating gravity waves with the same frequency, wavelength, and amplitude (i.e., a standing wave), with a mean-flow. This model was realised experimentally using an oscillating membrane at the boundary of a linearly-stratified layer of salty water [20–23]. The experiments can drive oscillating mean-flows similar to the QBO, as predicted by the Lindzen and Holton theory. More recently, [24] simulated the Plumb model numerically to explain the 2016 disruption of the QBO [25, 26]. Although they find regular oscillations in the mean-flow at low forcing amplitudes, the mean-flow becomes quasi-periodic, and eventually chaotic as the forcing amplitude increases. Atmospheric forcing amplitudes are in the chaotic mean-flow regime, suggesting that the Plumb model must be refined to explain the QBO.

Because of its influence on weather events, it is crucial that the period and amplitude of the QBO are accurately modelled in Global Circulation Models (GCMs). Due to their relatively coarse resolution, GCMs cannot compute small time- and length-scale motions like IGWs. Therefore, IGWs are parameterised in order to generate a realistic QBO. Some GCMs are able to self-consistently generate the QBO [27, 28], which is considered a key test of a model's wave parameterization. The dependence of the QBO on vertical resolution and wave spectrum properties is not yet understood [29–31].

Direct numerical simulations have found mean-flow oscillations generated by a broad spectrum of IGWs self-consistently excited by turbulence [14]. The influence of the forcing on the large-scale flow oscillations could not be studied extensively, because it is expensive to run 2D simulations for long integration times. Only a Plumb-like one-dimensional model can realistically allow for a systematic exploration.

Despite the existence of a broad spectrum of waves in nature, only [32] has studied multi-wave forcing. Although he only used three different forcing spectra, he found the QBO period is affected by the choice of spectrum. In this letter, we consider a wide class of wave spectra in the Plumb model. We find that forcing a broad frequency range produces regular mean-flow oscillations, even when the forcing amplitude is so large that monochromatic forcing produces a chaotic mean-flow. This suggests multi-modal forcing is an essential to understand wave–mean-flow interactions.

MODEL

Mean-flow evolution is determined by the spatially-averaged Navier-Stokes equations [33]. We define the horizontal mean-flow $\overline{u}$; overbar indicates horizontal (x) average. Gravity points in the $-z$ direction, and the velocity fluctuations are (u', w'). Then

$$\partial_t \overline{u} - \nu \partial_{zz} \overline{u} = -\partial_z \overline{u'w'} \tag{1}$$

where ν is the kinematic viscosity. The mean-flow is forced by the Reynolds stress term on the right-hand side of (1). In the Plumb model, the Reynolds stress comes from the self-interaction of IGWs. We excite the waves at the bottom boundary $z = 0$, and propagate the waves through a linearly-stratified domain characterized by a fixed buoyancy frequency N. We non-dimensionalize the

problem by setting the top boundary at $z = 1$ and setting $N = 1$. Wave damping leads to vertical variation in the Reynolds stress, driving the mean-flow. Conversely, the waves are Doppler-shifted by the mean-flow, changing their propagation and damping.

We consider a superposition of plane waves $\psi_i = A_i(z)e^{i(k_x x - \omega_i t)}$, where ψ_i is the streamfunction, k_x the horizontal wavenumber, and ω_i the angular frequency. Assuming a time-scale and length-scale separation between the fast, short vertical scale IGWs, and the slowly evolving, long vertical scale mean flow, we use the WKB approximation to derive an expression $A_i(z)$ in terms of the wave forcing spectrum. We also make use of the following approximations. We take the "weak" dissipation approximation, assume the background stratification is constant in space and time, and neglect wave-wave nonlinearities, except when they affect the mean flow; see details in [34] and Supplementary Materials A.1. Unlike the classical model which uses the hydrostatic approximation [19, 34], we solve the full vertical momentum equation for the wave, which allows for high-frequency IGWs. We neglect Newtonian cooling but consider diffusion of the stratifying agent (with diffusivity D), which is relevant for both laboratory experiments and the Direct Numerical Simulations described below. The inverse damping lengthscale is given by

$$l_i^{-1} = \frac{1}{2k_x} \times \frac{\nu + D}{\left(1 - k_x^2 c_i^2\right)^{1/2} c_i^4} \tag{2}$$

where $c_i = \frac{\omega_i \mp k_x \overline{u}}{k_x}$; $\mp$ accounts for the wave direction of propagation. The right-hand side of (1) is written as a sum of independent forcing terms $\sum_i \tilde{F}_i(z)$, where $\tilde{F}_i(z)$ is related to the amplitude $A_i(z)$ for each wave.

The classic Plumb model considers a single value of ω, k_x, and forcing amplitude $A(z = 0)$. To account for the multi-modal excitation of waves in natural systems, we consider excitation by multiple frequencies with different forcing amplitudes. The kinetic energy of the waves is given by $E_{tot} = \int (dE/d\omega)d\omega$, and we force the waves so the energy density $dE/d\omega$ is a Gaussian in frequency centered at $\omega = \omega_0$ with a standard deviation σ. We discretize this spectrum with N_ω standing waves of frequency $\{\omega_i\}$ with frequency-spacing $\omega_{i+1} - \omega_i = \Delta\omega$. The forcing amplitude is $A_i = \sqrt{2(dE/d\omega)\Delta\omega \frac{\omega_i^2}{k_x^2}}$. Our results depend only on $dE/d\omega$, not on the amplitudes of the individual modes (which vary with N_ω). We only consider a single value of $k_x = 4\pi$. This general forcing spectrum allows us to study the transition from monochromatic forcing ($\sigma \to 0$) to multi-modal forcing (white noise in the limit $\sigma \to \infty$). We consider the dimensionless dissipation $\nu = 2.8 \times 10^{-6}$ and $D = \nu/700$, estimated from laboratory experiments [23]; we explored the ranges $\omega_0 \in [0.1; 0.55]$, $\sigma \in [10^{-4}; 3 \times 10^{-1}]$ and $E_{tot} \in [7 \times 10^{-7}; 10^{-5}]$. For comparison with previous monochromatic studies [19, 24], the wave forcing Reynolds number of each individual wave goes up to ~ 100, which is comparable to the range explored in [24]. We initialize $\overline{u}$ with a small amplitude sinusoid. Boundary conditions for the mean-flow are no-slip ($\overline{u} = 0$) at the bottom and free-slip ($\partial_z \overline{u} = 0$) at the top ($z = 1$). The waves freely propagate out of the domain's top boundary without reflection. Section A.2 of the Supplementary Materials describes our spatial and temporal discretization, and demonstrates numerical convergence of our simulations.

We investigated the influence of top boundary conditions (BCs) on the mean-flow evolution using two-dimensional direct numerical simulations of the Navier-Stokes equations [35, 36]. We found the top BCs only marginally influence the period and amplitude of the oscillations, and do not affect their dynamical regime (see Supplementary Materials C). We thus focus on results from our 1D model, which allows for the systematic exploration of a larger parameter space. The vertical extent of the simulation domain also does not qualitatively change our results, even though some high-frequency waves have attenuation lengths greater than the domain height (see Supplementary Materials D).

RESULTS

We first investigate the influence of the forcing bandwidth on the mean-flow evolution, varying the standard deviation σ of our Gaussian excitation spectrum, but fixing the central frequency and total energy. Figure 1 shows that for narrow Gaussian distributions $10^{-4} \leqslant \sigma < 10^{-2}$, the system produces frequency-locked oscillations, with slow oscillations in the upper part of the domain and fast oscillations in the bottom part (Figure 1e). The frequency power spectrum for $\sigma = 3 \times 10^{-4}$ (Figure 1h) shows peaks at these two frequencies (f_0 and $f_0/2$), as well as at harmonic/beating frequencies. Frequency-locked regimes are characterised by a signal with two or more frequencies whose ratios are rational.

At $\sigma \approx 10^{-2}$, the oscillations transition from a frequency-locked regime to a quasi-periodic regime (Figure 1d, g). A second bifurcation to periodic oscillations occurs at $\sigma = 5 \times 10^{-2}$, with only one dominant frequency (plus harmonics) appearing in the corresponding spectrum (Figure 1f). Forcing spectra with wide bandwidths lead to more organised, QBO-like states.

A wide bandwidth forcing spectrum is more complicated and includes more frequencies; naively this would lead to chaotic mean-flows. However, a wider spectrum also excites higher frequency waves. High-frequency waves experience less damping than low-frequency waves, so they can propagate higher in the domain. Because the QBO reversal occurs at the top, we hypothesize the period and regularity of the oscillation is determined by the highest frequency wave above a threshold amplitude (See Supplementary Materials e). At fixed wave forcing amplitude, higher frequency waves correspond to more regular oscillations with longer periods (Figure 2a). Fur-

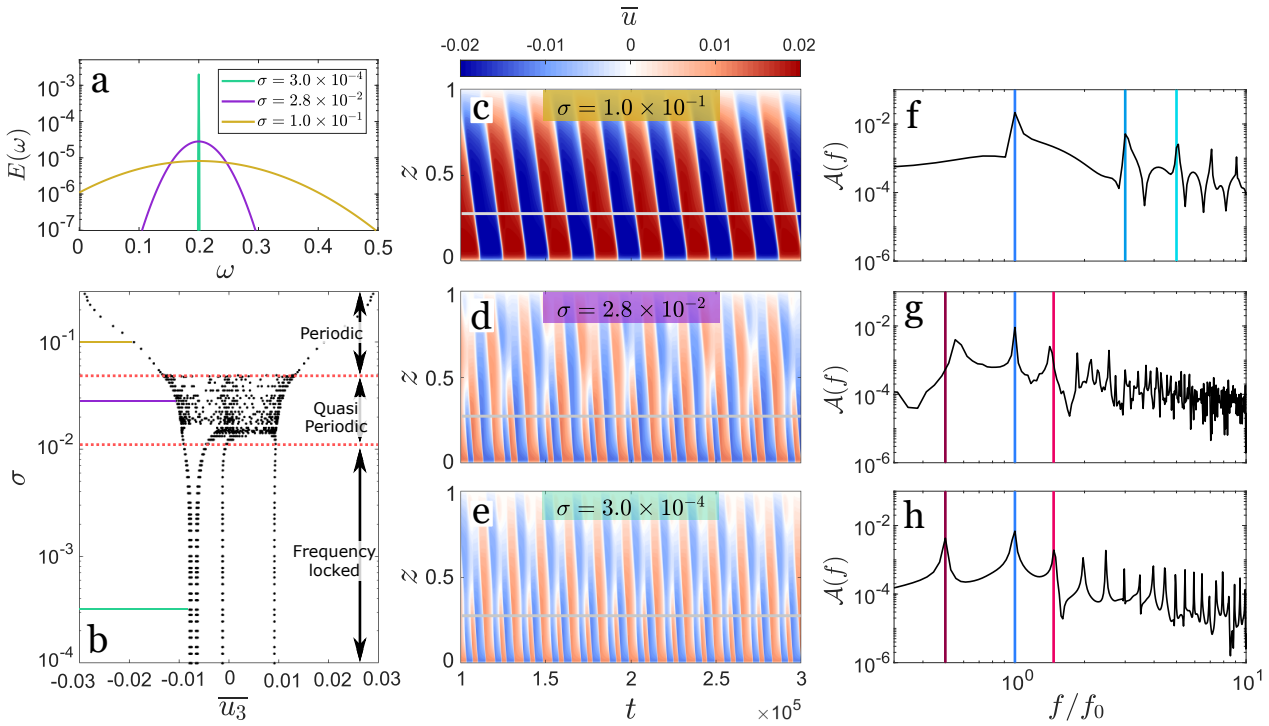

FIG. 1. Mean-flows generated by a Gaussian forcing spectrum with standard deviation σ, central frequency $\omega_0 = 0.2$ and total kinetic energy $E_{tot} = 2 \times 10^{-6}$. (a) Example forcing spectra: $\sigma = 1 \times 10^{-1}$ in brown, $\sigma = 2.8 \times 10^{-2}$ in purple and $\sigma = 3 \times 10^{-4}$ in green. (b) Poincaré map: each dot is the value of the flow $\overline{u}(z,t)$ at $z = 0.5$ (denoted $\overline{u_3}$) when $\overline{u}(z = 0.1) = 0$. Periodic oscillations are represented by two points, symmetric about $\overline{u_3} = 0$ (more details in Supplementary Materials B). The asymmetry for the points below $\sigma \sim 10^{-2}$ is due to the initial condition. (c-e) Hovmöller diagrams of the mean-flow $\overline{u}$ for different σ. (f-h) Amplitudes of the temporal Fourier transform taken at $z = 0.25$ for each Hovmöller diagram. Frequencies are normalised by the frequency of maximum amplitude f_0, indicated by the dark blue line. The dark red line shows $f = f_0/2$, and the other vertical lines represent harmonics.

thermore, the amplitude of the mean-flow is larger when forced by higher frequency waves, because the phase velocity is larger. This means the amplitude of the mean-flow is larger for the periodic oscillations forced by a wide spectrum (Figure 1b).

Figure 2 shows Poincaré maps for simulations forced with different central frequencies ω_0, at fixed total energy E_{tot} (see Supplementary Materials B for details of this calculation). We used either a narrow distribution ($\sigma = 10^{-4}$) or a broad distribution ($\sigma = 10^{-1}$). The top panel ($\sigma = 10^{-4}$, very close to monochromatic forcing) shows a transition from periodic oscillations to non-periodic oscillations at $\omega_0 = 0.184$. There is a second bifurcation at $\omega_0 = 0.22$ leading to periodic oscillations. The amplitude of the oscillations rises with ω_0 because the phase velocity increases. The Poincaré map for variable ω_0 (Figure 2) is qualitatively similar to the Poincaré map for variable σ (Figure 1b), suggesting that the primary effect of increasing σ is to put more power into high-frequency waves. Note, the frequency of the second bifurcation to periodic oscillations changes with domain height because the forced wave has a viscous attenuation length greater than our domain height. However, the periodic oscillations for large σ are not due to the finite domain size (Supplementary Materials D). The bottom panel of Figure 2 ($\sigma = 10^{-1}$, wide spectrum) shows periodic oscillations for all ω_0. Once again, we find that a wide forcing spectrum with many frequencies will almost always generate regular, periodic oscillations.

In Figure 3, we plot Poincaré maps for different forcing amplitudes, with fixed ω_0 and σ. The top panel ($\sigma = 10^{-4}$, very close to monochromatic forcing) qualitatively reproduces the results from [24]. As the amplitude of the monochromatic forcing increases, periodic oscillations bifurcate into frequency-locked oscillations ($E_{tot} \approx 1.4 \times 10^{-6}$), and then again into quasi-periodic or chaotic oscillations ($E_{tot} \approx 2.4 \times 10^{-6}$). On the other hand, when forcing with a wide spectrum ($\sigma = 10^{-1}$, bottom panel), we only find regular periodic oscillations.

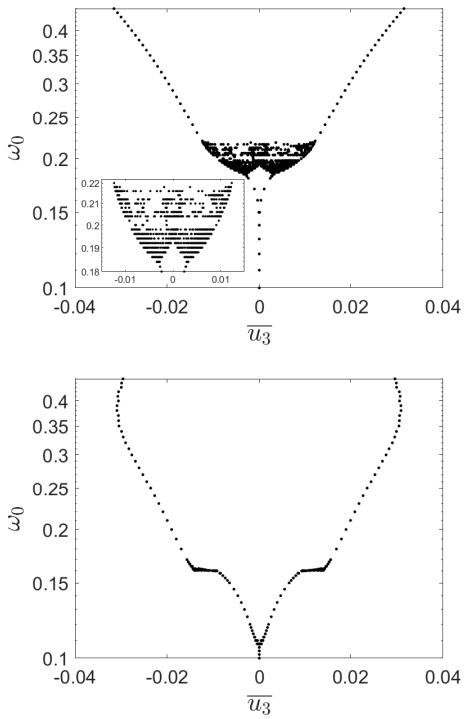

FIG. 2. Poincaré maps using the same method as Figure 1b for simulations with different ω_0, with $E_{tot} = 2 \times 10^{-6}$ and $\sigma = 10^{-4}$ (top) or $\sigma = 10^{-1}$ (bottom). The inset zooms in on the frequency range $\omega_0 \in [0.18; 0.22]$ to show the transitions between periodic, frequency-locked, and quasi-periodic regimes.

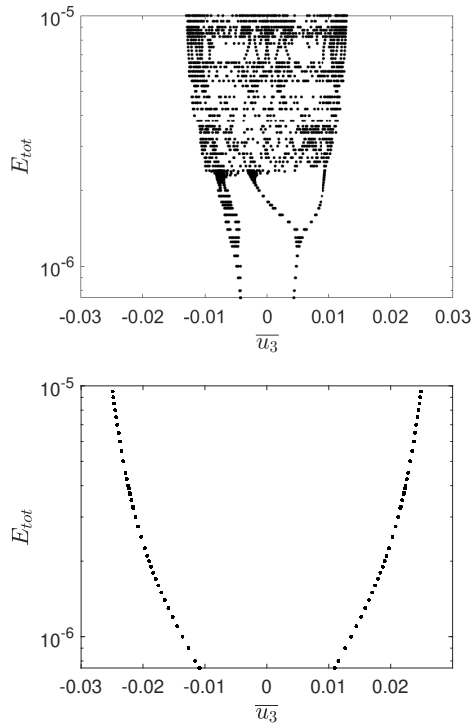

FIG. 3. Poincaré maps using the same method as Figure 1b for simulations with different E_{tot}, with $\omega_0 = 0.2$ and $\sigma = 10^{-4}$ (top) or $\sigma = 10^{-1}$ (bottom).

DISCUSSION

Our study demonstrates that a broad spectrum of IGWs can generate regular mean-flow oscillations. Whereas large-amplitude monochromatic forcing often generates chaotic mean-flows [24], forcing a broad spectrum of waves consistently generates periodic mean-flows, similar to what is observed in the Earth's atmosphere. The mean-flow evolution appears to be determined by high-frequency waves which can propagate higher, and control the mean-flow's reversal. We hypothesize the disruption observed in 2016 [25, 26] is due to intense events which focused significant energy into waves with similar frequency and wavenumber. Those waves could then trigger non-periodic reversals for a short time, as suggested by [24].

We have run several simulations with forcing spectra more representative of turbulence. In these simulations, we assume $dE/d\omega$ is constant for $\omega < \omega_c$, and decreases as a power-law for $\omega > \omega_c$. We tested an $\omega^{-5/3}$ power-law corresponding to Kolmogorov's law and Taylor's "frozen turbulence" hypothesis, and an ω^{-3} power-law corresponding to the energy cascade observed in rotating turbulence. In both cases, the waves drive periodic mean-flow oscillations.

We find that different forcing spectra can lead to the same mean-flow evolution. For example, the top panel of Figure 4 shows a Hovmöller diagram for the $\omega^{-5/3}$ spectrum with total energy $E_{tot} = 2.5 \times 10^{-6}$. It is quantitatively similar to the Hovmöller diagram of Figure 1c, obtained with a Gaussian forcing and 20% less energy (oscillation periods differ by 4.5% and amplitudes by 15%). The ω^{-3} spectrum with $E_{tot} = 2.8 \times 10^{-6}$ also generates a similar mean-flow (bottom panel of Figure 4; oscillation periods are equal and amplitudes differ by 14%). Since multiple wave spectra can produce the same mean-flow oscillations, reproducing the Earth's QBO in a GCM does not mean the IGW parameterization is correct.

Our simulations use parameters similar to laboratory experiments of the QBO [20, 23]. In the atmosphere, wave attenuation also occurs via Newtonian cooling, which we did not include in our simulations. Besides, the forcing is stronger and viscosity is weaker. Waves deposit their energy either via critical layers (which we include in our model), or via breaking due to wave amplification from density variations. Our calculations show the mean-flow period and amplitude is set by high-frequency waves with large viscous attenuation lengths. Although many more atmospheric waves have small viscous attenuation lengths, high-frequency waves are still more important than low-frequency waves because they do not encounter critical layers. Thus, we believe high-frequency waves

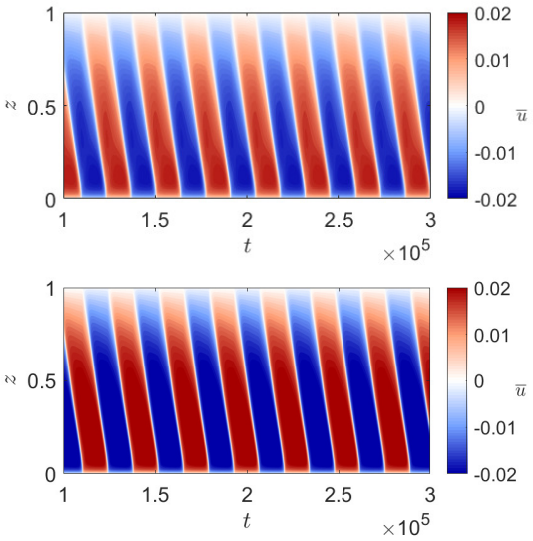

FIG. 4. Hovmöller diagram of the mean-flow $\overline{u}$ in simulations with different forms of the forcing spectrum. In the top panel, $dE/d\omega$ is constant up to $\omega_c = 0.2$, and decreases as $\omega^{-5/3}$ for higher frequencies; the total energy is $E_{tot} = 2.5 \times 10^{-6}$. In the bottom panel, $dE/d\omega$ is constant up to $\omega_c = 0.23$, and decreases as ω^{-3} for higher frequencies; the total energy is $E_{tot} = 2.8 \times 10^{-6}$.

likely play a key role in setting the QBO properties, just as they are important in our simulations.

In conclusion, this letter shows that the frequency spectrum of internal gravity waves plays a key role in the generation and properties of periodic large-scale flow reversals like the QBO. Although we studied general frequency spectra, we limited our investigation to a single wavenumber. Future work should also include the wide range of horizontal wavenumbers ($10-1000$ km) observed in the atmosphere, including low-frequency, planetary-scale waves which may also be an important source of momentum for the QBO [37]. Additionally, the study of the QBO in a fully coupled, convective–stably-stratified model system by [14] showed that accounting for only the energy spectrum in a Plumb-like model is not sufficient to reproduce the realistic reversals; it also requires information about higher order statistics. Clearly, reliable parameterization of this climatic metronome in GCMs still demands additional work.

ACKNOWLEDGMENT

The authors acknowledge funding by the European Research Council under the European Union's Horizon 2020 research and innovation program through Grant No. 681835-FLUDYCO-ERC-2015-CoG. They also thank Benjamin Favier (IRPHE, CNRS, Marseille, France) for fruitful discussions. DL is funded by a Lyman Spitzer Jr. fellowship.

[1] C. Garrett and W. Munk, "Internal waves in the ocean," Annual Review of Fluid Mechanics, vol. 11, no. 1, 1979.
[2] D. C. Fritts and M. J. Alexander, "Gravity wave dynamics and effects in the middle atmosphere," Reviews of Geophysics, vol. 41, no. 1, 2003.
[3] S. D. Miller, W. C. Straka, J. Yue, S. M. Smith, L. Hoffmann, M. Setvák, and P. T. Partain, "Upper atmospheric gravity wave details revealed in nightglow satellite imagery," Proceedings of the National Academy of Sciences, vol. 112, no. 49, 2015.
[4] B. Buffett, N. Knezek, and R. Holme, "Evidence for MAC waves at the top of Earth's core and implications for variations in length of day," Geophysical Journal International, vol. 204, pp. 1789–1800, Mar. 2016.
[5] C. Charbonnel and S. Talon, "Mixing a stellar cocktail," Science, vol. 318, no. 5852, 2007.
[6] T. Straus, B. Fleck, S. M. Jefferies, G. Cauzzi, S. W. McIntosh, K. Reardon, G. Severino, and M. Steffen, "The energy flux of internal gravity waves in the lower solar atmosphere," The Astrophysical Journal, vol. 681, no. 2, 2008.
[7] T. M. Rogers, D. N. C. Lin, J. N. McElwaine, and H. H. B. Lau, "Internal gravity waves in massive stars: Angular momentum transport," The Astrophysical Journal, vol. 772, p. 21, July 2013.
[8] F. P. Bretherton, "Momentum transport by gravity waves," Quarterly Journal of the Royal Meteorological Society, vol. 95, pp. 213–243, Apr. 1969.
[9] M. P. Baldwin, L. J. Gray, T. J. Dunkerton, K. Hamilton, P. H. Haynes, W. J. Randel, J. R. Holton, M. J. Alexander, I. Hirota, T. Horinouchi, D. B. A. Jones, J. S. Kinnersley, C. Marquardt, K. Sato, and M. Takahashi, "The quasi-biennial oscillation," Reviews of Geophysics, vol. 39, pp. 179–229, May 2001.
[10] A. G. Marshall and A. A. Scaife, "Impact of the QBO on surface winter climate," Journal of Geophysical Research, vol. 114, p. D18110, Sept. 2009.
[11] Z. Labe, Y. Peings, and G. Magnusdottir, "The effect of QBO phase on the atmospheric response to projected arctic sea ice loss in early winter," Geophysical Research Letters, vol. 453, no. 13, pp. 7663–7671, 2019.
[12] T. Fouchet, S. Guerlet, D. F. Strobel, A. A. Simon-Miller, B. Bézard, and F. M. Flasar, "An equatorial oscillation in Saturn's middle atmosphere," Nature, vol. 453, pp. 200–202, May 2008.
[13] C. B. Leovy, A. J. Friedson, and G. S. Orton, "The quasi-quadrennial oscillation of Jupiter's equatorial stratosphere," Nature, vol. 354, pp. 380–382, Dec. 1991.
[14] L.-A. Couston, D. Lecoanet, B. Favier, and M. Le Bars, "Order out of chaos: slowly-reversing mean flows emerge from turbulently-generated internal waves," Physical Review Letters, vol. 120, p. 12, June 2018.
[15] M. Berhanu, R. Monchaux, S. Fauve, N. Mordant, F. Pétrélis, A. Chiffaudel, F. Daviaud, B. Dubrulle,

L. Marié, F. Ravelet, M. Bourgoin, P. Odier, J.-F. Pinton, and R. Volk, "Magnetic field reversals in an experimental turbulent dynamo," Europhysics Letters (EPL), vol. 77, p. 59001, Mar. 2007. Publisher: IOP Publishing.

[16] F. F. Araujo, S. Grossmann, and D. Lohse, "Wind reversals in turbulent rayleigh-bénard convection," Physical review letters, vol. 95, no. 8, p. 084502, 2005.

[17] R. S. Lindzen and J. R. Holton, "A Theory of the Quasi-Biennial Oscillation," Journal of the Atmospheric Sciences, p. 13, 1968.

[18] R. S. Lindzen, "An updated theory for the quasi-biennial oscillation cycle of the tropical stratosphere," Journal of the Atmospheric Sciences, 1972.

[19] R. A. Plumb, "The interaction of two internal waves with the mean flow: Implications for the theory of the quasi-biennial oscillation," Journal of the Atmospheric Sciences, 1977.

[20] R. A. Plumb and A. D. McEwan, "The instability of a forced standing wave in a viscous stratified fluid: a laboratory analogue of the quasi-biennial oscillation," Journal of the Atmospheric Sciences, 1978.

[21] N. Otobe, S. Sakai, S. Yoden, and M. Shiotani, "Visualization and wkb analysis of the internal gravity wave in the qbo experiment," Nagare: Japan Soc. Fluid Mech, vol. 17, no. 3, 1998.

[22] B. Semin, G. Facchini, F. Pétrélis, and S. Fauve, "Generation of a mean flow by an internal wave," Physics of Fluids, vol. 28, p. 096601, Sept. 2016.

[23] B. Semin, N. Garroum, F. Pétrélis, and S. Fauve, "Nonlinear saturation of the large scale flow in a laboratory model of the quasi-biennial oscillation," Physical Review Letters, vol. 121, Sept. 2018.

[24] A. Renaud, L.-P. Nadeau, and A. Venaille, "Periodicity disruption of a model quasi-biennial oscillation of equatorial winds," Physical Review Letters, vol. 122, no. 21, p. 214504, 2019.

[25] S. M. Osprey, N. Butchart, J. R. Knight, A. A. Scaife, K. Hamilton, J. A. Anstey, V. Schenzinger, and C. Zhang, "An unexpected disruption of the atmospheric quasi-biennial oscillation," Science, vol. 353, pp. 1424–1427, Sept. 2016.

[26] P. A. Newman, L. Coy, S. Pawson, and L. R. Lait, "The anomalous change in the QBO in 2015–2016," Geophysical Research Letters, vol. 43, pp. 8791–8797, Aug. 2016.

[27] F. Lott, L. Guez, and P. Maury, "A stochastic parameterization of non-orographic gravity waves: Formalism and impact on the equatorial stratosphere," Geophysical Research Letters, vol. 39, no. 6, 2012.

[28] F. Lott and L. Guez, "A stochastic parameterization of the gravity waves due to convection and its impact on the equatorial stratosphere: stochastic GWS due to convection and QBO," Journal of Geophysical Research: Atmospheres, vol. 118, pp. 8897–8909, Aug. 2013.

[29] X.-H. Xue, H.-L. Liu, and X.-K. Dou, "Parameterization of the inertial gravity waves and generation of the quasi-biennial oscillation: IGW in WACCM and generation of QBO," Journal of Geophysical Research: Atmospheres, vol. 117, pp. n/a–n/a, Mar. 2012.

[30] J. Anstey and J. Scinocca, "Simulating the QBO in an atmospheric general circulation model: Sensitivity to resolved and parameterized forcing," Journal of the Atmospheric Sciences, vol. 73, no. 4, 2016.

[31] C. Yu, X.-H. Xue, J. Wu, T. Chen, and H. Li, "Sensitivity of the quasi-biennial oscillation simulated in waccm to the phase speed spectrum and the settings in an inertial gravity wave parameterization," Journal of Advances in Modeling Earth Systems, vol. 9, no. 1, 2017.

[32] S. Saravanan, "A multiwave model of the quasi-biennial oscillation," Journal of Atmospheric Sciences, vol. 47, no. 21, 1990.

[33] F. P. Bretherton, "On the mean motion induced by internal gravity waves," Journal of Fluid Mechanics, vol. 36, no. 4, pp. 785–803, 1969.

[34] A. Renaud and A. Venaille, "On the holton-lindzen-plumb model for mean flow reversals in stratified fluids," Quarterly Journal of the Royal Meteorological Society, vol. in press, 2020.

[35] K. Burns, G. Vasil, J. Oishi, D. Lecoanet, and B. Brown, "Dedalus: Flexible framework for spectrally solving differential equations," Astrophysics Source Code Library, 2016.

[36] K. J. Burns, G. M. Vasil, J. S. Oishi, D. Lecoanet, and B. P. Brown, "Dedalus: A Flexible Framework for Numerical Simulations with Spectral Methods," arXiv e-prints, p. arXiv:1905.10388, May 2019.

[37] T. J. Dunkerton, "The role of gravity waves in the quasi-biennial oscillation," Journal of Geophysical Research: Atmospheres, vol. 102, pp. 26053–26076, Nov. 1997.

Discussion over the top conditions and confinement

The following subsections are from the supplementary materials of our submitted publication to *Physical Review Letters*.

Top boundary conditions

The high-frequency forced waves have viscous attenuation lengths larger than the domain size. These waves are affected by the vertical size of the domain and the top boundary condition. In our idealised Plumb-like 1D model, we use a stress-free boundary condition for the mean-flow ($\partial_z \overline{u} = 0$), and a radiation boundary condition where waves flow out of the domain. Here we explore other top boundary conditions.

We compute two-dimensional Direct Numerical Simulations (DNS) using the open spectral solver Dedalus [Burns et al., 2016, Burns et al., 2019]. We solve the following equations:

$$\partial_t u - \nu \nabla^2 u + \partial_x P = -(\mathbf{u} \cdot \nabla) u \tag{2.60a}$$

$$\partial_t w - \nu \nabla^2 w + \partial_z P - b = -(\mathbf{u} \cdot \nabla) w \tag{2.60b}$$

$$\partial_t b - D \nabla^2 b + w = -(\mathbf{u} \cdot \nabla) b \tag{2.60c}$$

$$\nabla \cdot \mathbf{u} = 0 \tag{2.60d}$$

where b is the buoyancy, P the pressure, and $\nabla = (\partial_x, \partial_z)$. The geometry is two dimensional and periodic along the horizontal axis. We use $n_z = 256$ Chebyshev polynomial functions in the z direction and $n_x = 32$ complex exponential functions in the x direction. We use $\nu = 2.8 \times 10^{-6}$ and $D = \nu/7$, representative of thermally stratified water. To compute nonlinear terms without aliasing errors, we use 3/2 padding in both x and z. For timestepping, we use a second order, two stage implicit-explicit Runge-Kutta type integrator [Ascher et al., 1997], with time steps $\mathcal{O}(10^{-2})$. Waves with random phases are forced at the bottom domain by setting velocity and buoyancy perturbations at the boundary. We use a forcing spectrum given by $E_{tot} = 2 \times 10^{-6}$, $\omega_0 = 0.2$, $N_\omega = 20$ with either $\sigma = 10^{-1}$ or $\sigma = 2.8 \times 10^{-2}$.

We tested four different top boundary conditions:

- (i) No-slip: $u|_{z=1} = 0$ and $w|_{z=1} = 0$.
- (ii) Free-slip: $\left.\frac{\partial u}{\partial z}\right|_{z=1} = 0$ and $w|_{z=1} = 0$.
- (iii) Buoyancy damping layer for $1 < z < 1.5$ to damp the waves but not the large-scale flow. We implement this by adding a damping term in the right-hand side of equation (2.60c), $-bf(z)/\tau$ where $f(z) = \tanh((z - 1.15)/0.05) + 1)/2$ is a z-dependent mask, and the damping timescale $\tau = N^{-1} = 1$ in our non-dimensionalization.
- (iv) Layer with $N = 0$ between $1 < z < 1.5$. Specifically, we use $N(z) = (1 + \tanh((z - 1)/0.05))/2$.

In (iii) and (iv), boundary conditions at the new domain top boundary $z = 1.5$ were no-slip.

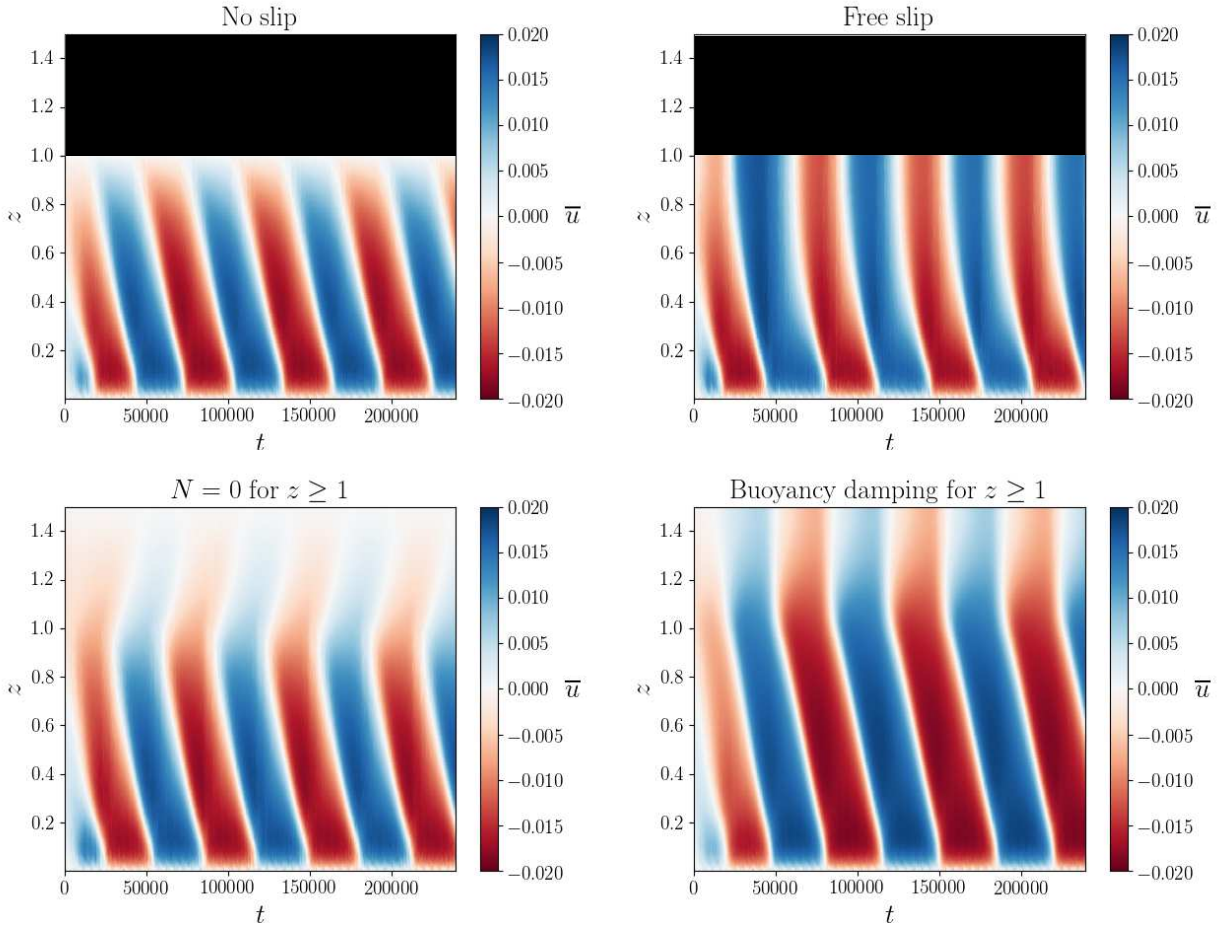

Figure 2.11: Hovmöller diagrams of the horizontal mean-flow driven by a multi-wave forcing for different top boundary conditions in our 2D numerical model. The forcing spectrum is gaussian centred at $\omega_0 = 0.2$ with standard deviation $\sigma = 10^{-1}$ and total energy $E_{tot} = 2 \times 10^{-6}$. This corresponds to the wide forcing spectrum case shown in figure 1 of main text. In the top panels, the computational domain goes to $z = 1$.

In figures 2.11 and 2.12 we plot Hovmöller diagrams for simulations with two different values of σ. In both cases, we find that the top boundary condition does not strongly affect the mean-flow evolution. We find the same dynamical regimes as in the 1D model. Therefore, using a 1D model with an easy to implement top boundary condition, such as free-slip, does not alter the results. The free-slip condition for $\overline{u}$ that we use in our 1D simulations should be physically similar to having a layer with $N = 0$. A layer with $N = 0$ is model for the mesosphere, which is weakly stratified ($N^2 \sim 0$) compared to the stratosphere ($N^2 \neq 0$). While wave reflection occurs at the interface, we find that in our 1D simulations, at most $\sim 10\%$ of the total wave energy reaches the top domain and is lost. This study of top boundary conditions suggests this does not qualitatively affect the results.

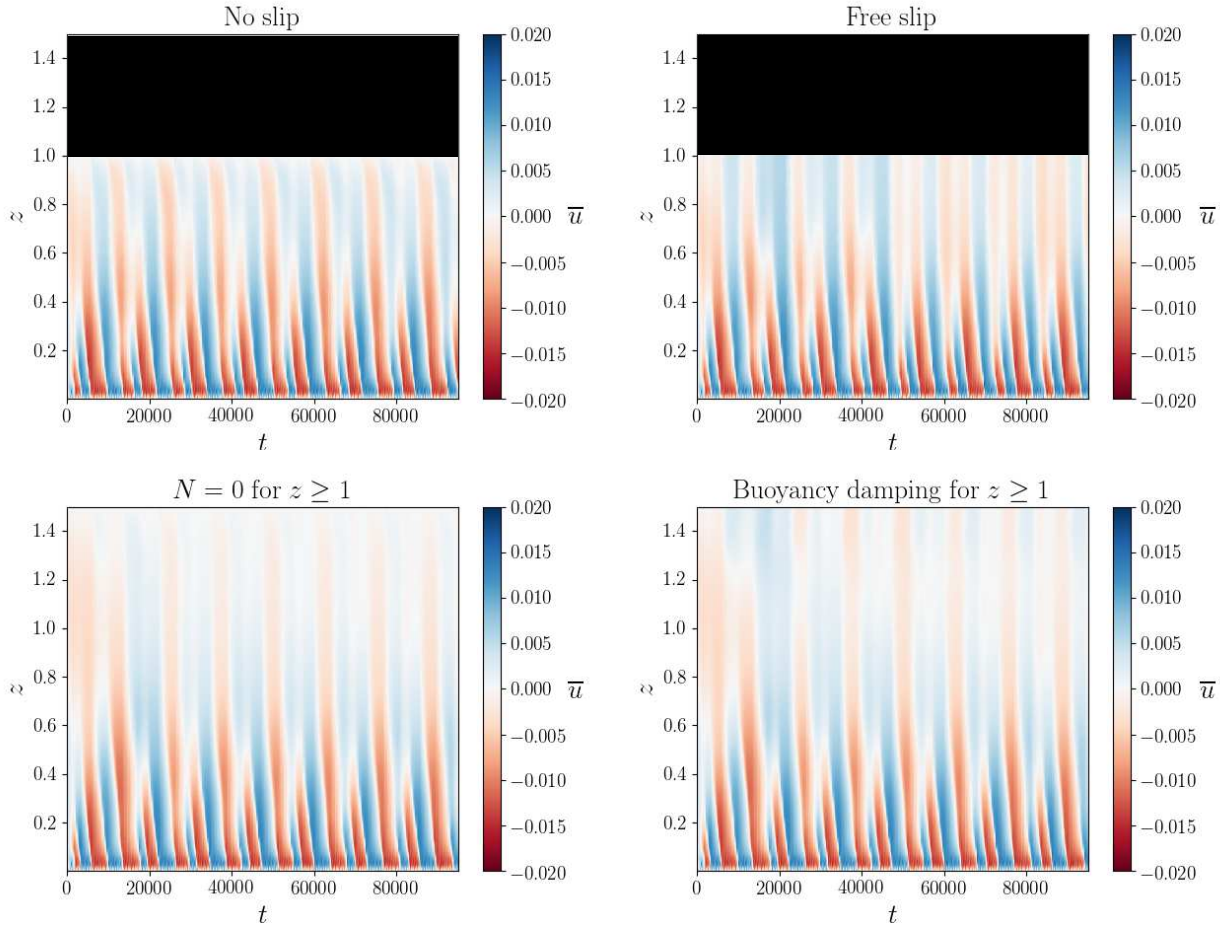

Figure 2.12: Same as Figure 3, but with a Gaussian forcing spectrum with standard deviation $\sigma = 2.8 \times 10^{-2}$.

Domain height

In the main text we show that as the forcing spectrum becomes broader, at fixed energy, the mean-flow transitions from quasiperiodic to periodic. This could be due to the excitation of high-frequency waves whose attenuation length is much larger than the domain height. Using the forcing spectrum parameters of the first figure presented in the PRL article, we do find that the transition occurs at larger and larger σ as the domain size increases. For those parameters, the periodic mean-flow oscillations appear to be dictated by waves with large attenuation lengths. However, this is not always the case. Here we preset simulations with $\omega_0 = 0.15$ and $E_{tot} = 5 \times 10^{-6}$. For these parameters, we find the transition from quasiperiodic to periodic oscillations occurs at $\sigma \sim 2.5 \times 10^{-2}$. This is lower than the transition value in Figure 1 of the main text, where we used the larger value of $\omega_0 = 0.2$. In this case, all forced waves have attenuation lengths smaller than the domain height. Thus, the top boundary is not required for periodic mean-flow oscillations at large σ.

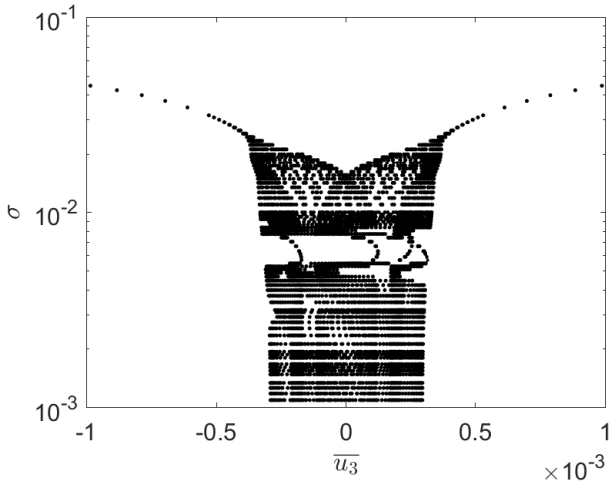

Figure 2.13: Poincaré map for simulations with different σ, with $\omega_0 = 0.15$ and $E_{tot} = 5 \times 10^{-6}$. The transition from quasiperiodic to periodic reversals occurs at a value of σ where all forced waves have an attenuation length smaller than domain height.

2.5 Conclusion

We investigated the Plumb's model considering a multi-wave forcing. Surprisingly, our results show that considering many different waves for the forcing can drive periodic oscillations, whereas gathering the same amount of energy into a monochromatic forcing, drives non-periodic oscillations, *i.e.* oscillating signals characterised by several frequencies. Also, it turns out that different spectra can drive oscillations with similar properties. This is hugely important for GCMs in which the wave are parameterised in order to drive QBO. Moreover, the QBO is used as a benchmark for the GCMs, whereas we saw that driving the right QBO does not imply that the wave properties were chosen rightly.

However, many assumptions and approximations are done to develop the Plumb's model. Even if experiments [Plumb and McEwan, 1978,Semin et al., 2018] and numerical simulations [Wedi and Smolarkiewicz, 2006] confirm the validity of the monochromatic model, a systematic investigation, either numerical or experimental, could be interesting to confirm our results. Indeed, it is known that the weak dissipation assumption tends to overestimate the damping of low frequency waves [Lecoanet et al., 2015] and neglecting wave–wave interactions may not be appropriated. Moreover, only the stratified layer is resolved and the wave forcing is parameterised. The coupling between the wave-generating mechanisms and the internal gravity waves are not solved and very little is currently known on the energy transfer function from the turbulent layer to the generated internal gravity waves. Simulating a whole domain reproducing the complex dynamics occurring at the interface is needed.

The next chapter will introduce an experiment designed to generate mean-flow reversals from turbulently-generated internal gravity waves, aiming to reproduce and complete the results observed in this chapter.

CHAPTER 3

LARGE-SCALE FLOW GENERATION BY TURBULENTLY GENERATED INTERNAL GRAVITY WAVES

Contents

The Plumb's model [Plumb, 1977], derived from the preliminary work of [Lindzen and Holton, 1968], has successfully reproduced the main features of the QBO, both numerically [Plumb, 1977, Saravanan, 1990, Renaud et al., 2019] and experimentally [Plumb and McEwan, 1978, Otobe et al., 1998, Semin et al., 2018]. Even if the model was extended in GCMs [Lott and Guez, 2013] and in our work described in the previous chapter to account for the stochastic generation of internal gravity waves in the Earth's atmosphere, there is,

to the best of our knowledge, no experiment that managed to drive oscillating mean-flows from a multi-wave forcing. We present here our up-to-now unsuccessful attempts.

This chapter will introduce in section 3.1 the original Plumb & McEwan's experiment [Plumb and McEwan, 1978], which reproduced the features of the QBO. Then, our multi-wave experiment, in a geometry reminescent of the original set-up [Plumb and McEwan, 1978], is presented in section 3.2. The different results are shown and discussed in section 3.3 and a numerical investigation conducted in order to solve some unanswered questions is described in section 3.4.

3.1 How to drive a QBO from stochastically generated waves ?

3.1.1 The monochromatic Plumb & McEwan's experiment

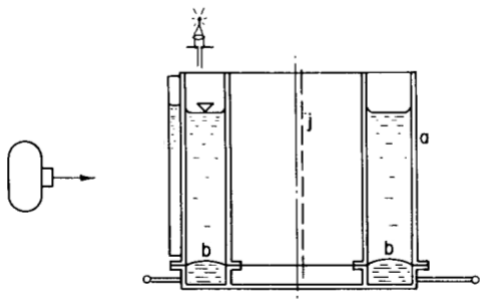

Figure 3.1: Sectional view of the set-up of [Plumb and McEwan, 1978] showing the annular cylinder geometry (a) and the rubber membrane at the bottom (b).

The Plumb & McEwan's experiment successfully generates a reversing horizontal flow from a standing gravity wave forcing, using an oscillating membrane to generate waves in a stratified environment. The oscillating membrane, divided in 16 moving pieces, generates two contra-propagating waves, with the same frequency. In order to experimentally reproduce the QBO, Plumb and McEwan had the bright idea to use a cylindrical shell as geometry (see figure 3.1 showing a sectional view of the set-up). Neglecting the radial variation due to the narrow gap between the walls, the geometry can be considered as 2D $(\mathbf{e}_\theta, \mathbf{e_z})$ and is periodic in the $\mathbf{e}_\theta$ direction, with gravity pointing in the $-\mathbf{e_z}$ direction. Neglecting Earth's curvature (the stratosphere is thin compared to the Earth's radius), this geometry has the relevant features to mimic the QBO phenomenon along the equator. Besides, Coriolis force cancels out at the equator and thus, rotation is not needed in the experiment in order to model QBO. Generated at the bottom of the tank, the wave group velocity is directed upward (hence energy is transported upward) and an oscillating flow appears. The results are in a good agreement with the analytical model derived in [Plumb, 1977] (shown in figure 3.2a), confirming the validity of the model. Only one period could be visualised because the oscillatory motion of the membrane locally mixed the fluid. At some point, the stratification was destroyed near the membrane and the internal gravity waves could not propagate anymore.

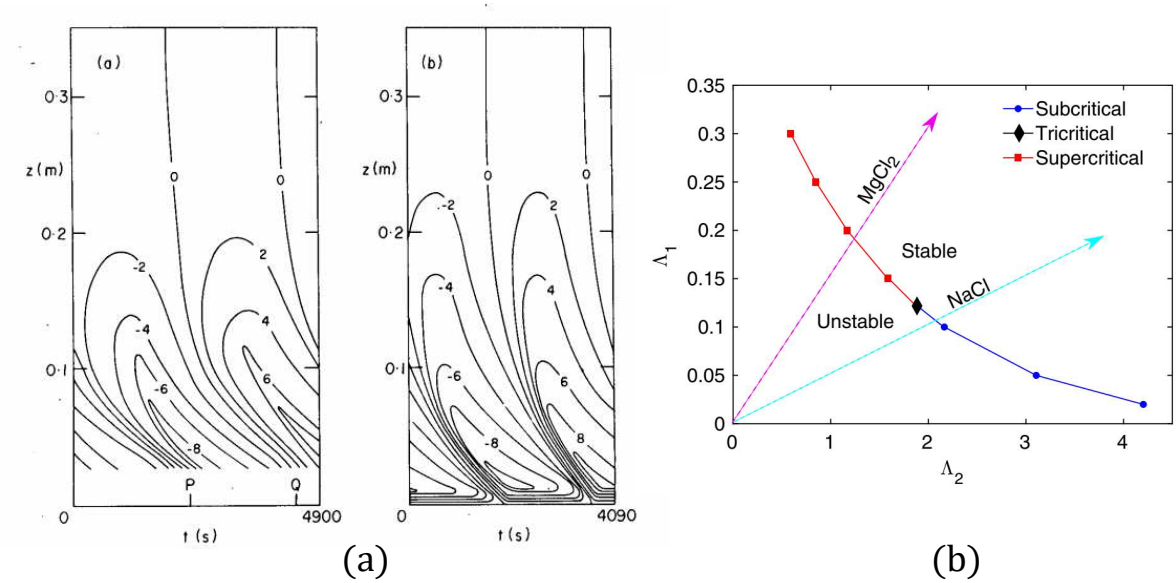

Figure 3.2: (a) Contour of horizontally averaged horizontal velocity for the experiment (left) and for the analytical model (right). Amplitude of the forcing is $\epsilon = 8$ mm and its frequency is $\omega = 0.43$ s^{-1}. Reproduced from [Plumb and McEwan, 1978]. (b) Parameter space showing the transition between stable (*i.e.* no mean-flow) and unstable (*i.e.* mean-flow) regions. Using the salt MgCl2 for stratification allows to reach higher values of N while NaCl gives small N. $1/\Lambda_1$ is the Reynolds number associated with the wave. $1/\Lambda_2$ is a Reynolds-like number associated with the wall friction for the wave. Tricritical denotes the transition from subcritical to supercritical. Reproduced from [Semin et al., 2018].

The experiment was later reproduced and improved [Semin et al., 2018] in order to visualise a greater number of periods. Salty fluid was continuously injected at the bottom and the corresponding volume was removed at the top, where the forcing membrane is located (the set-up from [Semin et al., 2018] is turned upside down compared to the one of [Plumb and McEwan, 1978]). The linear stratification was thus replenished during a long period of time, up to 18 hours. The aim was to investigate the nature of the bifurcation of the large-scale flow emergence. Two salts ($MgCl_2$ and NaCl) were used, resulting in different buoyancy frequencies N. For large values of N, the wave attenuation is mostly due to the fluid viscosity while for small values of N, the attenuation comes from wall friction. The bifurcation from stable to unstable states is either subcritical or supercritical depending on the dissipative processes involved (supercritical if the wave attenuation is mostly in the bulk, subcritical if the wave attenuation is induced by wall friction. See figure 3.2b). The bifurcation from stable state to oscillating periodic behaviour in the Plumb's model was also studied theoretically [Yoden and Holton, 1988].

Note that the Plumb & McEwan experiment was also reproduced in 1998 by [Otobe et al., 1998]. The results, including films of the oscillating flow, are accessible at the following URL: `http://www2.nagare.or.jp/mm/98/otobe/index.htm`.

These experiments successfully drove reversing mean-flows from monochromatic forc-

ing. Hence, we will reproduce this annular cylinder geometry in our set-up and adapt the forcing to our needs. With a review of laboratory experiments studying internal gravity waves, we now discuss several ways to generate internal gravity waves randomly, reproducing the stochastic wave generation in the stratosphere.

3.1.2 Waves generation in experiments

Topographic generation

It is possible to mimic the generation of orographic waves by moving the top or bottom boundary of a tank, with regularly spaced reliefs attached to the boundary. The tank is filled with stratified fluid. The boundary is moved horizontally and internal gravity waves are generated. This configuration, studied by [Aguilar et al., 2006], is similar to a flow above topography in the atmosphere or above bathymetry in the ocean.

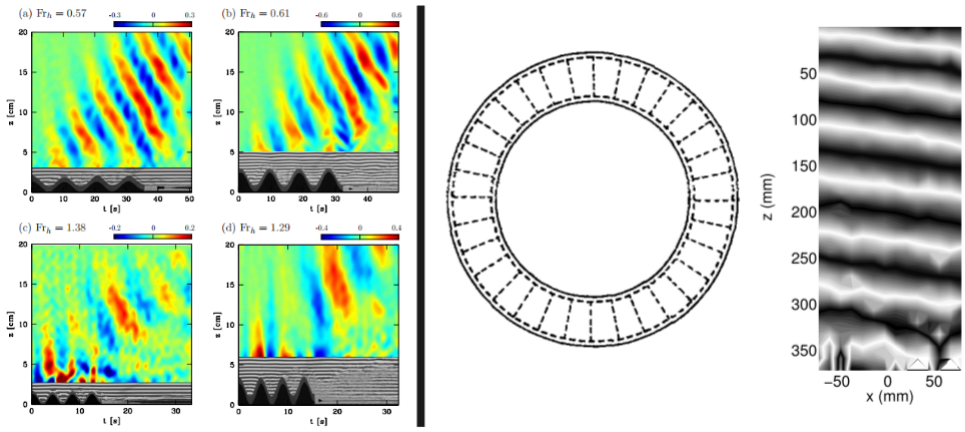

Figure 3.3: (Left) Vertical time series of $\partial_t N^2$ for the small (left) and large (right) amplitude hills and for the cases $Fr < 1$ (top) and $Fr > 1$ (bottom), with $Fr = \frac{Uk_x}{N}$ the Froude number. U is the speed of the moving boundary, k_x the wavenumber associated with the hill pattern. One sees that the wave field is much more coherent for $Fr < 1$. Reproduced from [Aguilar et al., 2006]. (Right) Scheme of the oscillating membrane, reproduced from [Delisi and Dunkerton, 1989], and an example of a wave field generated by an oscillating membrane, reproduced from [Semin et al., 2016]. The field shows the phase φ_0 of the wave component. Black: $\varphi_0 = 0$ and white: $\varphi_0 = \pi$.

The left panel of figure 3.3 shows the internal gravity wave field generated by moving hills at the bottom of a stratified fluid. For equivalent Froude numbers $Fr = \frac{Uk_x}{N}$, the small amplitude hills generate less intense waves than the high amplitude hills. The wave field is less coherent for $Fr > 1$ but waves are still generated. The frequency and wavenumber of the generated waves are set by the speed U of the moving boundary and by the wavenumber associated with the hill pattern. Because the wave properties are directly linked to the topography, orographic waves in the atmosphere are rather predictable and can be implemented quite precisely in GCMs. By considering *e.g.* a fractal bathymetry generated by a 3D printer, this generation technique could allow to excite spatially stochastic wave; however they would all have the same time dependence so we

have not pursued this idea yet.

As previously described, several experiments used an up-and-down moving boundary to generate internal gravity waves [Plumb and McEwan, 1978, Delisi and Dunkerton, 1989, Semin et al., 2016]. In these experiments, the tank is a cylindrical shell, and the moving boundary is composed of 16 or 32 pieces of a flexible membrane which can individually be moved up and down by a piston. The right panel of figure 3.3 shows a schematic representing a top view of the membrane and an example of generated wave field in the cylindrical shell.

Those mechanisms are not easy to set up in an experiment, even to generate monochromatic waves. They require a precise control of the devices displacing the boundary and they would be quite challenging to adapt in order to generate waves stochastically. Note finally the wave-maker developped by [Gostiaux et al., 2007] which is more easy to implement: this would allow some temporal stochastic wave generation but with a given spatial geometry.

Waves driven by plumes and convection

In the Earth's atmosphere, a significant part of the internal gravity waves is generated by the turbulent convection taking place in the troposphere. The mechanical oscillator effect (see section 1.2) can be used to easily generate internal gravity waves. A single buoyant plume can generate a wave field [Ansong and Sutherland, 2010]. The plume forms in a homogeneous layer and then penetrates in a stratified layer until it reaches its neutral-density altitude. Waves are generated at the cap of the plume and are characterised by very narrow frequency and wavenumber ranges (see figure 3.4 where the phases line are almost aligned). The plume then spreads horizontally, like a gravity current.

The wave field generated by penetrative convection can be experimentally studied. The transient investigation of these dynamics by [Michaelian et al., 2002] shows that waves at different frequencies are generated. The set-up consists in initially stably stratified water heated from below in order to trigger convection. The convective layer then generates waves in the upper stratified layer. The convective layer grows in time and eventually at some point the whole tank is convective. Therefore, convection seems to be a good candidate to stochastically generate internal gravity waves. This topic will be described in details in the next chapter.

Other mechanisms exist to generate waves such as devices that create a shear (see [Gostiaux, 2006]) or an oscillating solid within a stratified layer (remember the St Andrew's cross described in chapter 1). Since the wave properties are directly linked to the object typical dimension and velocity, they all generate waves with a finite number of frequencies and wavenumbers. Moreover, the wave generation is also deterministic. These mechanisms would be quite challenging to adapt in order to generate waves stochastically.

To us, the best and easiest way to have a stochastic generation of waves is to use a turbulent layer, like in the atmosphere, to generate the waves. Different manners to drive turbulence exist, such as Von Kármán turbulent flow using rotating disks [Ravelet

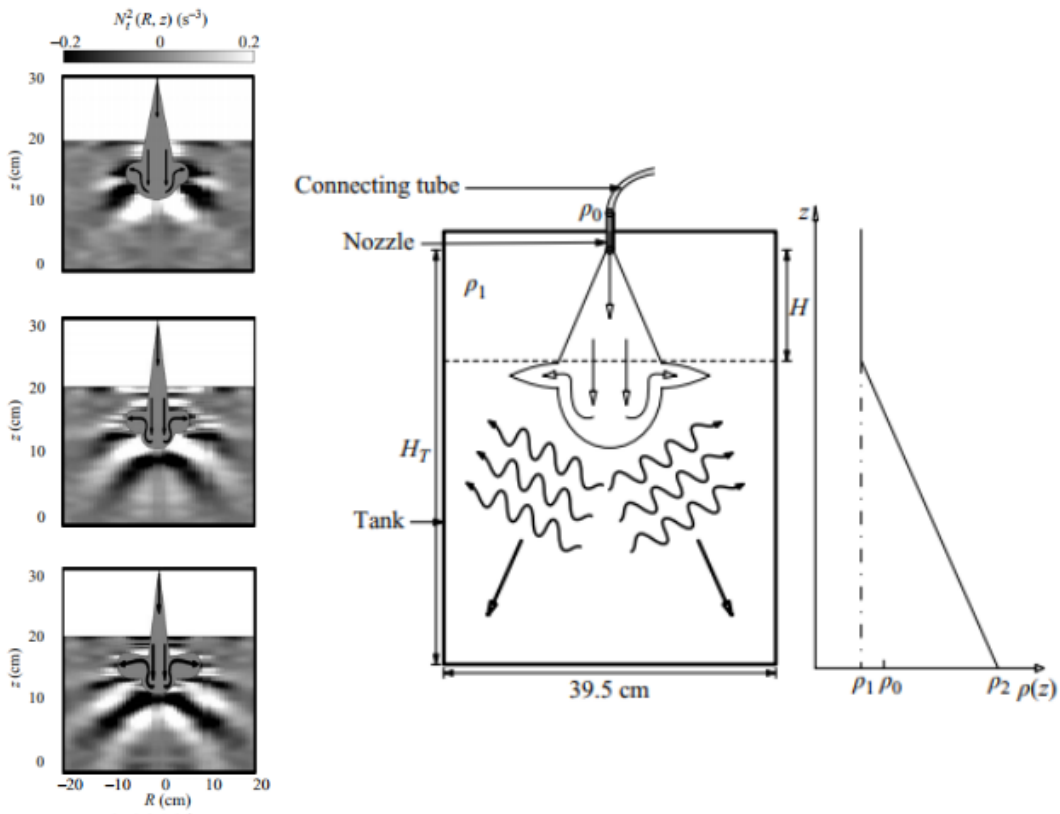

Figure 3.4: (Left) Field of $\partial_t N^2$ at different times showing the wave field generated by the penetration of the buoyant plume. (Right) Schematic of the experiment. Reproduced from [Ansong and Sutherland, 2010].

et al., 2004, de la Torre and Burguete, 2007, Ravelet et al., 2008, Monchaux et al., 2009, Gay et al., 2018], grid turbulence [Shy et al., 1997, Antonia et al., 1998] and convection [Deardorff et al., 1969, Michaelian et al., 2002] for example. The internal gravity wave field generated by a turbulence induced by an oscillating grid was studied both experimentally and numerically by [Dohan and Sutherland, 2005]. As said above, waves generated by penetrative convection will be developed in the next chapter. For the experimental study described here, we chose to use a turbulent layer created by several jets to force the internal gravity waves. It is possible to easily control some jet properties, such as the flow rate. Doing so, we are able to have a certain control upon some of the turbulence properties, hence having a control on the wave spectrum.

Turbulence by jets

In order to explore a large range of behaviours between monochromatic forcing and completely randomly generated waves in our experiment, we generate a turbulent layer using several jets with controlled location, mean flow rate and flow rate fluctuation in time. Therefore, we create a turbulent layer superimposed to a large-scale periodic oscillation, in order to control the properties of the internal gravity waves generated, but with an important part of noise, coming from the energy cascade.

Free turbulent round jets were vastly studied in fluid dynamics, especially in the aerospace community. One can read for instance the review from [Ball et al., 2012] or the book on turbulent flow by [Pope, 1962]. In a nutshell, turbulent jets are characterised by an universal opening angle of 11.8°, giving 23.6° from one side to opposite side. It follows that the relation between the jet radius R and the downstream distance x is:

$$R(x) = \tan(11.8°)\, x = \frac{1}{5}x \tag{3.1}$$

Turbulent jets also exhibit a Gaussian transverse shape. Therefore, the longitudinal speed can be written as:

$$u(x,r) = u_{max}(x)\, \exp\left(-\frac{r^2}{2\sigma^2(x)}\right) \tag{3.2}$$

where $u_{max}(x)$ is the maximum speed at the centreline and therefore depends on the downstream position x and $\sigma(x)$ is the standard deviation related to the spread of the jet. From statistics, 4σ is the width for a Gaussian that encompasses 95% of the area under the curve. We write $4\sigma \approx 2R$.

The main issue of generating waves with a turbulent layer above (or below) the stratified layer of interest is the mixing occurring at the interface. The turbulence will slowly penetrate in the stratified layer. The height of the turbulent layer and its density will increase over time, while the stratified layer height will decrease. The interaction of a turbulent jet impacting an interface with a fluid at a higher density (typically fresh water above salty, not stratified, water) had been investigated in numerous studies [Baines, 1975,Cotel et al., 1997,Shrinivas and Hunt, 2014,Herault et al., 2018,Herault et al., 2017], Yet, the entrainment of a turbulent jet impinging an interface is still not well understood as shown in figure 3.5. The entrainment rate is linear for large Froude numbers. The scaling law is either $\sim Fr^2$ or $\sim Fr^3$ for small Froude numbers. [Herault et al., 2018] suggests that the surface waves excited by the jet impact on the interface play a major role in the entrainment.

In our experiment, it is crucial that the entrainment rate is as low as possible. The turbulence induced by the jet will slowly mix the stratified layer. It is necessary that the height of the stratified layer remains unchanged for a long time, long enough for a potential large-scale flow to emerge and reverse. Moreover, if the turbulent layer grows larger, the turbulence at the interface will decrease in intensity over time (since the distance between the jet exits and the interface will increase), and so will the generated waves. Ideally, we do not want the properties of the system to change over time. The problem is that we also need a layer turbulent enough to generate internal gravity waves stochastically. We need to find the right balance between the transfer of energy at the interface from turbulence into waves, and the entrainment rate which destroys the stratified layer.

The next section will introduce in details our setup, in a geometry reminiscent of [Plumb and McEwan, 1978], and the different solutions tested in order to prevent the mixing at the interface.

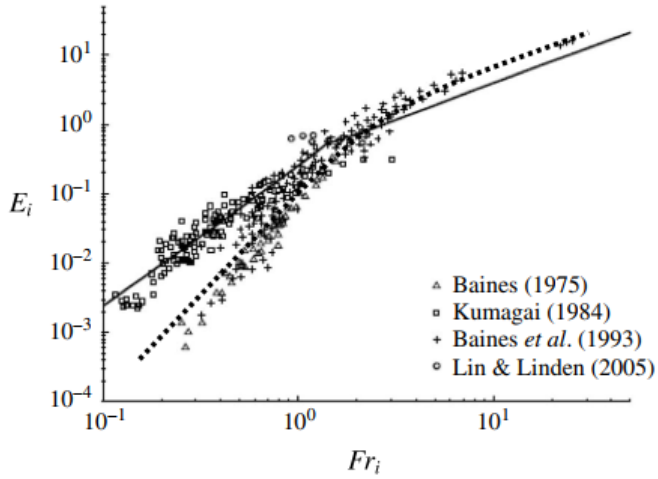

Figure 3.5: Entrainment rate as a function of the Froude number. The dashed curve represents the model suggested by [Herault et al., 2018], the black lines are from [Shrinivas and Hunt, 2014]. The figure displays data from different studies. Reproduced from [Herault et al., 2018].

To the best of our knowledge, the internal gravity wave field generated by a turbulent jet impinging an interface with a stratified layer remains unstudied, both numerically and experimentally.

3.2 Set-up and methods

3.2.1 Description of the setup

The tank used is reminiscent of the one from [Semin et al., 2018]. It consists in two cylinders of respective diameter $d_1 = 40$ cm for the outer cylinder and $d_2 = 20$ cm for the inner cylinder (figure 3.6). The gap of the obtained cylindrical shell is $\delta = 10$ cm. Total height is $H = 60$ cm. For practical reasons, these two cylinders are placed in a rectangular tank whose dimensions are $50 \times 50 \times 75$ cm^3. The different volumes (outside the outer cylinder, the cylindrical shell and inside the inner cylinder) are all connected and filled with salty water.

At the top, a circular plate allows to place the nozzle exits for the turbulent jets. It is made of 12 regularly-spaced holes with a wavelength $\lambda_x = 16$ cm similar to the one from [Semin et al., 2018]. Each hole is connected to a device that equally divides the flow coming from a pump *via* the system described in figure 3.7. Basically, one every two holes are connected to distributor #1. The remaining holes are connected to distributor #2. The two distributors are connected to two different pumps, which can be controlled individually, allowing to have different amplitude or period for the two pumps, or to impose a phase lag. The pumps take water from the top of the tank, ~ 10 cm above the nozzle exits, in order to attenuate their effects on the turbulent layer. In our experiments, we modulate the flow rate of each pump with a sinusoidal shape. The period is set at $T = 20$ s and the phase lag at $\varphi = 180°$. The motivation of this choice is to impose a large-

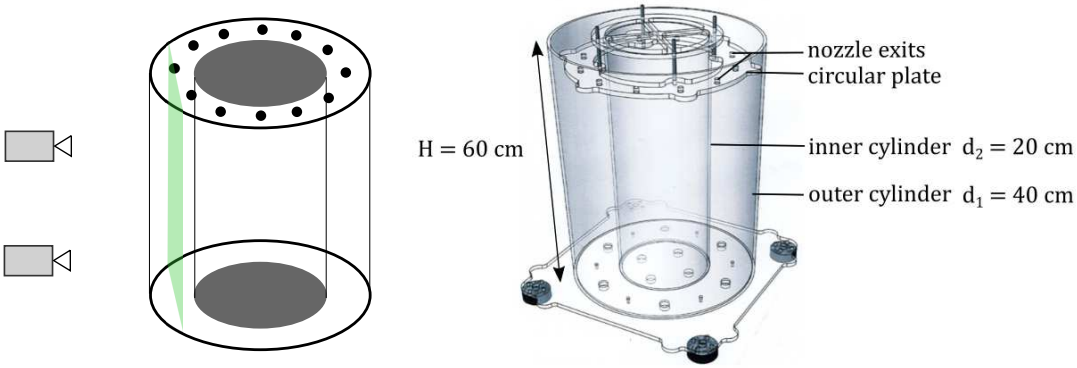

Figure 3.6: Schematics of the double cylinder set-up. The zone of interest is the gap between the two cylinders, which is equivalent to a 2D periodic geometry. The gap between the two cylinder is $\delta = 10$ cm and the total height is $H = 60$ cm, similar to the dimensions of [Semin et al., 2018]. The circular plate at the top allows to place several nozzles to create the turbulent layer. On the left, the laser sheet and camera positions are visible.

scale circulation which is similar to the forcing in [Plumb, 1977, Semin et al., 2018] which remain to this day the only experiment to drive a QBO-like flow. In our set-up, turbulent motions at all scales coming from the energy cascade will add up to this large-scale forcing.

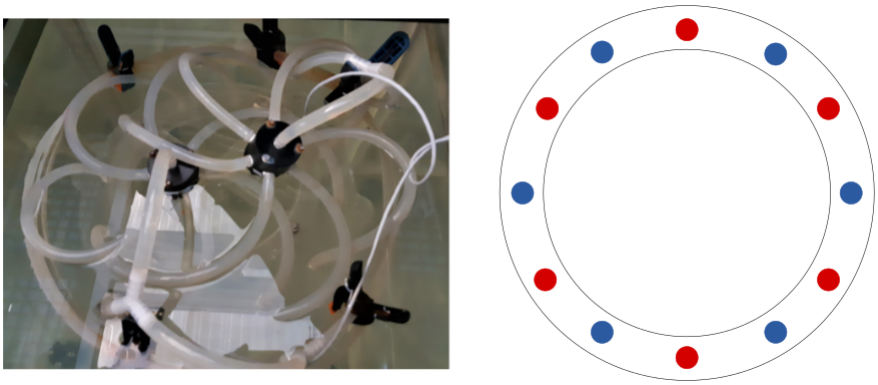

Figure 3.7: (Left) Photography from the top of the experiment, showing the circular plate, the tubes and the two distributors (in black) which equally divide the flow in 6 tubes each, for a total of 12 tubes. (Right) Schematic of the circular plate. The red exits are connected to distributor #1, the blues ones are connected to distributor #2.

To fill the tank, we place 25 cm of fresh water in the bottom. Then, we use the double-bucket technique described in [Oster, 1965] to create the stratification below the fresh water. We use two buckets of ~ 100 L each to fill 45 cm the tank with salty stratified fluid. The top of the stratified layer is at the density of fresh water, in order to avoid a density jump. For the experiments, the filling of the experimental tank with the double bucket was slowly pursued during the experiment in order to keep the interface at the same height, following the method of [Semin et al., 2018]. Indeed, the mixing induced by

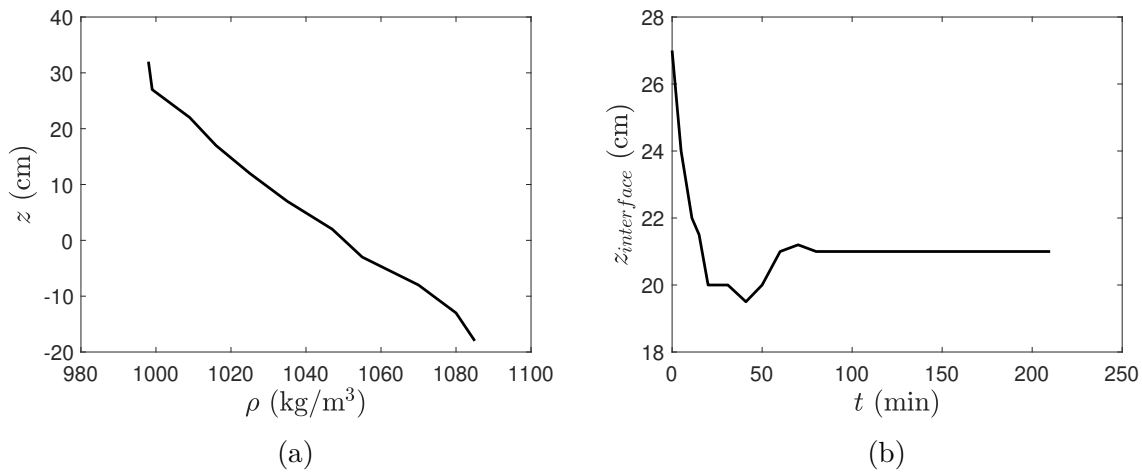

Figure 3.8: (a) Typical density profile for the experiments, before the jets are turned on. The corresponding buoyancy frequency is $N = 0.21$ Hz. (b) Time evolution of the interface depth for an experiment. The interface location reaches lower and lower position at early times. When the tendency decelerates, we re-start the filling with the double-bucket in order to stabilise the position of the interface. Here, the re-filling process started at $t \sim 45$ min. Once the refilling velocity and the mixing at the interface balance, the interface remains at a steady position located at $z = 21$ cm.

the turbulence makes the stratified layer decrease in size over time.

Figure 3.8a shows the density profile for one of the experiments. Density measurements are made every 5 cm, starting just above the interface. The interface is easily visible due to the refractive index gradient. The profile is linear in the stratified layer, initially starting at $z = 27$ cm. The bottom field of view for the acquisitions is located at $z = 0$ cm. From this linear profile, we can compute the Brunt-Väisälä frequency:

$$N = \frac{1}{2\pi}\sqrt{\frac{-g}{\rho_0}\frac{\partial \rho}{\partial z}} = 0.21 \text{ Hz} \tag{3.3}$$

Figure 3.8b shows the time evolution of the interface position. After approximately 45 min, the stratified water filling was started again in order to maintain the interface at a fixed position $z = 21$ cm. Since the mixing is very important when the interface is too close to the jet exits, it is not possible to maintain the interface at the initial depth $z = 27$ cm for a long time, because our buckets have a finite volume. We thus have to compromise between the duration of the experiment and the position (the higher the better) of the interface.

3.2.2 Measurements

Particle Image Velocimetry (PIV) was used to study the turbulence inside the top layer and the wave dynamics in the stratified layer. The fluid was seeded with particles of diameter 10 µm coated with silver in order to have a better laser reflection. The small diameter of the particles gives small sedimentation speeds which is crucial for the long-time measurements in the stratified layer. The tank is illuminated with a 532 nm continuous

laser. The laser plane is placed vertically and is tangent to the virtual cylinder of diameter $d_3 = \frac{d_1+d_2}{2}$ (see figure 3.6). Two camera are used. A Nikon D5500 filming at 60 fps with a resolution of 1280×720 pixel^2 is used to visualise the turbulent layer. A Point Grey camera at 2 fps with a resolution of 2048×2448 pixel^2 is filming the stratified layer. All data are processed with DPIVSoft2010 [Meunier and Leweke, 2003] with 32×32 pixel^2 interrogation areas and 50 % overlap. The entrainment of the salty fluid from the stratified layer by the convective layer blurs the captured frames at the interface and PIV algorithms cannot compute the corresponding velocity vectors.

3.2.3 Solutions tested to prevent the mixing at the interface

Even if we slowly refill the tank with stratified water in order to keep the interface at a steady position, mixing occur at the interface and a density jump appears between the turbulent and stratified layers. As we will see in section 3.3, we think that this density jump is highly problematic in our experiment since it affects wave generation. Therefore, it became necessary to limit the mixing by other means that the re-filling process, so the density jump could not appear. The density jump generation process is schematised in figure 3.9.

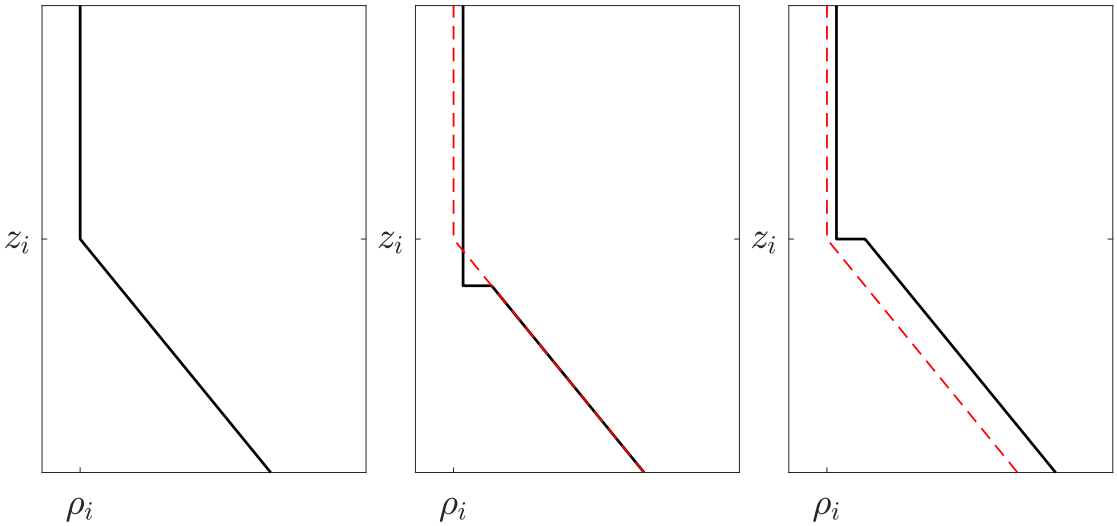

Figure 3.9: Time evolution (from left to right) of the density profile. Initially the density profile is constant in the top layer $\rho = \rho_i$ and is linearly increasing with decreasing z in the bottom layer. Once the jet are turned on, the top of the stratified layer is entrained by the jets. The density of the top layer slightly increases and the interface is lowered at a new location $z = z_i + \Delta z$. Once the re-filling process is on, the interface, previously displaced downwards by the mixing, is now displaced upward, up to its original position. The black lines show the density profile at each time. The red dashed lines show the initial density profile.

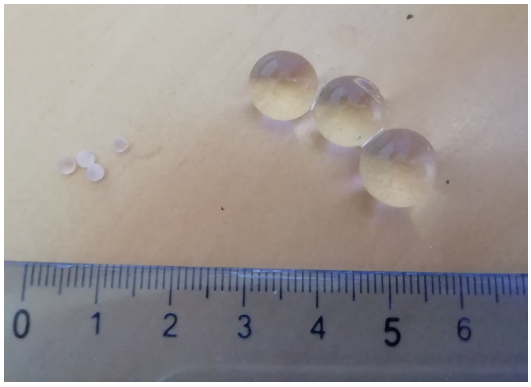

Figure 3.10: Photography of the hydro-gel spheres. Four dry spheres are visible on the left and three spheres after water absorption are visible on the right.

To limit the entrainment at the interface, several solutions were tested. The first one was to lower the turbulence intensity by using a fluid more viscous than water. An industrial oil, named UCON, miscible with water, was added in the convective layer only. The mixture was composed of 70 % of distilled water and 30 % of UCON oil. That results in a dynamical viscosity μ 100 times higher than the viscosity of water with similar density ρ. The second solution was to add a physical membrane at the interface. Different membranes were tested:

- hydro-gel spheres. The spheres absorb ambient water and are then at a density close to the ambient fluid (see figure 3.10),
- a neoprene membrane,
- a latex membrane,
- a very thin plastic membrane.

In the end, our tests to prevent the mixing at the interface and to favour low-frequency waves did not reach the aimed purpose. They are briefly discussed at the end of the next section.

3.3 Internal gravity waves generated by jet turbulence

Several experiments were conducted with different periods and different flow rates for the pumps. They all gave very similar results so only one experiment is thoroughly described in section 3.3.1. Results using membranes and hydro-gel spheres are quickly described and discussed in section 3.3.2. Lastly, results from an experiment focusing on the interface dynamics are discussed in section 3.3.3.

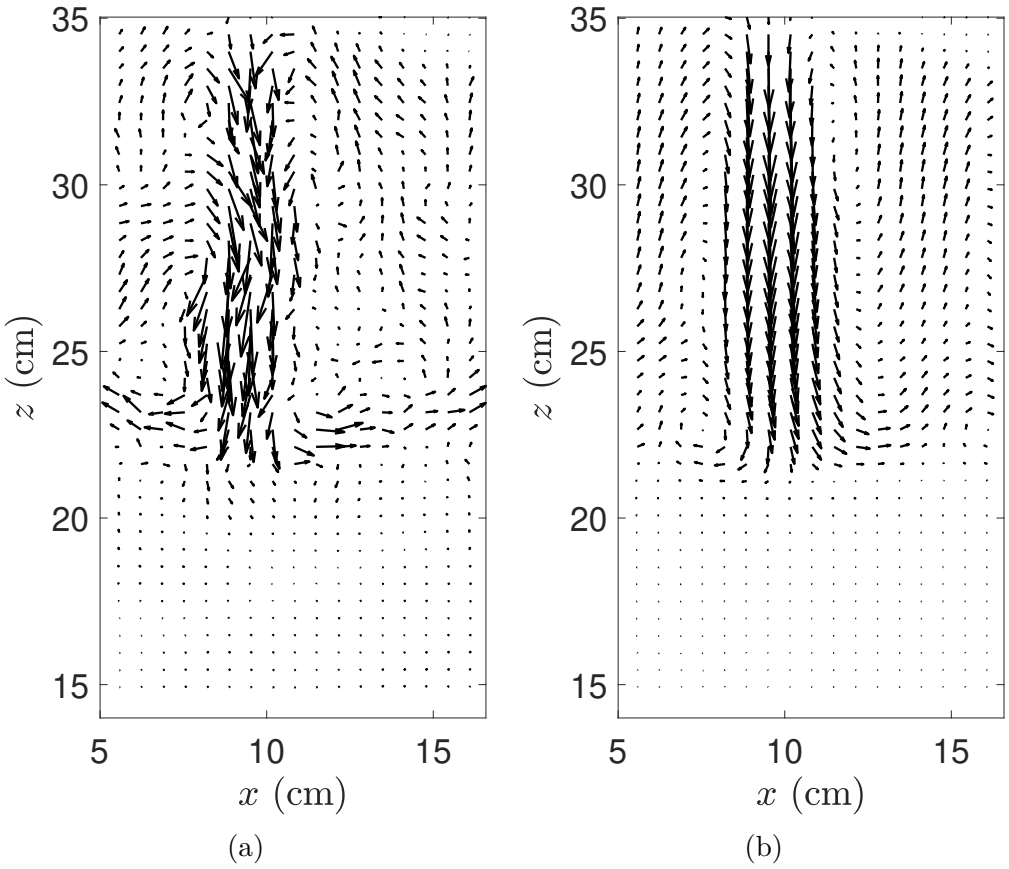

Figure 3.11: (a) Instantaneous velocity field. (b) Time-averaged velocity field over a 2 min acquisition time.

3.3.1 Experiment with refilling process

Jet structure

The maximum flow rate for the pumps is $8\,\mathrm{l}\cdot\mathrm{min}^{-1}$. The imposed sinusoid modulates the flow rate between 12% and 25% of the maximum flow rate, with a period of $T = 20$ s and a phase lag between the two pumps of $\varphi = 180°$. We use a period and wavelength for the large-scale forcing similar to the ones from [Semin et al., 2018], where these parameters drive an oscillating flow. We add a stochastic noise *via* the jet turbulence to see if it affects the QBO-like flow generation. The velocities at the exit of the jets are not accessible with PIV because particles move too fast for the 60 fps acquisition. Maximum recorded velocities reach $15\,\mathrm{cm}\cdot\mathrm{s}^{-1}$. Therefore, given the diameter of the holes of $d_{jet} = 1$ cm, the Reynolds numbers for the experiment is close to $Re = 1500$. The jet is thus weakly turbulent. The structure of the jet is displayed in figure 3.11. The left panel shows an instantaneous field at a random time. One jet is visible in the camera frame. The right panel shows the time average. The origin for the experimental figures presented in this chapter is the bottom left corner of the field taken in the stratified layer (it will be specified if the origin is different). Thus, the interface is located at $z \sim 21$ cm and the jet is centred at $x = 10$ cm.

The instantaneous field presents small vortices within the jet. For both panels, the jet spreads horizontally at $z = 23$ cm, where it is deviated by the interface with the

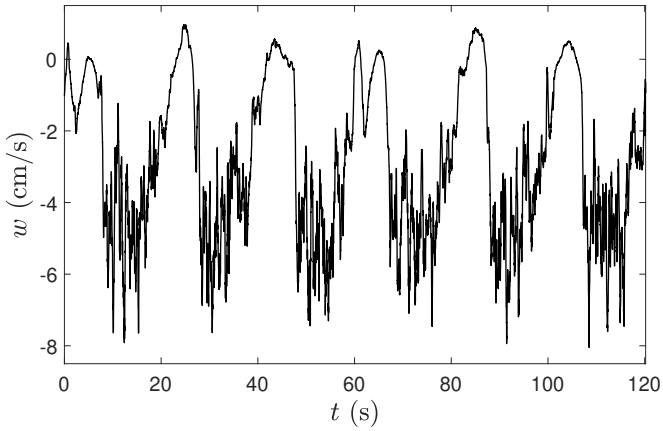

Figure 3.12: Vertical velocity signal at a single point located at $x = 10$ cm and $z = 27$ cm. One can notice the imposed period of $T = 20$ s.

stratified layer. In that layer, the velocities are much smaller. The time-averaged jet presents strong coherent downward structure with upward velocities surrounding the jet while in the instantaneous field, the vertical upward motions are less present. Both the instantaneous and mean fields show that the jet penetrates deeper in the stratified layer at its centre.

It is important to keep in mind that the jet does not blow continuously and is modulated by a sinus shape. The imposed sinus of period $T = 20$ s can be seen in figure 3.12. The vertical velocity, taken at a single point at the centre of the jet at $z = 27$ cm, oscillates from ~ 0 cm $\cdot$ s^{-1} to ~ 5 cm $\cdot$ s^{-1} with a period of 20 s. When the jet in the camera field of view is at its lowest flow rate, the two adjacent jets, not visible in the field of view, are at their maximum flow rate. They create an upward flow and the vertical velocities observed with the camera at these times have very low amplitude and can even reach positive values, whereas the jet observed is still directed downwards.

From the mean profile of figure 3.11, we extract horizontal profiles at different depths, represented by different colors in figure 3.13. One sees the radius increase of the jet. As the maximum velocity decreases, the Gaussian shape of the jet becomes wider and wider. Another striking feature of this figure is that the maximum velocity at each depth is located at different horizontal position x, whereas the jet is initially vertical. Indeed, it is shifted towards increasing x as the jet goes deeper. This deviation is explained by a horizontal large-scale flow quickly appearing in the turbulent layer. This large-scale flow is present in all our experiments, and always going in the same direction *i.e.* in the positive x direction. Despite our efforts, we did not manage to remove this large-scale flow. However, its amplitude (~ 0.1 cm $\cdot$ s^{-1}) is relatively small compared to the velocity of the jet (a few cm $\cdot$ s^{-1}). The large-scale flow only deviates the jets towards positive x.

Figure 3.14a shows the inverse of the maximal amplitude w_m at each height, renormalised by the exit velocity w_0. The exit velocity is not accessible *via* the PIV measurements. It is theroetically computed from the imposed flow rate, when the sinusoid reaches its maximum value. One can see that the velocity is almost constant between $z = 33$ cm and $z = 27$ cm. Then, the velocity decreases. Theoretically, the decrease is linear with

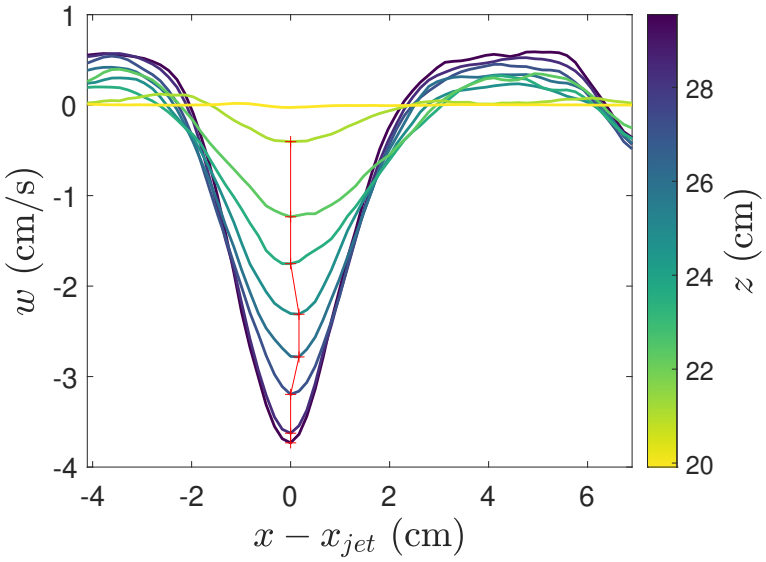

Figure 3.13: Horizontal profiles of vertical velocities at different depths. The color indicates the depth, with dark purple located at the top of the jets and yellow located just below the interface. The red line with crosses shows the position of maximal downward velocity at each height. The position is shifted to the right at mid heights.

respect to z, with a slope of 5 [Pope, 1962]. Here, the evolution trend is not linear. This difference can be explained by the fact the jet may not have reached its asymptotic regime but also by the presence of the interface, stopping the jet expansion brutally, or also by interactions with neighbour jets.

Figure 3.14b shows the evolution of the radius R of the jet as a function of depth z. The radius is taken at the x_r position where w crosses the $w = 0$ horizontal axis (see figure 3.13). Then the radius is computed from $R(z) = x_0(z) - x_r(z)$, where $x_0(z)$ is the position where w reaches its maximum at the z location. As seen in figure 3.13, it differs at each height, shifting toward $+x$ direction with increasing depth. As seen in equation (3.1), the radius should evolves in $R(z) = \frac{1}{5}z$. Here, it increases in $\frac{1}{8}$, until it reaches the stratified layer. Again, the asymptotic regime is perhaps not reached and the 1/5 slope may not apply here. Also, the presence of the interface and the neighbour jets may confine the jet and affect the evolution of the radius.

Figure 3.15a shows the vertically- and time-averaged power spectral densitiy (PSD) with respect to horizontal wavenumber k_x. It is computed from PSDs at each time and each depth within the turbulent layer. The profile obtained shares similar slope with turbulent jets described in [Fellouah and Pollard, 2009], for both the horizontal and vertical velocities. Figure 3.15b shows the frequency PSD, computed at each point and then spatially averaged. The vertical and horizontal velocity PSDs exhibit similar trends. Energy peaks at $f = 5 \times 10^{-2}$ Hz, corresponding to the 20 s period imposed to the jets. Then the energy decreases, with a slope slightly less steep than the $-5/3$ Kolmogorov's law.

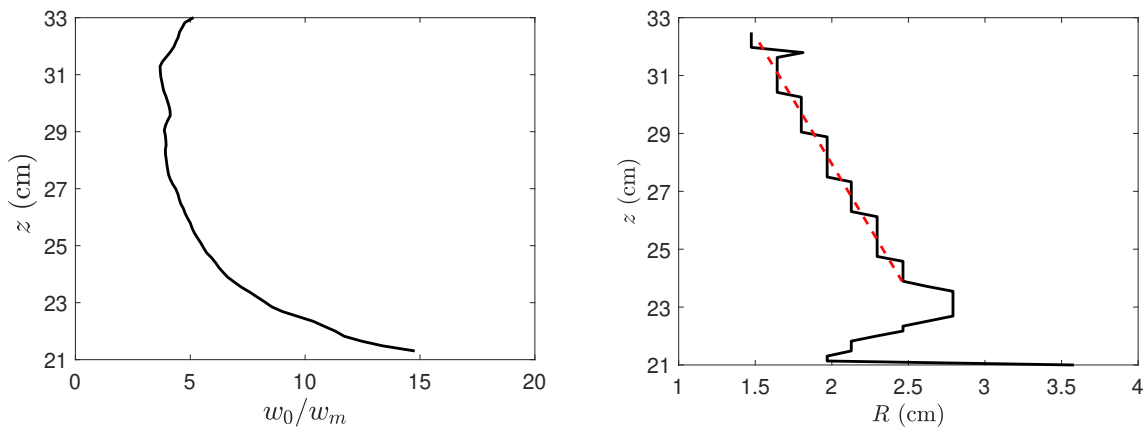

(a) (b)

Figure 3.14: (a) Inverse of the maximal velocity at a given height $w_m(z/d)$, normalised by the exit velocity w_0. (b) Evolution of the radius $R(z)$.The theoretical slope for a turbulent free jet is 1/5. Here the experiment value, shown by the red dashed line, in the presence of the stratified layer is 1/8 for the linear part.

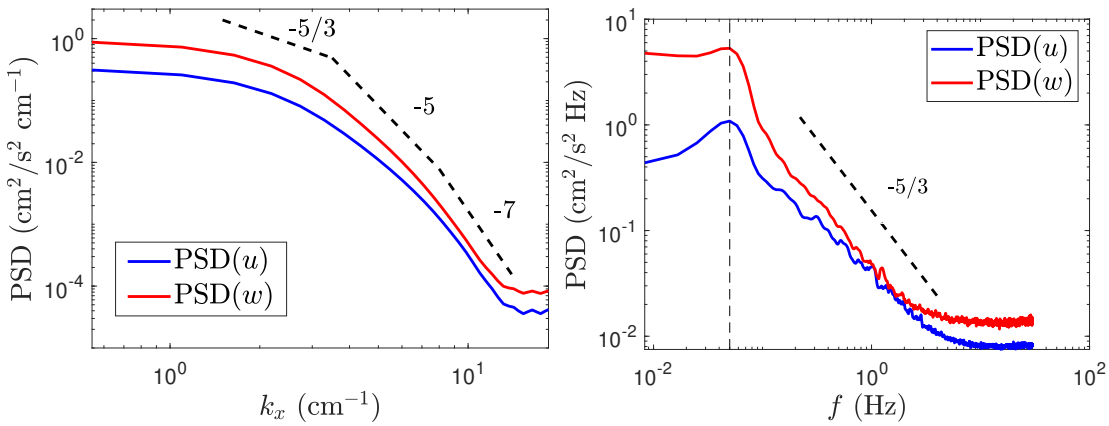

(a) (b)

Figure 3.15: (a) Power spectral density of the horizontal (blue) and vertical (red) velocities as a function of the horizontal wavenumber k_x. Different slopes characterising the spectrum for turbulent jets [Fellouah and Pollard, 2009] are reproduced in dashed lines. (b) Power spectral density of the horizontal (blue) and vertical (red) velocities as a function of the frequency f. The dashed line shows the $-5/3$ slope for reference. The vertical dashed line indicates the frequency of the forcing 5×10^{-2} Hz.

Stratified layer

The stratified layer is initially ~ 40 cm deep. Yet, due to the entrainment at the interface with the turbulent layer, the height of the stratified layer slowly decreases in time, since the interface is displaced downwards. The field captured by the camera is approximately 23 cm high and 20 cm width. The jet impact is located in the middle of the frame, at $x \sim 10$ cm. The interface is also captured since we are interested in the coupling between the turbulent and stratified layers. Initially located at the very top of the captured images,

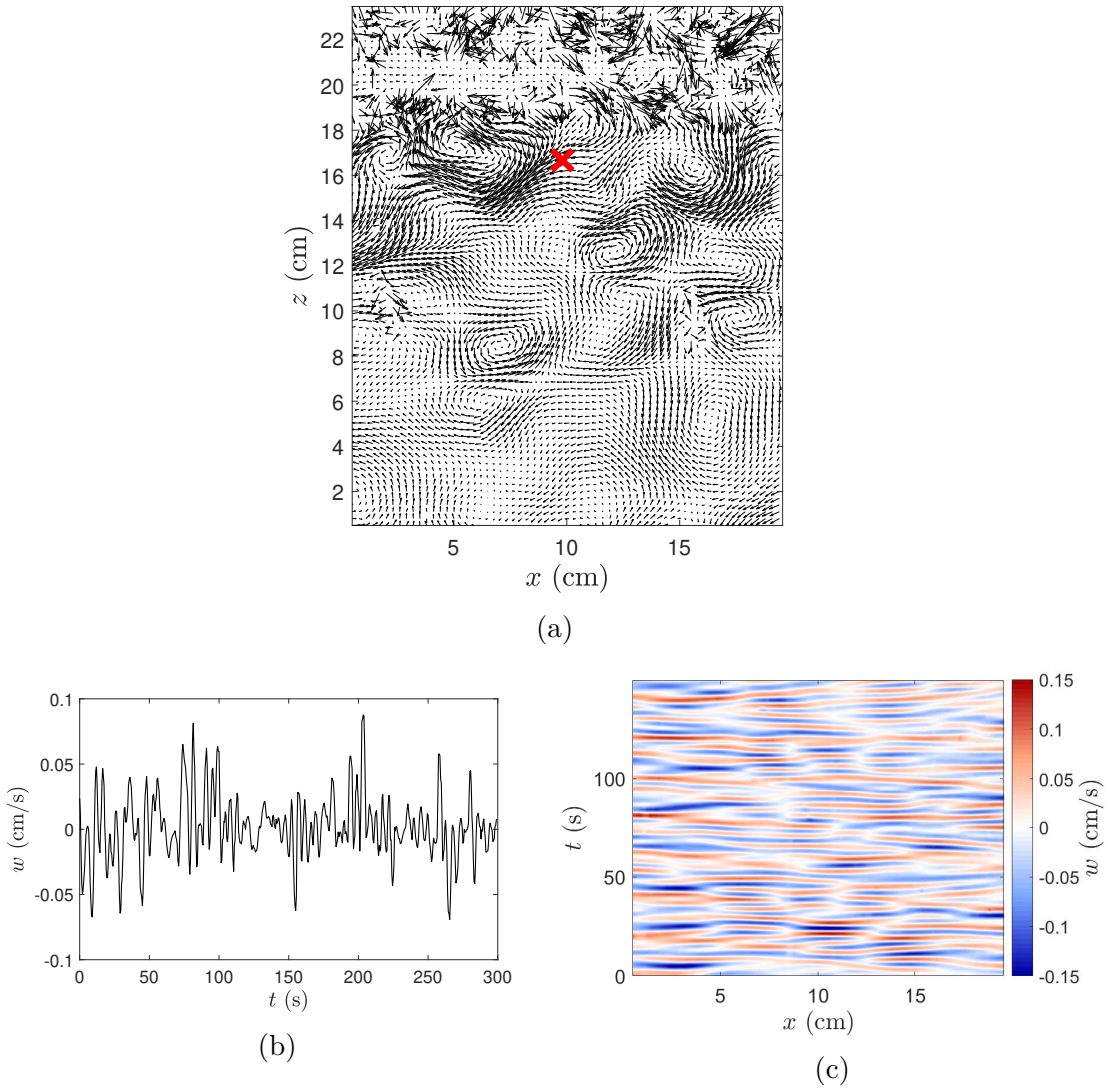

Figure 3.16: (a) Velocity vector field in the stratified layer. The red cross shows the point where the velocity is extracted to plot figure 3.16b. Note that the camera framerate is too small to solve for the velocity field in the upper turbulent layer. (b) Vertical velocity w signal at $x = 10$ cm and $z = 16.5$ cm. (c) Spatio-temporal graph for w at $z = 16.5$ cm along an horizontal line. Maximum velocities are approximately $2\,\mathrm{mm} \cdot \mathrm{s}^{-1}$.

and since it is displaced downwards in time, the interface moves within a few centimetres at the top of the captured images and stops at $z \sim 21$ cm. Figure 3.16a shows an instantaneous field in the stratified layer. Horizontal and vertical motions are seen and are the signature of internal gravity waves propagating in the stratified layer. Maximum velocities for the waves are a few millimetres per second.

Figure 3.16b shows a 5-minutes temporal signal of vertical velocities at the point $x = 10$ cm and $z = 16.5$ cm, highlighted by the red cross in figure 3.16a. The oscillating behaviour of the vertical velocity is obviously noticeable. Yet, the forcing period $T = 20$ s does not particularly stand out, suggesting that we indeed generate waves with several frequencies. A spatio-temporal diagram is shown in figure 3.16c. It shows the time

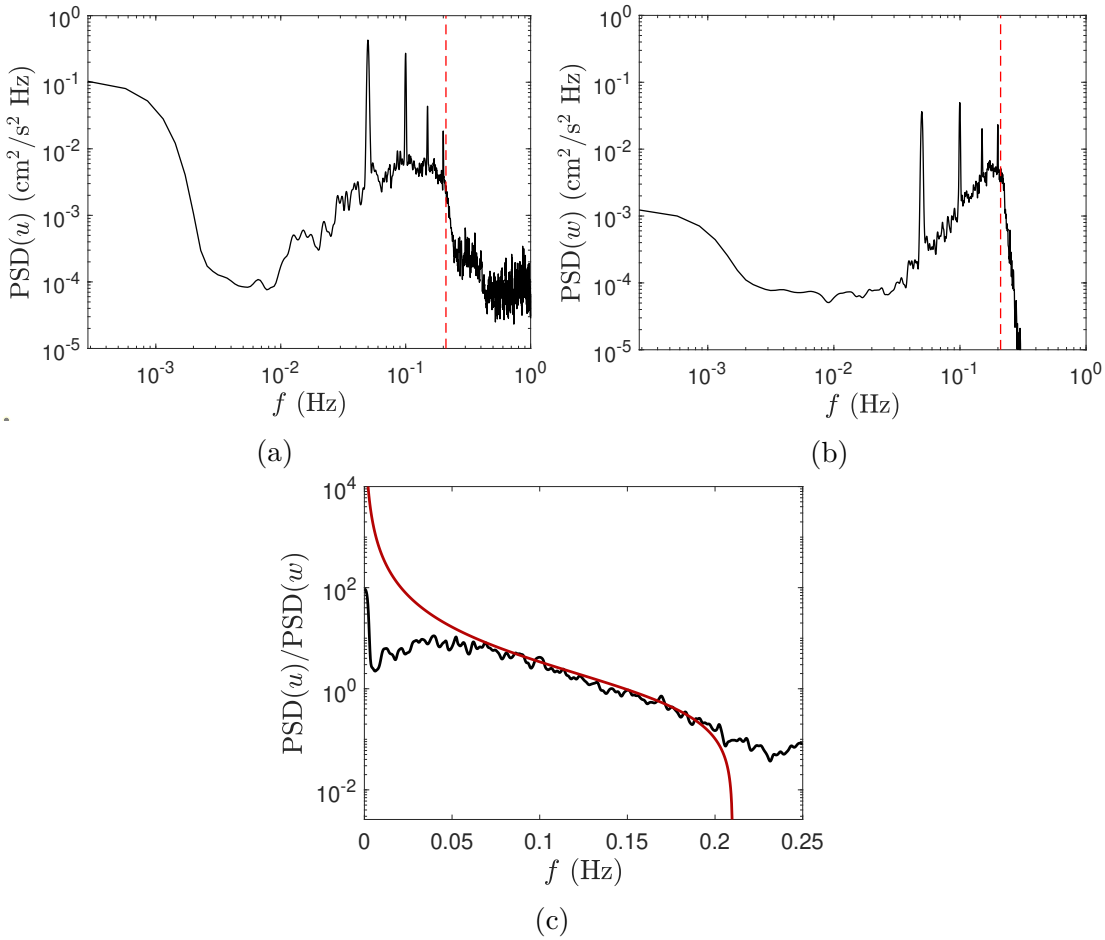

Figure 3.17: Power spectral density for the horizontal velocity u (a) and the vertical velocity w (b). They are computed at each x abscissas for $z = 16.5$ cm, and then horizontally averaged, from a one hour long signal. The buoyancy frequency $N = 0.21$ Hz is indicated by the red dashed line. (c) The ratio PSD(u)/PSD(w) (black) fits very well the polarisation relation of internal gravity waves $(u/w)^2 = (N/\omega)^2 - 1$ (red) between 0.05 Hz $< f < N$, showing the motions observed at these frequencies are mostly internal gravity waves.

evolution of the vertical velocity along a horizontal virtual line located at $z = 16.5$ cm. One sees that the waves appear along the whole width of the camera field. The observed period is again close to the imposed period $T = 20$ s with a superimposition of shorter period waves.

Spectra are computed for the horizontal velocity u and the vertical velocity w. They are computed at $z = 16.5$ cm, at each x location from a one hour long signal. The PSDs are then horizontally averaged and results are displayed in figures 3.17a and 3.17b. Figure 3.17a shows a significant amount of energy at very low frequencies. This is the signature of a large-scale flow which will be detailed later. Then the energy drops at $f \sim 10^{-3}$ Hz. At $f = 10^{-2}$ Hz, the energy increases with frequency until $f \sim 10^{-1}$ Hz. A high energy peak can be seen at $f = 5 \times 10^{-2}$ Hz. It corresponds to the frequency of the sinusoidal forcing of the jets. Peaks at higher frequencies are harmonics. The energy then drops for $f > 2.1 \times 10^{-1}$ Hz corresponding to the cut-off for frequencies higher than N, a charac-

teristic of internal gravity waves. The PSD for the vertical velocity in figure 3.17b reaches lower values at low frequencies compared to figure 3.17a. The PSD is almost constant for 3×10^{-3} Hz $< f < 3 \times 10^{-2}$ Hz. The PSD then increases until frequency reaches $f \sim 2.1 \times 10^{-1}$ Hz, which corresponds to the buoyancy frequency. The peak and harmonics corresponding to the forcing are also visible. Figure 3.17c shows the ratio of the two spectra with the dispersion relation plotted in red. The good agreement between the experimental values and the theoretical prediction for frequencies between 0.05 Hz $< f < N$ shows that the motions observed at these frequencies are mostly internal gravity waves.

Figures 3.18 and 3.19 show the horizontally-averaged PSDs for horizontal and vertical velocities, computed at each height. The PSD for the horizontal velocity (figure 3.18) exhibits a lot of energy at low frequencies. It attenuates with depth. Between $f = 2 \times 10^{-3}$ Hz and $f \sim 8 \times 10^{-3}$ Hz, almost no energy appears in the spectra at any height. Between $f = 10^{-2}$ Hz and $f = 2 \times 10^{-1}$ Hz, energy is present but at much lower levels compared to the corresponding range in the jet spectrum (see figure 3.15b, where $\log_{10}(\text{PSD}) > -1$ for $f < 2.1 \times 10^{-1}$). The peaks associated with the periodical forcing and its harmonics are also visible. The cut-off at $f = N$ is also seen. However, one could have expected to see a wave attenuation depending on the frequency f (see [Lecoanet et al., 2015] for example). Indeed, the dispersion relation links the pulsation of the wave with its angle of propagation $\frac{\omega}{N} = \cos(\theta)$. θ is the angle between gravity and the group velocity direction (perpendicular to the wavevector). For low (resp. close to N) frequency waves, $\theta \to \pi/2$ ($\theta \to 0$) and therefore the energy propagates almost perpendicular to the gravity, *i.e.* horizontally (resp. vertically). Therefore, we expect frequencies close to N to propagate deeper than frequencies small compared to N. This dependence of the attenuation on the wave frequency is not clearly visible here (except for frequency close to 10^{-2} Hz) and most of the waves seem to reach the bottom of the tank. We have thus excited eigenmodes of the system. It is yet important to note that the attenuation length depends on the horizontal wavenumber k_x and there is no reason to believe that waves at different frequencies share the same k_x. This could hide the attenuation length dependence on the frequency on figures 3.18 and 3.19.

We see in figure 3.18 that a lot of energy is present in low frequency horizontal motions. That may be the trace of a slowly-varying horizontal flow in the stratified layer. We horizontally and window-time average (in order to filter out the wave signal) the horizontal velocity and plot its evolution through time, at every depth. Results for the averaged horizontal velocity $\overline{u}$ are displayed in figure 3.20a and in figure 3.20b for the vertical velocity.

Figure 3.20a shows that a horizontal flow takes place in the stratified layer. It is directed towards negative x and is present in the whole depth of the stratified layer. Starting at $t \sim 600$ s, a positive horizontal flow appears. It is likely due to the viscous entrainment of the top of the stratified layer by the large-scale flow of the turbulent layer described in the previous section. Even if the typical velocities are small (~ 0.5 mm $\cdot$ s^{-1}), it is quite surprising that the strong shear between the flow in the stratified layer for $z < 18$ cm and the entrainment of the top of the layer is visible for quite a long time (more than an hour, see figure 3.22). The measurements of the flow in the stratified layer started 10 min after the jets are turned on. At the very beginning, the mixing is very important and the

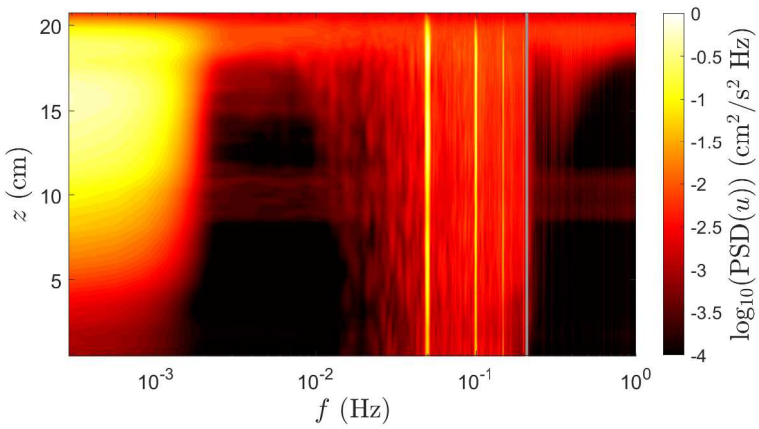

Figure 3.18: PSDs of the horizontal velocity u in the stratified layer, at each height. The grey line shows the buoyancy frequency $N = 0.21$ Hz. The horizontal stripe at $z \sim 10$ cm is likely due to tape patches which are located at this height.

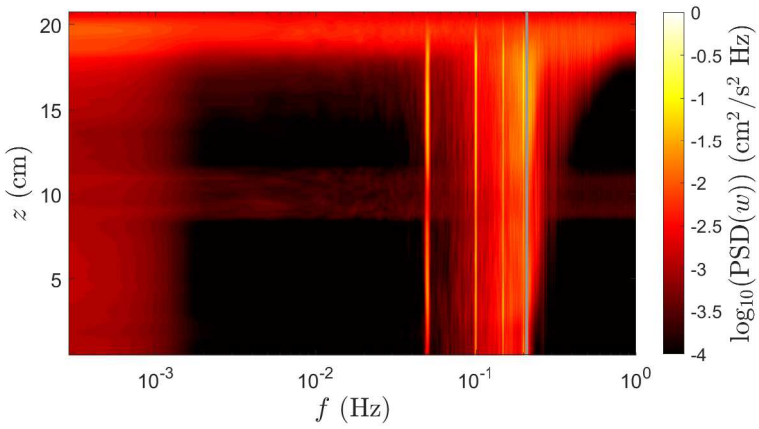

Figure 3.19: PSDs of the vertical velocity w in the stratified layer, at each height. The grey line shows the buoyancy frequency $N = 0.21$ Hz.

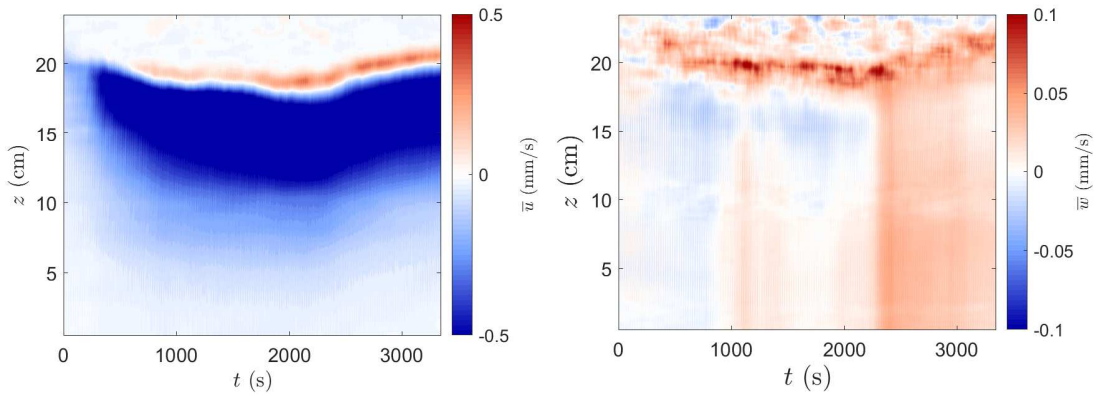

(a) (b)

Figure 3.20: Time series of horizontal averaged and window-time averaged ($\sim$ 150 s) horizontal velocity (a) and vertical velocity (b).

interface is rapidly displaced. At $t \sim 2200$ s, the interface (above the red patch of velocity) moves upwards. This is because, at that time, we started the re-filling of the tank, in order to have an almost constant-in-time depth for the interface. Figure 3.20b is only displayed here to compare the magnitude of the velocities. $\overline{u}$ is two orders of magnitude higher than $\overline{w}$. The beginning of the sustain of the stratification is also visible, with $\overline{w}$ having small positive values at all height after $t \sim 2200$ s.

To ensure that the waves play a role in the generation of this horizontal mean-flow, we compute from our experimental data the term $-\partial_z(\overline{u'w'})$, which is the forcing term in the theoretical model described in chapter 2. Since the mean-flow $\overline{u}$ displayed in figure 3.20a shows small variations in time, we show in figure 3.21, the vertical profile of $\overline{u}$, $-\partial_z(\overline{u'w'})$ and $E_{waves} = u'^2_{RMS} + w'^2_{RMS}$ averaged in time over the duration of acquisition #1, *i.e.* one hour, in order to reduce the noise / signal ratio. u' (resp. w') denotes the horizontal (resp. vertical) velocity fluctuations and is computed by subtracting the temporal averaged to the total field u (resp. w) calculated by the PIV algorithm.

The blue line shows the vertical profile of the normalised mean flow $\overline{u}$ and the red line shows the vertical profile of the z-derivative of the Reynolds stress $-\partial_z(\overline{u'w'})$. The dashed green line shows the profile of the wave energy in order to represent the attenuation of the wave field with depth. The profile for the forcing term is a bit noisy since we took the derivative of an experimental signal, but it gives insightful information on the wave forcing in our experiment. One sees that, when the mean-flow is positive at $z \sim 20$ cm, $-\partial_z(\overline{u'w'})$ is also positive. That means that the waves force the mean-flow towards positive values at this height, corresponding to the model described in the previous chapter. The positive part of the mean-flow is thus viscously entrained by the turbulent layer and forced by waves. From $z = 0$ cm to $z \sim 18$ cm, the mean-flow is negative. At $z = 18$ cm, where the mean-flow changes sign, $-\partial_z(\overline{u'w'})$ suddenly reaches negative values, indicating that the waves now force the mean-flow in the $-x$ direction. We see that the waves force the mean-flow in the $+x$ direction near the interface and in the $-x$ direction below.

Hence, we now look at the long time evolution (several hours) of the horizontal mean-flow $\overline{u}$ and the horizontal velocity power spectrum density PSD(u). Figure 3.22 shows

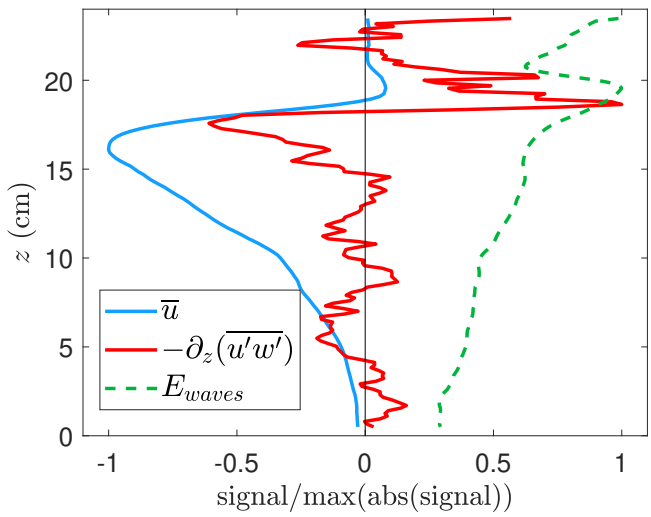

Figure 3.21: Vertical profile of the time-averaged and normalised mean-flow $\overline{u}$ in blue, z-derivative of the Reynolds stress $-\partial_z(\overline{u'w'})$ in red and u_{RMS} in dashed-green, for acquisition #1.

the corresponding measurements for the second acquisition in the top panel, and a third acquisition in the bottom panel. Acquisition #2 starts few minutes after the ending of acquisition #1, which is displayed in the previous figures. Acquisition #3 starts few minutes after acquisition #2. We notice that for acquisition #2 (top panel of figure 3.22), much less energy is present in the range $[10^{-2} - 2 \times 10^{-1}]$ Hz, corresponding to the wave signal. The peak at the forcing frequency and harmonics are still visible. The spatio-temporal diagram for $\overline{u}$ shows that the negative mean-flow slowly disappears. For acquisition #3, the wave signal is again less energetic compared to acquisition #2 and the negative mean-flow $\overline{u}$ has completely vanished. It seems that, through time, the generation of internal gravity waves is much less efficient, resulting in less transported energy in the stratified layer. Therefore, the horizontal mean-flow seen at early time in figure 3.20a slows down and eventually vanishes, since the waves which drive it are less and less energetic. We have obviously checked that no large scale mixing of the stratified layer has taken place and that the buoyancy frequency at the end of experiment (end of acquisition #3) is still constant and about the same as during acquisition #1.

Figure 3.23a shows the vertical velocity signal at $x = 10$ cm and $z = 16.5$ cm for acquisition #3. The 20 s period of the forcing obviously appears and it is quite more visible here compared to figure 3.16b. This illustrates that, for acquisition #3, the magnitude of internal gravity waves has decreased compared to acquisition #1, in which the internal gravity waves signal was of the same order of magnitude of the oscillation due to the forcing.

Figure 3.23b shows the vertical profile of $\overline{u}$, $-\partial_z(\overline{u'w'})$ and E_{waves} averaged in time over the duration of acquisition #3, and re-scaled by the maximum value of each of their quantities during the acquisition #1, in order to compare the evolution of the magnitude of these quantities over time. We see that the negative part of $\overline{u}$ has disappeared and the flow is now completely positive. Also, the forcing term and the energy in the waves

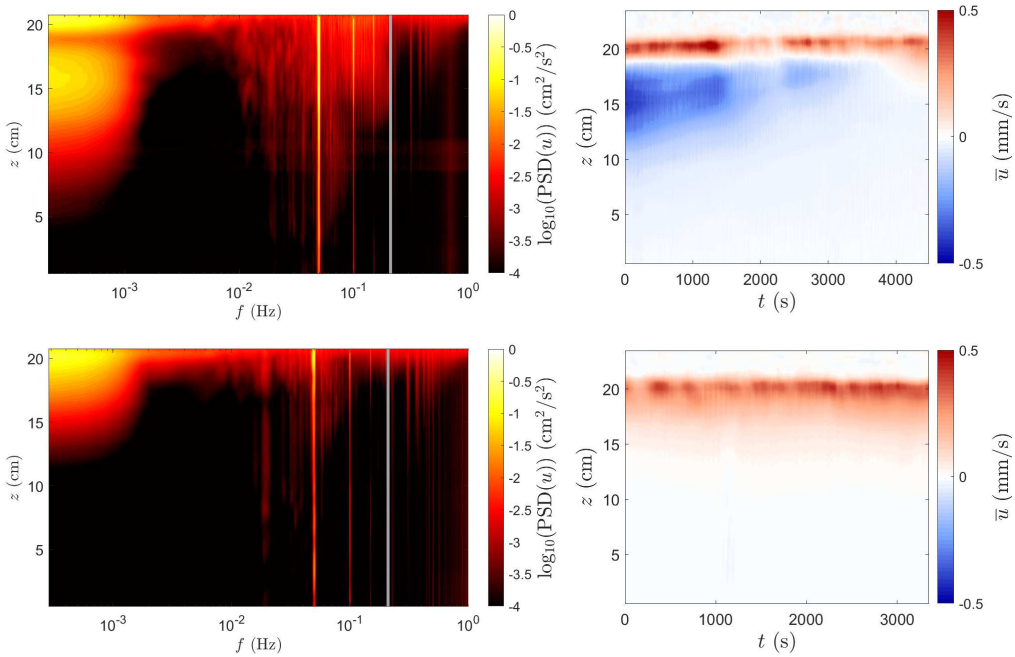

Figure 3.22: (Top) PSD of horizontal velocity u (left) and time series of $\overline{u}$ (right) for acquisition #2, starting at the end of acquisition #1. (Bottom) Same figures for acquisition #3, starting at the end of acquisition #2.

has drastically diminished, except within the few centimetres at the top of the stratified layer, corroborating the fact that the wave generation is less and less efficient over time.

The stratified layer is animated by internal gravity waves and a horizontal large-scale flow, with a strong shear near the interface with the turbulent layer. This large-scale flow is partly driven by wave forcing, and partly entrained viscously by the turbulent layer. The energy transfer into the waves seems to decrease over time, while the mean-flow slowly vanishes. During the experiment, the jets locally mix the two layers, creating a density jump at the interface which becomes bigger and bigger over time. We suppose that the increasing density jump affects the wave generation by decreasing the energy transfer across the interface. Moreover, a part of the energy from the turbulent layer is visible in the stratified layer in high-energetic peaks that correspond to the forcing frequency and harmonics. This mode does not attenuate with height while wave attenuation is a key process for large-scale flow apparition (see previous chapter). Since, less energy is present within the waves and the mode does not attenuate, less energy can go to the large-scale flow. The large-scale flow thus slowly decreases in amplitude and vanishes after some time, even if oscillations are still visible in the stratified layer.

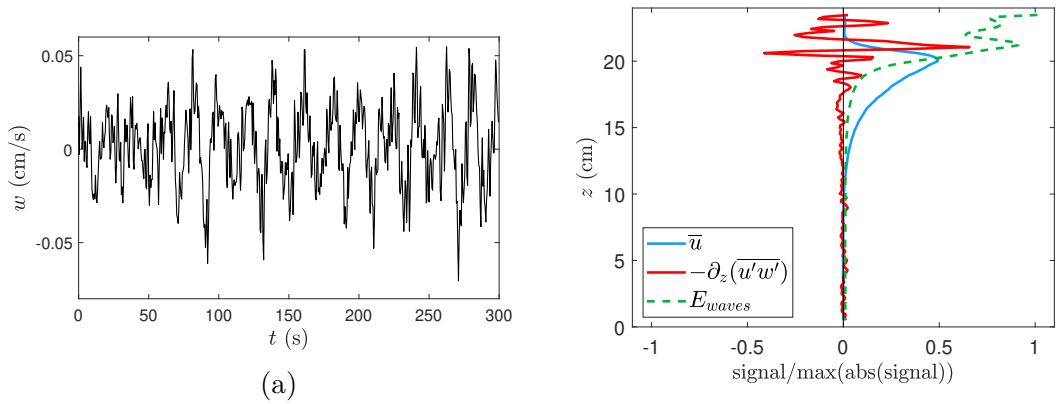

(a) (b)

Figure 3.23: (a) Vertical velocity signal w at $x = 10$ cm and $z = 16.5$ cm. The 20 s period forcing is remarkably visible, compared to the signal at the exact same position as acquisition #1, seen in figure 3.16b. (b) Vertical profile of the time-averaged and normalised mean-flow $\overline{u}$ in blue, z-derivative of the Reynolds stress $-\partial_z(\overline{u'w'})$ in red and u_{RMS} in dashed-green, for acquisition #3.

3.3.2 Results of the experiments trying to prevent mixing

Since we believe that the mixing induced by the turbulent layer slowly decreases the energy transfer to internal gravity waves, several protocols were tested (see section 3.2.3) to limit the mixing. The results were not convincing and are very briefly described here.

Hydro-gel spheres

Hydro-gel spheres are small balls that absorb the ambient fluid. They reach a diameter of ~ 1 cm and have a density close to the fluid they have absorbed. The aimed purpose was to have balls at a density larger than the density of the turbulent layer, and lower than the density at the top of the stratified layer. Doing so, the hydro-gel balls would stay at the interface and reduce the mixing by the turbulent layer, but would still let some energy pass in the stratified layer.

In practice, the hydro-gel balls are always at a slightly higher density than the surrounding fluid and continuously exchange with the ambient fluid. Therefore, even if initially the balls have a density lower than the density of the top of the stratified layer, they become a little denser than the fluid after some time. The balls then slowly sink in the stratified layer. Eventually, all the hydro-gel balls sink to the bottom of the tank, leaving the interface "unprotected". Due to the sinking motion of the balls, and the fact that, after some time, mixing between the two layer appears, this experiment did not solve the mixing issue.

Solid deformable membranes

Coming back to the idea of having a solid barrier between the two layers, we tried to make a solid but deformable membrane and to place it at the interface between the two layers. The jets, alternatively activated as described before, would push locally the membrane,

generating the internal gravity waves in the stratified layer. Despite the different ways tested to attach the membranes to the cylinders or the different materials used to create the membrane, we did not succeed in making a membrane which would be flexible enough. Indeed, if the membrane is attached to the cylinders, it did not move at all. Even for a membrane made from a plastic bag with the pumps set at their maximum flow rate. Therefore, no internal gravity waves were generated when using a membrane.

UCON oil

The last solution tested was to increase the viscosity of the fluid in the turbulent layer, in order to generate a less turbulent layer with the jets, resulting in a less important mixing. In the studied configuration with a viscosity 100 times larger than water, *i.e.* $\nu = 10^{-4}\ \mathrm{m}^2 \cdot \mathrm{s}^{-1}$, the upper layer was not turbulent enough at early stages to generate internal gravity waves. As time goes, the upper layer and the stratified layer mix, and the viscosity of the upper layer decreases. Therefore, the layer becomes more turbulent and waves are generated. The problem is that the mixing also increases and eventually a density jump appears. The spectra observed in the stratified layer is similar to the spectra of figure 3.23a with some energy visible at low frequencies and a few very energetic peaks corresponding to the forcing frequency and harmonics.

Despite our efforts, we did not succeed in preventing the mixing and the apparition of a density jump at the interface. The problem is that, at some moment, this density jump becomes too important and the energy going from the turbulence into the waves is tremendously diminished, thus greatly restricting the possibility to see a large-scale flow appear.

3.3.3 Index matching

A last set of experiments was conducted, focusing on the flow at the interface, in order to see the peak emergence and to qualitatively visualise how energy transfers into the waves. The problem of studying the interface dynamics is that salt affects both density and refractive index. Therefore, a gradient in salt also results in a gradient for the refractive index and the mixing taking place at the interface gives blurry frames, where the PIV particles are not distinctly discernible. The variation of the refractive index is problematic for the acquisition. To capture the most light possible with the camera, we need to open the diaphragm of the lens as much as possible. This results in a very thin depth of field. Therefore, it is possible to have either the turbulent layer in focus, or the stratified layer. But having both layers in focus is not an option. Closing the diaphragm would increase the depth of field, but would also considerably decrease the luminosity of our image, and PIV algorithms would have trouble to compute the right results from the images.

To deal with this issue, we use an experimental technique named index matching. The idea is to use another fluid mixed in the experimental fluid to correct its refractive index. Here, we use ethanol to mix with water [Hannoun, 1985, Daviero et al., 2001]. The refractive index increases with increasing salt or ethanol concentration. However, the ethanol also affects the density. The fluid density decreases with increasing ethanol concentration. Because the evolution of the density and refractive index on the concentrations of ethanol

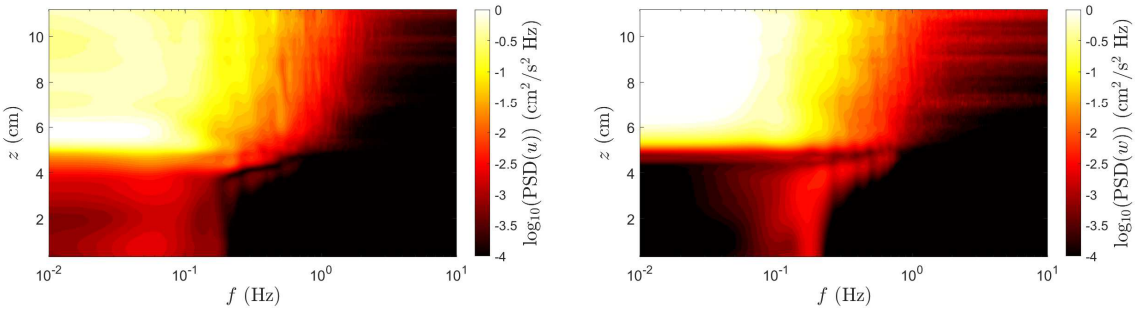

(a) (b)

Figure 3.24: PSDs for the horizontal velocity u (a) and vertical velocity w (b). The interface is located at $z \sim 5$ cm.

and salt are known, it is possible to determine the right concentrations of ethanol and salt to use. We fill one of two buckets with salty water. The second one is filled with water and ethanol, with a refractive index equal to the one of the first bucket. Then we use the double bucket technique in order to have the desired stratification N with a constant refractive index. The process to determine the right concentrations is described in [Daviero et al., 2001].

We set the pumps at a flow rate similar to those used in previous experiments and we run experiments for 2 minutes, recorded at 60 fps, with the Nikon camera centred on the interface. The height of the frame is ~ 11 cm. We see ~ 6 cm of the turbulent layer and ~ 5 cm of the stratified layer. The acquisition is started as soon as the jets are turned on, unlike the previous experiments, in which it was a few minutes after. The origin $(0, 0)$ is taken at the bottom left of the camera frame.

Figure 3.24 shows the frequency PSDs for a 2-minute acquisition for the horizontal velocity u (figure 3.24a) and for the vertical velocity w (figure 3.24b). The most striking feature is the absence of the peak and its harmonics at the frequency of the forcing $f = 5 \times 10^{-2}$ Hz, suggesting that it takes some time for this peak to appear in the tank. The sudden decrease of energy density with height is visible at $z \sim 5$ cm, where the interface is located. The buoyancy frequency is $N \sim 0.2$ Hz. Energy is present at all frequencies below N and a small peak is visible around 5×10^{-2} Hz, but not as energetic as in the previous spectra seen above. Energy is also present at $z = 4$ cm at frequencies $f > 0.2$ Hz. It may be explained by the mixing occurring at the interface where the buoyancy frequency N may strongly vary locally. For the vertical velocity spectra (figure 3.24b), the energy is mostly present at frequencies close to the buoyancy frequency N. The energy at $f > 0.2$ Hz and $z = 4$ cm is also visible here. Energy for the band $[0.1 - 0.2]$ Hz reaches its lowest values at $z = 4.5$ cm and then increases inside the stratified layer. The interface stops the vertical motion of the jets but nearly vertical waves are still generated in the stratified layer. The decrease in energy at the interface is much more brutal in the vertical velocity spectra compared to the horizontal velocity spectra. This illustrates the deviation of the initially vertical jet into horizontal streams at the interface. We also see the signature of this deviation through the increase of energy in the horizontal velocity spectra, just above the interface.

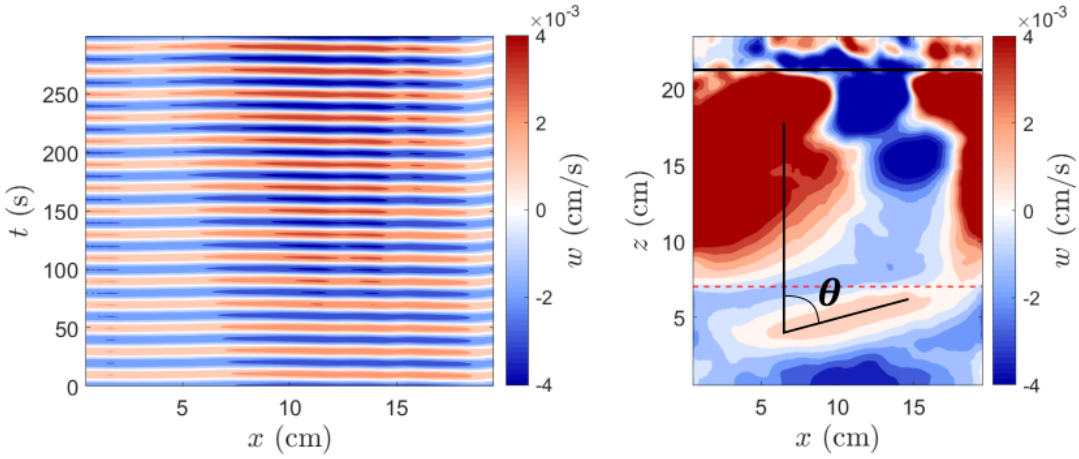

Figure 3.25: (Left) Oscillations for 5 minutes during acquisition #3 taken along an horizontal line located deep in the tank at $z = 7$ cm, displayed in dashed red line in the right panel. (Right) Snapshot at a given time of the frequency and direction filtered vertical velocity w in the stratified layer. Only frequencies $f = 5 \times 10^{-2}$ Hz and left propagating waves are shown here. The waves angle θ is in agreement with the dispersion relation of internal gravity waves: $\theta = \cos^{-1}(\omega/N) = 75.5°$, while the measured value is $\theta = 76.6°$. The interface is highlighted by a black thick line at $z \sim 21$ cm.

Basically, at early time, some of the energy present in the turbulent layer is transferred into the stratified layer. A whole spectra of waves is generated from low frequency waves $\omega/N < 0.1$ to high frequency waves $\omega/N \sim 1$. Since at early times, the peak at $f = 5 \times 10^{-2}$ Hz is not visible, but appears later in time, we wonder if the peak is not a mode of internal gravity waves bouncing at the bottom boundary (keeping in mind that there is ~ 20 cm of stratified water between the bottom of the tank and the bottom of the camera field for the previous experiment). Indeed, waves at this frequency are generated and barely attenuated (figure 3.18). Moreover, if we frequency filter the signal in acquisition #3 in order to only see the oscillations at $f = 5 \times 10^{-2}$ Hz, we see waves propagating at the bottom of the tank (figure 3.25), while energy is only visible at the peak. We thus conclude that the wave $f = 5 \times 10^{-2}$ Hz reaches the bottom of the tank, bounces back up and forms an oscillating standing mode in the whole layer. The existence of this mode poses a question: is it possible to generate a large-scale flow in the stratified layer oscillating as a global mode, if the wave energy is focused in the frequency of the mode ? The mode does not attenuate with height (see spectrograms of figure 3.22) while attenuation is needed in order to drive a large-scale flow from waves (see previous chapter). This question is numerically investigated in the next section.

3.4 Numerical approach

Using Dedalus, we investigate several points that are left unclear with the experimental study. Is it possible to drive a large-scale flow if a global mode manages to form in the tank ? Since the waves reach the bottom of the tank (at least at early times), does the limited height prevent the apparition of a large-scale flow ?

We investigate these questions using Dedalus. The equations solved are the same as

in chapter 2. They are non-dimensionalised by the depth of the stratified layer H and the buoyancy frequency N. They are reproduced below:

$$\partial_t u - \nu\nabla^2 u + \partial_x P = -(\mathbf{u}\cdot\nabla)u \tag{3.4a}$$
$$\partial_t w - \nu\nabla^2 w + \partial_z P - b = -(\mathbf{u}\cdot\nabla)w \tag{3.4b}$$
$$\partial_t b - D\nabla^2 b + w = -(\mathbf{u}\cdot\nabla)b \tag{3.4c}$$
$$\nabla\cdot\mathbf{u} = 0 \tag{3.4d}$$

where b is the buoyancy, P the pressure, and $\nabla = (\partial_x, \partial_z)$. The geometry is two dimensional and periodic along the horizontal axis. We use $n_z = 256$ Chebyshev polynomial functions in the z direction and $n_x = 64$ complex exponential functions in the x direction. We use $\nu = 2.8 \times 10^{-6}$ and $Pr = 7$, representative of water considering thermal diffusion instead of salt diffusion. To compute nonlinear terms without aliasing errors, we use 3/2 padding in both x and z. For timestepping, we use a second order, two stage implicit-explicit Runge-Kutta type integrator [Ascher et al., 1997], with time steps $\mathcal{O}(10^{-2})$. Waves with random phases are forced at the bottom by setting velocity and buoyancy perturbations at the boundary. Top boundary condition is no slip. Note than this numerical set-up is upside down compared to the experimental one, with the waves generated at the bottom boundary.

3.4.1 Influence of the domain size

In the experiments, the domain height H is finite and the attenuation length of the waves l is not small compared to H. Therefore, waves bounce at the bottom boundary and propagate back up. We wonder if this effect can influence the large-scale flow generation. We run three simulations with the exact same forcing: two monochromatic, contra-propagating waves are generated at the bottom (numerical simulations are turned upside down compared to the experiment, in which the forcing is at the top), with amplitude $A_0 = 18 \times 10^{-5}$, frequency $\omega = 0.2$ and horizontal wavenumber $k_x = 12.8$. The simulations only differ by their domain height. Firstly we run a simulation with total height $H^* = 1$ (figure 3.26a). Then we shorten the domain height and use $H^* = 0.5$ for the first simulation (figure 3.26b) and $H^* = 0.1$ for the second simulation (figure 3.26c). The colorbars are the same but the total time is shorter for the $H^* = 0.1$ case.

For the $H^* = 1$ and the $H^* = 0.5$ cases, no large-scale flow is seen at early times. At the beginning, waves are created at the bottom boundary and propagate upward in the stratified layer. It takes some time for the waves to reach the top of the domain and even more time to create a large-scale flow. However, at $t \sim 3000$ the large-scale flow appears and quickly begins to reverse. The oscillating regime is quasi-periodic.

For the $H^* = 0.1$ case, again, no large-scale flow is seen at early times. It appears at $t \sim 1000$. However, in this case, it does not reverse through time. This steady horizontal flow is characterised by a shear between a layer moving in the $+x$ direction and a layer moving in the $-x$ direction, located at $z \sim 0.075$. This steady solution can appear in the Plumb's model for some cases. In the schematic from [Plumb, 1984], for the two first steps (shown in figure 3.27), the passage from (a) to (b) is not trivial and suggests that

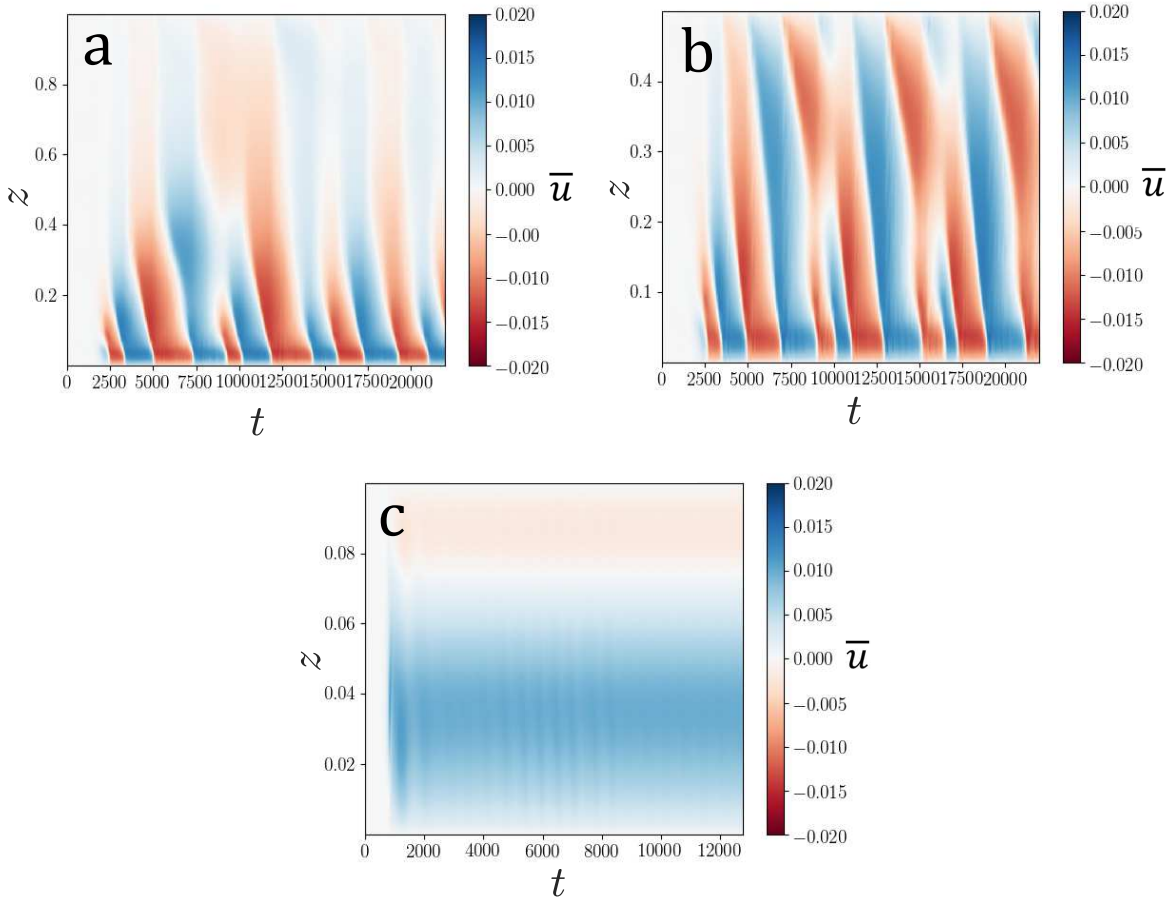

Figure 3.26: Hovmöller diagrams for $H^* = 1$ (a), $H^* = 0.5$ (b) and $H^* = 0.1$ (c). The other parameters are the same for the two cases.

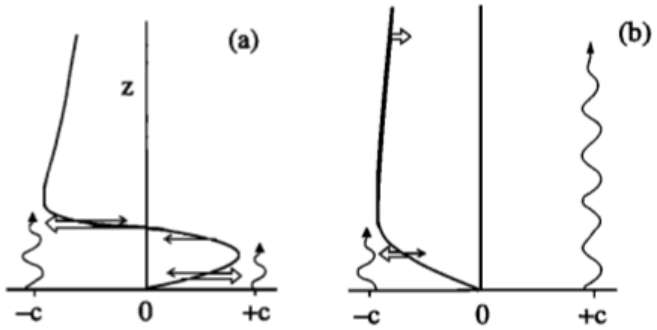

Figure 3.27: Schematic of the oscillations driven by two contra-propagating waves. Reproduced from [Plumb, 1984].

viscosity plus the $-c$ waves can "destroy" the layer of positive velocity located in the bottom domain. For some forcing parameters and kinematic viscosity, it is not the case and the flow remains blocked in the steady state displayed in (a), as seen in figure 3.26c.

The domain height H^* influences whether or not the large-scale flow oscillates. For small H^*, the waves bounce on the top of the domain and create a large-scale flow which does not oscillate. In the opposite, a large domain height the typical oscillating large-scale flow to emerge. This dependence on the domain height H^* is quite well apprehended by the fact that, in order to appear, the oscillations need that to extract momentum from the waves and thus, waves need to attenuate. Yet, if the height is too small compared to the wave attenuation length, the waves cannot give enough momentum to the large-scale flow, and the flow does not reverse. Additionally, if a wave reaches the top and bounces with a significant amount of remaining energy, it will force the flow at the top of the domain, and will force less and less as it propagates downward and the theory described in the Plumb's model cannot be applied. It thus means that our experimental set-up is not deep enough to excite a QBO. A question nevertheless remains: why it is sufficiently deep in Semin's experiment [Semin et al., 2018], which is about the same size and considers equivalent waves ?

3.4.2 Importance of the mode

From the experiment described in section 3.3.1, a mode seems to appear at least at long time in the stratified layer (see figure 3.22). The frequency 5×10^{-2} Hz, corresponding to the forcing frequency, appears over the whole depth of the stratification and shows little attenuation with depth and even seems to reinforce at $z = 5$ cm compare to the values at $z > 5$ cm. Since the wave attenuation is crucial for the emergence of a large-scale flow (see chapter 2), we wonder if a large-scale flow can emerge if the forcing waves excite a mode of the domain. To answer this question, we use Dedalus to solve the equations (3.4). At early times, we subtract the horizontal flow $\overline{u}$ from the velocity field u. The idea is to remove any large-scale contribution and to let the mode develops at early times. Then, once the mode is present, we stop subtracting $\overline{u}$ and see if a large-scale flow emerges from the existing mode. Results for the same parameters as in figure 3.26 are displayed in figure 3.28.

The left panel shows the results for $H^* = 0.5$ and the right panel shows the results for

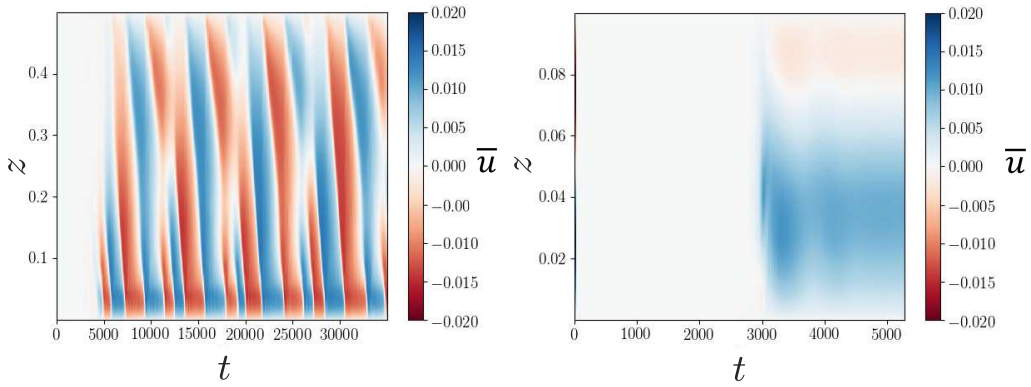

Figure 3.28: Hovmöller diagrams for $H^* = 0.5$ (left) and $H^* = 0.1$ (right). The other parameters are the same for all cases.

$H^* = 0.1$. We see that at early stages $t < 3000$, there is no large-scale flow. Horizontally averaging the mode leads to $\overline{u} = 0$. However, as soon as we stopped to remove the large-scale contribution at $t \sim 2500$, the mode is destabilised and vanishes (observable in figure 3.29 for the $H^* = 0.5$ case), letting the place to the reversing large-scale flow. For both cases, we find results equivalent to figure 3.26, meaning that the presence of the mode at early times does not prevent a large-scale flow to emerge.

2D snapshots for the $H^* = 0.5$ case are shown in figure 3.29. The panel (a) shows the waves propagating in the stratified layer. In panel (b), the waves have reached the top of the domain and the mode has appeared. The snapshot (c) is taken few time steps after we stopped subtracting $\overline{u}$. One can see that the mode is destabilised. In panel (d), the mode has disappeared and we see that the waves are affected by the large-scale flow: waves propagating in the $+x$ direction (in blue) are attenuated at $z < 0.05$ while red propagating in the $-x$ direction (in red) are attenuated above at $0.1 < z < 0.2$. The large-scale flow has emerged and is affecting wave propagation: the mode cannot remain in the layer and the oscillations take place. Therefore, if a mode appears at some point in the stratified layer, it will not prevent the emergence of a large-scale flow, if the conditions in order to drive the flow are met. We also show in figure 3.30 the RMS of the horizontal velocity u for $H^* = 0.5$. In figure 3.30a, the mode is visible for $t < 2500$. Then, it disappears and the oscillating large-scale flow appears. We see the apparition of the mode in figure 3.30b, focusing on time $t < 1500$. The wave propagation is noticeable: it takes time for the waves to reach the top of the domain. The bouncing on the top boundary and the reflection downwards is also noticeable. The nodes of the mode, visible by darker colors passed $t = 500$ appear at the top first, and then at lower and lower altitude with time: the node at $z = 0.1$ appears after the one at, *e.g.*, $z = 0.25$.

Figure 3.31 shows 2D snapshots at different times to see the evolution of the flow for $H^* = 0.1$. Again, we see the mode appearing at early time (figure 3.31a). Then, it is destabilised when we stop subtracting the mean-flow $\overline{u}$ (figure 3.31b). Finally, in figure 3.31c, the waves are Doppler-shifted by the mean-flow seen in figure 3.28c and the waves propagating in the $+x$ direction are attenuated at the bottom whereas the $-x$ waves reach the top of the domain. Figure 3.31d shows the RMS of the horizontal velocity u. Again,

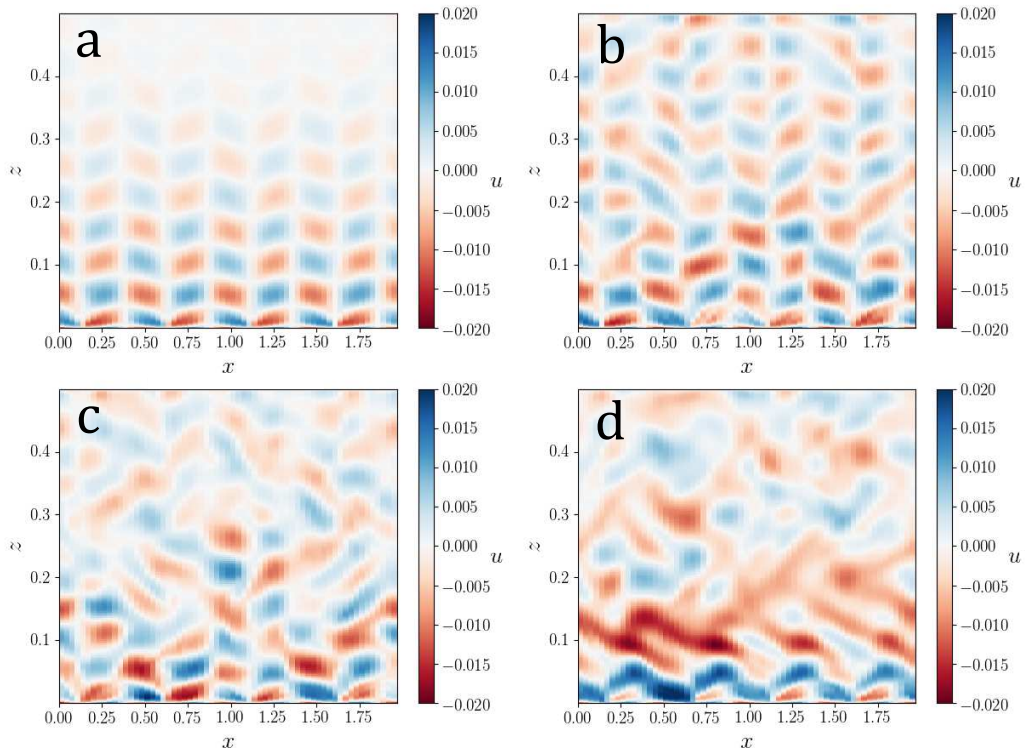

Figure 3.29: 2D snapshots of the horizontal velocity field u at different times for the $H^* = 0.5$ case. (a) $t = 360$ (b) $t = 2160$ (c) $t = 3360$ (d) $t = 4500$.

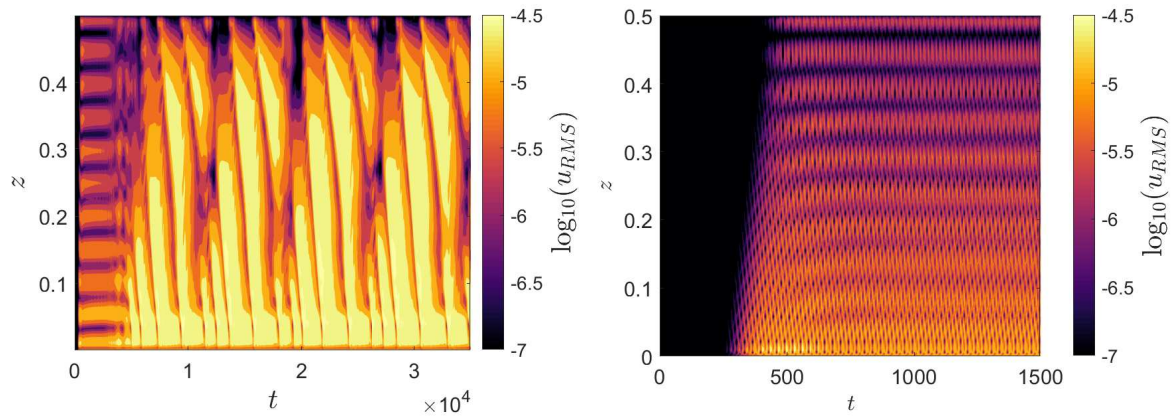

(a) (b)

Figure 3.30: (a) Time series of the RMS of the horizontal velocity u, displayed in a log scale. (b) Same figure for $t < 1500$ in order to visualise the mode apparition.

the mode appears at early times and is destroyed when we stop subtracting the mean-flow.

We thus conclude that, in our experiment, it is not the presence of a global mode that prevents the formation of QBO if it should take place. It is thus probably the excitation process that makes the different behaviour between our system and Semin's [Semin et al., 2018].

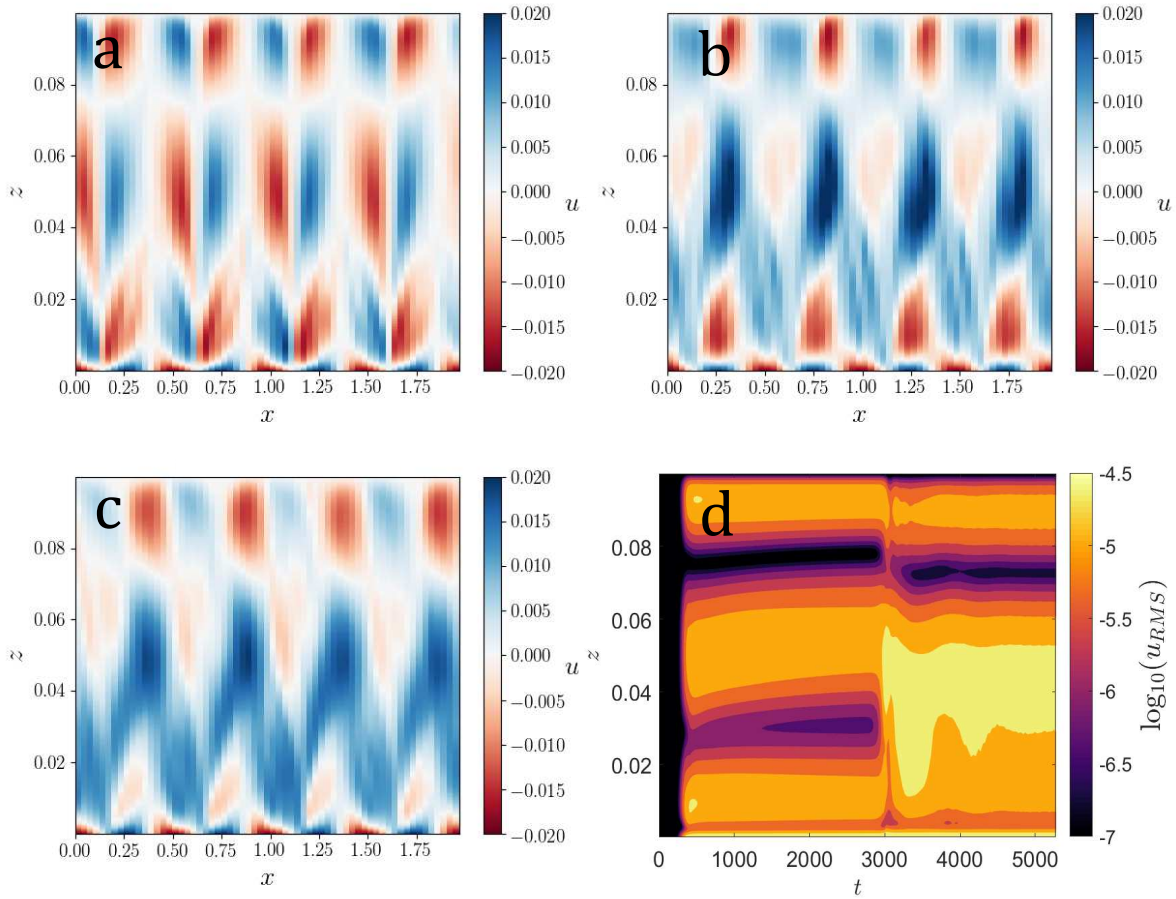

Figure 3.31: 2D snapshots of the horizontal velocity field u for the $H^* = 0.1$ case at time $t = 1570$ (a) $t = 2985$ (b) and $t = 4400$ (c). Times series of the RMS of u (d).

3.5 Conclusion

In this chapter, we have introduced our set-up to experimentally study the results found in the previous chapter with the extended Plumb's model. We have designed an experiment reproducing the geometry of the famous Plumb & McEwan's experiment. Yet, the forcing is not an oscillating membrane but a superposition of jets, for which we can tune the flow rate and impose a phase lag if necessary. The issue of the diminishing depth of the stratified layer over time was solved by continuously injecting dense fluid at the bottom of the tank, constantly rebuilding the stratification as in [Semin et al., 2018].

Our results show that, at early time, waves are generated and propagate in the stratified layer. A horizontal large-scale flow appears in the whole stratified layer with a shear at the interface. This flow is partly due to wave forcing, and a part of it is also viscously entrained by the large-scale flow in the convective layer. However, rapidly the mixing induced by the jets creates a density jump at the interface. This density jump affects wave generation. Over time, less and less energy is present in the waves and the large-scale flow decreases in magnitude and eventually vanishes, with only the $+x$ part remaining, forced at the same time by some wave attenuation and viscous entrainment by the turbulent layer.

Some experiments were conducted, trying to stop the mixing at the interface, while still generating internal gravity waves stochastically. Sadly, our efforts remain vain and our numerous attempts did not succeed to stop the mixing.

Some points remained unclear with the experiments. Energy is mostly present at high frequencies (so waves are confined in the tank) and a mode appears in the stratified layer. Both effects do not fit in the Plumb's model approach and it is a possibility that they prevent the emergence of a QBO-like flow. It is also surprising that with similar geometry and fluid properties, the wave propagation differs a lot from the previous monochromatic experiments [Plumb and McEwan, 1978, Otobe et al., 1998, Semin et al., 2018] . Despite the different generation mechanism which brings the density jump issue, the horizontal wavenumber k_x might also differ from the theoretical one. We expect to have a wavenumber set by the gap between two jets: $k_x = \dfrac{2\pi}{\lambda}$ with $\lambda = 2\pi R/6$ where $R = 15$ cm is the radius of the circle where the nozzle exits are located. It is possible that the wavenumber is smaller, resulting in a larger dissipation length. Since the view field is limited, we cannot measure small horizontal wavenumbers.

The numerical investigation using Dedalus addressed the questions of the height and mode influence upon mean-flow generation. The domain height H has an effect on the oscillating behaviour of the large-scale flow. However, the mode does not prevent the apparition of the large-scale flow.

The set-up described in this chapter does not seem to be appropriate to generate waves during a long period in order to generate an oscillating large-scale flow. The interface properties change through time and affect wave generation. Therefore, a better way to generate a QBO-like flow from stochastically generated waves would be to work on a stationary experiment, without any density jump at the interface. This can be achieved by using a peculiar property of water and the corresponding experiment will be presented in the next chapter.

CHAPTER 4

PENETRATIVE CONVECTION IN WATER AROUND ITS MAXIMUM DENSITY AT 4 °C

Contents

Water has a quite unusual property: its equation of state, relating density to temperature, is non-linear and reaches a maximum at $T \sim 4$ °C. Thanks to this feature, we can study penetrative convection in water around its maximal density with a continuous density profile between the convective and stratified layers. By cooling the bottom of a tank at 0 °C and leaving the free surface at the top at air temperature, one would see water convecting at the bottom of the tank while the upper part remains thermally stratified. This system seems particularly appropriate to mimic the troposphere–stratosphere interaction, in which the convective motions of the troposphere strongly interact with the stratosphere located above.

Section 4.1 will introduce general concepts of thermal convection and describe the particular case of penetrative convection with past studies as illustration. Section 4.2

will give insight on the experimental set-up and on its associated numerical investigation. Lastly, section 4.3 will detail the results obtained with the experiment and numerical simulation. The work presented in this chapter has been published in *Physical Review Fluids* [Léard et al., 2020].

4.1 A brief introduction to penetrative convection

4.1.1 Some theoretical aspects of Rayleigh-Bénard convection

General description

Convection is the heat transfer due to fluid motion. It results from the competition between buoyancy forces and diffusion (thermal diffusion κ and momentum diffusion ν). A simple demonstration of convection is to boil water in a pan. The water at the bottom will rise due to buoyancy forces created by the hot surface below the pan, while the water at the free surface will exchange heat with the air above, cool down and hence sink in the pan. This system will be sustained as long as there is a temperature difference ΔT sufficiently large between the top and the bottom boundary. Convection can also occur if one vertical wall is set at a different temperature than the other boundaries. The typical Rayleigh-Bénard convection (figure 4.1) corresponds to a system where a temperature difference is imposed between the top and bottom boundaries.

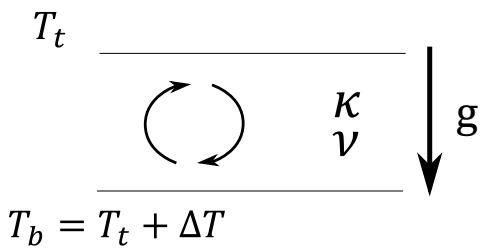

Figure 4.1: Schematic of the principle of Rayleigh-Bénard convection. The fluid is heated from below ($\Delta T > 0$) and gravity points downward. The convection is triggered if the buoyancy forces can overpass the dissipative mechanisms.

Since the first experiment of Bénard in 1901 [Bénard, 1901] and the theoretical modelling of Lord Rayleigh in 1916 [Lord Rayleigh, 1916], convection has been and still is a vastly investigated topic. Studies have described the different regimes of turbulence as a function of the Rayleigh number Ra (a dimensionless number representing the balance between buoyancy forces and dissipative processes, hence representing convection intensity). The topic is studied for its industrial applications but also for its fundamental aspects, especially the evolution of the convective heat flux with respect to Ra [Castaing et al., 1989, Chavanne et al., 1997, Chavanne et al., 2001]. It is particularly investigated in the geophysical community since, as we have seen in the very beginning of this manuscript, the Earth's core, oceans and atmosphere are animated with convective motions. Therefore, convection in presence of rotation is particularly of interest [Rossby, 1969, Stevens et al., 2009, Brun and Toomre, 2002] as well as more exotic systems such as convection in the presence of a melting boundary [Favier et al., 2019, Purseed et al., 2020], of a magnetic

field [Libchaber et al., 1982], or convection in the compressible regime [Menaut et al., 2019].

Equations

Convection is described by the Navier-Stokes equations, non-dimensionalised by the length scale H, the temperature difference ΔT and the time scale H^2/κ. The equations, considering the Boussinesq approximation described in chapter 2, are:

$$\frac{1}{Pr}\frac{\mathrm{D}\mathbf{u}}{\mathrm{Dt}} = -\nabla P + Ra(T - T_0)\mathbf{e_z} + \nabla^2\mathbf{u} \tag{4.1}$$

$$\frac{\mathrm{D}T}{\mathrm{D}t} = \nabla^2 T \tag{4.2}$$

$$\nabla \cdot \mathbf{u} = 0 \tag{4.3}$$

These equations are governed by two dimensionless numbers: the Rayleigh number $Ra = \frac{\alpha_T g \Delta T H^3}{\kappa\nu}$, with α_T the thermal expansion coefficient, and the Prandtl number $Pr = \frac{\nu}{\kappa}$. As already mentioned, the Rayleigh number describes the balance between the buoyancy forces which are the key mechanism for driving convection and the dissipative processes (heat and momentum diffusivities). Threshold values Ra_c exist for the Rayleigh number and allow to predict if the system will convect or not. The values are $Ra_c = 1707.76$ for rigid boundaries, $Ra_c = 657.51$ for free boundaries and $Ra_c = 1100.65$ for rigid-free boundaries [Chandrasekhar, 1961]. If $Ra > Ra_c$, the buoyancy forces dominate and convection appears, with more or less intensity depending on the values of Ra and Pr.

The Prandtl number Pr is the ratio between the characteristic time of thermal diffusion H^2/κ and momentum diffusion H^2/ν. For large Prandtl numbers, the inertia term becomes negligible and the convection is a balance between buoyancy forces and dissipation. For small Pr, viscous effects are negligible and the convective motion persists thanks to inertia even if the buoyancy forces have vanished due to the fast temperature diffusion.

In the atmosphere, the tropopause is a free boundary. The troposphere and the stratosphere interact at the interface and the upward plumes of the convection enter in the stratosphere. This particular case of convection is called penetrative convection. It also takes place in stellar interiors, at the interface between the convective and radiative layers. It has been investigated in experimental and numerical studies, with or without rotation, and in different geometries (periodic Cartesian [Augustson and Mathis, 2019, Couston et al., 2020] or spherical shell [Dietrich and Wicht, 2018] for astrophysical and geophysical applications). We detail the results of some of these studies.

4.1.2 Penetrative convection

Penetrative convection in experiments

The laboratory experiment of [Deardorff et al., 1969] investigated this mechanism. The tank was filled with temperature-stratified water, so the tank is initially stratified from bottom to top boundaries. At $t = 0$, the tank is heated from below and convection starts. Temperature measurements allowed to describe the time evolution of the temperature profile and heat flux. [Michaelian et al., 2002] re-investigated this set-up using coupled thermal and PIV measurements in order to investigate the coupling between convection and the internal gravity waves generated. The wave frequencies change through time as shown in figure 4.2. Low frequency waves are contained close to the interface while higher frequency waves propagate to the top of the tank. The experiment stops when the whole tank is convective and the stratified layer no longer exists. This transient system is not suited for the investigation of large-scale flows driven by waves.

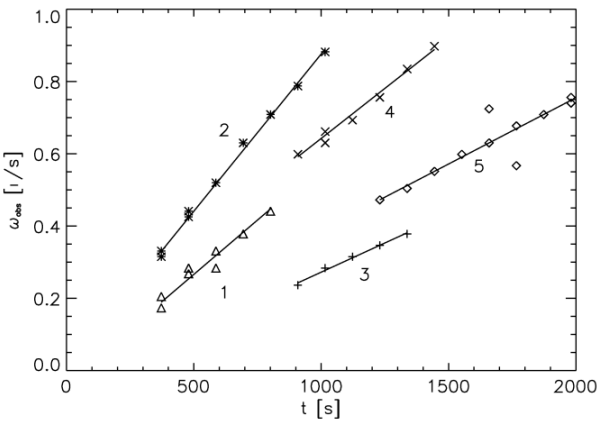

Figure 4.2: Frequency variations with time for an experiment with $N = 0.90$ s^{-1}. Each line represents the time evolution of the frequency corresponding to different peaks in the frequency spectrum. All peak frequencies increase with time, at different rates. Reproduced from [Michaelian et al., 2002].

Townsend [Townsend, 1964] introduced an original set-up to investigate penetrative convection in a stationary system. The equation of state of water is non-linear with a maximum density at around 4 °C (International Equation of State of Seawater, 1980):

$$\rho(T) = 999.842594 + 6.793952.10^{-2}T - 9.095290.10^{-3}T^2 + 1.001685.10^{-4}T^3 \\ -1.120083.10^{-6}T^4 + 6.536332.10^{-9}T^5. \tag{4.4}$$

with T the temperature in °C and ρ the density in kg $\cdot$ m^{-3}.
Thus, Townsend covered the bottom of a tank with ice and maintained the upper boundary at about 25 °C. The fluid is then convective in the lower part of the tank, between the isotherms 0 °C and 4 °C, with a mean temperature of $T \sim 3.2$ °C. The upper part of the tank is stably stratified, between 4 °C and the imposed top temperature 25 °C (see the density profile in figure 4.3, shown between $T = 0$ °C and $T = 15$ °C and computed from the equation of state of water displayed in equation 4.4). As long as the heat flux remains constant, the interface position does not change location, and the buoyancy frequency

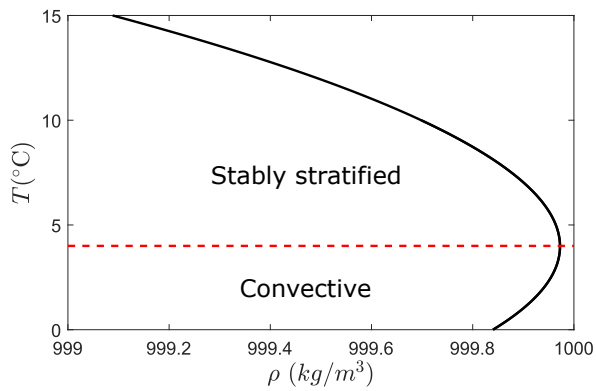

Figure 4.3: Evolution of the density with respect to temperature for water, between $T = 0$ °C and $T = 15$ °C, in order to visualise the maximum density reached at $T = 4$ °C (red dashed line). If $T = 0$ °C is imposed at the bottom boundary, the density profile is unstable between $T = 0$ °C and $T = 4$ °C and stable between $T = 4$ °C and $T = 15$ °C.

in the stratified layer does not vary either. Using temperature and dye measurements, internal gravity waves were observed close to the maximum penetration height.

A similar set-up was studied in a laminar flow with low Rayleigh number [Le Gal, 1997]. A hexagonal pattern was observed in the convective layer and the upper layer was viscously entrained by the convective rolls.

Recently, experimental studies [Perrard et al., 2013,Le Bars et al., 2015] re-investigated the turbulent 4 °C convection in a quasi-2D geometry (see figure 4.4a), with coupled temperature (local probes) and velocity measurements (field measurements with PIV). The temperature and density profiles are constant in the convective layer and the temperature linearly increases with height in the stratified layer. [Perrard et al., 2013] reported the existence of an intermediate layer, named "buffer layer". In this layer cohabit convective motions and internal gravity waves. Water at 0 °C has approximately the same density as water at 8 °C. Therefore, fluid at initially 0 °C can rise up to the 8 °C isotherm (neglecting dissipative mechanisms), while the fluid is stratified between 4 °C and 8 °C. Internal gravity waves were observed (figure 4.4b) and studied [Le Bars et al., 2015], showing that only waves with frequencies close enough to N could reach the top of the stratified layer. However, the energy is mostly concentrated in low frequency waves which attenuate close to the interface, corroborating the results from [Michaelian et al., 2002]. The 2D geometry of the set-up does not allow for any oscillating horizontal large-scale flow to develop in the stratified layer.

Penetrative convection in numerical studies

Direct numerical simulations [Lecoanet et al., 2015] investigated penetrative convection in a fluid with a non-linear equation of state, in a 2D geometry, periodic along its horizontal direction. The density dependency upon temperature is modelled with a quadratic law $\frac{\delta\rho}{\rho_0} = -\alpha_T(T - T_0)^2$, with $T_0 = 4$ °C, the maximum density temperature. Convection takes place in the bottom of the tank and a stratified layer is located above. Spectra of

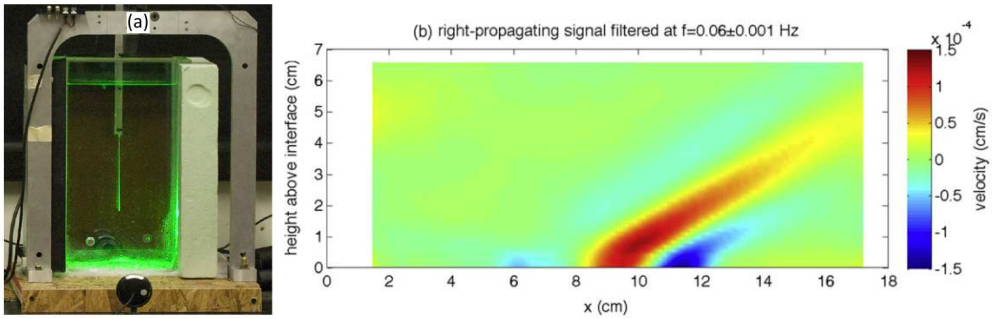

Figure 4.4: (a) Photography of the experimental set-up. Water is cooled down from below at 0 °C. The tank is convective in its bottom half and stratified in its upper half. (b) Internal gravity waves generated in the stratified layer by the convection located below. The signal is frequency filtered at $f = 0.06$ Hz with $N = 0.07$ Hz. Only right propagating waves are displayed. Reproduced from [Le Bars et al., 2015].

waves at different heights were plotted. They suggest that the weak dissipation limit for internal gravity waves discussed in chapter 2 tremendously overestimates the dissipation for low frequency waves. The study also suggests that, in this configuration, internal gravity waves are generated by the Reynolds stress in the convective bulk below the interface, rather than by the displacement of the interface, placed at the $T = 4$ °C isotherm.

Similar studies were conducted in 2D and 3D geometries, periodic along their horizontal directions [Couston et al., 2017, Couston et al., 2018a, Couston et al., 2018b, Couston et al., 2020]. The density anomaly was modelled by a piecewise linear relation:

$$\rho(T) = -\alpha_T T = \begin{cases} -T & T \geqslant 0 \\ \mathcal{S}T & T < 0 \end{cases} \tag{4.5}$$

with $\mathcal{S}$ a free parameter that controls the stiffness of the stratification. The fluid is then convectively unstable for $T \geqslant 0$ and stably stratified for $T < 0$. $T = 0$ is the temperature of maximum density. Large (resp. small) values of $\mathcal{S}$ result in a strong (resp. weak) stratification. The dynamics of the convective layer in 2D was thoroughly described [Couston et al., 2017] showing the influence of $\mathcal{S}$. The long-time evolution investigation of the 2D geometry reveals that an oscillating horizontal large-scale flow appears in the stratified layer [Couston et al., 2018a], driven by the internal gravity waves generated by the convective layer (see figure 4.5). Results show that the emergence of the oscillating large-scale flow depends on the value of the Prandtl number. Large-scale flow emergence is compromised for $Pr > 1$. The dynamics in the 3D geometry were investigated with [Couston et al., 2018b] and without [Couston et al., 2020] rotation. The large-scale flow generation could not be studied since these kind of simulations cannot be run for long-enough time. The 3D geometry, coupled with the need of small time step to solve the fast convective motions, results in very expensive simulations.

The 2D DNS of [Couston et al., 2018a] showed that oscillating horizontal mean-flows can emerge from turbulently-generated internal gravity waves (figure 4.5) in a configu-

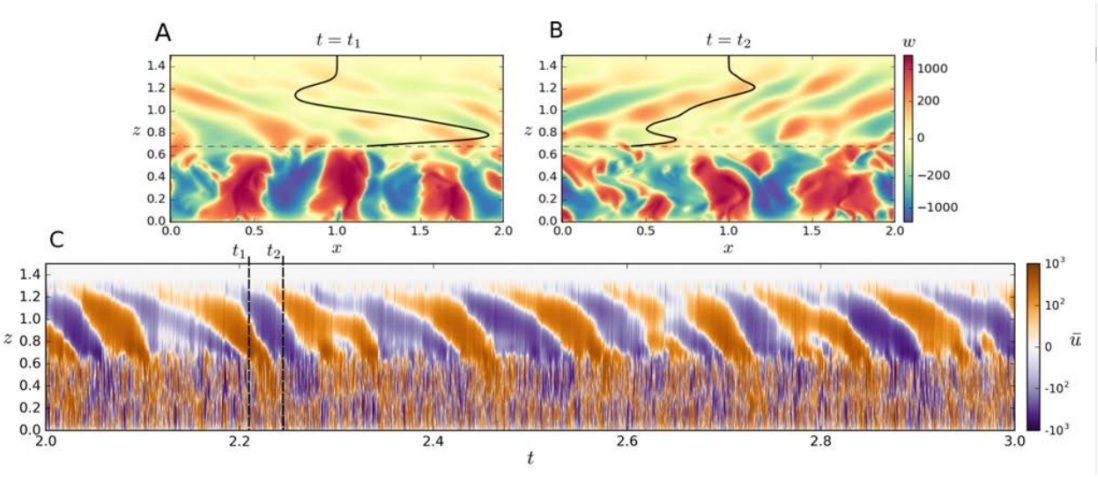

Figure 4.5: DNS results from [Couston et al., 2018a]. (A) and (B) show 2D snapshots of the vertical velocity w at $t_1 = 2.21$ and $t_2 = 2.24$. Time is non-dimensionalised by the thermal diffusivity time. The solid line shows the horizontally averaged horizontal velocity $\overline{u}$. The interface between the convective and stratified layers is located at $z = 0.68$. (C) shows the time evolution of the horizontally averaged flow $\overline{u}(z, t)$. In the stably stratified layer, $\overline{u}$ oscillates from positive values to negative values, with downward propagating phase, in a QBO-like oscillating flow. The Prandtl number is $Pr = 0.2$ and the effective Rayleigh number (based the effective height of the convective layer) $Ra_{eff} = 4 \times 10^7$.

ration with a fluid characterised by a non-linear equation of state. Therefore, the 4 °C convection with water seems to be a good candidate to drive QBO-like flow from a stochastic forcing.

In the two following sections, we introduce our experimental 3D set-up to investigate penetrative convection in a steady regime, using the non-linear equation of state of water. The convection properties, internal gravity wave generation and large-scale flow emergence will be investigated with PIV measurements. A numerical simulation, with parameters close to the experiment, is also performed to answer remaining questions from the experiment. The description of the set-up and numerical model in section 4.2 and the presentation of the results in section 4.3 are a reproduction of the corresponding parts of our article pubished in *Physical Review Fluids* [Léard et al., 2020].

4.2 Experimental and numerical investigation of the 4 °C convection in a 3D geometry

4.2.1 Description of the experimental set-up

The set-up consists in a cubic tank whose lateral boundaries are made of 2 cm thick acrylic walls. The bottom boundary is a chrome plated copper plate in which refrigerated fluid is forced to circulate. The top boundary is a commercial, transparent electric heater. The tank inner dimensions are 32×32 cm for the horizontal section and $H = 20$ cm in height. Preliminary experiments were conducted in this cubic geometry. Eventually, a cylinder of outer diameter $D = 29$ cm and thickness $e = 0.4$ cm was added inside the cubic tank, to reproduce the axisymmetric geometry of [Plumb and McEwan, 1978,Semin et al., 2016,Semin et al., 2018], which seems prone to the development of large-scale flows. We are interested in the flow within the cylinder: the fluid in the gap between the cylinder and the cubic tank follows a similar dynamics and thus imposes to the working fluid a (close to) no-flux lateral boundary condition.

The temperature of the bottom boundary is controlled by water circulating in the copper plate. Water is cooled down by a thermal bath with a fixed temperature set at -1.25 °C. Due to thermal losses in the pipes alimenting the copper plate, bottom tank temperature is 0.2 ± 0.05 °C. Plate thickness and circulation circuit were optimised so as to ensure a uniform temperature over the whole plate. At the top boundary, the heater is set at a temperature of 35 °C. Its temperature control is custom made: a PT100 probe measures the heater temperature in real time, driving through a feed-back loop the input power injected in the heater. This is a very simple and inexpensive system to impose a temperature while having a transparent top boundary, allowing visualisation and velocity measurements by PIV. Nonetheless, it is necessary to point out that the temperature over the heater area is not perfectly homogeneous. Temperature is maximal at the centre where $T \sim 38$ °C, while the edges are indeed at the requested $T = 35 \pm 0.1$ °C. This inhomogeneity of the top temperature by $\delta T = 3$ °C induces slow convective motions below the heater, in a ~ 2 cm high layer. By performing an experiment where the whole fluid is stably stratified with an overall temperature gradient similar to the one in the stratified layer studied here, but above the density reversal at 4 °C (i.e. bottom boundary set at 10 °C and top boundary at 70 °C), we have checked that those top convective motions have no significant impact on the dynamics of the two-layer system. It is also important to say that despite the thick acrylic wall and the intermediate fluid layer between the cylinder and the tank, the working region is not fully thermally insulated on the sides. Nevertheless, our fully stratified, test experiment has shown no motion within the fluid driven by these lateral losses.

The equation of state of water is non-linear with a maximum density close to 4 °C. Thus, due to the imposed temperature at top and bottom boundaries, the bottom part of the tank, between 0 °C and 4 °C, is convectively unstable (see figure 4.6). Cold plumes detach from the bottom plate and rise in the tank due to buoyancy. Reciprocally, "hot" fluid sinks from the 4 °C interface due to gravity. While convective motion takes place in the lower layer, the upper part of the tank, between 4 °C and 35 °C, is stably stratified, with an assumed linear temperature profile at equilibrium. The temperature is indeed

linear for an ideal case without thermal losses, assuming that the stratified layer has a bottom boundary at fixed temperature 4 °C and top boundary at 35 °C (*i.e.* constant diffusive flux through the whole layer). However, the density profile is not linear, due to the non-linear equation of state of water. Stratification is characterised by the Brunt-Väisälä frequency $N^* = \frac{1}{2\pi}\sqrt{-\frac{g}{\rho_0}\frac{\partial\rho}{\partial z}}$. Because of the non-linear equation of state, N^* is not constant with depth, as shown in figure 4.6. For simplicity, we also use below the global buoyancy frequency defined as $N = \frac{1}{2\pi}\sqrt{-\frac{g}{\rho_0}\frac{\Delta\rho}{\Delta z}}$, where $\Delta\rho$ is the global density contrast within the stratified layer of depth Δz.

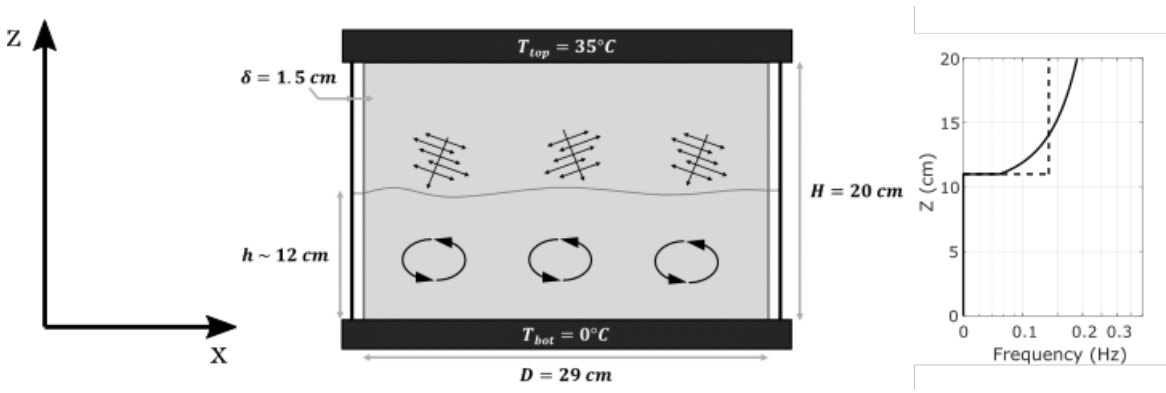

Figure 4.6: 2D sketch of the tank. A cylinder (light grey shaded area) is placed in a larger cubic tank. The system is cooled down at the bottom at 0 °C and heated up at the top at 35 °C. The bottom half is convective with an almost constant density, apart from the bottom boundary layer. The upper half is stably stratified and waves are generated due to the fluid motions in the convective layer. The graph on the right shows the theoretical profile for the buoyancy frequency N^*. It is computed considering a linear temperature profile and the equation of state of water (4.4). The dashed line is the global buoyancy frequency N calculated on the stratified layer. The various length scales are the cylinder diameter D, the vertical extent of the tank H and the vertical extent of the convective layer h. δ is the minimal width between the outer square tank and the inner cylinder. The x, y and z-velocity components are noted u, v and w respectively.

Before starting the experiment, the bath and the heater are allowed to reach their assigned temperature. Then, the upper half of the tank is filled with water stratified in temperature from 4 °C to 35 °C, using the double bucket technique [Oster, 1965]. The bottom half is filled with water with a temperature close to 4 °C. This filling process is used to avoid tremendously long transient before reaching steady state by thermal diffusion. Typically, we fill the tank at the end of a day and start the measurements the next day in order to let the system reach its equilibrium state over night. Each experiment then lasts four days, with no change in the location of the interface. Note that this steady interface position is the result of the heat budget equilibrium between the convective heat flux extracted from the bottom plate, the diffusive heat flux through the stratified layer, and the lateral heat losses.

To perform PIV measurements, particles are chosen as small as possible and with a density as close as possible to water density in order to avoid their sedimentation in the stratified layer over the long duration of the experiment. We use fluorescent orange

polyethylene micro-spheres whose size ranges from 10 µm to 20 µm and density is 1.00 ± 0.01 g/cc. The fluorescent property allows us, with a high pass filter on the camera, to remove any laser reflection, significantly enhancing the images quality. The tank is illuminated with a green laser 532 nm. Power is set at 1 W. We perform side view PIV to measure convection and IGWs spectral characteristics, and top view PIV to observe the large scale flow and its fluctuations over time. The camera used for the side view PIV is a HiSense Zyla 2560 × 2160 pixels recorded on 12 bits. Acquisition rate is 2 Hz with 100 ms exposure time. Typical acquisition time for spectral characteristics is 50 min. For the top view, we use a Point grey camera 1920 × 1080 pixels on 8 bits. Exposure time is 1 s, acquisition rate 0.1 Hz and acquisition time 8 hours. Captured movies are processed either by the DantecDynamics software DynamicStudio for the side view or by DPIVSoft [Meunier and Leweke, 2003] for the top view. Both are resolved into 32 × 32 pixels boxes with 50% overlapping.

Side view PIVs are performed in the middle of the tank at $y = 16$ cm in a laser sheet crossing the cylinder along its diameter. This is the case for all figures shown in the (x, z) plane and thus not mentioned in the results section. The vertical fields (see an example in figure 4.7) do not show the whole (x, z) plane (where the origin $(0, 0)$ is located in the bottom left corner of the cubic tank): it was indeed chosen to zoom in, in order to have the best resolution for the very weak motions in the stratified layer. The interface between the layers is localised between 11 cm $\leqslant z \leqslant$ 12 cm. Typical Rayleigh number for the convection based on this depth is $Ra = 7 \times 10^7$, and the global Brunt-Väisälä frequency is $N = 1.35 \times 10^{-1}$ Hz.

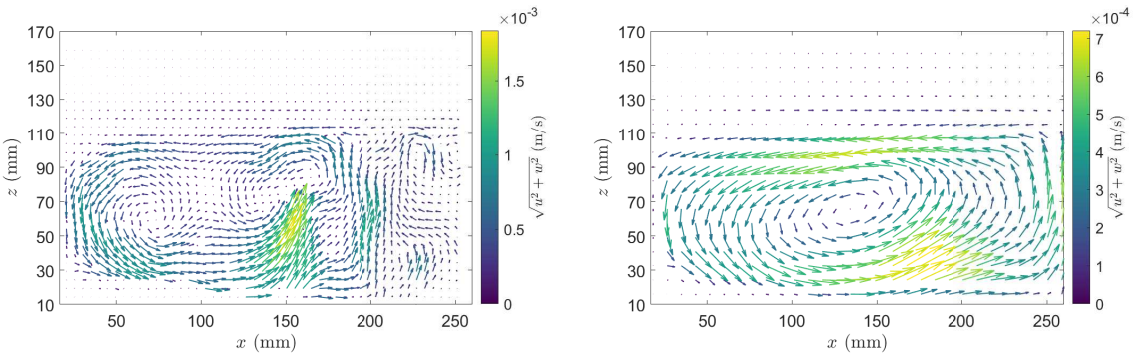

(a) (b)

Figure 4.7: (a) Instantaneous velocity field. An ascending plume is visible at $x = 150$ mm, and transported by the large-scale circulation. (b) Large-scale circulation in the convective layer obtained by time-averaging velocities over a 50 minutes signal. The large-scale circulation is a counter clockwise cell. No inversion of the circulation has been seen in our experiment. The velocities under $z = 10$ mm are noisy and thus not shown here. Maximum instantaneous velocities are 2.5 times bigger than the maximum averaged velocities. The left edge of the cylinder is located at $x = 19$ mm and the centre of the cylinder is at $x = 160$ mm. Approximately 40 mm of the right side of the cylinder is not captured with our PIV measurments.

To observe the large-scale flow, horizontal views at different heights are performed. A linear translation axis platform from Igus, driven by home-made software, is used to automate the process. With two mirrors, one fixed at the exit of the laser head and the

other fixed on the translating platform, it is possible to sweep along one direction with the laser sheet. We typically make measurements during 15 s in each of 11 successive planes separated by 0.5 cm. The full scan duration is about 3 min, and is repeated during at least 8 hours.

The cylindrical geometry described here differs from the cylindrical shell geometry in [Plumb and McEwan, 1978, Semin et al., 2016, Semin et al., 2018]. We first tried to work in that annular geometry by adding a second, smaller cylinder in our cubic tank. Three different gap sizes were tested but none showed any interesting dynamics. Indeed, the convection was too confined in the shell to provide an efficient chaotic excitation, and IGWs did not propagate well within the stratification, attenuated quite fast by wall friction. During these tests, we observed the most interesting dynamics within the innermost cylinder, so we decided to use that geometry. The point of the cylindrical shell geometry is that it is a close analogue to the equatorial band of the stratosphere where QBO takes place. By working in a cylinder, the geometry analogy is lost but the physics of the problem remains the same, still a priori allowing for large-scale, reversing, axisymmetric horizontal flows.

4.2.2 Numerical model

To complement the experiments, we also performed Direct Numerical Simulations (DNS) of the same configuration. We solve the Navier Stokes equations using a non-Oberbeck Boussinesq model. The density variations are consider small compared to the reference density $\frac{\Delta\rho}{\rho_o} \ll 1$. Therefore, density fluctuations only appear in the buoyancy force. However, temperature variations affect the value of the thermal expansion coefficient to account for the non-linear equation of state of water. Variations of the thermal diffusivity κ and kinematic viscosity ν are neglected. Governing equations are given in dimensionless form by:

$$\frac{\partial \mathbf{u}}{\partial t} + \mathbf{u}\cdot\nabla\mathbf{u} = -\nabla P + Pr\nabla^2\mathbf{u} - PrRa\,\theta^2\mathbf{e}_z \tag{4.6}$$

$$\frac{\partial \theta}{\partial t} + \mathbf{u}\cdot\nabla\theta = \nabla^2\theta \tag{4.7}$$

$$\nabla\cdot\mathbf{u} = 0 \tag{4.8}$$

where we used the depth H of the container as a unit of length, the thermal diffusive timescale H^2/κ as a unit of time and the difference between the bottom and the inversion temperature $T_0 - T_i$ as a temperature scale. These equations are characterised by the Prandtl number $Pr = \nu/\kappa$, the global Rayleigh number $Ra = \alpha_T g(T_0 - T_i)^2 H^3/(\nu\kappa)$ and the imposed dimensionless top temperature $\theta_{top} = (T_{top} - T_i)/(T_0 - T_i)$. Note that the quadratic temperature term in the momentum equation is a direct consequence of the non-linear equation of state of water given by equation (4.4), which is approximated in our model by the quadratic equation $\rho(T) \approx \rho_0(1 - \alpha_T(T - T_i)^2)$. The coefficient α_T is not the usual thermal expansion coefficient but has a unit of (°C)$^{-2}$ and is given by $\alpha_T \approx 8.1 \times 10^{-6}$(°C)$^{-2}$ (see also [Lecoanet et al., 2015]).

We consider a cylindrical fluid cavity of diameter $D = 3H/2$ as in the experiments. Both horizontal plates are assumed to be no-slip and with fixed temperature. The side

wall is assumed to be no-slip and perfectly insulating. This is of course not the case in the experiment, for which lateral heat losses are inevitable and top temperature is not exactly constant, but the objective is to check whether the conclusions drawn from the experimental results are robust and do not depend on these effects. Since the experiment runs with water, we use $Pr = 7$. The Rayleigh number of the experiment is $Ra = 7 \times 10^7$ while its dimensionless top temperature is $\theta_{top} = -7.75$. If we were to run the simulation with these parameters, the interface will be located very close to the top boundary. It is not the case in the experiment because of the lateral heat losses, which tend to reduce the effective Rayleigh number. For that reason, and instead of taking into account these losses as in [Lecoanet et al., 2015], we kept the insulating lateral boundaries and use the slightly adjusted parameters $Ra = 10^7$ and $\theta_{top} = -11$ instead, which leads to an interface located approximately at $z \approx 120$ mm, as in the experiment. The Rayleigh number could not be lowered under 10^7 in order to keep the convective flow turbulent enough, thus we had to increase the top temperature to have the interface located at $z \approx 120$ mm.

We perform DNS of equations (4.6)-(4.8) using the spectral element solver Nek5000 [Fischer et al., 2017]. The global geometry is decomposed into hexahedral elements, with vertical refinement close to the horizontal boundaries and around the mid-plane where the inversion isotherm is expected to be located. Velocity, buoyancy and pressure variables are represented as tensor product Lagrange polynomials of order N and $N-2$ based on Gauss or Gauss-Lobatto quadrature points. The total number of grid points is given by $\mathcal{E}N^3$ where $\mathcal{E}$ is the number of elements. For all the results discussed in this paper, the number of elements is $\mathcal{E} = 8960$ and we use a polynomial order of $N = 11$. Numerical convergence was checked by increasing the polynomial order N. Time integration is performed with a third-order mixed implicit-explicit scheme. The simulations are initialised with a small amplitude buoyancy perturbation and a temperature profile varying linearly between the top and bottom boundaries. Simulations are run until a quasi-steady state is reached, after which data is accumulated to compute statistics.

4.3 Description of the flow in the 4 °C set-up

4.3.1 Experiment results

Convection

PIV side view is used to quantify horizontal and vertical velocities in the convection zone. Examples of vertical velocities measured at one point in a given location are shown in figure 4.8, for both ascending cold and descending hot structures. Measurements are consistent with the numerical simulations [Lecoanet et al., 2015,Couston et al., 2017] showing intense, localised, cold rising plumes and more diffusive descending plumes. Moreover, these structures are advected by a large-scale circulation encompassing the whole convective layer, as shown in figure 4.7.

Spectral analysis is performed to extract power spectral density (PSD) from the velocity signals. Figure 4.9 shows the PSD of the convection vertical velocity w. For the two panels, the spectrum is flat with a lot of energy for low frequencies, then the energy drops above some cut-off frequency. Left panel of figure 4.9 shows the vertical velocity PSD at a single point close to the top of the convective layer. A small peak can be seen

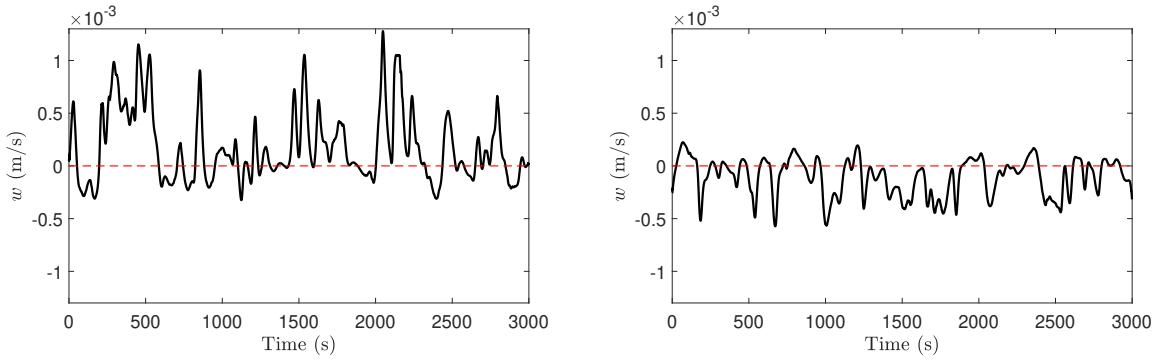

Figure 4.8: Time evolution of the vertical velocity w within: (a) upward plumes at $x = 200$ mm, $z = 45$ mm, (b) downward structures at $x = 100$ mm, $z = 95$ mm.

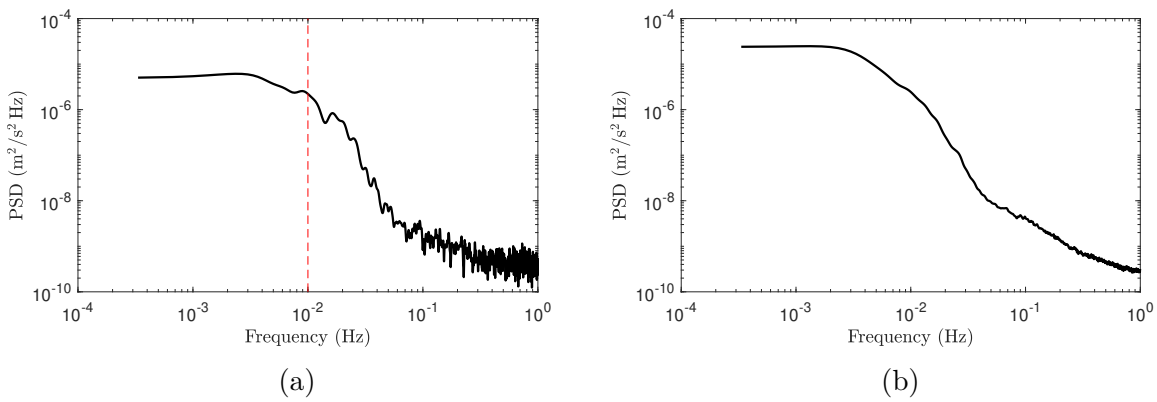

Figure 4.9: PSD for the vertical velocity fluctuations. (a) PSD computed at a single point $x = 100$ mm, $z = 95$ mm (signal shown in figure 4.8 right). The plume forcing frequency can be seen around $f = 10^{-2}$ Hz (red dashed line). (b) PSD spatially averaged over the whole convective cell in the measured (x, z) plane (all points above $z = 10$ mm and below $z = 110$ mm).

close to $f = 10^{-2}$ Hz. This is the quasi-periodic signal of the plumes dropping from the top thermal boundary layer. The theoretical characteristic time of convection can be computed from [Howard, 1966]:

$$\tau = \frac{h^2}{\pi\kappa}\left(\frac{\Delta T}{\Delta T_{local}} \times \frac{Ra_c}{Ra}\right)^{2/3} \tag{4.9}$$

with h the height of the convective layer, κ the thermal diffusivity, ΔT the temperature difference between the top and bottom of the convective domain, ΔT_{local} the temperature difference between the top and bottom of the thermal boundary layer, and Ra_c the critical Rayleigh number. The critical Rayleigh number in the presence of free and solid interfaces and for fixed temperature is $Ra_c = 1100.65$. For our experiment, the characteristic time is $\tau = 96$ s, thus characteristic frequency is $1/\tau \sim 10^{-2}$ Hz, which is close to the observed peak in the left panel of figure 4.9. At frequencies lower than this characteristic frequency, the spectrum is flat. This is explained by the combined effect of the randomness of the

plumes (see figure 4.8) and of the slow fluctuations of the large-scale circulation. Right panel of figure 4.9 shows the PSD of vertical velocities, averaged over the whole convective cell in the (x, z) plane. It shows a similar trend, with a lower cut-off frequency compared to right panel spectrum. Actually, the plumes signal is more localised and less intense on average than the large-scale circulation signal, which hence dominates the space-averaged PSD.

The probability density function (PDF) of the vertical velocities in the whole convective layer $\mathrm{P}(w)$ is computed and shown in figure 4.10. It is normalised such that $\int \mathrm{P}(w)\mathrm{d}w = 1$. The PDF describes important features of the convection: it is skewed towards positive values, with positive velocities reaching higher magnitude than negative velocities, *i.e.* the ascending plumes are stronger than the descending structures. However, the central part of the PDF is close to gaussian profile. The distribution obtained here is in good agreement with the probability density function computed in an idealised 2D numerical model by [Couston et al., 2017]. Note that this asymmetry is specific to our model, for which the usual upside-down symmetry in Boussinesq Rayleigh-Bénard convection is broken.

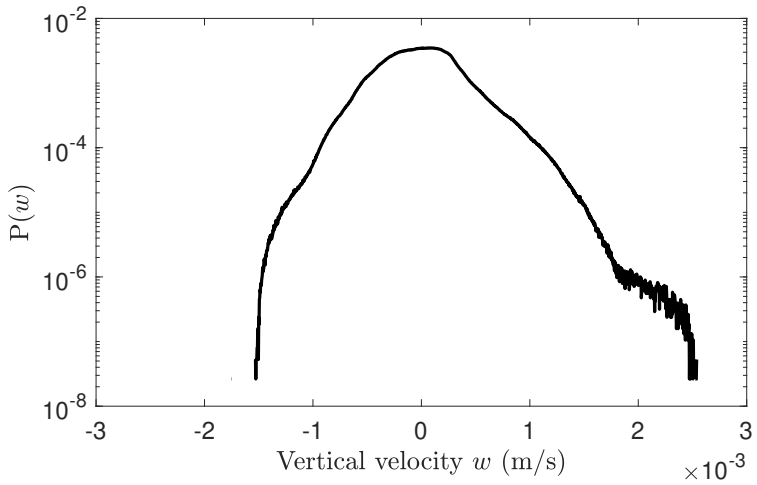

Figure 4.10: Probability density function of the vertical velocities in the convective layer. All PIV points under $z = 110$ mm have been used to compute the PDF.

Buffer layer

An intermediate layer (we name it the buffer layer in the following) is present between the convective layer and the stratified layer. As mentioned before, it was previously reported in the quasi-2D 4°C convection experiment by [Perrard et al., 2013]. The buffer layer is a very specific location supporting simultaneously convective overshooting motions and IGWs, as observed with PIV measurements.

To complete the description of the buffer layer of [Perrard et al., 2013] now using velocity measurements, we plot in figure 4.11 the spatio-temporal graph of the horizontal average of the horizontal velocity u. The graph exhibits a strong shear around $z = 120$ mm. Since the fluid is going in opposite directions above and below $z = 120$ mm with a sharp interface, viscous entrainment by the convective layer is excluded. A special

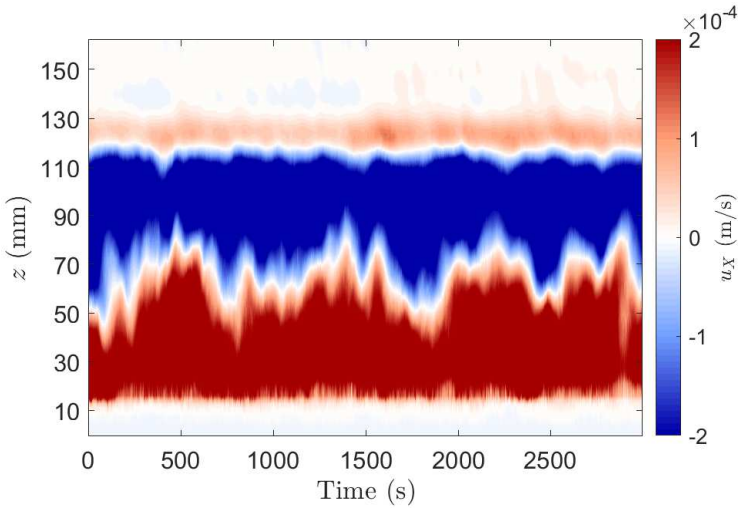

Figure 4.11: Time evolution of the horizontal average of the horizontal velocity, noted u_X. Red (resp. blue) regions correspond to mean flow going towards the right (resp. left).

kind of thermal coupling might explain the observed dynamics, as sketched in figure 4.12. Indeed, when a cold ascending plume from the convection zone reaches the interface and overshoots in the buffer region, its associated velocity perturbation dissipates more rapidly than its temperature perturbation. Due to gravity, the distorted part of the buffer region wants to sink back to its initial state (pictured by the green arrows), while the fluid above the buffer layer moves towards the impact point of the plume to take the place of the falling water (pictured by the red arrows).

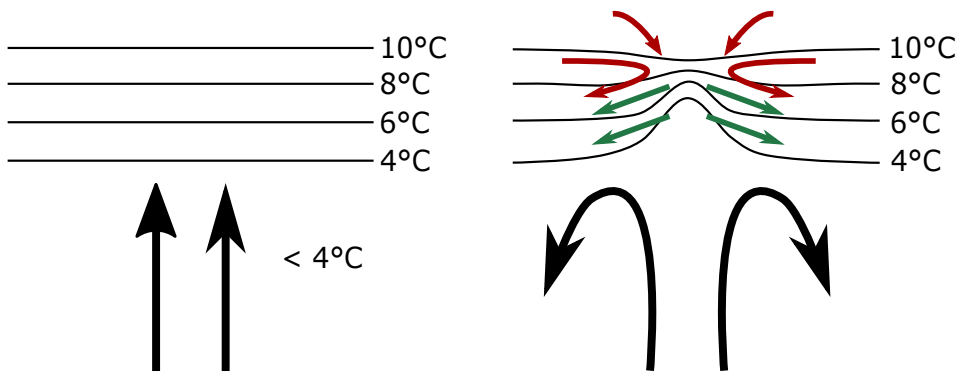

Figure 4.12: Sketch of the thermal coupling between the convective and buffer layers. On the left, a cold plume moves upwards towards the interface between the two layers. On the right, isotherms are deflected due to the impact.

This mechanism works when the velocity perturbation of the plume at the interface dissipates more rapidly than the thermal perturbation, hence for a Prandtl number $Pr \geqslant 1$. One might expect the shearing zone to decrease in size and amplitude when thermal diffusion increases (i.e. when the Prandtl number decreases), since the overshooting rising cold plume will then equilibrate thermally during its ascent more rapidly. This may explain why no interfacial shear was reported in the systematic numerical study of [Couston et al., 2017, Couston et al., 2018a] where $Pr \leqslant 1$. Global temperature field measurements (using e.g. Temperature Dependent, Laser Induced Fluorescence) are now required to confirm

or infirm the proposed model, but those are beyond the scope of the present study. Note that by extension, we call "buffer layer" in the following the region including the $T = 4$ °C to $T = 8$ °C overshooting region and the shear region. In the experiment, the shear region extends from $z = 120$ mm to $z \approx 135$ mm.

Internal gravity waves

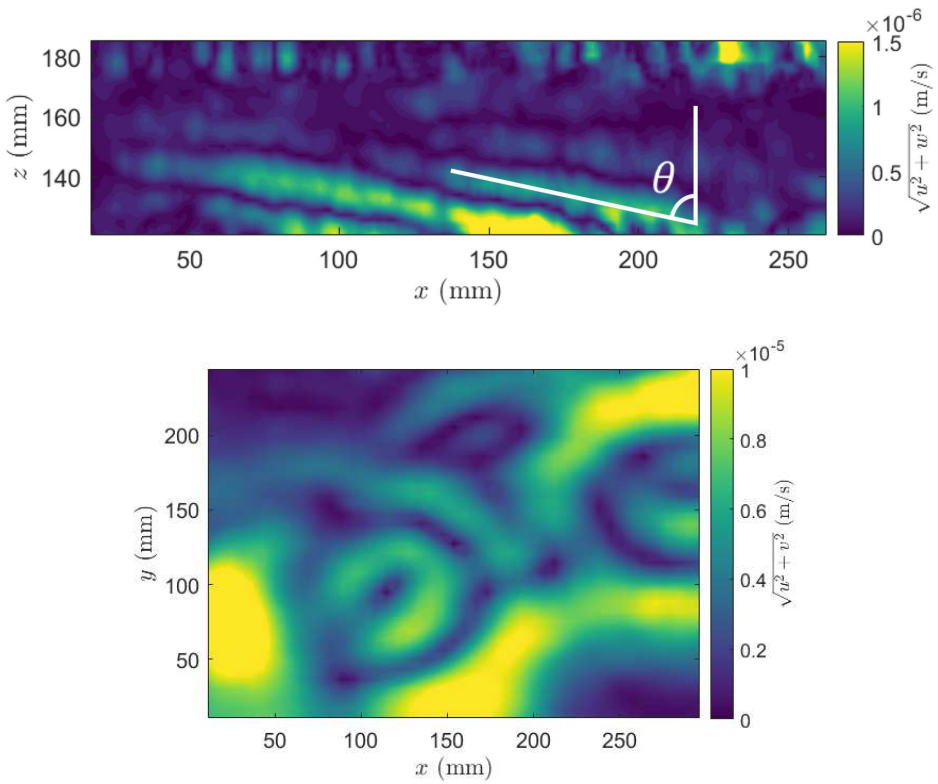

Figure 4.13: Velocity fields showing IGWs propagating. (Top) Velocities in (x, z) plane. The signal is frequency-filtered to enhance the visualisation of oscillatory motions: only frequencies between 0.02 and 0.03 Hz are shown, propagating at an angle of roughly 75 ° with the vertical. The angle of propagation is the angle between the constant phase line and the vertical. (Bottom) Velocities in (x, y) plane located at $z \approx 125$ mm. In the (x, y) plane, IGWs take the form of oscillating rings. Note that this figure is from a previous experiment without any internal cylinder and is therefore only displayed here as an illustration of the IGWs seen from above.

The convective motions induce a Reynolds stress at and below the interface which generates IGWs propagating in the stratified area [Lecoanet et al., 2015]. An example is shown in the top panel of figure 4.13. The vector field has been frequency filtered in the band $[0.02 - 0.03]$ Hz to isolate a single propagating wave train. We can measure an angle close to $\theta \simeq 75°$ between constant phase lines and the vertical. This observation is in good agreement with the inviscid dispersion relation $\omega = \pm N \cos(\theta)$, which relates the frequency and the propagation angle of IGWs. Indeed, at $z = 120$ mm, $N \sim 0.1$ Hz, thus $\theta = \cos^{-1}\left(\frac{\omega}{N}\right) = 78.5$ °. The motion within the stratified area is a superimposition of many such IGWs oscillating at different frequencies.

To further investigate the waves signal, waves spectra are plotted in figure 4.14, showing the power spectral density of oscillatory motions within the stratified layer at every height, averaged horizontally for each height. The grey line is the theoretically computed buoyancy frequency profile. Figure 4.14 shows that energy is present in a wide frequency band, from the lowest measured frequencies to the buoyancy frequency N. Low frequency motions $f < 4 \times 10^{-3}$ Hz are very intense and propagate high in the stratified layer. Motions with frequency ranging from 4×10^{-3} Hz to N are less intense, but still propagate into the stratified layer. Motions propagating at frequencies higher than the buoyancy frequency N are greatly attenuated after a centimetre as IGWs of frequency larger than N are evanescent. The weak signal at low frequencies above $z = 180$ mm comes from the convective motions due to the non-homogeneous heating at the top. These motions are confined at the very top of the experimental container.

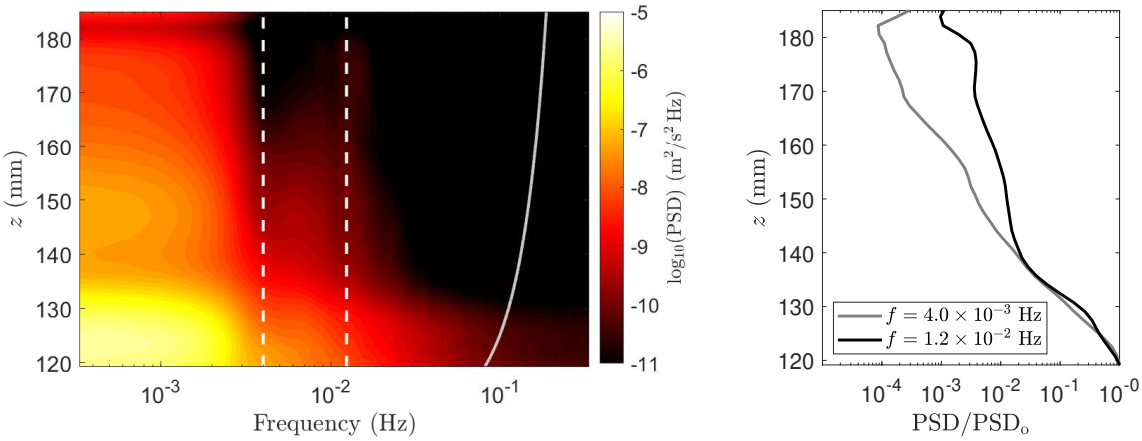

Figure 4.14: (Left) Power spectral density of the absolute velocity $\sqrt{u^2 + w^2}$ above the convective layer. The grey curve shows the theoretical buoyancy frequency profile, assuming a linear profile for the temperature, from 4 °C to 35 °C. (Right) Two selected profiles (taken at frequencies shown by dashed lines on the left graph) of the re-scaled PSDs by the PSD at the top of the convective layer, *i.e.* $z = 120$ mm (noted $\mathrm{PSD_o}$). The PIV measurements are performed for 50 minutes and results (using the pwelch Matlab function) are horizontally averaged at each height to obtain the averaged power spectral density.

Right panel of figure 4.14 shows two vertical profiles of the PSD re-scaled by the PSD at the top of the convective layer ($z = 120$ mm), taken at two different frequencies. The energy decrease is quite similar between $z = 120$ mm and $z = 140$ mm for both frequencies. However, for $z > 140$ mm, the energy for the higher frequency decreases slower than the energy for the lower frequency. This dependence of the attenuation length regarding the frequency of the signal is a characteristic of IGWs. Indeed, the dispersion relation of IGWs relates the frequency and the wave vector direction. Moreover, energy propagates perpendicularly to the wave vector for IGWs (i.e. group and phase velocities are perpendicular). The closer to N the wave frequency ω is, the more horizontal the phase propagates, hence the more vertical energy propagates. High frequency waves are thus capable of transporting energy to high altitudes before being damped. On the opposite, waves with low frequency compared to N propagate energy almost horizontally, and are

thus attenuated before reaching high altitudes. At frequencies $f < 4 \times 10^{-3}$ Hz, a lot of energy is seen and the attenuation length does not depend on the frequency. There is no reason why IGWs should disappear below a certain frequency, but we would expect to see the attenuation length to keep decreasing with decreasing frequency. We thus deduce that IGWs at frequencies $f \leqslant 4 \times 10^{-3}$ Hz are hidden in the energy spectrum by some very energetic large-scale slowly-varying flow, which we will describe below.

More than one order of magnitude separates the buoyancy frequency and the fastest large-scale flow fluctuations. The large-scale flow penetrates deep into the stratified layer. It globally decreases in amplitude with height, but with some local increases at $z \sim 125$ mm (i.e. close to the interface between convective and buffer layers) and $z \sim 145$ mm. The IGWs signal can be seen between $f = 4 \times 10^{-3}$ Hz and the buoyancy frequency. A peak that reaches the top of the stratified layer is seen around $f = 1.2 \times 10^{-2}$ Hz, *i.e.* the same frequency as the convective forcing discussed in section 4.3.1. It corresponds to the strong excitation provided by the cold rising and hot sinking turbulent plumes. However, left panel of figure 4.14 also shows a sudden drop of the energy at frequencies $f > 1.2 \times 10^{-2}$ Hz. Indeed, wave attenuation is strong at these frequencies, even if they are close to (but below) the buoyancy frequency N. Actually, energy dissipation also depends on the norm of the wave vector squared. There is no reason that all excited waves have the same wave vector norm; one could even expect that fastest waves are excited by fastest, hence smallest convective patterns, and are thus also at smallest scale: they then dissipate more rapidly.

Large-scale flow in the stratified layer

Figure 4.14 shows an important amount of energy at low frequencies which has been interpreted as the signature of a large-scale slowly-varying flow in the stratified layer. We will now investigate the nature of these fluctuations to see if they relate to reversals similar to the QBO.

Figure 4.15 shows horizontal vector fields at the same depth at different times. In figure 4.15(a), the flow goes counter-clockwise inside the cylinder. Figure 4.15(b) shows that two contra-rotating vortices with a smaller amplitude typical velocities have appeared. Figure 4.15(c) shows a mostly clockwise rotating flow, where one of the preceding eddy pairs has nearly disappeared. The large-scale flow thus evolves drastically over time. A criterion is computed to extract a typical mean velocity from those fields that accounts for the "direction" of the large-scale flow: as illustrated in figure 4.16, we compute a mean azimuthal velocity, taken along a ring centred in the cylinder. Other criteria to extract a representative value for the large scale flow direction have also been tested, including: the mean vorticity over the cylinder area, the average of the azimuthal velocity over several rings with different radii, and the azimuthal velocity averaged over thick rings. They all give similar results for the large-scale flow measurement.

In order to investigate the vertical phase propagation of the reversals, and thus, to compare the reversal dynamics observed to a QBO-like phenomenon, the setup has been equipped with a linear translating platform that allows us to perform horizontal laser sheet sweeping along the vertical. Horizontal velocities are measured in a horizontal plane, every 5 mm from the top of the convective layer $z = 110$ mm to the middle of the stratified layer $z = 160$ mm. Any trace of downward phase propagation of the reversals,

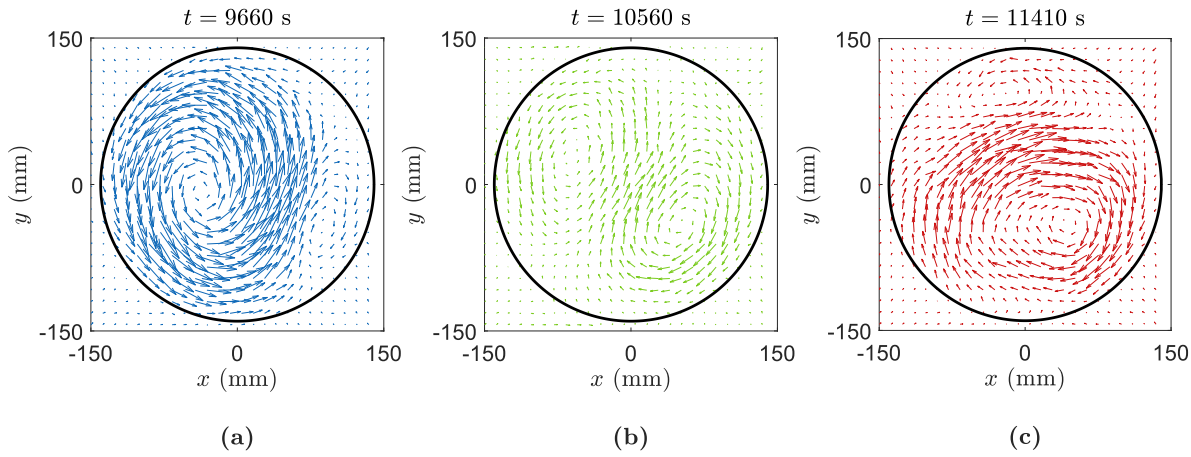

Figure 4.15: Horizontal velocity vector fields in the stratified layer at different times. The laser sheet is located at $z = 150$ mm. The large-scale flow reverses from (a) to (c). Time between (a) and (c) is approximately half an hour. Maximum velocities are 0.1 mm/s.

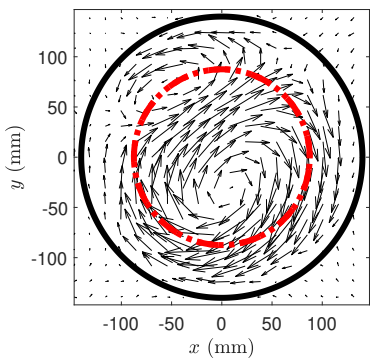

Figure 4.16: Criterion used to extract a significant value for the large scale flow and its direction: the azimuthal velocity is averaged over the ring shown in red.

as observed on the QBO on Earth [Baldwin et al., 2001] and on the historical Plumb experiment [Plumb, 1977, Semin et al., 2018], would be a significant evidence for QBO-like phenomenon in the experiment. For recall, the phase propagation of the reversals due to IGWs non-linear interactions is theorised as follows: an IGW propagating in a stratified layer with a horizontal phase velocity in the same direction as the existing base flow propagates upward until reaching a critical height z_c, where it deposits all its energy locally. At $z = z_c$, the flow accelerates. Thus the critical height where the flow is intense enough to damp the wave is lowered. As time goes on, this critical height moves towards the location where the waves are emitted. Here, the waves are emitted at the bottom of the stratified layer. We would expect a downward phase propagation if the reversals are driven by IGWs non-linear interactions.

We performed long time experiments (around 8 hours). Typical results extracted from the criterion described above are shown in figure 4.17. Blue patches (resp. red patches) represent large-scale flow going counter clockwise (resp. clockwise). The present measurements mainly confirm the interpretation of figure 4.14 for the lowest frequencies:

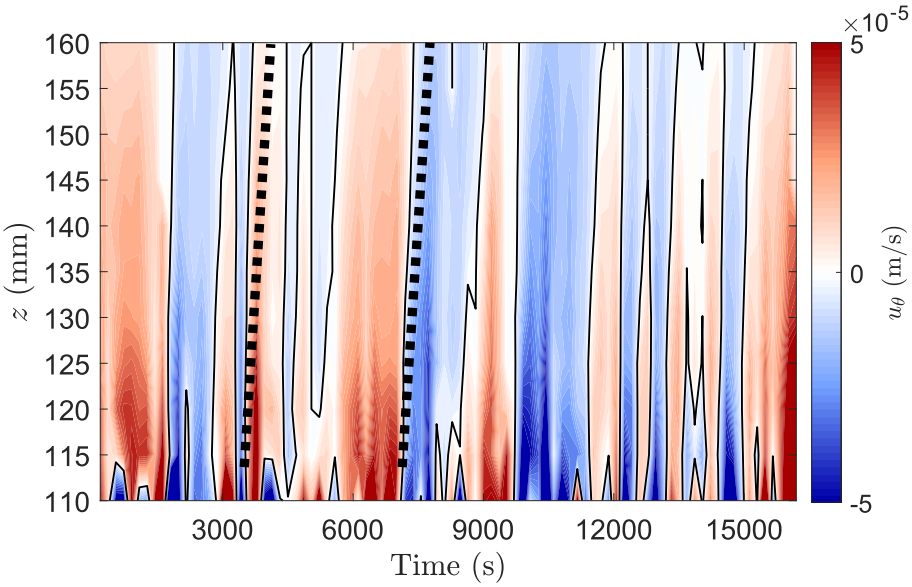

Figure 4.17: Reversals of the large-scale flow. $z = 115 - 120$ mm is the convective / buffer layers interface. Ascending plumes often perturb the buffer layer flow. The velocity was measured at 11 heights, marked by each tick in the vertical axis of the figure, and interpolated in between. The slope of the black dot lines represent the viscous coupling phase velocity.

the large-scale flow is horizontal and extends over the whole depth of the stratified layer with an amplitude attenuated with height, and exhibits slow reversals. Additionally, some intense events at $z = 110$ mm are directly related to penetrative plumes from the convection. Reversals times range from 400s to 1800s. However, no downward phase propagation of the reversals is observed. On the contrary, the reversals seem to occur along the whole stratification height at the same time, or even with a steep upward phase propagation. Since the phase propagation is not towards the location where the waves are emitted, the reversals are unlikely to be driven by the non-linear interactions of IGWs. However, as seen in the previous section, IGWs propagate in the stratified layer and carry energy. Therefore, they give energy to the large-scale flow through non-linear interactions. Yet, the process is not dominant in the reversals dynamics.
Since the reversals observed in figure 4.17 do not have a downward phase propagation, we look for other mechanisms than the QBO mechanism to explain the reversals. Two other mechanisms can be investigated. The first one relies on a specific convective dynamics within the overall stratified layer driven by horizontal gradients related to imperfect top and side boundary conditions. The second mechanism relies on viscous coupling with the underlying convective and buffer layers.

Our fully stratified reference experiment described in section 4.2 precludes the first scenario. Indeed, setting the bottom boundary at 10 °C and the top boundary at 70 °C, no motion is observed for the bottom 3/4 of the tank. In this test-experiment, the top 1/4 of the tank is animated by convective motions due to the non-homogeneous top heat source (in the standard 4 °C experiment, where $T_{top} = 35$ °C, only ~ 2 cm are affected by the convection at the top of the tank, because the non-homogeneity of the heat source is less important for lower temperature, thus the horizontal convection is weaker). However,

these are inefficient to generate waves below and to drive any large-scale flow observable away from the top region.

This leaves viscous entrainment as a possible driving mechanism. The dotted lines on figure 4.17 show a theoretical viscous time, computed from the time for viscous entrainment to drive 20% of the horizontal velocity at $z = 115$ mm to $z = 160$ mm, starting from a base state flow at rest. The 20% value corresponds to the measured value of the large scale flow at $z = 160$ mm compared to the value at $z = 115$ mm (noted u_b). The theoretical viscous entrainment time is given by $t = \frac{z^2}{4\,\nu\,\mathrm{erf}^{-2}\left(\left(\frac{u}{u_b}-1\right)\right)}$. The reversals occur in a time scale comparable with this theoretical viscous time. The similarity between the slope of the dashed lines and the slope of the upward phases suggests that reversals are driven viscously.

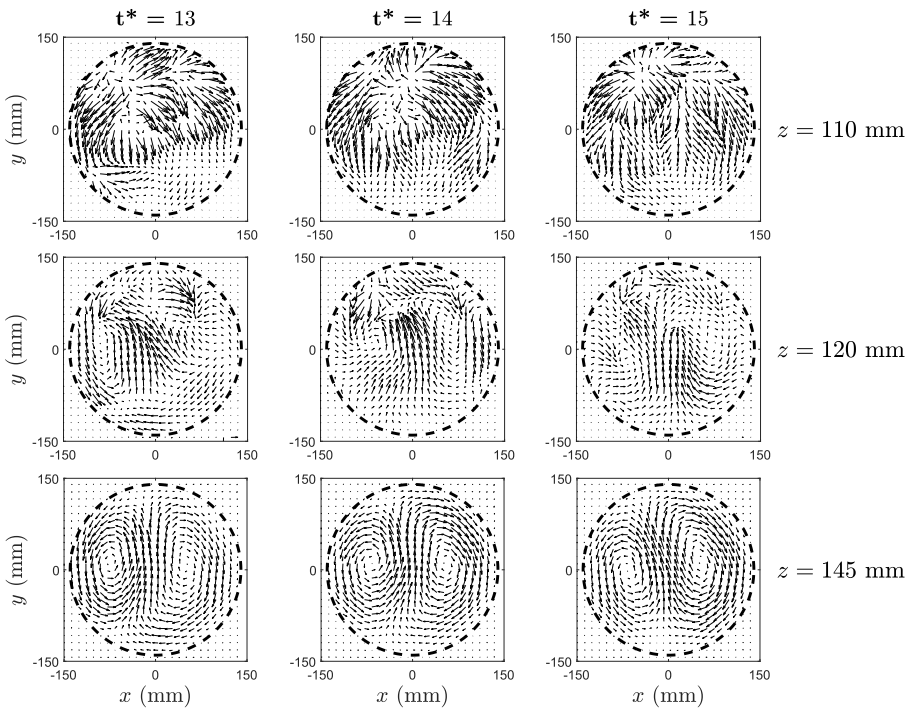

Figure 4.18: Velocity vector fields in the horizontal plane. Different columns represent different sweeping cycles t^* (one sweeping cycle corresponds to the 11 steps needed to go from the lowest position $z = 110$ mm to the highest position $z = 160$ mm). Different rows represent different heights within the same sweeping cycle: first row is the top of the convection $z = 110$ mm, second row is in the buffer layer $z = 120$ mm and third row is in the stratified layer $z = 145$ mm. Convective plumes are easily noticeable on the first row fields.

However, the existence of the buffer layer and its associated intense shear, with opposite horizontal velocities compared to the convective layer below (see figure 4.11) precludes direct viscous coupling between the convective and stratified layers. Besides, no reversal has been observed in the convective region. We thus propose a thermal coupling between the convective and buffer layers, associated with a viscous coupling between the buffer and stratified ones. To further quantify this possibility, figures 4.18 and 4.19 show horizontal

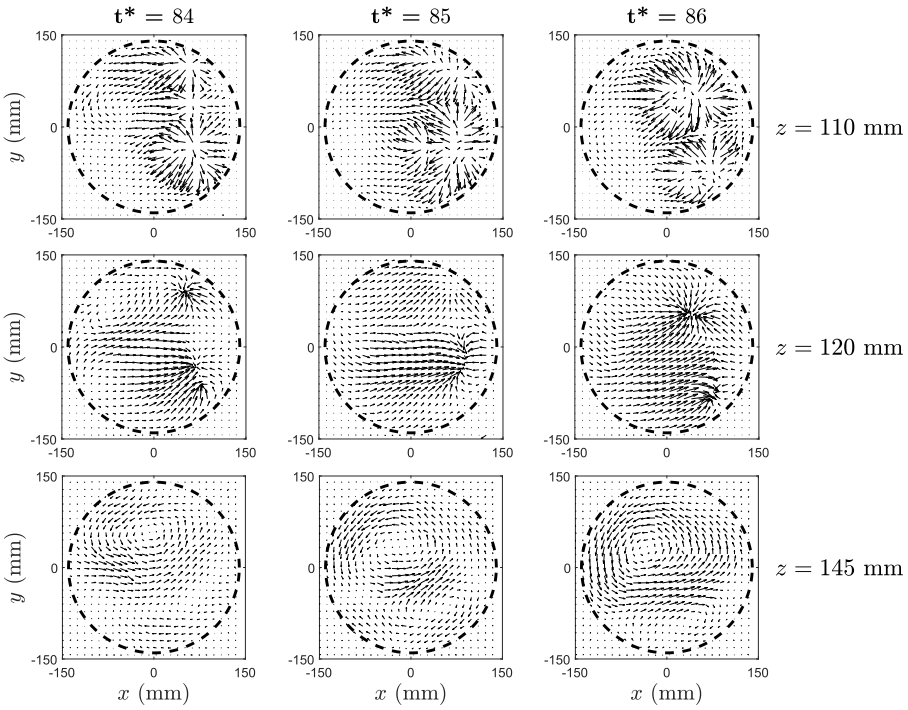

Figure 4.19: Same as figure 4.18 but for different sweeping cycles. Note that in this set of velocity fields, the buffer and stratified layers are less correlated than they are in figure 4.18.

velocity fields at different heights and at different times. For each of the columns shown, first row is the mean flow in the convective layer at depth $z = 110$ mm, second row is the mean flow in the buffer layer at depth $z = 120$ mm and third row is the mean flow in the stratified layer at depth $z = 145$ mm. The correlation coefficients through time between (i) the convective and buffer layers, (ii) the buffer and stratified layers, and (iii) the convective and stratified layers have been computed. It consists in a scalar product of the velocity vector for each position at two different heights rescaled by the product of the norm of the velocity vector at the two heights, *i.e.*:

$$R_{ij} = R(x_i, y_j) = \frac{u(x_i, y_j, z_1) \times u(x_i, y_j, z_2) + v(x_i, y_j, z_1) \times v(x_i, y_j, z_2)}{\left(u(x_i, y_j, z_1)^2 + v(x_i, y_j, z_1)^2\right)^{1/2} \times \left(u(x_i, y_j, z_2)^2 + v(x_i, y_j, z_2)^2\right)^{1/2}}$$

This gives a correlation coefficient R_{ij} for each PIV position in the horizontal plane. The global correlation coefficient R is computed by spatially averaging the local correlation coefficients.

Results are shown in figure 4.20. The convective and buffer layers are negatively correlated: the correlation coefficient is most of the time close to $R = -0.5$. This can also be seen at all times in figures 4.18 and 4.19, where horizontal velocities in the convective and buffer layers have opposite direction. A diverging flow coming from an impinging plume in the convective zone corresponds to a converging flow in the buffer layer towards the impact zone, hence confirming the thermal coupling mechanism described in section 4.3.1. This converging flow may lead either to a clockwise or anticlockwise azimuthal

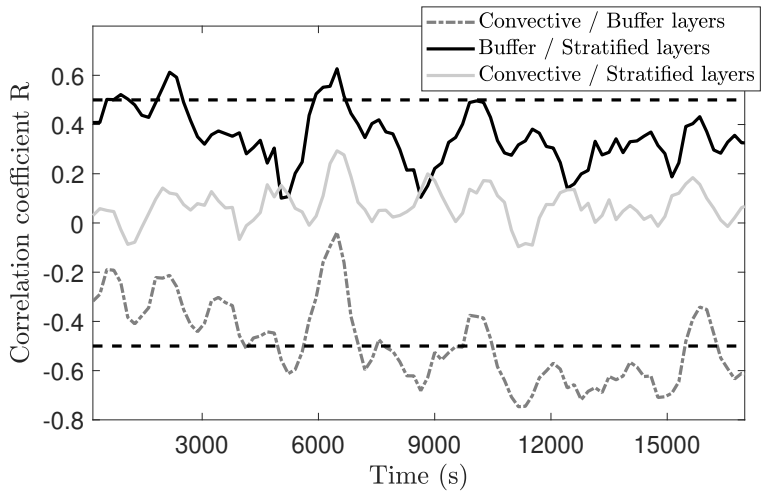

Figure 4.20: Velocity correlation between the three layers. Dashed black lines are the -0.5 and 0.5 values. Correlation coefficient are window-averaged over 10 min to smooth the curve.

mean flow, depending on the details of the chaotic excitation from the convective plumes. The correlation coefficient between the convective and stratified layers can be positive or negative, and is anyway most of the time less than 0.2, in absolute value. The correlation coefficient between the buffer and stratified layers shows a lot of temporal variations. However, it remains always positive. At a given time, the large-scale flow in the stratified layer may switch between a regime strongly dominated by the buffer layer (see also figure 4.18), and a second regime where the flow in the stratified layer is quite different from the flow in the buffer layer (see also figure 4.19).

We thus conclude that the stratified layer is globally viscously driven by the buffer layer. However, the stratified layer exhibits additional complexities. These might be due to IGWs interacting with the large-scale flow. The results from Couston et al. [Couston et al., 2018a] show that the lower the Prandtl number, the more regular the QBO. In the experiment, the Prandtl number is close to $Pr = 7$: the typical associated QBO-type flow is irregular, with low amplitude. We thus propose that large-scale flow driven by IGWs non-linear interactions superimposes on the viscously driven flow, but remains secondary. We do not know at this point how to disentangle those two potential contributions from the available data.

4.3.2 Numerical results

The experimental results are not fully sufficient to explain, with complete certainty, the origin of the buffer layer and of the large-scale flow observed in the stratified layer. In addition, the effects of the lateral heat losses and top temperature heterogeneity are difficult to distinguish. To answer these questions, 3D DNS of a configuration similar to our experiments are performed, reproducing the 4 °C convection but with idealised boundary conditions (i.e. no flux on the sides, and fixed temperature at the top and bottom). As mentioned in section 4.2.2, the Rayleigh number Ra and T_{top} are tuned so that the interface depth in the experiment and the numerical simulation are similar. We

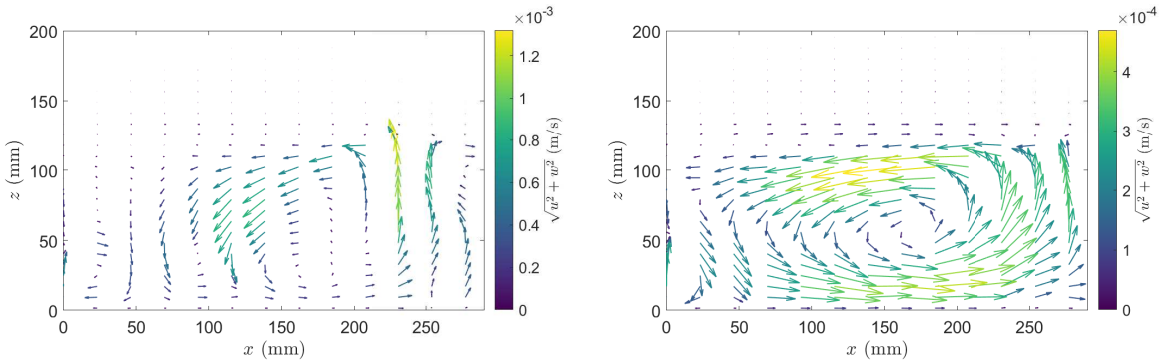

(a) (b)

Figure 4.21: (a) Instantaneous velocity field. An ascending plume is visible at $x = 230$ mm. (b) Large-scale circulation in the convective layer obtained by time-averaging velocities over a 50 minutes recording. The large-scale circulation is a counter clockwise cell. Maximum instantaneous velocities are 3 times bigger than the maximum averaged velocities.

have $Ra = 10^7$ and $T_{top} = 48$ °C. All the numerical simulations are run dimensionless, but results are shown in dimensional values. The length scale is $H = 200$ mm, the vertical extent of the whole domain (hence diameter is $D = 300$ mm), the timescale is the thermal diffusive time $\tau = \dfrac{H^2}{\kappa} = \frac{0.2^2}{1.5\,10^{-7}} = 2.67 \times 10^5$ s, and the temperature is given by the dimensionless temperature $\theta = \dfrac{T - T_i}{T_0 - T_i}$, where T, T_i, T_0 are respectively the dimensional temperature, the inversion temperature of the equation of state (i.e. 4 °C), and the bottom temperature (i.e. 0 °C). Results for convection and wave analysis are computed from a (x, z) vertical plane located along a cylinder diameter. Results for the mean-flow study are computed from (x, y) horizontal planes taken at each height.

Large-scale circulation in the convection zone and buffer layer

Figure 4.21 shows that a large-scale circulation takes place in the convective layer. It consists of a cell filling the whole convective layer, and exhibits no reversal over the whole course of the simulation. The fluid rotates counter clockwise in the vertical plane. This is qualitatively consistent with the mean flow observed in the experiment and shown in the right panel of figure 4.7. As in the experiments, a counter current exists on the top of the convective layer at $z = 120$ mm, creating a strong shear and demonstrating the existence of a buffer layer in the numerical simulation as well.

The space-time diagram of the mean horizontal flow shown in figure 4.22 confirms it. Observing the buffer layer in the absence of side thermal losses and top temperature heterogeneity is an additional argument accounting for the fact that it is not an artefact driven by imperfect experimental conditions. We also observe that the flow within the convection stays positive through time at the bottom and negative at the top. This is evidence of the steady large scale circulation taking place in the convective layer. Some events appear at $t > 1.42 \times 10^5$ s and are interpreted as quasi-reversal of the large-scale circulation.

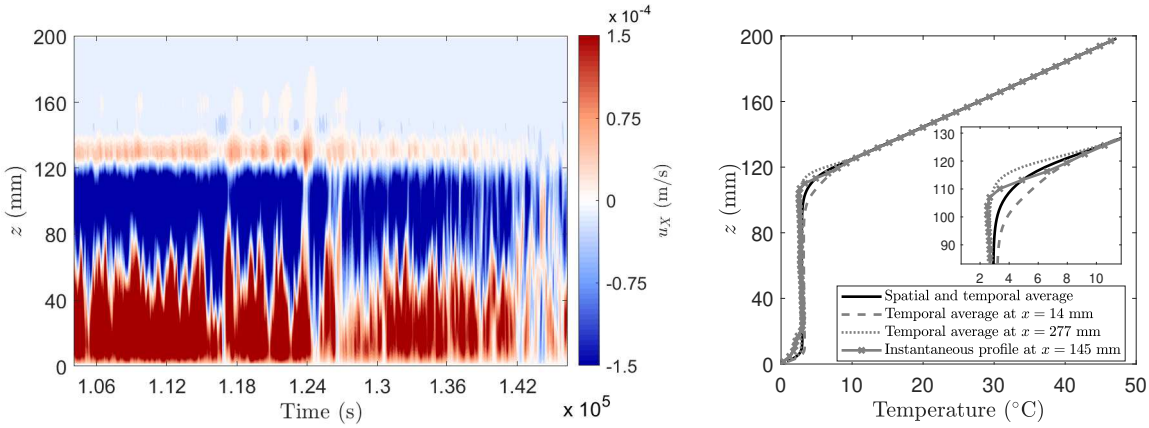

Figure 4.22: (Left) Horizontal average of the horizontal velocity u over a vertical cross-section in the middle of the tank. The buffer layer can be seen above $z = 120$ mm. A stationary large-scale circulation is present in the convective layer, even if it appears quite perturbed at the end of the signal. (Right) Temperature profiles along the z-axis.

The temperature profile along the z axis is also plotted on the right panel of figure 4.22. The figure shows a temporal and horizontal average of the temperature field (black thick curve), two temporal averages at two different positions $x = 14$ mm (left side of the tank - dashed grey) and $x = 277$ mm (right side - dotted grey) and an instantaneous profile at $x = 145$ mm (middle of the tank - thick grey with crosses). The thermal boundary layer can be seen, between $z = 0$ mm and $z = 10$ mm. Then, between $z = 10$ mm and $z = 100$ mm lies a layer of constant temperature $T \sim 2.8$ °C. Between 100 mm $\leqslant z \leqslant$ 115 mm, the temperature profile evolves from constant to linear for $z > 115$ mm. The $T = 4$ °C (respectively $T = 8$ °C) isotherm is located at $z = 110$ mm (resp. $z = 120$ mm). Note that the temporal average of the temperature profiles are different on the left and right sides of the tank. Indeed, the constant temperature height goes to $z = 90$ mm for the left side whereas it goes to $z = 115$ mm for the right side. This suggests that the convective / buffer layer interface does not lies at one height over the whole tank but is a function of time and space. This is very likely due to the large-scale circulation. Thus, the thermal coupling described in 4.3.1 will likely occur at different heights, depending on time and horizontal position.

The thermal coupling as schematised in figure 4.12 can be found in the numerical simulation. This is represented in figure 4.23. An upward plume impacting the convective / buffer layer interface is seen. The isotherms ranging from $T = 4$ °C to $T = 11$ °C are deflected upward, due to the plume bringing cold fluid upward. On the contrary, the isotherms $T = 12 - 14$ °C are deflected downward by the converging flow. Isotherms at $T \geqslant 15$ °C remain horizontal. After the impact on the interface, the plume is deflected outwards. One could expect the fluid above the impact to be viscously entrained by this outward deflection. However, as observed in figure 4.23 for the simulation and figures 4.18-4.19 for the experiment, the fluid above the interface is going towards the plume, *i.e.* in the opposite direction of the fluid below, hence explaining the observed shear (see figure 4.12). The time evolution of these dynamics is shown in figure 4.24.

Figure 4.24 shows the time evolution of the horizontal velocity u in the shear layer at $z = 128$ mm and the time evolution of the vertical velocity w in the convective layer

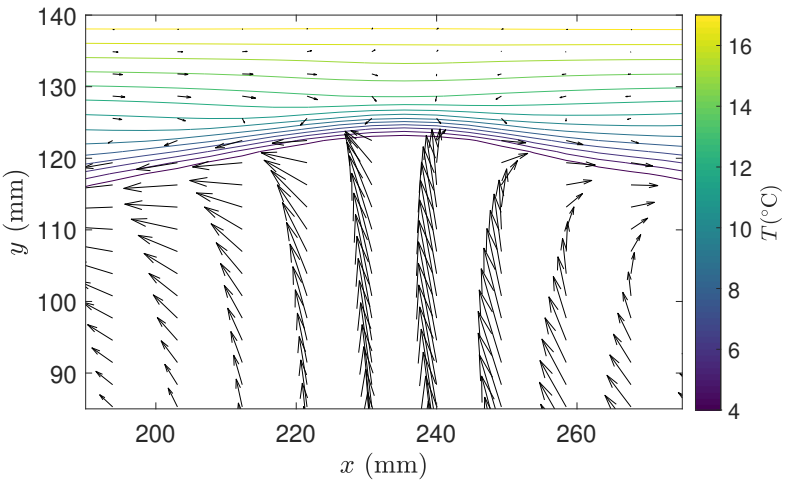

Figure 4.23: Velocity field and temperature isotherms at the end of an upward plume impact on the interface.

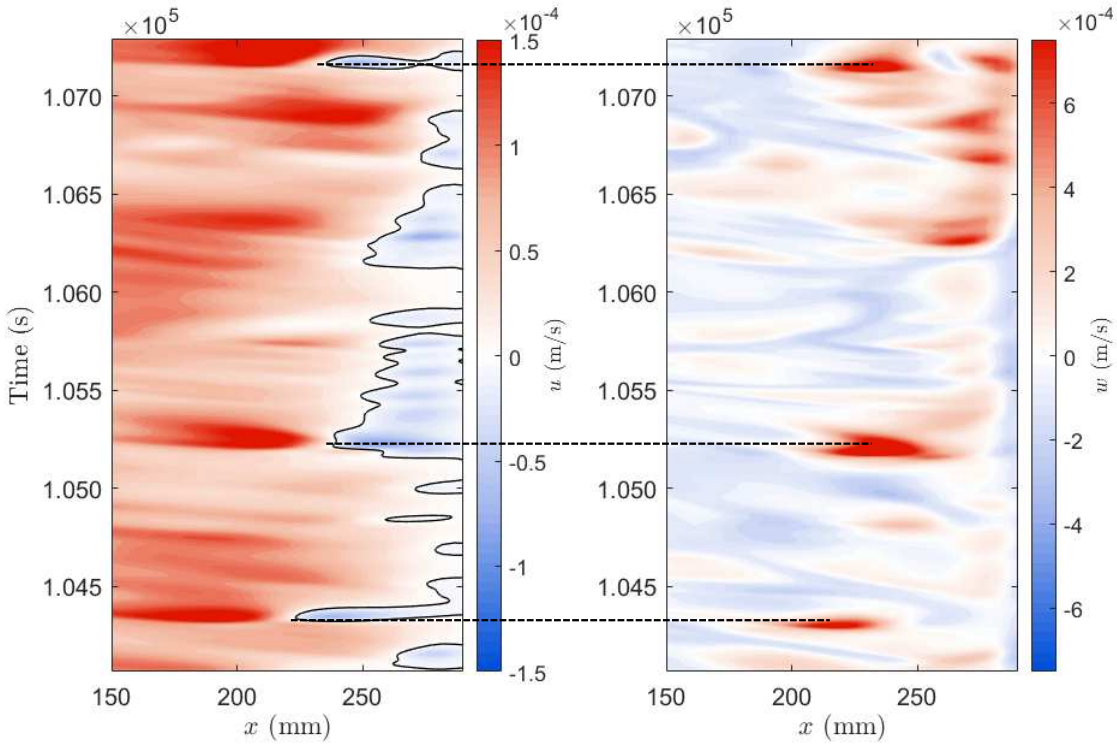

Figure 4.24: (Left) Spatio-temporal diagram of the horizontal velocity u at $z = 128$ mm. (Right) Spatio-temporal diagram of the vertical velocity w at $z = 108$ mm. The event at $t \approx 1.052 \times 10^5$ s is shown in figure 4.23.

at $z = 108$ mm. Comparing the two panels of figure 4.24 shows that upward plumes are concomitant with converging horizontal velocities towards the plume impact. Indeed, the spatio-temporal diagram of w exhibits local strong upward plumes. These plumes, as suggested by the dashed black lines, are correlated in time and space with converging

horizontal velocities. For instance, an upward plume is seen at $x \approx 220$ mm and $t \approx 1.043 \times 10^5$ s. At the same horizontal position and time, the positive horizontal velocity becomes stronger and the negative horizontal velocity patch increases in size to reach $x \approx 220$ mm. The converging horizontal velocities event occurs a short time after the impact of the plumes. Thus, it can be concluded that the plume induces the converging flow, as suggested by our explanation in section 4.3.1.

Internal gravity waves

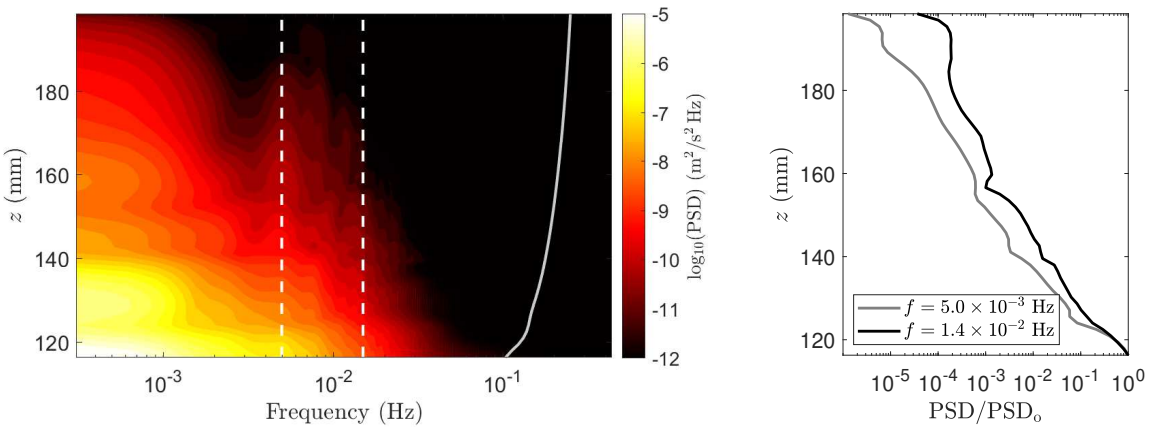

Figure 4.25: (Left) Power spectral density of the absolute velocity $\sqrt{u^2 + w^2}$ in the buffer and stratified layers. The grey curve shows the buoyancy frequency profile computed from the spatial and temporal average of the temperature field. (Right) Two selected profiles (taken at frequencies shown by dashed lines on the left graph) of the re-scaled PSDs by the PSD at the top of the convective layer, *i.e.* $z = 118$ mm.

PSDs are computed in the stratified and buffer layers and are plotted in figure 4.25. As for the experiment (figure 4.14), numerical results show oscillatory motions at different frequencies attenuated with height. Experimental results (figure 4.14) and numerical results (figure 4.25) show strongly similar dynamics: most of the energy is present at low frequencies ($f < 3 \times 10^{-3}$ Hz). The motion with frequencies ranging from 3×10^{-3} Hz to N are less intense, and almost no energy is seen at frequencies $f > N$.

Right panel of figure 4.25 shows two selected vertical profiles (shown by the white dashed line on the left panel figure) of the the PSD re-scaled by the PSD at $z = 118$ mm. The energy for the higher frequency ($f = 1.4 \times 10^{-2}$ Hz) decreases slower than the energy for the lower frequency ($f = 5.0 \times 10^{-3}$ Hz). This is, like experimental results, in agreement with the dispersion relation of IGWs. The overall behaviour of waves spectra is similar in experiment and numerical simulation, with an attenuation length independent of the frequency in the low-frequency signal thus confirming a viscous coupling origin of the large-scale flow, and increasing when the frequency goes towards N in the wave domain.

Large-scale flow within the stratified layer

Similarly to what has been done for the experimental data, figure 4.26 shows the mean azimuthal velocity over the whole height of a virtual cylinder of radius $r = 140$ mm. We

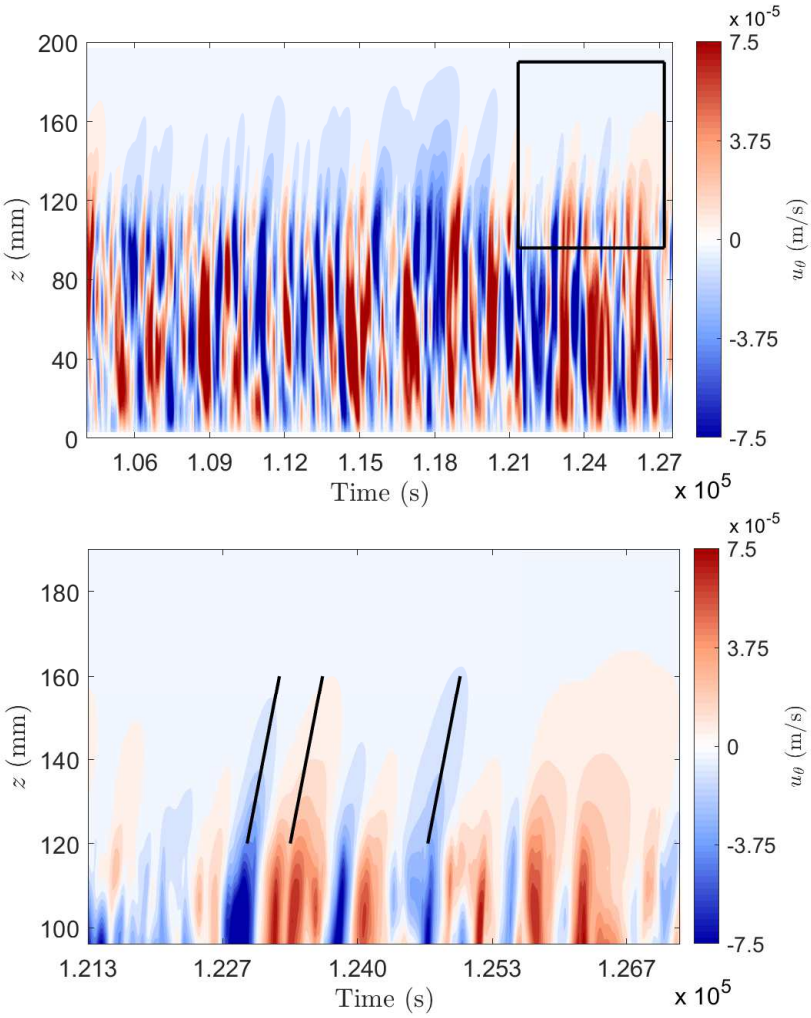

Figure 4.26: Spatio-temporal diagrams of the azimuthal averaging of the azimuthal velocity over a virtual ring of radius $r = 140$ mm. The bottom figure is a zoom on the stratified zone, delimited in the top figure by the black square. The slope of the black lines shows the theoretical viscous diffusive time.

observe reversals within the convective layer ($z < 120$ mm), which are not systematically correlated with the signal in the stratified layer. The mean velocity in the stratified layer also exhibits reversals. They are characterised by an upward phase propagation from the buffer zone at $z = 120$ mm, as shown in the zoom (bottom panel of figure 4.26). The phase velocity seen in figure 4.26 is in good agreement with the theoretical time for viscous propagation $t = \frac{z^2}{4\,\nu\,\mathrm{erf}^{-2}\left(\left(\frac{u}{u_b}-1\right)\right)}$. This corroborates the fact that the reversals observed within the stratified layer are viscously driven from the dynamics occurring in the buffer layer, as it has been seen for the experiment. Reversal time ranges from 300 s to 1500 s. Those reversal times are similar to the experimental ones, though slightly shorter (numerical reversals are $\sim 20\%$ faster than experimental reversals).

4.4 Conclusion

The 4 °C convection experiment, originally performed by [Townsend, 1964], has been re-investigated using long-term PIV measurements in a vertical cross-section, and in several horizontal cross-sections within the stratified layer. This last type of measurements has allowed to investigate the long-term horizontal mean flow in the stratified layer. Experiments have been complemented by direct numerical simulations. The first result is the confirmation, in 3D and with ideal boundary conditions, of the presence of a buffer layer, including an overshooting region as first observed by [Perrard et al., 2013], and a shear region. We have argued that the buffer layer is driven by thermal coupling with the convection, due to the non-linear equation of state of water, and that this mechanism is a priori related to a Prandtl number larger than one. The second result is that the buffer layer viscously drives slow reversals of the horizontal large-scale flow within the stratified layer.

Additionally, IGWs at different frequencies propagate in the stratified layer. They likely interact with the horizontal large-scale flow, and probably also produce a reversing flow, which superimposes to the viscously driven one. From [Couston et al., 2018a], we know that the Prandtl number has a strong influence on this QBO-like mechanism: the lower the Prandtl number, the stronger the amplitude of the QBO. In water, $Pr \sim 7$, and the expected amplitude of the large-scale QBO flow is weak, hence dominated by the viscous driving.

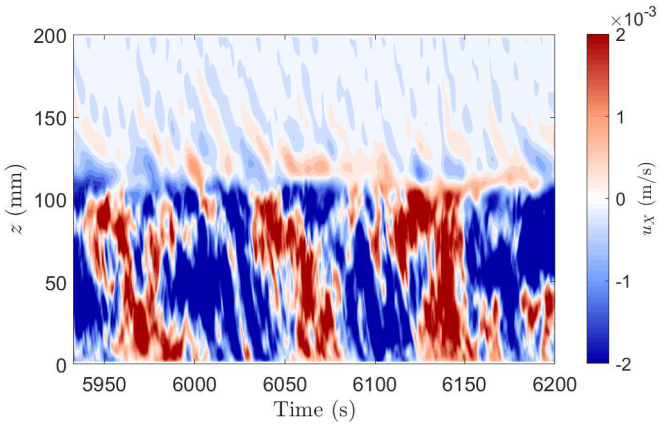

Figure 4.27: Horizontal average of the horizontal velocity u over a vertical cross section in the middle of the numerical domain for $Pr = 0.1$.

It is straightforward to change the Prandtl number in the numerical simulation of our set-up. We have thus run a second simulation with the same Rayleigh number $Ra = 10^7$ and top temperature $\theta_{top} = 11$ but with $Pr = 0.1$. In this simulation, as shown in figure 4.27, no buffer layer is observed, but signatures of a QBO like mechanism are visible, marked by downward phase propagation of the reversals of the large-scale flow. This configuration thus deserves a more systematic study in the future.

Experimentally, it is possible to work with $Pr \sim 0.7$ by using gases as working fluids. The next chapter will introduce another experiment focusing on penetrative convection in a transient state with SF_6 and air in order to work with a lower Prandtl number compared to the 4 °C convection, which would increase our chance to observe a QBO-like flow in the stratified layer.

CHAPTER 5

PENETRATIVE CONVECTION AT LOW PRANDTL NUMBER

Contents

In Nature, internal gravity waves driven flows, whether they are oscillating or not, are observed in planets' atmospheres and in stars, *i.e.* in fluids characterised by Prandtl numbers $Pr \leqslant 1$ ($Pr \sim 0.7$ for the Earth's atmosphere, $Pr \sim 10^{-8}$ in the Sun's convective zone). According to [Couston et al., 2018a], the Prandtl number has a significant impact on the oscillating mean-flow emergence, with less and less QBO-like flow signature with increasing Pr. Therefore, our experiments described in the previous chapters may not be suited to drive this kind of flows since the working fluid was water ($Pr \sim 7$ for thermal stratification and $Pr \sim 700$ for salt). In this chapter, we introduce a newly designed experiment, reproducing penetrative convection with gases as working fluids in order to reach low Prandtl numbers ($Pr \sim 0.7$). We use two gases, air and sulfur hexafluoride. Sulfur hexafluoride (SF_6) is a non-toxic gas generally used for its excellent electrical insulator properties. Its density is approximately six times larger than the density of air

($\rho_{SF_6} = 6.04$ kg $\cdot$ m^{-3} and $\rho_{air} = 1.18$ kg $\cdot$ m^{-3} at $T = 298$ K and $P = 1013$ hPa). To experimentally study penetrative convection, SF_6, because of its large density, is used in the bottom, convective layer, and air is located above. A stratification in chemical composition then rapidly forms because of the diffusion of the two gases. However, the visualisation of the flow in air and SF_6 is quite challenging. The PIV technique, which works excellently in liquids, is less suited for measurements in gases when velocities involved are small because common tracer particles have a relatively large sedimentation speed. Moreover, since we work with two different gases, double-diffusive instabilities can take place during the experiment, with the combined effects of chemical and temperature diffusions. Yet, these instabilities are relevant for massive star or planetary interior dynamics, where semi-convection participates in the global dynamics [Merryfield, 1995, Kellogg, 1991]. This chapter will focus on the astrophysics problematic developed in 5.1. Section 5.2 will detail the experimental set-up, the measurement techniques tested so far, and will give ideas for others experimental measurements that could be of interest. Finally, section 5.3 will present the analysis of one preliminary experimental movie, visualising the convective and stratified layers.

The experiment presented here is a new set-up, born out of a collaboration between M. Rieutord and IRPHE, and has been built during the last year of my PhD. The density measurement could not be performed so far because the pressure sensors are not installed in the tank yet. Measuring velocities in gases is quite a challenge and preliminary tests were required to come up with a relevant visualisation technique. What is introduced in the following is the promising start of the project.

5.1 Astrophysical context

Penetrative convection deeply affects star evolution by locally mixing chemical species and, as seen earlier in the manuscript, generating internal gravity waves in the radiative zone. The overshooting region can also contain double-diffusive phenomena since gradients of temperature and chemical composition are locally mixed. Hence, the dynamics operating in the small region contained between the two layers are essential. This section will present the problematic of penetrative convection in the astrophysical context and introduce the basic concepts of double-diffusive convection.

5.1.1 Importance of penetrative convection in stellar models

The time evolution of stars in only known through models. Some of them study the global dynamics of the star, and others focus on a specific phenomenon and look at smaller scales. The same is true for time-scales, with models investigating dynamic scales (*e.g.* convective turnover time) and other investigating the long-time evolution of stars.

The current models studying the long-time dynamics have difficulties to properly reproduce turbulent flows. This relatively imprecise implementation of those flows may explain that the recent observations of chemical abundance or differential rotation speeds are not well represented in models. Figure 5.1 shows the time evolution of a star in the Hertzsprung-Russell diagram computed from different numerical models. One sees that the models all predict different evolutions for the star's life.

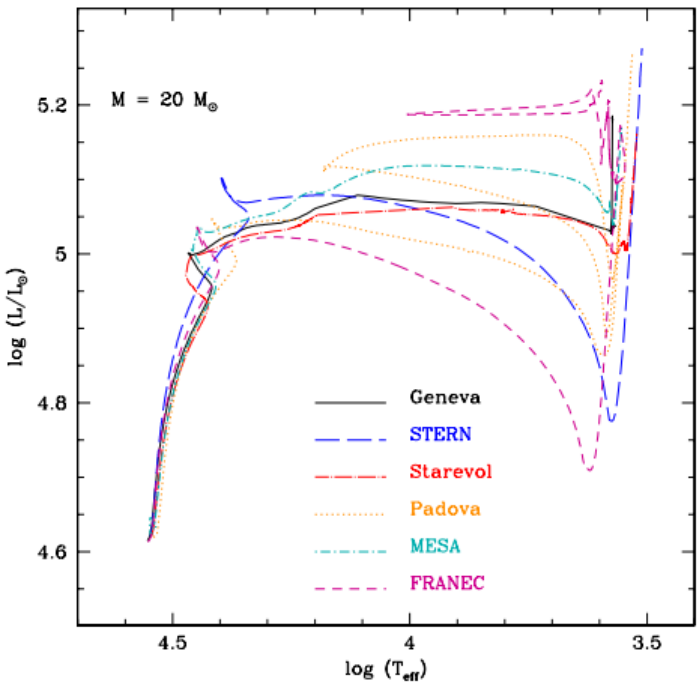

Figure 5.1: Evolutionary tracks for a $M = 20M_\odot$ with $M_\odot$ being the Sun mass. The evolutionary track follows the evolution of the luminosity L as a function of temperature (linked to the color of the star) T_{eff}. This kind of diagram, named Hertzspreung-Russel diagram, is used to represent the broad population of stars. Note that the temperature is represented on the x axis with decreasing values from left to right. Reproduced from [Martins and Palacios, 2013].

The particular case of overshooting / penetrative convection [1] is poorly modelled. That is a major issue due to the impact this phenomenon has on star dynamics. Penetrative convection is invoked to explain the mixing taking place at the border of the convective layer. For example, in massive stars in which nuclear burning occurs in the convection zone (located at the core), overshoots can bring nuclear fuel from the radiative layer back into the convective layer and feed the burning. This extends the lifetime of main-sequence stars [Maeder, 1975, Rosenfield et al., 2017]. For the Sun, overshooting can explain the transport of lithium out of the convection zone into the core [Andrássy and Spruit, 2013, Baraffe et al., 2017]. The overshooting zone may also be of importance for the solar dynamo [Parker, 1975, Nordlund et al., 1992].

So far, the key process that drives mixing during an overshoot is not well understood and therefore, the parametrisation of the phenomenon within models is not appropriate. Different studies using global models [Briquet et al., 2007, Lovekin and Goupil, 2010, Guenther et al., 2014] have tried to predict the depth and position of the overshoot region but

[1] The terms penetrative convection and overshooting are quite often interchanged. Penetrative convection is used when local mixing is produced by the intrusion of convective plumes within the stratified layer. Overshooting denotes the intrusion of plumes, but without any information on the entrainment involved. Since the density profiles before and after the intrusion are rarely known, both terms are used to name the intrusion of plumes into the stratified layer, without any quantitative implications on the mixing.

gives contradictory predictions. Others [Hurlburt et al., 1994, Brummell et al., 2002] have focused on the basis of the problem and studied only the penetrative convection phenomena. But these simulations are far from the parameter values expected for stars and only give hints on the dynamics involved. Besides, their numerical cost limits the investigation to a small parameter range and a model could not be constructed from the numerical results. Recent LES [Kitiashvili et al., 2016, Pratt et al., 2017] suffer the same limited parameter range issue.

Moreover, internal gravity waves are generated at the interface between the convective and stratified zones, *i.e.* in the overshooting region. A correct implementation of internal gravity waves in numerical model is crucial since they transport angular momentum [Press, 1981, Schatzman, 1993, Zahn et al., 1996, Aerts et al., 2019]. Internal gravity waves are also invoked in the lithium transport and chemical mixing problematics [Charbonnel, 2005, Rogers and McElwaine, 2017], can explain the differential rotation of the layers [Rogers et al., 2012] and influence the time-variations of the tachocline in the Sun (the Shear Layer Oscillation) [Kim and MacGregor, 2001, Talon et al., 2002, Talon and Charbonnel, 2005].

The overshooting region is strongly mixed by penetrating plumes, wave generation and a potential shear layer. The temperature and chemical composition gradients are affected by the mixing involved and locally, double-diffusive processes can appear.

5.1.2 Double-diffusive convection

A particular case of convection can occur when both thermal and compositional effects can drive buoyancy forces. It is called thermochemical or double-diffusive convection [Turner, 1974, Huppert and Turner, 1981] and has been vastly investigated, especially due to its importance in ocean dynamics (where salt and temperature gradients can drive thermohaline convection). It is also of interest in star and planet' interiors where a chemical composition gradient cohabits with a temperature gradient. In the experiment that will be described in section 5.2, we study penetrative convection with two gases (SF_6 and air) as working fluids and double-diffusive convection can take place.

Unlike Rayleigh-Bénard convection in which diffusivities have a stabilising effect, double-diffusive convection is driven by diffusive processes. The key mechanisms of double-diffusive convection is the time-scale difference between the molecular diffusion rate of the temperature and compositional fields. Their ratio is called the Lewis number:

$$Le = \frac{\kappa}{D} \tag{5.1}$$

with κ and D the thermal and compositional diffusivities. The Lewis number is estimated close to 100 for oceans [Stern, 1960] and giant planets [Stevenson and Salpeter, 1977] and reach 1000 for metallic planetary cores [Braginsky and Roberts, 1995]. In our experiment, the Lewis numbers are much smaller: 2.22 for the air and 0.33 for the SF_6 ($\kappa_{\text{air}} = 2.2 \times 10^{-5}$ m$^2 \cdot$ s^{-1}, $\kappa_{SF_6} = 3.3 \times 10^{-6}$ m$^2 \cdot$ s^{-1} and $D = 10^{-5}$ m$^2 \cdot$ s^{-1})

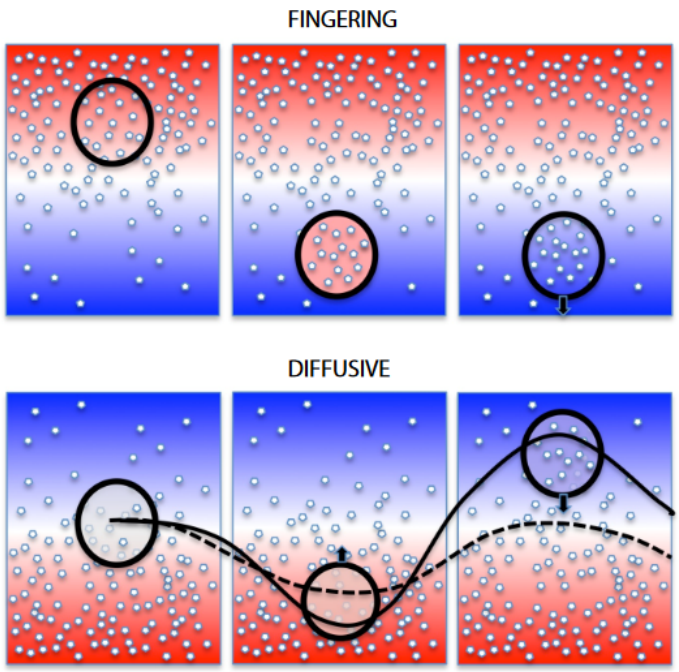

Figure 5.2: Schematics illustrating the double-diffusive convection mechanisms, with fingering convection (top) and oscillatory diffusive convection (bottom). Reproduced from [Garaud, 2013].

Double-diffusive convection occurs when the global contribution of the two fields gives a stably-stratified density profile, but one of the two fields has a destabilising effect. In this case, and due to the different rates for the diffusivites, vertical motions can develop. Two different mechanisms are identified, depending on whether the slow diffuser has a stabilising or destabilising effect. They will be described in a heat/salt system in the following.

Fingering convection

When the slow diffuser (salt) is unstable, fingering convection appears (see top panel of figure 5.2). When a parcel of hot and salty fluid is displaced downward by a perturbation, it becomes surrounded by cold fresh fluid. Because thermal diffusion operates faster than salt diffusion, the parcel equilibrates thermally with its surrounding and loses heat, whereas it retains its salinity. The parcel is thus denser than the surrounding fluid and sinks deeper in the tank. The same reasoning applies for a initially cold and light parcel of fluid displaced upward. Therefore, initially small perturbations are amplified by the destabilising effect of thermal diffusivity and give rise to ascending or descending fluid called fingers because of their narrow horizontal scale.

Oscillatory diffusive convection

When the slow diffuser is stabilising, oscillatory diffusive convection occurs (see bottom panel of figure 5.2). When a fresh and cold parcel of fluid is displaced downwards, it retains salinity and equilibrates thermally. Since the salinity background is here stable,

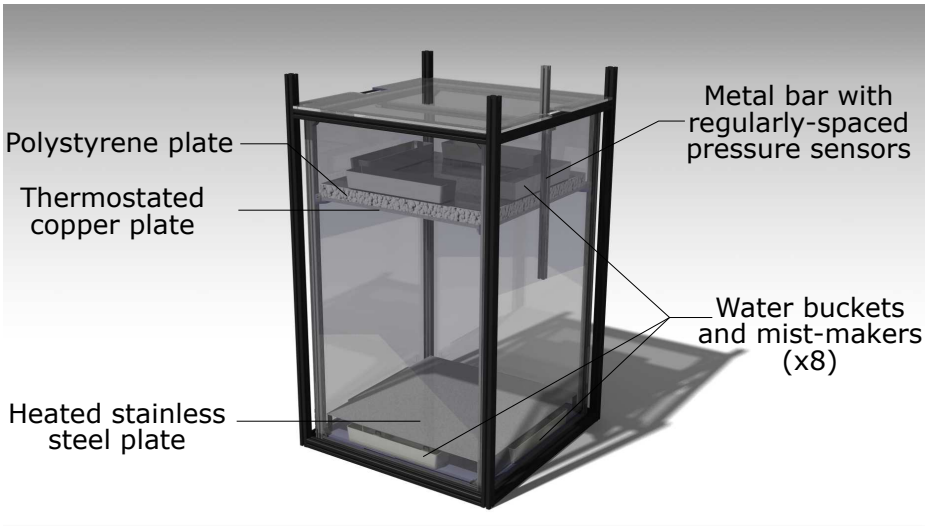

Figure 5.3: 3D sketch of the set-up. The heating plate is located at the bottom with the nine heating plates being stuck under. At the top, the cooling plate is thermally isolated from the exterior with polystyrene plate. Below the heating plate and above the cooling plate are placed water buckets containing the mist-makers.

the parcel becomes lighter than the ambient fluid and thus experiences an upward acceleration. When it comes back to its original position, the parcel is still lighter than the ambient fluid, because of the heat gained. It then overshoots to reach a higher equilibrium position, where the parcel loses heat with the ambient fluid, hence becoming denser and experiencing a downward acceleration. This oscillatory process repeats over and over. In astrophysics, oscillatory diffusive convection is called semi-convection.

In the overshooting region occur several fast events which have a deep influence on star evolution. Mixing is induced by penetrative convection and can transport fuel for the nuclear reaction. Internal gravity waves are generated and affect global dynamics at large time- and length-scales. It is crucial that the local and short-time scale dynamics of the penetrative convection are well captured in order to refine the numerical models. The next section will introduce our newly designed experiment to investigate penetrative convection in gases. Working with gases instead of water has the advantage to lower the Prandtl number by one order of magnitude compared to water and reach a Prandtl number $Pr \sim 0.7$, which is a relevant value for atmospheric and astrophysical applications and allows to experimentally reach $Pr < 1$.

5.2 Experimental set-up

The tank is rectangular with dimensions $85 \times 85 \times 150$ cm^3. At the bottom of the tank is placed a stainless steel plate with dimensions 75×75 cm^2 and thickness $e = 2$ mm. Below this plate are attached 9 heating silicone patches with dimension 25×25 cm^2, presented in figure 5.4. The patch temperatures are controlled with two power supplies through a feedback loop: a thermocouple measures the temperature at the patch location and adjusts the input power into the patch. The central patch is individually controlled, the

Figure 5.4: Photography of the heating silicone plates attached to the bottom of the stainless steel plate. The central plate is linked to a power supply and the 8 others to another power supply, in order to control the central plate individually.

others are powered by one single supply and are thus grouped together. At 110 cm above the heating plate stands a copper plate, delimiting the top domain of our experiment. This copper plate is linked to a thermostated bath and we impose a temperature $T = 23$ °C, approximately the room temperature.

Below the heating plate and above the cooling plate are placed small buckets filled with distilled water. We use mist-makers, placed into these buckets in order to seed the tank with small water drops. For the mist-makers located at the top, water drops slowly fall in the tank, since they are denser than air. Two ventilators are placed below the heating plate in order to bring the mist created by the bottom mist-makers above the plate, *i.e.* in the area of interest for the experiment. A 3D drawing of the set-up is displayed in figure 5.3.

Typically, to set up an experiment, we fill approximately 20 cm of the bottom of the tank with pure SF_6. The remaining is initially pure air, but a stratified layer of air and SF_6 rapidly forms above the pure SF_6 layer. This layer is stably stratified with a stable gradient of chemical composition (heavy SF_6 below light air) and an unstable gradient of temperature (hot gas below cold gas) when the heating is turned on. The top cooling plate is set at $T = 23$ °C, the air temperature. Then we proceed to fill the tank with water drops. To seed the entire tank, we turn on the mist-makers at the top of the tank and wait for the drops to sink in the tank, so that water particles are present in the whole height. The bottom mist-makers are only used to re-seed the bottom convective layer later on, if needed. Once the tank is seeded, we turn on the heating at the bottom plate, and convection starts in the bottom layer. At the interface between the convective and stratified layers occurs a strong mixing of the two gases because of the convective motion but also by diffusion. Above the stratification, pure air is slowly convective because of a

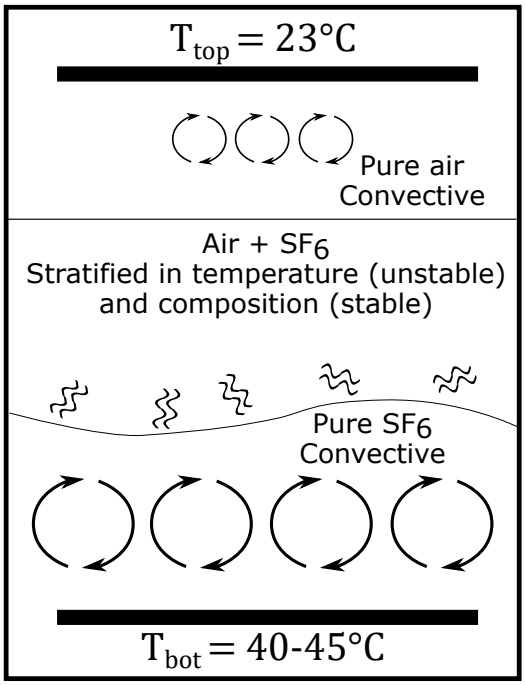

Figure 5.5: Schematic of the experiment. Note that fingering instabilities are observed at the interface between the layer of pure air and the stratified layer during the seeding process. Instabilities disappear once the seeding is stopped and are not observed during the experiment.

small ΔT between the top cooling plate and the interface with the stratified layer. This third and last layer rapidly disappears because of gas diffusion and the second layer of stratified air and SF_6 takes the whole height. The flows taking place in the tank once the heating is turned on are represented in figure 5.5.

5.2.1 Diffusion of gases

During the whole experiment duration (including the filling and seeding steps), gas diffusion will occur and smooth the interface. The length scale over which the two gases are mixed is:

$$h = \sqrt{Dt} \tag{5.2}$$

where $D \sim 10^{-5}$ m$^2 \cdot$ s^{-1} is the coefficient associated with the diffusion between air and SF_6. This results in a typical length scale $l = 1$ cm for a given time $t = 10$ s or 10 cm for about 15 min. The diffusion between gases is quite fast and will impact the dynamics in the experiments.

5.2.2 Double-diffusive instabilities in the experiment

At the interface we have a stable chemical composition gradient $\partial_z C$ and an unstable temperature gradient $\partial_z T$. Yet, it is important to notice that that air has $Le > 1$ whereas SF_6 has $Le < 1$. Consequently, the slow diffuser is different for the two gases: it is the chemical diffusion for air and temperature diffusion for SF_6. We can thus expect to see

both double-diffusive instabilities in the tank. So far, none of the instabilities have been observed during an experiment, only during the seeding of the tank (probably because of the diffusion of the water drops). A theoretical criterion can be computed to know if double-diffusive instabilities can take place. However, it relies on the gradient of temperature and chemical species. These quantities are not yet accessible in our experiment.

5.2.3 Measurements

Particle Image Velocimetry

To measure the flow within the tank, we use PIV with water drops as fluid tracers. The water particles are denser than air and SF_6, but the sedimentation speed remains slow compared to the motion observed so the tracer is adequate for PIV measurements. The seeding with water particles has another advantage (compared to oil particles for example): it does not create a deposit on the tank walls, so the upkeep of the set-up is not an issue. Yet, the tracer is not perfect. The main issue with using water particles as tracer is that the particle properties change through time. The water drops tend to agglomerate: the particle concentration diminishes while their size increases. Moreover, since particles are made of water, and we bring heat into the tank through the heating plate at the bottom, the water tends to evaporate and the particles disappear over time, which is problematic for long-time measurements. Since the humidity of the air in the tank increases, we also have the problem of condensation forming on the tank wall which poses visualisation issues. This has been solved by heating the wall where the camera is placed, preventing condensation to form. However, this solution is not ideal since it brings heat in the system through one side wall and it breaks the configuration symmetry. Moreover, it is not possible to seed the tank while the experiment is on, since the seeding process very likely affects the flow dynamics.
Yet, we succeeded in seeding both layers with a concentration in particles suited for PIV algorithm. The water particles last a few minutes in the tank. There is a sweet spot in time of about 2 min when the particles are large enough to be visualised properly in the camera field, and when the particle concentration is still high enough to fill the camera field. It starts few minutes after the tank was completely filled with water particles. We launch the experiment (turning on the heating) and acquire PIV frames during this moment. The acquisition is 1 min long, acquired at 100 fps with a camera resolution of 2560×1600 pixel^2. With a 50 mm focal length, the view field is 26 cm wide and 42 cm high. We use a continuous laser with 532 nm wavelength and set at 2 W power. A stacking of 10 PIV frames, without any tracer in the convective layer is displayed in figure 5.6. The interface is clearly visible because of the hight contrast between the two layers. Fast motions and mixing are visible at the interface, with parts of the stratified (and thus seeded) fluid being entrained into the convection.
The buffer memory of the camera being limited, we can only record ~ 1 min at 100 fps. For the internal gravity waves, the framerate can be lowered and acquisitions longer than one minute should be easily reachable. Up to 5 minute recordings may be performed in the stratified layer. However, the seeding process is, at the moment, the limiting factor for our visualisations. Still, we can probably increase the particle lifetime by working at lower temperatures in the tank, hence diminishing the evaporation speed. Moreover, preliminary tests show that we may adjust the size of the particles in the mist by adding

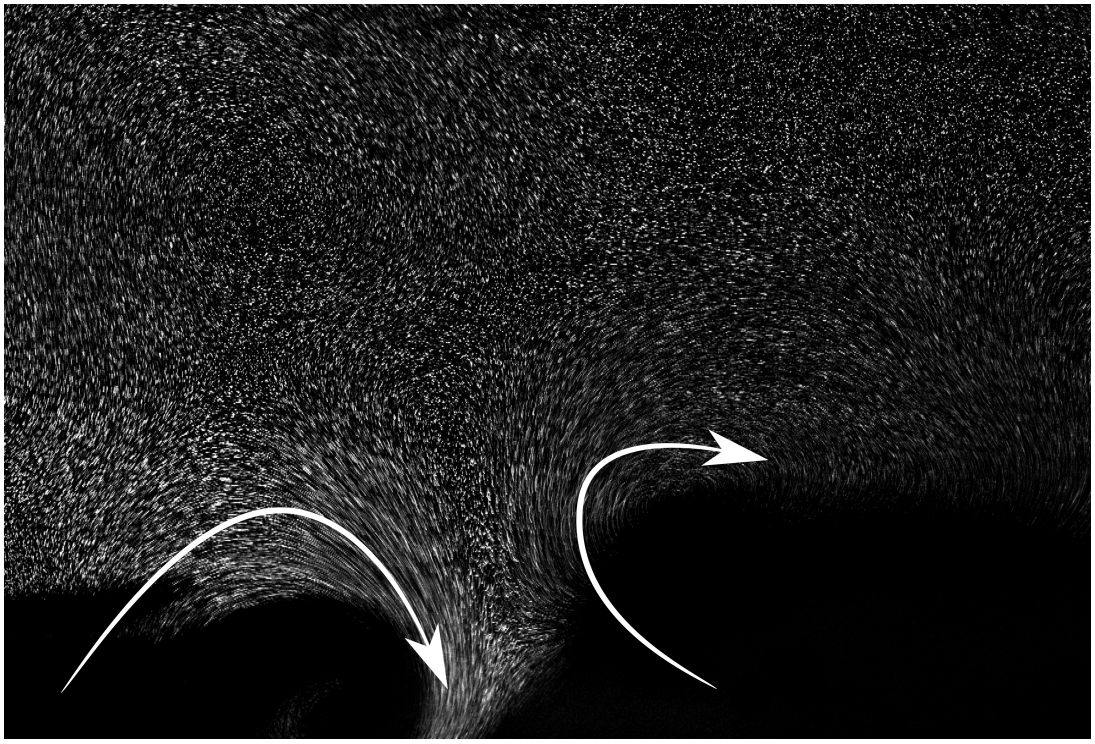

Figure 5.6: Stacking of 10 PIV frames. Here, the convective layer at the bottom is not seeded and convective motion cannot be measured. The stratified layer is seeded suitably for PIV. The interface is enlightened by the high contrast between the two layers. One sees at the bottom centre that the convection entrains a part of seeded fluid, illustrating the mixing taking place at the interface. It is also noticeable that the movements near the interface are much faster (the particles form lines that illustrate their trajectories during 0.1 s) than the ones taking place up in the stratified layer.

UCON oil and/or surfactant in the water buckets, in which are placed the mist-makers. We noted that the particle size is more suited for PIV and their lifetime is extended to tens of minutes when UCON oil is used.

Density profile

Two metal bars with regularly-spaced pressure sensors are placed in the tank along side walls. One has 10 sensors with a 10 cm gap between two sensors. The second one has 10 sensors with a 2 cm gap. The first bar allows to know the density vertical profile along the whole domain, while the second one gives precise measurements of the density profile at the interface location. The second metal bar can be easily lifted up or down so that the interface upward drift can be followed over time. The pressure sensors measure the total pressure with a precision of 1 Pa. If we look at the hydrostatic pressure $P = \rho g H$, $\Delta H = 1$ m results in $\Delta P = 10$ Pa for pure air and $\Delta P = 60$ Pa for pure SF_6. Therefore, the pressure profile would give insight about the evolution of the density profile in the tank. Unfortunately, the pressure sensors could not be tested during experiments so far, but the hydrostatic density profile could be measured in pure air.

5.2.4 Ideas about other measurement techniques

Flow visualisation : Molecular Tagging Velocimetry

Molecular Tagging Velocimetry (hereafter MTV) is a flow visualisation technique using two pulsed lasers and one camera. A single beam is shot from the first laser (the "write" laser). A chemical process is triggered by an optical excitation along the laser beam, resulting in a new chemical species which could be distinguished from the surrounding fluid due to their fluorescence. For a single simple shot, the newly created species will form a line discernible from the rest of the fluid. The second laser (the "read" laser) will allow to follow the displacement of this line, with correlation algorithms. For 2D measurements, optical devices are used to form a grid pattern in the region of interest. The displacement and deformation of this grid over time then give precise measurements about the 2D velocity field in the area. The experimental apparatus and other information are described in literature [Gendrich and Koochesfahani, 1996, Gendrich et al., 1997, Stier and Koochesfahani, 1999].

The main advantages of MTV over PIV is: (i) the problem of seeding particle sedimentation no longer exists, (ii) the tagging can be repeated over and over by shooting with the write laser. The major issue we have with PIV is that the seeding disappears over time, and it is not an option to keep seeding during the experiment. Therefore, long time measurements cannot be performed with PIV at the moment. That is problematic to investigate for low frequency waves and have statistically converged results. But this is especially troublesome if we want to study large-scale dynamics. Indeed, those would happen on time-scale much larger than the waves dynamics, probably of the order of the hour. MTV visualisation allows to bypass this issue, since the tagging can be simply performed again and again, and it does not affect flow dynamics.

Sound speed measurements

Another way to measure density profiles is to measure the sound speed and temperature at different heights. With these measurements, it is possible to deduce the value of ρ locally. In any fluid, the sound speed writes:

$$c_s = \sqrt{\left(\frac{\partial P}{\partial \rho}\right)_S} = \sqrt{\frac{1}{\chi_S \rho}} \tag{5.3}$$

with χ_S the coefficient of isentropic compressibility. For perfect gases, we have:

$$\gamma = \frac{\chi_T}{\chi_S} \tag{5.4}$$

with γ the Laplace coefficient, and $\chi_T = \frac{-1}{V}\left(\frac{\partial V}{\partial P}\right)_T$ the isotherm compressibility coefficient. Using the perfect,gas relation $PV = nRT$, we write $\chi_T = \frac{1}{P}$.

The sound speed thus writes:

$$c_s = \sqrt{\frac{P\gamma}{\rho}} \tag{5.5}$$

ρ is the density of the fluid and writes $\rho = \frac{m}{V}$. In our case, we have two gases with different concentration x_{air} and x_{SF_6}. The density can thus be written $\rho = x_{\text{air}}\rho_{\text{air}} + x_{\text{SF}_6}\rho_{\text{SF}_6}$. For an ideal mixing of two perfect gases, we have

$$\rho = \frac{MP}{RT} \tag{5.6}$$

with $M = x_{\text{air}} M_{\text{air}} + x_{\text{SF}_6} M_{\text{SF}_6}$. We know M_{air} and M_{SF_6} and we have $x_{\text{air}} = 1 - x_{\text{SF}_6}$.

Besides, the Laplace coefficient can also be written $\gamma = \frac{C_P}{C_V}$ with C_P (resp. C_V) the heat capacity at constant pressure (resp. volume). As for the molar mass M, we can write the heat capacities of the gas mixture as:

$$C_P = x_{\text{air}} C_{P,\text{air}} + x_{\text{SF}_6} C_{P,\text{SF}_6} \qquad C_V = x_{\text{air}} C_{V,\text{air}} + x_{\text{SF}_6} C_{V,\text{SF}_6}$$

Finally, the sound speed in a air and SF_6 mixture writes:

$$c_s = \sqrt{\frac{RT\left(x_{\text{SF}_6} C_{P,\text{SF}_6} + (1 - x_{\text{SF}_6}) C_{P,\text{air}}\right)}{\left(x_{\text{SF}_6} C_{V,\text{SF}_6} + (1 - x_{\text{SF}_6}) C_{v,\text{air}}\right)\left(x_{\text{SF}_6} M_{\text{SF}_6} + (1 - x_{\text{SF}_6}) M_{\text{air}}\right)}} \tag{5.7}$$

In this equation, if we measure the sound speed c_s and the temperature T, the only unknown is x_{SF_6}. The equation, which is a second order polynomial, can thus be analytically solved and gives the concentration in SF_6 at the position of the measurement.

The derivation is not exact since we assumed that air and SF_6 are perfect gases. But this simple relation, along with a calibration performed in mixture of air and SF_6 with known concentration and temperature, in order to see the dependence of c_s on the mixture concentrations, could allow to access a relatively precise estimation of the density profile. Piezoelectric sensors were bought to test these measurements. The idea is to impose a current to one of the two piezoelectric sensors, which will behave like an emitter. The emitter will vibrate at a given frequency set by its geometry. A second piezoelectric, serving as a receptor, will vibrate due to the pressure wave received and will thus generate an electric signal. By measuring the phase lag Δt between the two signals, and by knowing the distance Δl between the two sensors, one can measure the sound speed. Unfortunately, this method could not be implemented so far.

5.3 Analysis of a preliminary experiment

This section introduces the analysis of our preliminary experiments. Here we explore the internal gravity wave field generated by the convection and the evolution in time of the interface position in order to address the specific issues of the overshooting zone, developed in section 5.1. For the data analysed, the camera is centred horizontally in the tank and the bottom edge of the camera frame is placed a few centimetres above the heating plate in order to avoid laser reflection into the camera lens. The interface position varies with time because of the mixing from the convective motion and diffusion.

5.3.1 Interface

The interface cannot be followed by density measurements yet. Hence, we capture its displacement by looking at the time evolution of the horizontally averaged RMS of the horizontal velocity measured by PIV. Velocities are much larger in the convective layer compared to wave velocities. We expect a sharp decrease of the RMS values at the

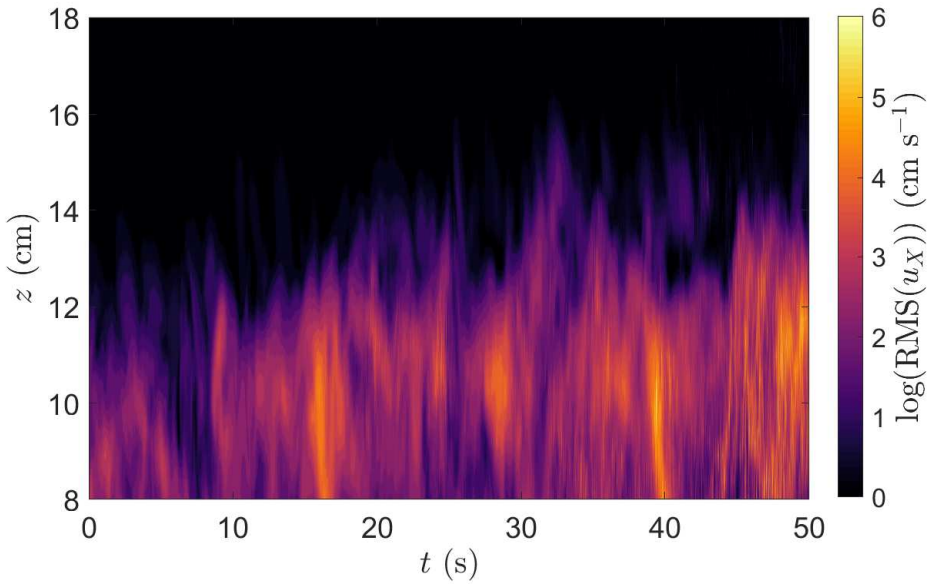

Figure 5.7: Horizontally averaged RMS of the horizontal velocity u, plotted as a function of altitude z and time t. The colourful region at the bottom shows the convective motion while the black area above shows the stratified layer, where velocities are much smaller than the ones present in the convective layer. The Rayleigh number, based on an averaged height and total $\Delta T = 17$ °C, is $Ra = 1.2 \times 10^8$.

interface between the two layers. Figure 5.7 shows the averaged RMS as a function of time and altitude. The interface is located at $z \sim 11$ cm at $t = 0$ s and ends at $z \sim 14$ cm at $t = 54$ s. The position of the interface does not rise continuously with time: one sees that the RMS reaches high vertical positions ($z = 16$ cm) at $t = 33$ s while few seconds later, the interface is located at $z = 14$ cm. These short time-scale fluctuations of the interface are explained by rising plumes from the convection overshooting within the stratified layer above and then falling back in the convective layer. However, if we do not take into account these fast fluctuations, the interface position rises with time overall. We chose an arbitrary threshold of $u_{rms} = 0.5$ cm $\cdot$ s^{-1} to set the interface.

We compute an average position for the first 5 s and the last 5 s of our acquisition. We find that the interface rises of $\Delta z = 2.75$ cm during $\Delta t = 54$ s. Yet, diffusion acts on both direction of the interface and the front created by diffusion would grow upward and downward in our set-up. Here, the mixing induced by convection only create the upward front. Therefore, the effective Δ_z created by convection is $\Delta_z = 2 \times 2.75 = 5.5$ cm. The "effective diffusion" coefficient associated is $D_{eff} = \frac{\Delta_z^2}{\Delta_t} = 5.6 \times 10^{-5}$ m$^2 \cdot$ s, which is 560% larger than the mutual gas diffusivity $D \sim 10^{-5}$ m$^2 \cdot$ s^{-1}. Longer measurements are needed to see how the mixing rate changes over time.

5.3.2 Stratified layer

Internal gravity waves are observed in the stratified layer. A snapshot of a vorticity field, in which waves are visible, is displayed in figure 5.8. Examples of temporal signals are displayed in figure 5.9a. Vertical velocity signals are plotted at three different locations

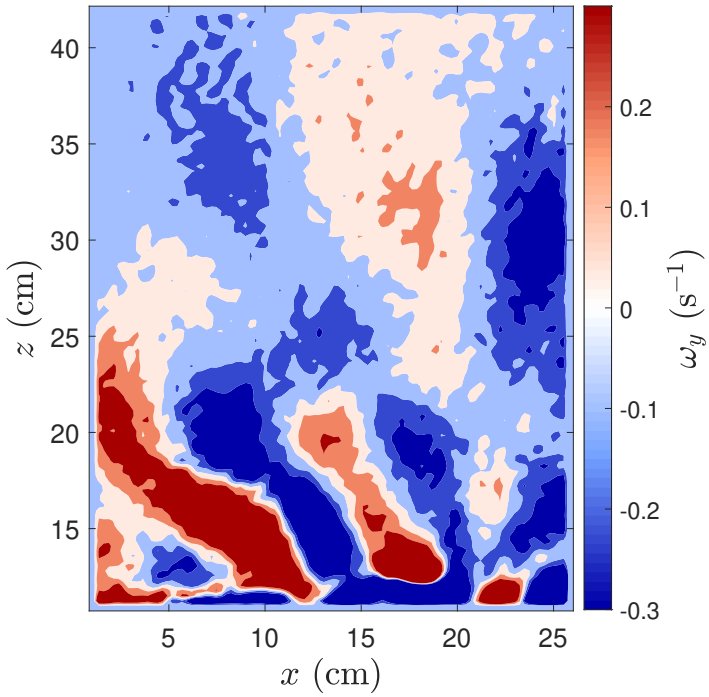

Figure 5.8: 2D snapshot of the y-component of the vorticity field in the stratified layer. A wave pattern is clearly visible at the bottom.

chosen randomly and displayed in the right panel. The signals are oscillating in a sinusoidal way around $w = 0$ cm $\cdot$ s^{-1}, indicating that these are wave motions. One sees that the amplitude of the oscillations is larger for the signal taken at the lowest altitude (blue curve, $z = 15$ cm), suggesting that wave amplitude attenuates with height, as expected. Additionally, the blue curve oscillates faster than the two others. This is more noticeable in figure 5.9b which displays the spectrum for each signal. The peak in the spectrum is reached at a higher frequency at the bottom of the stratification compared to to the top. This is surprising since we would expect that high frequency waves propagate high in the tank whereas low frequency waves stay at the bottom of the stratified layer. We thus would expect fast oscillations with superimposed slower oscillations at the bottom with only fast oscillations visible at the top of the domain.

Spectra at different heights are plotted in figure 5.10 for the horizontal velocity u and in figure 5.11 for the vertical velocity w. They are computed over the whole duration of the signal (54 s) even if, as seen in figure 5.7, the system is not in a steady state. The spectra may be hard to interpret in the vicinity of the interface, where the fluid is initially stratified and is slowly mixed over time.

Yet, the contrast in power density is striking between the convective layer and the stratified layer, in both figures. The interface is approximately located at $z \sim 13$ cm, with very high power density values below. The convective motions are intense compared to the wave motion. In the spectra for u in figure 5.10, one can notice an increase in power density at $z = 10$ cm for the lowest frequencies. This is caused by the deviation of rising plumes by the interface. At this height, the plumes rise vertically and are deflected horizontally by the stratified layer. Oscillatory motions are seen for both components of the velocity in the stratified layer. Additionally, we observe a drop in energy for frequencies

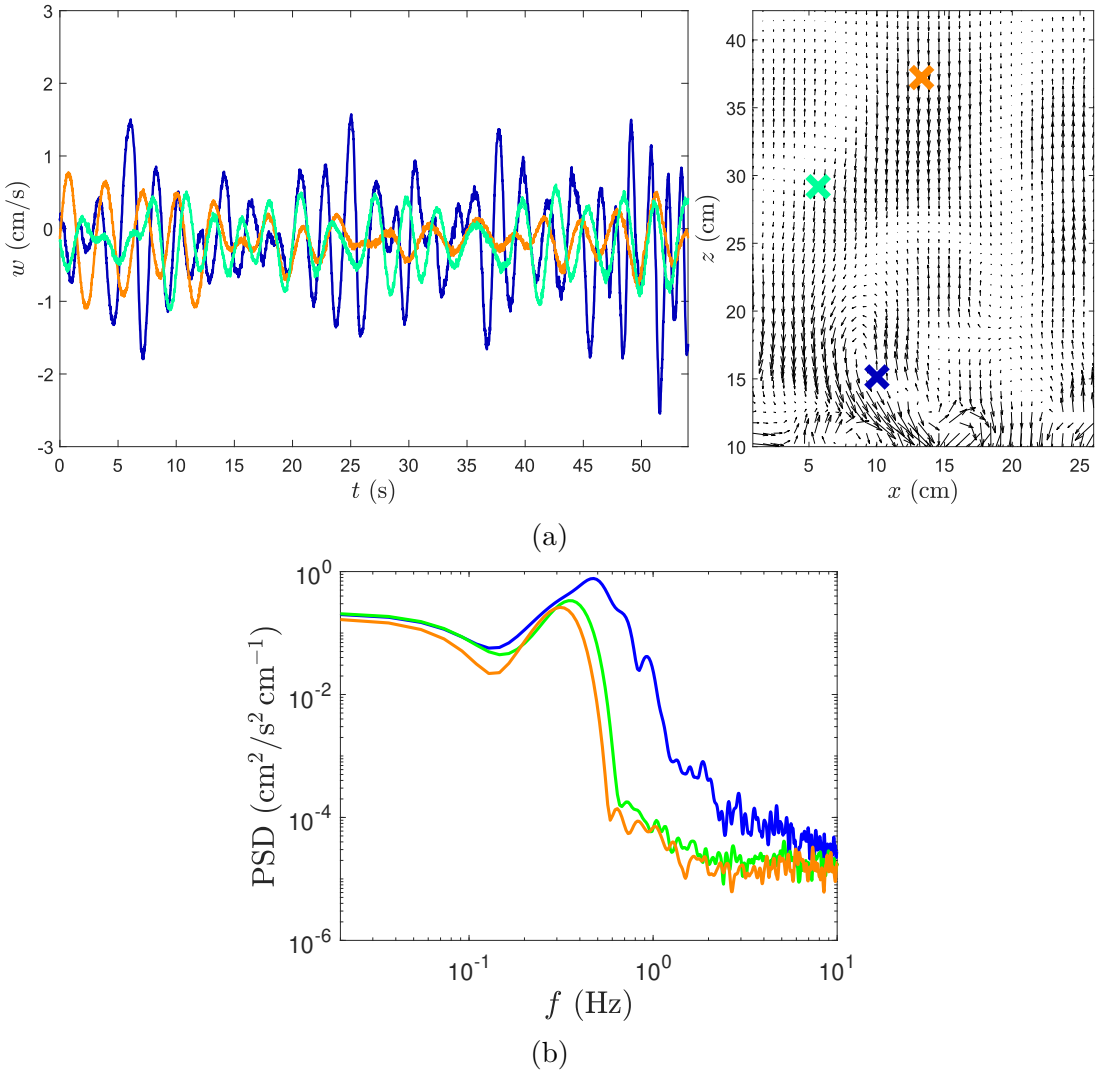

Figure 5.9: (a) Time signals of the vertical velocity w at three different locations: $x = 11$ cm and $z = 15$ cm (blue), $x = 8$ cm and $z = 29$ cm (green), $x = 13$ cm and $z = 37$ cm (orange). The quiver in the right panel shows the three different locations, marked with crosses with corresponding colors. (b) Corresponding spectra for each velocity signal.

$f > 0.6 - 0.8$ Hz in the stratified layer. That may indicate that the buoyancy frequency in this experiment is approximately $N = 0.6 - 0.8$ Hz, since we expect that internal gravity waves are evanescent if they have a frequency higher than N. Spectra for the vertical velocity (figure 5.11) shows a very intense peak close to $f \sim 0.8$ Hz, indicating that high frequencies dominate the oscillations in the stratified layer. These high frequency waves propagate high in the tank and have a magnitude similar to the one observed in the convective layer at the same frequencies.

Additionally, the cut-off frequency is lower at the top of the captured domain compared to the bottom of the stratification. This suggests that the vertical density profile is not linear, and that the buoyancy frequency is therefore not constant with height. This also explains why, in figure 5.9a, the fast oscillations visible at the bottom of the tank were not visible at the top. Due to N decreasing with height, faster oscillations are reachable

at the bottom of the stratification compared to the top.

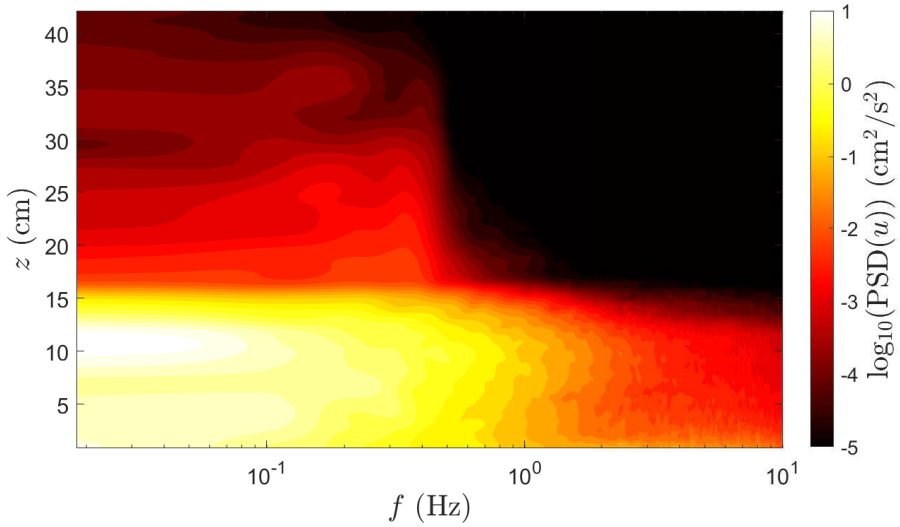

Figure 5.10: Power Spectral Density of the horizontal velocity u. Spectra are computed at each location and then horizontally averaged, from a 54 s acquisition.

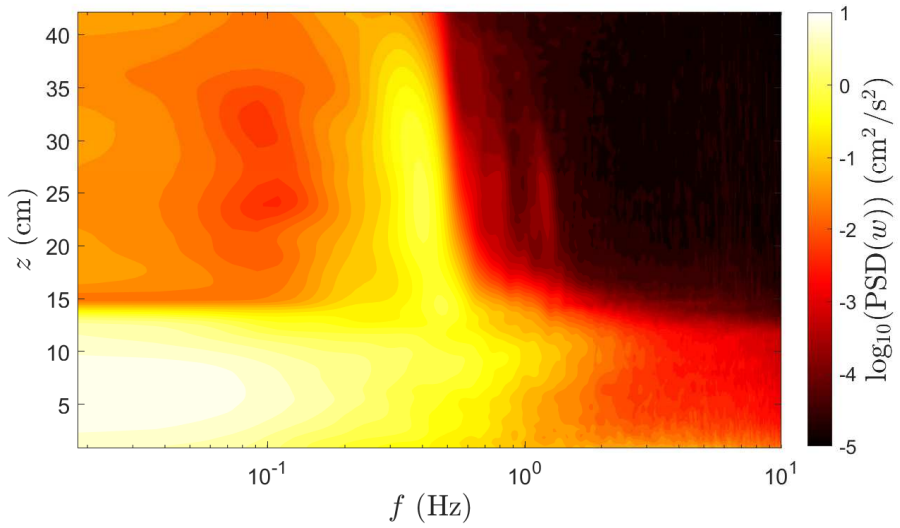

Figure 5.11: Power Spectral Density of the vertical velocity w. Spectra are computed at each location and then horizontally averaged, from a 54 s acquisition.

Even if the total acquisition time is relatively short (54 s), we can horizontally and time average the horizontal speed to visualise a potential horizontal mean-flow. The profile is displayed in figure 5.12a. We see that the mean flow is positive at the bottom and goes to negative value between 8 cm $< z <$ 13 cm. This is likely the signature of the convective cell, with a rising plume close to the center of the camera frame. The rising plume is deflected to the left as it encounters the interface, resulting in negative horizontal velocity. Positive horizontal flow is located at the bottom to close the convective

cell. However, just above the convective layer, one sees a positive mean-flow, resulting in a shear close to the interface. Due to the very short acquisition time, it is difficult and too early to deduce anything from this feature. It could be driven by waves, due to thermal losses at the tank walls, coupled with motions in the convective layer. Yet, seeing this shear between the two layers at $Pr \sim 0.7$ is quite intriguing and deserves a special attention in future experiments.

About the energy transfer from convection to waves, we plot in figure 5.12b the vertical profile of $u_{\mathrm{RMS}}^2 + w_{\mathrm{RMS}}^2$, averaged over 54 s. The energy is significantly higher in the convective layer $z < 12$ cm compared to the stratified layer. The ratio between the almost constant energy value reached between 20 cm $< z <$ 30 cm and the peak in energy just above the interface is 0.02, suggesting that $\sim 2\%$ of the convection energy goes into the wave. At $z > 30$ cm, the energy decreases exponentially.

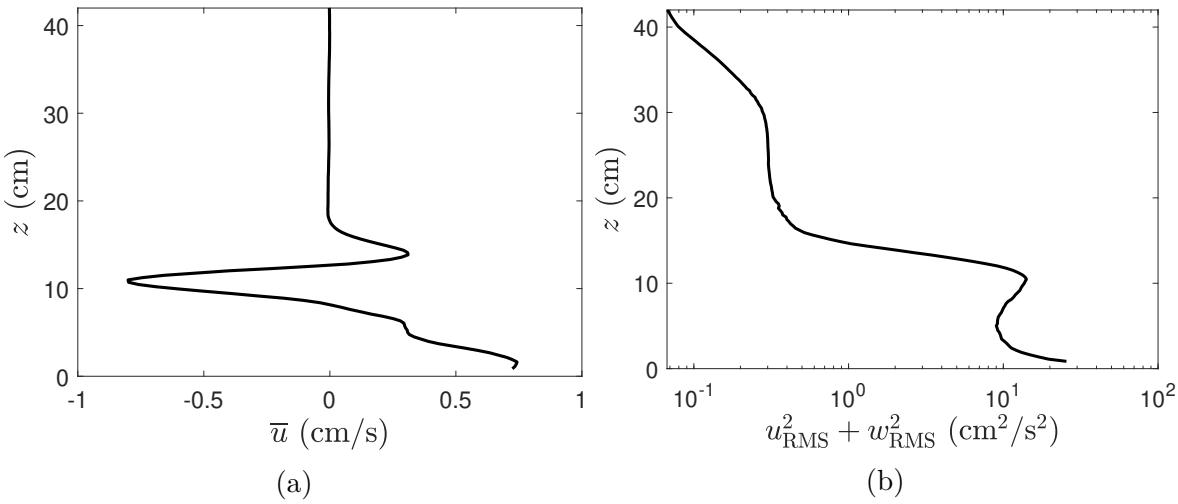

Figure 5.12: (a) Horizontally and time averaged horizontal velocity $\overline{u}$, shown as a function of the height z. (b) Time averaged profile of $u_{\mathrm{RMS}}^2 + w_{\mathrm{RMS}}^2$. The decrease in energy at the interface $z \sim 12$ cm is quite visible. Energy is then almost constant between 20 cm $< z <$ 30 cm. The energy then drops exponentially.

5.4 Conclusion

This chapter briefly introduced our new experiment studying penetrative convection with gases as working fluids, in order to reach low Prandtl number dynamics. The study of the entrainment at the interface is of particular interest for star modelling, due to the importance of the mixing on star lifetime. Also, working with low Prandtl number would increase our chance to observe an oscillating QBO-like flow according to [Couston et al., 2018a]. Yet, the current geometry needs to be adapted in order to be axisymmetric and long-time measurements need to be performed.
Nonetheless, our first results are quite encouraging. Once density measurements are accessible, and once the seeding process is mastered, we should be able to investigate the flow at various Rayleigh numbers and various buoyancy frequencies, and also to quantify the entrainment at the interface.

CONCLUSION

In this manuscript, we have broached some aspects of the interaction between turbulence and stratification. Through theoretical development and numerical integration, as well as experiments, we have adressed the issue of internal gravity wave and large-scale flow generation. This last section of the manuscript will briefly summarize our results and will in particular give thoughts and insight on the future investigations which could be lead from our findings.

Multi-modal model for the QBO

We showed that, in a 1D model, multi-modal forcing in a finite stratified domain favors the emergence of periodic reversals for the horizontal mean-flow. Additionally, forcing spectra with different characteristics can lead to very similar mean-flow oscillations. We related these results to the use of a similar model in GCMs. Finding the right features (amplitude and period) for the oscillations does not imply that the underlying forcing is correct.

Yet, the numerous approximations made for the analytical development of the model have to be reminded when interpreting our results, even if the monochromatic model is well reproduced in experiments [Plumb and McEwan, 1978,Otobe et al., 1998,Semin et al., 2018]. The study from [Couston et al., 2018a] also suggests that taking into account the distribution of energy is not sufficient, and higher order statistics should be considered to properly reproduce the effect of turbulently-generated waves.

However, by its simplicity and easiness to run on everyday-computer, the multi-modal model derived in this thesis from the work of [Plumb, 1977] allows a systematic exploration of the numerous parameters of the problem that cannot be performed with DNS. We have explored the influence of considering different frequencies for the waves. The influence of horizontal wavenumbers is still an open question. In the Earth's stratosphere, the QBO is generated by a wide range of wavenumbers, from small-scale internal gravity waves ($\mathcal{O}(10\text{ km})$) to large-scale planetary waves (Rossby and Kelvin waves, $\mathcal{O}(1000\text{ km})$). Taking into account this disparity in the model is some work that should be done to increase our comprehension of the mechanism. Moreover, even if we understand that considering rotation would break the symmetry of the problem, which is crucial for the reversals to appear, it may be interesting to run the model with small Coriolis parameter

f to really understand how the Earth's rotation impact the momentum exchange between the waves and the mean-flow at latitudes close to the equator.

Besides, the model can, with relative easiness, be relaxed from one approximation: the weak dissipation approximation, which overestimates the wave attenuation at low frequencies. The analytical derivation of the forcing term becomes a bit tedious, but the final expression obtained gives a better description for the low frequency wave attenuation [Lecoanet et al., 2015]. Some preliminary computations have been performed, in the monochromatic case. The first striking result is that, because of the lower attenuation at low frequency, momentum exchange mainly occurs through critical layers in the model, whereas viscous attenuation was sufficient to damp the wave with the "weak" dissipation assumption.

The jet experiment

We unsuccessfully tried to generate an oscillating flow from turbulently-generated internal gravity waves in salty water. Jets were used to create a turbulent layer. Unfortunately, the mixing occurring at the interface was too strong and rapidly, a density jump appeared at the interface. We think that this density jump tremendously affects the wave generation by lowering the energy transfer from the turbulent layer to the stratified layer and by promoting the emergence of a global mode over the whole depth. Even if, at early times, a mean-flow is observed, it quickly disappears, as the forcing waves diminish in intensity.

The effect of the density jump on the wave generation is not quantified yet. Nonetheless, an experiment with one single jet impacting an interface with a stratified layer of constant N could validate our theory. One only needs to vary the density jump at the interface $\Delta\rho$ with fixed Reynolds number Re for the jet. By measuring the wave field at a given depth, one could verify whether or not the density jump affects the wave generation. Varying Re with fixed $\Delta\rho$ would also be an interesting study.

On the experimental generation of a QBO-like flow from multi-wave forcing, our set-up does not seem to be ideal. Perhaps that using a higher tank to give space for the waves to attenuate would be enough to see an oscillating mean-flow since we have numerically seen that the domain height has an influence on the QBO emergence. Yet, this would not solve the mixing issue.

A solution would be to expand upon the existing experimental set-ups [Plumb and McEwan, 1978, Otobe et al., 1998, Semin et al., 2018] for the monochromatic case, and to adapt the forcing to control individually each piston that moves the membrane. Doing so, it could be possible to generate waves with different frequencies and wavenumbers. Additionally, it would allow a smoother transition from the monochromatic study to multi-wave study than our jet experiment. Indeed, controlling each piston would grant the possibility to consider two different frequencies, then 3, etc. in order to increment the complexity of the forcing step by step. Stratification mixing would still occur in this set-up, close to the oscillating membrane. Yet, the problem can be solved by constantly pouring some salty water near the membrane to rebuild the stratification [Semin et al., 2018].

Penetrative convection with water

The non-linear equation of water allows us to study penetrative convection in a stationary configuration. The flow observed has been thoroughly described. Along with the convective motions and internal gravity waves generated stands a thermal coupling at the interface that drives a third intermediate layer, which viscously entrains the stratified layer located above. A numerical simulation with parameters comparable to the experiment corroborates these observations.

The Prandlt number for water is $Pr = 7$ and [Couston et al., 2018a] showed that high Prandtl number fluids do not go along with QBO-like flow generation. Thus, the non-emergence of these kinds of flow in the experiment may not be surprising.

Despite that no QBO-like flow appears, the convection in water around 4 °C has one huge interest: it allows to study the dynamics in a quasi-stationary two-layer system. Coupled PIV/LIF measurement would give access to coupled velocity / temperature measurements, allowing for a better understanding of the mixing occurring at the interface and the transport in the stratified layer. Additionally, the existing set-up is relatively small and could easily be studied in the presence of rotation. Again, coupled PIV/LIF measurements would allow us to understand the impact of rotation on the temperature transport within the stratified layer.

Moreover, additional numerical simulations can also be performed to investigate the effect of the rotation and of the Prandtl number on the dynamics.

Penetrative convection with gases

This newly designed experiment is still work-in-progress, but the first obtained results are quite encouraging and suggest that, if we succeed in making longer visualisations of the flow, investigations with varying Rayleigh number Ra and buoyancy frequency N could be performed. Also, once density measurements are accessible, the entrainment at the interface by penetrative convection could be quantified.

To improve flow visualisation, two ideas come to mind. The first one is to use PIV with more appropriate seeding particles. Using the mist-makers with water mixed with chemicals could allow to control the size of the seeding particles, but also to increase their lifetime by limiting the evaporation. The second one is to implement MTV measurements for the experiment (see a short description in chapter 5). However, this experimental technique would be quite challenging to implement in the set-up, due to its complexity.

Since Prandtl numbers in stars are much lower than $Pr = 0.7$, it could be interesting to study penetrative convection in fluids with very low Prandtl numbers. Liquid metal are characterised by $Pr \sim 0.02$ and have been used in Rayleigh-Bénard convection studies [Fauve and Libchaber, 1981, Libchaber et al., 1982, Fauve et al., 1984, Chiffaudel et al., 1987] and liquid sodium allows to reach Prandtl as low as $Pr = 0.006$ [Kek and Müller, 1993]. However, the Rayleigh numbers reached remained relatively low $Ra = 10^3 - 10^5$ and other experimental issues appear when working with these fluids: 2D and 3D velocity measurements are hardly accessible in liquid metal, and liquid sodium was heated at 550 K in [Kek and Müller, 1993] to reach low Prandtl number values.

On the effect of the Prandtl number on mean-flow generation

The effect of the Prandtl number on QBO emergence seems unclear at first look. The study of [Couston et al., 2018a] shows that in flows with Prandtl number higher than 1, QBO-like flows do not appear, while the experiment of [Plumb and McEwan, 1978, Otobe et al., 1998, Semin et al., 2018] successfully drove a QBO in salty water, *i.e.* with a compositional Prandtl number (often refered as Schmidt number) $Pr = 700$. This may seem contradictory, but it may be just in appearance. Perhaps, the Pr effect applies to the wave generation and not to the QBO generation. Since the wave generation process differs from [Couston et al., 2018a], in which waves are driven by convective plumes, compared to the experiments, in which waves are directly forced by a moving boundary, the Prandtl effect is not contradictory.

From our study of penetrative convection in water ($Pr = 7$), we have seen a specific thermal coupling that drives the flow near the interface, in what we named the buffer layer. The numerical investigation performed at $Pr = 0.1$ has shown that this coupling disappears when the Prandtl is low enough. That means that the flow dynamics within the zone where the waves are generated is somehow controlled by the Prandtl number. This coupling cannot appear in the experiment of [Plumb and McEwan, 1978, Semin et al., 2018] in which the waves are directly generated by the moving membrane, and not by a turbulent flow. Therefore, the Prandtl number affects the dynamics where the waves are generated and therefore, very likely affects the wave properties. Through its effect on wave generation, the Prandtl number indirectly affects QBO emergence. This reasoning is only intuitive at the moment but could be checked in 2D DNS in a configuration similar to [Couston et al., 2018a] by measuring the internal gravity waves amplitude in the stratified layer, while varying the Pr number and keeping fixed the Ra number.

We can compare the experiments presented in the manuscript to start to investigate the Pr effect on wave generation. Figure 5.13 shows the spectrogram for the experiments presented in chapters 3, 4 and 5. First row is the penetrative convection with water, second row is the jet experiment and third row is the penetrative convection in gas. One sees that for the 4 °C experiment ($Pr \sim 7$), the waves signal is mostly at low frequency compared to the buoyancy frequency and is therefore mostly visible in the u spectra (5.13a). The spectra are continuous across the interface. In comparison, the spectra for the jet experiment show a sudden drop in energy at the interface. It is especially noticeable for the vertical velocity w (figure 5.13d). The gas experiment stands out by the intensity of the waves generated. On the spectra for the vertical velocity (figure 5.13f), one sees that the energy at $f \sim 0.6$ Hz has about the same magnitude in the convective layer and in the wave signal. For the two other experiments, a sharp decrease in magnitude was observed between the convective/turbulent layer and the waves. Additionally, the spectrograms for the gas experiment do not exhibit a sudden drop at the interface location, like it does for the jet experiment.

Comparing the penetrative convection experiments in water ($Ra \sim 7 \times 10^7$) and gases ($Ra \sim 1.2 \times 10^8$), we argue that the Prandtl number Pr may play a role in the wave generation. The plumes penetrate higher in the stratified region for the gases (low Pr) than they do for water. This difference results in low frequency wave with relatively little energy for the water experiment and energetic high frequency waves for the gas experiment. The jet experiment could lead us into thinking that high Prandtl numbers

create a stiff interface which completely separates the convective layer from the stratified layer by making a sudden drop in energy at the interface, because the jets cannot penetrate the stratification. Yet, this is likely an effect of the density jump created over time and we cannot conclude that the Pr number has a role here. Further studies using our gas set-up, coupled with systematic numerical simulations, will help deciphering these various effects. Clearly, the dynamics of coupled convective / stratified systems, their various effects, and their planetary / stellar applications deserve more studies. And for those studies, only combination of theoretical approach, numerical simulation, experiments and observations will allow significant progress.

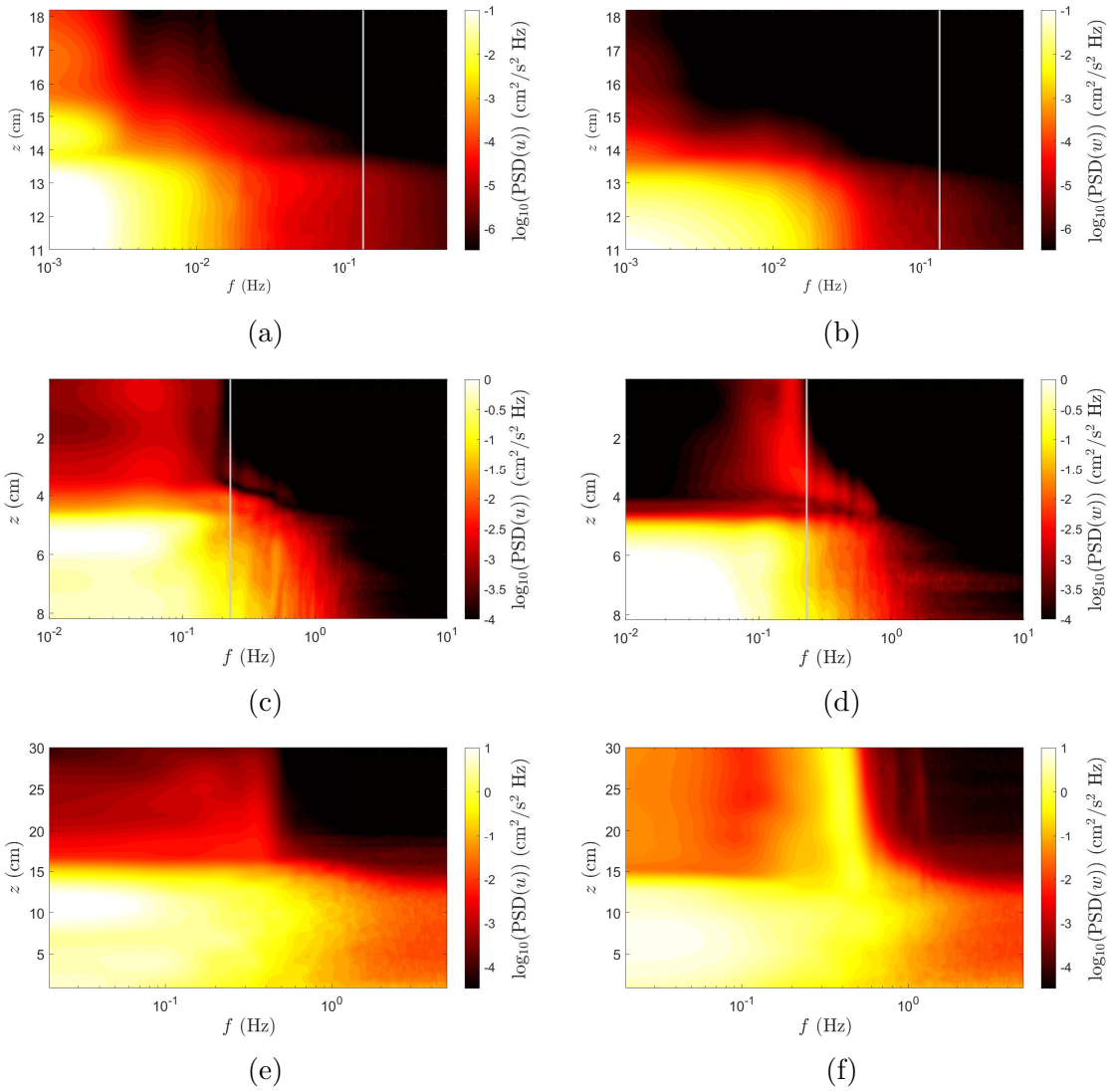

Figure 5.13: Spectrogram as a function of frequency f and height z for the 4 °C penetrative convection experiment: horizontal velocity u (a) and vertical velocity w (b); the turbulent jet experiment with index matching: horizontal velocity u (c) and vertical velocity w (d); penetrative convection with gases: horizontal velocity u (e) and vertical velocity w (f). The colorbars, horizontal axis and vertical axis have different ranges for the different experiments. The buoyancy frequency has been plotted except for the gas convection in which the density profile remains unknown. The figures for the turbulent jets (c-d) are turned upside down for an easier comparison.

APPENDICES

Numerical convergence of the multi-modal model

A numerical convergence study was performed for the model described in chapter 2 in order to find the best grid, time and spectrum spacings for our study. Figure 6.1 shows the mean-flow frequency and mean amplitude at four different heights ($z = 0.1$, $z = 0.25$, $z = 0.5$ and $z = 0.75$) as a function of the three numerical parameters δ_t, δ_z and N_ω for the case $\omega_0 = 0.2$, $\sigma = 10^{-4}$ and $E_{tot} = 2 \times 10^{-6}$ (the narrow Gaussian case of the σ systematic study presented in section 2.4).

Top panel of figure 6.1 shows convergence as $\delta_t \to 0$. Comparing results for $\delta_t = 1$ and $\delta_t = 0.05$ shows that frequencies differ by $< 1.7\%$ and the flow amplitudes differ by $< 1.5\%$. Other convergence studies were conducted for δ_z (see middle panel of figure 6.1) and N_ω (bottom panel of figure 6.1) to determine their best values for the systematic study in σ (displayed in figure 1 of the article submitted to *Physical Review Letters* displayed in section 2.4). Convergence studies with $\sigma = 10^{-1}$ are displayed in figure 6.2 (with $\omega_0 = 0.2$ and $E_{tot} = 2 \times 10^{-6}$).

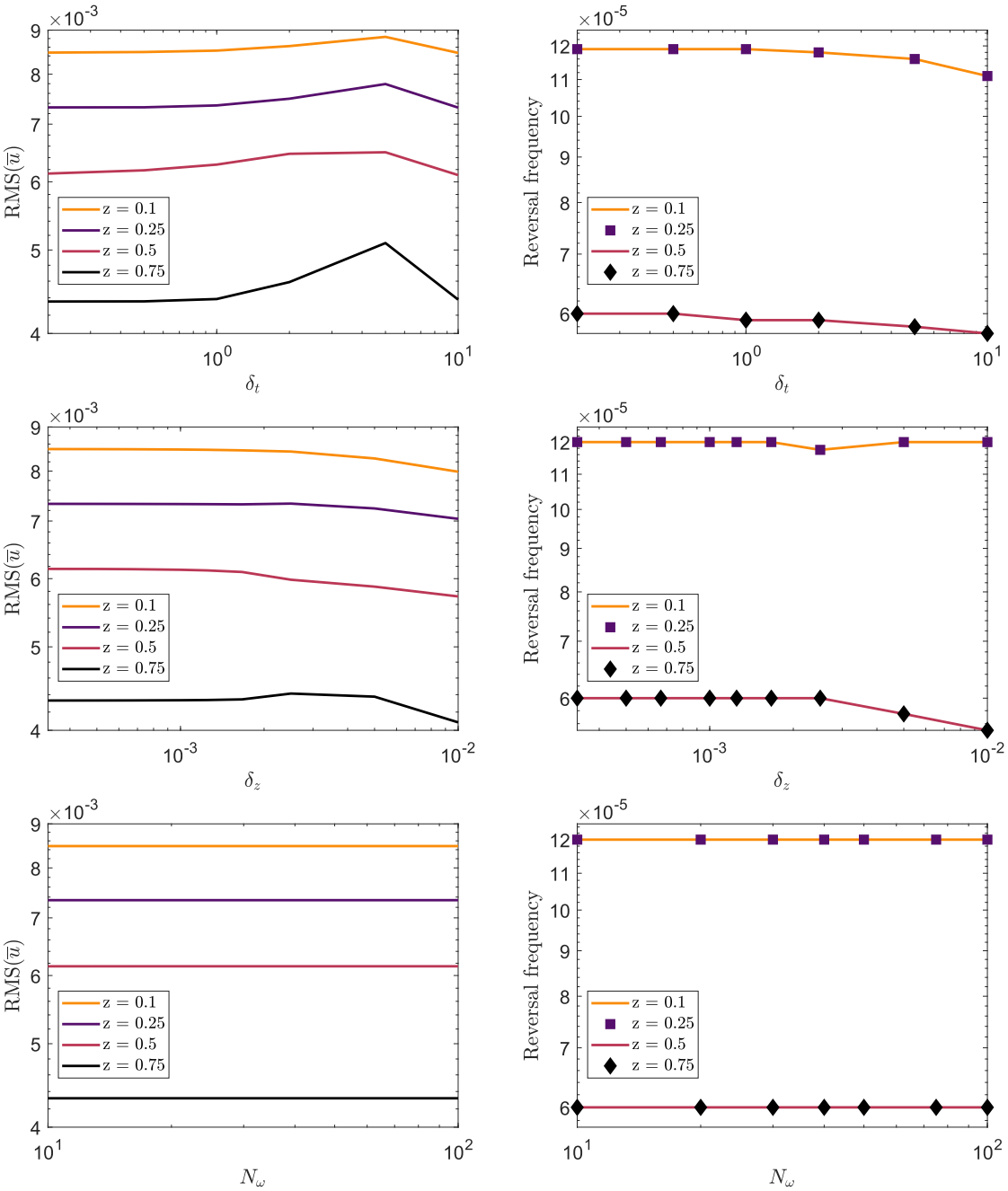

Figure 6.1: Mean-flow properties for $\omega_0 = 0.2$, $\sigma = 1 \times 10^{-4}$, and $E_{tot} = 2 \times 10^{-6}$. Convergence study for δ_t (top), δ_z (middle), and N_ω (bottom).

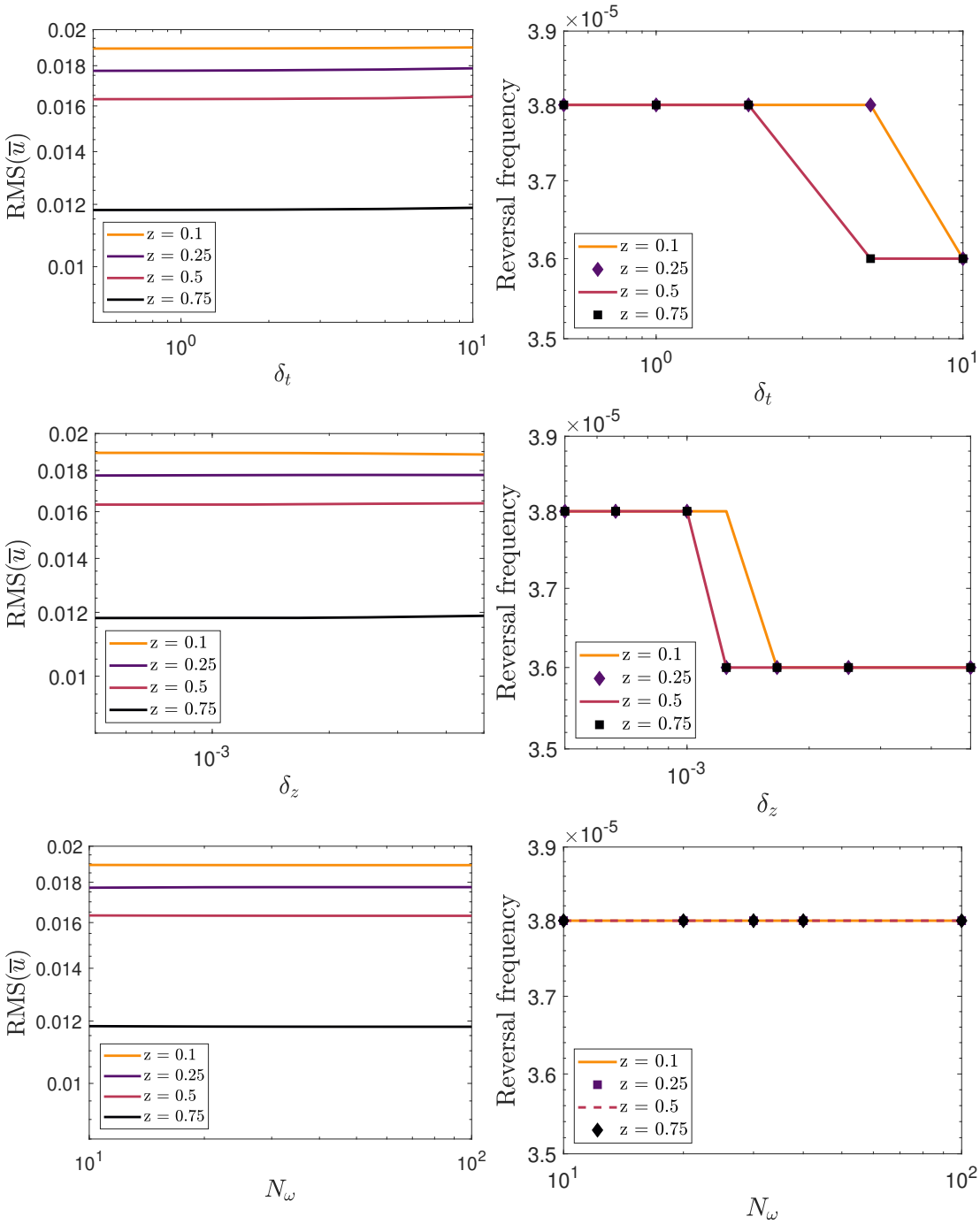

Figure 6.2: Mean-flow properties for $\omega_0 = 0.2$, $\sigma = 1 \times 10^{-1}$, and $E_{tot} = 2 \times 10^{-6}$. Convergence study for δ_t (top), δ_z (middle), and N_ω (bottom).

BIBLIOGRAPHY

[Aerts et al., 2019] Aerts, C., Mathis, S., and Rogers, T. M. (2019). Angular Momentum Transport in Stellar Interiors. *Annual Review of Astronomy and Astrophysics*, 57(1):35–78.

[Aguilar et al., 2006] Aguilar, D., Sutherland, B., and Muraki, D. (2006). Laboratory generation of internal waves from sinusoidal topography. *Deep Sea Research Part II: Topical Studies in Oceanography*, 53(1-2):96–115.

[Alexander, 1996] Alexander, M. J. (1996). A simulated spectrum of convectively generated gravity waves: Propagation from the tropopause to the mesopause and effects on the middle atmosphere. *Journal of Geophysical Research: Atmospheres*, 101(D1):1571–1588.

[Alford et al., 2015] Alford, M. H., Peacock, T., MacKinnon, J. A., Nash, J. D., Buijsman, M. C., Centurioni, L. R., Chao, S.-Y., Chang, M.-H., Farmer, D. M., Fringer, O. B., Fu, K.-H., Gallacher, P. C., Graber, H. C., Helfrich, K. R., Jachec, S. M., Jackson, C. R., Klymak, J. M., Ko, D. S., Jan, S., Johnston, T. M. S., Legg, S., Lee, I.-H., Lien, R.-C., Mercier, M. J., Moum, J. N., Musgrave, R., Park, J.-H., Pickering, A. I., Pinkel, R., Rainville, L., Ramp, S. R., Rudnick, D. L., Sarkar, S., Scotti, A., Simmons, H. L., St Laurent, L. C., Venayagamoorthy, S. K., Wang, Y.-H., Wang, J., Yang, Y. J., Paluszkiewicz, T., and (David) Tang, T.-Y. (2015). The formation and fate of internal waves in the South China Sea. *Nature*, 521(7550):65–69.

[Alvan, 2014] Alvan, L. (2014). *Ondes internes de gravité dans les étoiles de type solaire : Excitation, propagation et transport de moment cinétique*. PhD thesis. Thèse de doctorat dirigée par Brun, Allan Sacha et Mathis, Stéphane Astronomie et Astrophysique Paris 7 2014.

[Alvan et al., 2013] Alvan, L., Mathis, S., and Decressin, T. (2013). Coupling between internal waves and shear-induced turbulence in stellar radiation zones: the critical layers. *Astronomy & Astrophysics*, 553:A86.

[Andrássy and Spruit, 2013] Andrássy, R. and Spruit, H. C. (2013). Overshooting by convective settling. *Astronomy & Astrophysics*, 559:A122. Publisher: EDP Sciences.

[Ansong and Sutherland, 2010] Ansong, J. K. and Sutherland, B. R. (2010). Internal gravity waves generated by convective plumes. *Journal of Fluid Mechanics*, 648:405.

[Anstey et al., 2016] Anstey, J. A., Scinocca, J. F., and Keller, M. (2016). Simulating the QBO in an Atmospheric General Circulation Model: Sensitivity to Resolved and Parameterized Forcing. *Journal of the Atmospheric Sciences*, 73(4):1649–1665.

[Anstey et al., 2010] Anstey, J. A., Shepherd, T. G., and Scinocca, J. F. (2010). Influence of the Quasi-Biennial Oscillation on the Extratropical Winter Stratosphere in an Atmospheric General Circulation Model and in Reanalysis Data. *Journal of the Atmospheric Sciences*, 67(5):1402–1419.

[Antonia et al., 1998] Antonia, R. A., Zhou, T., and Zhu, Y. (1998). Three-component vorticity measurements in a turbulent grid flow. *Journal of Fluid Mechanics*, 374:29–57. Publisher: Cambridge University Press.

[Arregi et al., 2009] Arregi, J., Rojas, J., Hueso, R., and Sánchez-Lavega, A. (2009). Gravity waves in Jupiter's equatorial clouds observed by the Galileo orbiter. *Icarus*, 202(1):358–360.

[Ascher et al., 1997] Ascher, U. M., Ruuth, S. J., and Spiteri, R. J. (1997). Implicit-explicit Runge-Kutta methods for time-dependent partial differential equations. *Applied Numerical Mathematics*, 25:151–167.

[Augustson and Mathis, 2019] Augustson, K. C. and Mathis, S. (2019). A Model of Rotating Convection in Stellar and Planetary Interiors. I. Convective Penetration. *The Astrophysical Journal*, 874(1):83. Publisher: American Astronomical Society.

[Baines, 1975] Baines, W. D. (1975). Entrainment by a plume or jet at a density interface. *Journal of Fluid Mechanics*, 68(2):309–320. Publisher: Cambridge University Press.

[Baldwin et al., 2001] Baldwin, M. P., Gray, L. J., Dunkerton, T. J., Hamilton, K., Haynes, P. H., Randel, W. J., Holton, J. R., Alexander, M. J., Hirota, I., Horinouchi, T., Jones, D. B. A., Kinnersley, J. S., Marquardt, C., Sato, K., and Takahashi, M. (2001). The quasi-biennial oscillation. *Reviews of Geophysics*, 39(2):179–229.

[Ball et al., 2012] Ball, C., Fellouah, H., and Pollard, A. (2012). The flow field in turbulent round free jets. *Progress in Aerospace Sciences*, 50:1–26.

[Baraffe et al., 2017] Baraffe, I., Pratt, J., Goffrey, T., Constantino, T., Folini, D., Popov, M. V., Walder, R., and Viallet, M. (2017). Lithium Depletion in Solar-like Stars: Effect of Overshooting Based on Realistic Multi-dimensional Simulations. *The Astrophysical Journal*, 845(1):L6. Publisher: American Astronomical Society.

[Barton and McCormack, 2017] Barton, C. A. and McCormack, J. P. (2017). Origin of the 2016 QBO Disruption and Its Relationship to Extreme El Niño Events. *Geophysical Research Letters*, 44(21):11,150–11,157. _eprint: https://agupubs.onlinelibrary.wiley.com/doi/pdf/10.1002/2017GL075576.

[Bénard, 1901] Bénard, H. (1901). *Les tourbillons cellulaires dans une nappe liquide propageant de la chaleur par convection: en régime permanent.* Gauthier-Villars.

[Booker and Bretherton, 1967] Booker, J. R. and Bretherton, F. P. (1967). The critical layer for internal gravity waves in a shear flow. *Journal of Fluid Mechanics*, 27(3):513–539. Publisher: Cambridge University Press.

[Braginsky and Roberts, 1995] Braginsky, S. I. and Roberts, P. H. (1995). Equations governing convection in earth's core and the geodynamo. *Geophysical & Astrophysical Fluid Dynamics*, 79(1-4):1–97. Publisher: Taylor & Francis _eprint: https://doi.org/10.1080/03091929508228992.

[Brandt et al., 1996] Brandt, P., Alpers, W., and Backhaus, J. O. (1996). Study of the generation and propagation of internal waves in the Strait of Gibraltar using a numerical model and synthetic aperture radar images of the European ERS 1 satellite. *Journal of Geophysical Research: Oceans*, 101(C6):14237–14252.

[Briquet et al., 2007] Briquet, M., Morel, T., Thoul, A., Scuflaire, R., Miglio, A., Montalbán, J., Dupret, M.-A., and Aerts, C. (2007). An asteroseismic study of the β Cephei star θ Ophiuchi: constraints on global stellar parameters and core overshooting. *Monthly Notices of the Royal Astronomical Society*, 381(4):1482–1488. Publisher: Oxford Academic.

[Brönnimann, 2007] Brönnimann, S. (2007). Impact of El Niño–Southern Oscillation on European climate. *Reviews of Geophysics*, 45(3). _eprint: https://agupubs.onlinelibrary.wiley.com/doi/pdf/10.1029/2006RG000199.

[Brummell et al., 2002] Brummell, N. H., Clune, T. L., and Toomre, J. (2002). Penetration and Overshooting in Turbulent Compressible Convection. *The Astrophysical Journal*, 570(2):825–854. Publisher: IOP Publishing.

[Brun and Toomre, 2002] Brun, A. S. and Toomre, J. (2002). Turbulent Convection under the Influence of Rotation: Sustaining a Strong Differential Rotation. *The Astrophysical Journal*, 570(2):865–885.

[Burns et al., 2016] Burns, K., Vasil, G., Oishi, J., Lecoanet, D., and Brown, B. (2016). Dedalus: Flexible framework for spectrally solving differential equations. *Astrophysics Source Code Library*.

[Burns et al., 2019] Burns, K. J., Vasil, G. M., Oishi, J. S., Lecoanet, D., and Brown, B. P. (2019). Dedalus: A Flexible Framework for Numerical Simulations with Spectral Methods. *arXiv e-prints*, page arXiv:1905.10388.

[Bushell et al.,] Bushell, A. C., Anstey, J. A., Butchart, N., Kawatani, Y., Osprey, S. M., Richter, J. H., Serva, F., Braesicke, P., Cagnazzo, C., Chen, C.-C., Chun, H.-Y., Garcia, R. R., Gray, L. J., Hamilton, K., Kerzenmacher, T., Kim, Y.-H., Lott, F., McLandress, C., Naoe, H., Scinocca, J., Smith, A. K., Stockdale, T. N., Versick, S., Watanabe, S., Yoshida, K., and Yukimoto, S. Evaluation of the Quasi-Biennial Oscillation in global climate models for the SPARC QBO-initiative. *Quarterly Journal of the Royal Meteorological Society*, n/a(n/a). _eprint: https://rmets.onlinelibrary.wiley.com/doi/pdf/10.1002/qj.3765.

[Butchart et al., 2018] Butchart, N., Anstey, J. A., Hamilton, K., Osprey, S., McLandress, C., Bushell, A. C., Kawatani, Y., Kim, Y.-H., Lott, F., Scinocca, J., Stockdale, T. N., Andrews, M., Bellprat, O., Braesicke, P., Cagnazzo, C., Chen, C.-C., Chun, H.-Y., Dobrynin, M., Garcia, R. R., Garcia-Serrano, J., Gray, L. J., Holt, L., Kerzenmacher, T., Naoe, H., Pohlmann, H., Richter, J. H., Scaife, A. A., Schenzinger, V., Serva, F., Versick, S., Watanabe, S., Yoshida, K., and Yukimoto, S. (2018). Overview of experiment design and comparison of models participating in phase 1 of the SPARC Quasi-Biennial Oscillation initiative (QBOi). *Geoscientific Model Development*, 11(3):1009–1032. Publisher: Copernicus GmbH.

[Cairns and Williams, 1976] Cairns, J. L. and Williams, G. O. (1976). Internal wave observations from a midwater float, 2. *Journal of Geophysical Research*, 81(12):1943–1950.

[Camargo and Sobel, 2010] Camargo, S. J. and Sobel, A. H. (2010). Revisiting the Influence of the Quasi-Biennial Oscillation on Tropical Cyclone Activity. *Journal of Climate*, 23(21):5810–5825. Publisher: American Meteorological Society.

[Castaing et al., 1989] Castaing, B., Gunaratne, G., Heslot, F., Kadanoff, L., Libchaber, A., Thomae, S., Wu, X.-Z., Zaleski, S., and Zanetti, G. (1989). Scaling of hard thermal turbulence in Rayleigh-Bénard convection. *Journal of Fluid Mechanics*, 204(-1):1.

[Chandrasekhar, 1961] Chandrasekhar, S. (1961). *Hydrodynamic and Hydrodynamic stability*. OUP.

[Charbonnel, 2005] Charbonnel, C. (2005). Influence of Gravity Waves on the Internal Rotation and Li Abundance of Solar-Type Stars. *Science*, 309(5744):2189–2191.

[Charbonnel and Talon, 2007] Charbonnel, C. and Talon, S. (2007). ASTRONOMY: Mixing a Stellar Cocktail. *Science*, 318(5852):922–923.

[Chavanne et al., 1997] Chavanne, X., Chillà, F., Castaing, B., Hébral, B., Chabaud, B., and Chaussy, J. (1997). Observation of the Ultimate Regime in Rayleigh-Bénard Convection. *Physical Review Letters*, 79(19):3648–3651.

[Chavanne et al., 2001] Chavanne, X., Chillà, F., Chabaud, B., Castaing, B., and Hébral, B. (2001). Turbulent Rayleigh–Bénard convection in gaseous and liquid He. *Physics of Fluids*, 13(5):1300–1320.

[Chiffaudel et al., 1987] Chiffaudel, A., Fauve, S., and Perrin, B. (1987). Viscous and Inertial Convection at Low Prandtl Number: Experimental Study. *Europhysics Letters (EPL)*, 4(5):555–560. Publisher: IOP Publishing.

[Colin and Wong, 2019] Colin, M. H. and Wong, J. (2019). Stably stratified layers within Earth's core. *A&G*, 60(3):30–35.

[Cotel et al., 1997] Cotel, A. J., Gjestvang, J. A., Ramkhelawan, N. N., and Breidenthal, R. E. (1997). Laboratory experiments of a jet impinging on a stratified interface. *Experiments in Fluids*, 23(2):155–160.

[Couston et al., 2018a] Couston, L.-A., Lecoanet, D., and Favier, B. (2018a). Order out of chaos: slowly-reversing mean flows emerge from turbulently-generated internal waves. *Physical Review Letters*, 120(24):12.

[Couston et al., 2017] Couston, L.-A., Lecoanet, D., Favier, B., and Le Bars, M. (2017). Dynamics of mixed convective–stably-stratified fluids. *Physical Review Fluids*, 2(9).

[Couston et al., 2018b] Couston, L.-A., Lecoanet, D., Favier, B., and Le Bars, M. (2018b). The energy flux spectrum of internal waves generated by turbulent convection. *Journal of Fluid Mechanics*, 854.

[Couston et al., 2020] Couston, L.-A., Lecoanet, D., Favier, B., and Le Bars, M. (2020). Shape and size of large-scale vortices: A generic fluid pattern in geophysical fluid dynamics. *Physical Review Research*, 2(2):023143. Publisher: American Physical Society.

[Daviero et al., 2001] Daviero, G. J., Roberts, P. J. W., and Maile, K. (2001). Refractive index matching in large-scale stratified experiments. *Experiments in Fluids*, 31(2):119–126.

[de la Torre and Burguete, 2007] de la Torre, A. and Burguete, J. (2007). Slow dynamics in a turbulent von K\'arm\'an swirling flow. *Physical Review Letters*, 99(5):054101. arXiv: physics/0702151.

[Deardorff et al., 1969] Deardorff, J. W., Willis, G. E., and Lilly, D. K. (1969). Laboratory investigation of non-steady penetrative convection. *Journal of Fluid Mechanics*, 35(01):7.

[Delisi and Dunkerton, 1989] Delisi, D. P. and Dunkerton, T. J. (1989). Laboratory observations of gravity wave critical-layer flows. *pure and applied geophysics*, 130(2):445–461.

[Dietrich and Wicht, 2018] Dietrich, W. and Wicht, J. (2018). Penetrative Convection in Partly Stratified Rapidly Rotating Spherical Shells. *Frontiers in Earth Science*, 6. arXiv: 1811.04718.

[Dohan and Sutherland, 2005] Dohan, K. and Sutherland, B. (2005). Numerical and laboratory generation of internal waves from turbulence. *Dynamics of Atmospheres and Oceans*, 40(1-2):43–56.

[Dunkerton, 1997] Dunkerton, T. J. (1997). The role of gravity waves in the quasi-biennial oscillation. *Journal of Geophysical Research: Atmospheres*, 102(D22):26053–26076.

[Ebdon, 1960] Ebdon, R. A. (1960). Notes on the wind flow at 50 mb in tropical and sub-tropical regions in January 1957 and January 1958. *Quarterly Journal of the Royal Meteorological Society*, 86(370):540–542. _eprint: https://rmets.onlinelibrary.wiley.com/doi/pdf/10.1002/qj.49708637011.

[Ern and Preusse, 2009] Ern, M. and Preusse, P. (2009). Wave fluxes of equatorial Kelvin waves and QBO zonal wind forcing derived from SABER and ECMWF temperature space-time spectra. *Atmos. Chem. Phys.*, page 30.

[Fauve et al., 1984] Fauve, S., Laroche, C., Libchaber, A., and Perrin, B. (1984). Chaotic Phases and Magnetic Order in a Convective Fluid. *Physical Review Letters*, 52(20):1774–1777. Publisher: American Physical Society.

[Fauve and Libchaber, 1981] Fauve, S. and Libchaber, A. (1981). Rayleigh-Benard Experiment in a Low Prandtl Number Fluid, Mercury. In Haken, H., editor, *Chaos and Order in Nature*, Springer Series in Synergetics, pages 25–35, Berlin, Heidelberg. Springer.

[Favier et al., 2019] Favier, B., Purseed, J., and Duchemin, L. (2019). Rayleigh–Bénard convection with a melting boundary. *Journal of Fluid Mechanics*, 858:437–473. Publisher: Cambridge University Press.

[Fellouah and Pollard, 2009] Fellouah, H. and Pollard, A. (2009). The velocity spectra and turbulence length scale distributions in the near to intermediate regions of a round free turbulent jet. *Physics of Fluids*, 21(11):115101. Publisher: American Institute of Physics.

[Fischer et al., 2017] Fischer, P., Lottes, J., and Kerkemeier, S. (2017). Nek5000 v17.0. http://nek5000.mcs.anl.gov.

[Fletcher et al., 2017] Fletcher, L. N., Guerlet, S., Orton, G. S., Cosentino, R. G., Fouchet, T., Irwin, P. G. J., Li, L., Flasar, F. M., Gorius, N., and Morales-Juberías, R. (2017). Disruption of Saturn's quasi-periodic equatorial oscillation by the great northern storm. *Nature Astronomy*, 1(11):765–770.

[Fouchet et al., 2008] Fouchet, T., Guerlet, S., Strobel, D. F., Simon-Miller, A. A., Bézard, B., and Flasar, F. M. (2008). An equatorial oscillation in Saturn's middle atmosphere. *Nature*, 453(7192):200–202.

[Fritts and Alexander, 2003] Fritts, D. C. and Alexander, M. J. (2003). Gravity wave dynamics and effects in the middle atmosphere. *Reviews of Geophysics*, 41(1).

[Fritts and Chou, 1987] Fritts, D. C. and Chou, H.-G. (1987). An investigation of the vertical wavenumber and frequency spectra of gravity wave motions in the lower stratosphere. *Journal of the Atmospheric Sciences*, 44(24):3610–3624.

[Fukuhara et al., 2017] Fukuhara, T., Futaguchi, M., Hashimoto, G., Horinouchi, T., Imamura, T., Iwagaimi, N., Kouyama, T., Murakami, S.-y., Nakamura, M., Ogohara, K., Sato, M., Sato, T., Suzuki, M., Taguchi, M., Takagi, S., Ueno, M., Watanabe, S., Yamada, M., and Yamazaki, A. (2017). Large stationary gravity wave in the atmosphere of Venus. *Nature Geoscience*, 10(2):85–88.

[Garaud, 2013] Garaud, P. (2013). Double-diffusive convection. *European Astronomical Society Publications Series*, 63:285–295. Publisher: EDP Sciences.

[Garrett and Munk, 1971] Garrett, C. and Munk, W. (1971). Internal Wave Spectra in the Presence of Fine-Structure. *Journal of Physical Oceanography*, 1(3):196–202. Publisher: American Meteorological Society.

[Garrett and Munk, 1979] Garrett, C. and Munk, W. (1979). Internal Waves in the Ocean. *Annual Review of Fluid Mechanics*, 11(1):339–369.

[Gay et al., 2018] Gay, A., Favier, B., and Verhille, G. (2018). Characterisation of flexible fibre deformations in turbulence. *EPL (Europhysics Letters)*, 123(2):24001.

[Gendrich and Koochesfahani, 1996] Gendrich, C. P. and Koochesfahani, M. M. (1996). A spatial correlation technique for estimating velocity fields using molecular tagging velocimetry (MTV). *Experiments in Fluids*, 22(1):67–77.

[Gendrich et al., 1997] Gendrich, C. P., Koochesfahani, M. M., and Nocera, D. G. (1997). Molecular tagging velocimetry and other novel applications of a new phosphorescent supramolecule. *Experiments in Fluids*, 23(5):361–372.

[Giles et al., 2020] Giles, R. S., Greathouse, T. K., Cosentino, R. G., Orton, G. S., and Lacy, J. H. (2020). Vertically-resolved observations of Jupiter's quasi-quadrennial oscillation from 2012 to 2019. *Icarus*, 350:113905.

[Gostiaux, 2006] Gostiaux, L. (2006). *Étude expérimentale des ondes de gravité internes en présence de topographie. Émission, propagation, réflexion.* PhD thesis, ENS Lyon.

[Gostiaux et al., 2007] Gostiaux, L., Didelle, H., Mercier, S., and Dauxois, T. (2007). A novel internal waves generator. *Experiments in Fluids*, 42(1):123–130.

[Gray, 1984] Gray, W. M. (1984). Atlantic Seasonal Hurricane Frequency. Part I: El Niño and 30 mb Quasi-Biennial Oscillation Influences. *Monthly Weather Review*, 112(9):1649–1668. Publisher: American Meteorological Society.

[Gray et al., 1992a] Gray, W. M., Sheaffer, J. D., and Knaff, J. A. (1992a). Hypothesized mechanism for stratospheric QBO influence on ENSO variability. *Geophysical Research Letters*, 19(2):107–110. _eprint: https://agupubs.onlinelibrary.wiley.com/doi/pdf/10.1029/91GL02950.

[Gray et al., 1992b] Gray, W. M., Sheaffer, J. D., and Knaff, J. A. (1992b). Influence of the stratospheric QBO on ENSO variability. *Journal of the Meteorological Society of Japan. Ser. II*, 70(5):975–995.

[Guenther et al., 2014] Guenther, D. B., Demarque, P., and Gruberbauer, M. (2014). Modeling convective core overshoot and diffusion in procyon constrained bt asteroseismic data. *The Astrophysical Journal*, 787(2):164. Publisher: IOP Publishing.

[Guerlet et al., 2018] Guerlet, S., Fouchet, T., Spiga, A., Flasar, F. M., Fletcher, L. N., Hesman, B. E., and Gorius, N. (2018). Equatorial Oscillation and Planetary Wave Activity in Saturn's Stratosphere Through the Cassini Epoch. *Journal of Geophysical Research: Planets*, 123(1):246–261. _eprint: https://agupubs.onlinelibrary.wiley.com/doi/pdf/10.1002/2017JE005419.

[Hannoun, 1985] Hannoun, I. (1985). Matching the refractive index in density stratified flow. *Technical Morandum*, 85(1):1985.

[Herault et al., 2017] Herault, J., Duval, F., and Le Bars, M. (2017). Mass transport induced by a jet impinging on a density interface: The role of interfacial wave breaking. *EPL (Europhysics Letters)*, 117(6):64003.

[Herault et al., 2018] Herault, J., Facchini, G., and Le Bars, M. (2018). Erosion of a sharp density interface by a turbulent jet at moderate Froude and Reynolds numbers. *Journal of Fluid Mechanics*, 838:631–657.

[Hirose et al., 2013] Hirose, K., Labrosse, S., and Hernlund, J. (2013). Composition and State of the Core. *Annual Review of Earth and Planetary Sciences*, 41(1):657–691.

[Holton and Lindzen, 1972] Holton, J. R. and Lindzen, R. S. (1972). An Updated Theory for the Quasi-Biennial Cycle of the Tropical Stratosphere. *Journal of the Atmospheric Sciences*, 29(6):1076–1080. Publisher: American Meteorological Society.

[Howard, 1966] Howard, L. N. (1966). Convection at high Rayleigh number. In Görtler, H., editor, *Applied Mechanics*, pages 1109–1115. Springer Berlin Heidelberg, Berlin, Heidelberg.

[Howe et al., 2000] Howe, R., Christensen-Dalsgaard, J., Hill, F., Komm, R. W., Larsen, R. M., Schou, J., Thompson, M. J., and Toomre, J. (2000). Dynamic Variations at the Base of the Solar Convection Zone. *Science*, 287(5462):2456–2460. Publisher: American Association for the Advancement of Science Section: Report.

[Huppert and Turner, 1981] Huppert, H. E. and Turner, J. S. (1981). Double-diffusive convection. *Journal of Fluid Mechanics*, page 31.

[Hurlburt et al., 1994] Hurlburt, N. E., Toomre, J., Massaguer, J. M., and Zahn, J.-P. (1994). Penetration below a convective zone. *The Astrophysical Journal*, 421:245–260.

[Kek and Müller, 1993] Kek, V. and Müller, U. (1993). Low Prandtl number convection in layers heated from below. *International Journal of Heat and Mass Transfer*, 36(11):2795–2804.

[Kellogg, 1991] Kellogg, L. H. (1991). Interaction of plumes with a compositional boundary at 670 km. *Geophysical Research Letters*, 18(5):865–868. _eprint: https://agupubs.onlinelibrary.wiley.com/doi/pdf/10.1029/91GL01066.

[Kim and MacGregor, 2001] Kim, E.-j. and MacGregor, K. B. (2001). Gravity Wave–driven Flows in the Solar Tachocline. *The Astrophysical Journal*, 556(2):L117–L120. Publisher: IOP Publishing.

[Kitiashvili et al., 2016] Kitiashvili, I. N., Kosovichev, A. G., Mansour, N. N., and Wray, A. A. (2016). Dynamics of turbulent convection and convective ovsershoot in a moderate-mass star. *The Astrophysical Journal*, 821(1):L17. Publisher: American Astronomical Society.

[Koop, 1981] Koop, C. G. (1981). A preliminary investigation of the interaction of internal gravity waves with a steady shearing motion. *Journal of Fluid Mechanics*, 113(-1):347.

[Kunze, 2017] Kunze, E. (2017). Internal-Wave-Driven Mixing: Global Geography and Budgets. *Journal of Physical Oceanography*, 47(6):1325–1345.

[Labe et al., 2019] Labe, Z., Peings, Y., and Magnusdottir, G. (2019). The Effect of QBO Phase on the Atmospheric Response to Projected Arctic Sea Ice Loss in Early Winter. *Geophysical Research Letters*, 46(13):7663–7671.

[Le Bars et al., 2015] Le Bars, M., Lecoanet, D., Perrard, S., Ribeiro, A., Rodet, L., Aurnou, J. M., and Gal, P. L. (2015). Experimental study of internal wave generation by convection in water. *Fluid Dynamics Research*, 47(4):045502.

[Le Gal, 1997] Le Gal, P. (1997). Penetrative convection in water near 4°C. *Proceedings of IUTAM Symposium On Variable Density Low-Speed Turbulent Flow, Kluwer Academic Publishers, L. Fulcher, J.Lumley and F. Anselmet*, pages 221–228.

[Léard et al., 2020] Léard, P., Favier, B., Le Gal, P., and Le Bars, M. (2020). Coupled convection and internal gravity waves excited in water around its density maximum at 4°C. *Phys. Rev. Fluids*, 5:024801.

[Lecoanet et al., 2015] Lecoanet, D., Le Bars, M., Burns, K. J., Vasil, G. M., Brown, B. P., Quataert, E., and Oishi, J. S. (2015). Numerical simulations of internal wave generation by convection in water. *Physical Review E*, 91(6).

[Leighton et al., 1962] Leighton, R. B., Noyes, R. W., and Simon, G. W. (1962). Velocity Fields in the Solar Atmosphere. I. Preliminary Report. *ApJ*, 135:474.

[Leovy et al., 1991] Leovy, C. B., Friedson, A. J., and Orton, G. S. (1991). The quasiquadrennial oscillation of Jupiter's equatorial stratosphere. *Nature*, 354(6352):380–382.

[Li et al., 2020] Li, H., Pilch Kedzierski, R., and Matthes, K. (2020). On the forcings of the unusual Quasi-Biennial Oscillation structure in February 2016. *Atmospheric Chemistry and Physics*, 20(11):6541–6561.

[Libchaber et al., 1982] Libchaber, A., Laroche, C., and Fauve, S. (1982). Period doubling cascade in mercury, a quantitative measurement. *Journal de Physique Lettres*, 43(7):211–216. Publisher: Les Editions de Physique.

[Lighthill, 1978] Lighthill, S. J. (1978). Acoustic streaming. *Journal of Sound and Vibration*, 61(3):391–418.

[Lindzen, 1972] Lindzen, R. S. (1972). An updated theory for the quasi biennial oscillation cycle of the tropical stratosphere. *Journal of the Atmospheric Sciences*.

[Lindzen and Holton, 1968] Lindzen, R. S. and Holton, J. R. (1968). A Theory of the Quasi-Biennial Oscillation. *Journal of the Atmospheric Sciences*, 25(6):1095–1107. Publisher: American Meteorological Society.

[Lord Rayleigh, 1916] Lord Rayleigh, O. M. (1916). LIX. On convection currents in a horizontal layer of fluid, when the higher temperature is on the under side. *The London, Edinburgh, and Dublin Philosophical Magazine and Journal of Science*, 32(192):529–546. Publisher: Taylor & Francis _eprint: https://doi.org/10.1080/14786441608635602.

[Lott and Guez, 2013] Lott, F. and Guez, L. (2013). A stochastic parameterization of the gravity waves due to convection and its impact on the equatorial stratosphere: STOCHASTIC GWS DUE TO CONVECTION AND QBO. *Journal of Geophysical Research: Atmospheres*, 118(16):8897–8909.

[Lott et al., 2012] Lott, F., Guez, L., and Maury, P. (2012). A stochastic parameterization of non-orographic gravity waves: Formalism and impact on the equatorial stratosphere. *Geophysical Research Letters*, 39(6).

[Lovekin and Goupil, 2010] Lovekin, C. C. and Goupil, M.-J. (2010). Rotation and convective core overshoot in θ Ophiuchi. *Astronomy & Astrophysics*, 515:A58. Publisher: EDP Sciences.

[Madden and Julian, 1971] Madden, R. A. and Julian, P. R. (1971). Detection of a 40–50 Day Oscillation in the Zonal Wind in the Tropical Pacific. *Journal of the Atmospheric Sciences*, 28(5):702–708. Publisher: American Meteorological Society.

[Maeder, 1975] Maeder, A. (1975). Stellar evolution IV: Evolution of a star of 1.5 M sun from the main-sequence to red-giant branch with and without overshooting from convective core. *A&A*, 43(1):61–69.

[Marshall and Scaife, 2009] Marshall, A. G. and Scaife, A. A. (2009). Impact of the QBO on surface winter climate. *Journal of Geophysical Research*, 114(D18):D18110.

[Martins and Palacios, 2013] Martins, F. and Palacios, A. (2013). A comparison of evolutionary tracks for single Galactic massive stars. *Astronomy & Astrophysics*, 560:A16. Publisher: EDP Sciences.

[Menaut et al., 2019] Menaut, R., Corre, Y., Huguet, L., Reun, T. L., Alboussière, T., Bergman, M., Deguen, R., Labrosse, S., and Moulin, M. (2019). Experimental study of convection in the compressible regime. *Physical Review Fluids*, 4(3):033502. arXiv: 1812.04572.

[Merryfield, 1995] Merryfield, W. J. (1995). Hydrodynamics of Semiconvection. *The Astrophysical Journal*, 444:318.

[Meunier and Leweke, 2003] Meunier, P. and Leweke, T. (2003). Analysis and treatment of errors due to high velocity gradients in particle image velocimetry. *Experiments in fluids*, 35(5):408–421.

[Michaelian et al., 2002] Michaelian, M., Maxworthy, T., and Redekopp, L. (2002). The coupling between turbulent, penetrative convection and internal waves. *European Journal of Mechanics - B/Fluids*, 21(1):1–28.

[Miller et al., 2015] Miller, S. D., Straka, W. C., Yue, J., Smith, S. M., Alexander, M. J., Hoffmann, L., Setvák, M., and Partain, P. T. (2015). Upper atmospheric gravity wave details revealed in nightglow satellite imagery. *Proceedings of the National Academy of Sciences*, 112(49):E6728–E6735.

[Monchaux et al., 2009] Monchaux, R., Berhanu, M., Aumaître, S., Chiffaudel, A., Daviaud, F., Dubrulle, B., Ravelet, F., Fauve, S., Mordant, N., Pétrélis, F., Bourgoin, M., Odier, P., Pinton, J.-F., Plihon, N., and Volk, R. (2009). The von Kármán Sodium experiment: Turbulent dynamical dynamos. *Physics of Fluids*, 21(3):035108. Publisher: American Institute of Physics.

[Moore and Lien, 2007] Moore, S. E. and Lien, R.-C. (2007). Pilot whales follow internal solitary waves in the south china sea. *Marine Mammal Science*, 23(1):193–196.

[Newman et al., 2016] Newman, P. A., Coy, L., Pawson, S., and Lait, L. R. (2016). The anomalous change in the QBO in 2015–2016. *Geophysical Research Letters*, 43(16):8791–8797.

[Nordlund et al., 1992] Nordlund, A., Brandenburg, A., Jennings, R. L., Rieutord, M., Ruokolainen, J., Stein, R. F., and Tuominen, I. (1992). Dynamo action in stratified convection with overshoot. *The Astrophysical Journal*, 392:647–652.

[Osprey et al., 2016] Osprey, S. M., Butchart, N., Knight, J. R., Scaife, A. A., Hamilton, K., Anstey, J. A., Schenzinger, V., and Zhang, C. (2016). An unexpected disruption of the atmospheric quasi-biennial oscillation. *Science*, 353(6306):1424–1427.

[Oster, 1965] Oster, G. (1965). Density Gradients. *Scientific American*, 213(2):70–79.

[O'Sullivan, 1997] O'Sullivan, D. (1997). Interaction of extratropical Rossby waves with westerly quasi-biennial oscillation winds. *Journal of Geophysical Research: Atmospheres*, 102(D16):19461–19469. _eprint: https://agupubs.onlinelibrary.wiley.com/doi/pdf/10.1029/97JD01524.

[Otobe et al., 1998] Otobe, N., Sakai, S., Yoden, S., and Shiotani, M. (1998). Visualization and wkb analysis of the internal gravity wave in the qbo experiment. *Nagare: Japan Soc. Fluid Mech*, 17(3).

[Parker, 1975] Parker, E. N. (1975). The generation of magnetic fields in astrophysical bodies. X - Magnetic buoyancy and the solar dynamo. *The Astrophysical Journal*, 198:205–209.

[Perrard et al., 2013] Perrard, S., Le Bars, M., and Le Gal, P. (2013). Experimental and Numerical Investigation of Internal Gravity Waves Excited by Turbulent Penetrative Convection in Water Around Its Density Maximum. *Studying Stellar Rotation and Convection*, 865:239–257.

[Plumb, 1975] Plumb, R. A. (1975). Momentum transport by the thermal tide in the stratosphere of Venus. *Quarterly Journal of the Royal Meteorological Society*, 101(430):763–776.

[Plumb, 1977] Plumb, R. A. (1977). The interaction of two internal waves with the mean flow: Implications for the theory of the quasi-biennial oscillation. *Journal of the Atmospheric Sciences*.

[Plumb, 1984] Plumb, R. A. (1984). The quasi-biennial oscillation. In *Dynamics of the Middle Atmosphere*, page 217.

[Plumb and McEwan, 1978] Plumb, R. A. and McEwan, A. D. (1978). The instability of a forced standing wave in a viscous stratified fluid: a laboratory analogue of the quasi biennial oscillation. *Journal of the Atmospheric Sciences*.

[Pope, 1962] Pope, S. B. (1962). Turbulent flows. 2000.

[Pratt et al., 2017] Pratt, J., Baraffe, I., Goffrey, T., Constantino, T., Viallet, M., Popov, M. V., Walder, R., and Folini, D. (2017). Extreme value statistics for two-dimensional convective penetration in a pre-main sequence star. *Astronomy & Astrophysics*, 604:A125. Publisher: EDP Sciences.

[Press, 1981] Press, W. H. (1981). Radiative and other effects from internal waves in solar and stellar interiors. *The Astrophysical Journal*, 245:286.

[Purseed et al., 2020] Purseed, J., Favier, B., Duchemin, L., and Hester, E. W. (2020). Bistability in Rayleigh-B\'enard convection with a melting boundary. *Physical Review Fluids*, 5(2):023501. Publisher: American Physical Society.

[Ravelet et al., 2008] Ravelet, F., Chiffaudel, A., and Daviaud, F. (2008). Supercritical transition to turbulence in an inertially-driven von Karman closed flow. *arXiv:0801.3357 [physics]*. arXiv: 0801.3357.

[Ravelet et al., 2004] Ravelet, F., Marie, L., Chiffaudel, A., and Daviaud, F. (2004). Multistability and memory effect in a highly turbulent flow: experimental evidence for a global bifurcation. *Physical Review Letters*, 93(16):164501. arXiv: physics/0409112.

[Ray et al., 2020] Ray, E. A., Portmann, R. W., Yu, P., Daniel, J., Montzka, S. A., Dutton, G. S., Hall, B. D., Moore, F. L., and Rosenlof, K. H. (2020). The influence of the stratospheric Quasi-Biennial Oscillation on trace gas levels at the Earth's surface. *Nature Geoscience*, 13(1):22–27.

[Reed et al., 1961] Reed, R. J., Campbell, W. J., Rasmussen, L. A., and Rogers, D. G. (1961). Evidence of a downward-propagating, annual wind reversal in the equatorial stratosphere. *Journal of Geophysical Research (1896-1977)*, 66(3):813–818. _eprint: https://agupubs.onlinelibrary.wiley.com/doi/pdf/10.1029/JZ066i003p00813.

[Renaud, 2018] Renaud, A. (2018). *On wave-mean flow interactions in stratified fluid*. PhD thesis. Thèse de doctorat dirigée par Venaille, Antoine Physique Lyon 2018.

[Renaud et al., 2019] Renaud, A., Nadeau, L.-P., and Venaille, A. (2019). Periodicity disruption of a model quasi-biennial oscillation. *Physical Review Letters*. arXiv: 1901.05076.

[Rogers and Glatzmaier, 2006] Rogers, T. M. and Glatzmaier, G. A. (2006). Angular Momentum Transport by Gravity Waves in the Solar Interior. *The Astrophysical Journal*, 653(1):756–764.

[Rogers et al., 2012] Rogers, T. M., Lin, D. N. C., and Lau, H. H. B. (2012). Internal Gravity Waves Modulate the Apparent Misalignment of Exoplanets around Hot Stars. *The Astrophysical Journal*, 758(1):L6. arXiv: 1209.2435.

[Rogers et al., 2013] Rogers, T. M., Lin, D. N. C., McElwaine, J. N., and Lau, H. H. B. (2013). Internal gravity waves in massive stars: Angular momentum transport. *The Astrophysical Journal*, 772(1):21.

[Rogers and McElwaine, 2017] Rogers, T. M. and McElwaine, J. N. (2017). On the Chemical Mixing Induced by Internal Gravity Waves. *The Astrophysical Journal*, 848(1):L1.

[Rosenfield et al., 2017] Rosenfield, P., Girardi, L., Williams, B. F., Johnson, L. C., Dolphin, A., Bressan, A., Weisz, D., Dalcanton, J. J., Fouesneau, M., and Kalirai, J. (2017). A New Approach to Convective Core Overshooting: Probabilistic Constraints from Color–Magnitude Diagrams of LMC Clusters. *The Astrophysical Journal*, 841(2):69. Publisher: American Astronomical Society.

[Rossby, 1969] Rossby, H. T. (1969). A study of Bénard convection with and without rotation. *Journal of Fluid Mechanics*, 36(2):309–335. Publisher: Cambridge University Press.

[Saravanan, 1990] Saravanan, R. (1990). A Multiwave Model of the Quasi-biennial Oscillation. *Journal of the Atmospheric Sciences*, 47(21):2465–2474.

[Schatzman, 1993] Schatzman, E. (1993). Transport of angular momentum and diffusion by the action of internal waves. *Astronomy and Astrophysics*, 279:431–446.

[Schirber, 2015] Schirber, S. (2015). Influence of ENSO on the QBO: Results from an ensemble of idealized simulations. *Journal of Geophysical Research: Atmospheres*, 120(3):1109–1122. _eprint: https://agupubs.onlinelibrary.wiley.com/doi/pdf/10.1002/2014JD022460.

[Schoeberl, 1978] Schoeberl, M. R. (1978). Stratospheric warmings: Observations and theory. *Reviews of Geophysics*, 16(4):521–538. _eprint: https://agupubs.onlinelibrary.wiley.com/doi/pdf/10.1029/RG016i004p00521.

[Semin et al., 2016] Semin, B., Facchini, G., Pétrélis, F., and Fauve, S. (2016). Generation of a mean flow by an internal wave. *Physics of Fluids*, 28(9):096601.

[Semin et al., 2018] Semin, B., Garroum, N., Pétrélis, F., and Fauve, S. (2018). Nonlinear saturation of the large scale flow in a laboratory model of the quasibiennial oscillation. *Physical Review Letters*, 121(13).

[Serva et al., 2020] Serva, F., Cagnazzo, C., Christiansen, B., and Yang, S. (2020). The influence of ENSO events on the stratospheric QBO in a multi-model ensemble. *Climate Dynamics*, 54(3):2561–2575.

[Shrinivas and Hunt, 2014] Shrinivas, A. B. and Hunt, G. R. (2014). Unconfined turbulent entrainment across density interfaces. *Journal of Fluid Mechanics*, 757:573–598. Publisher: Cambridge University Press.

[Shy et al., 1997] Shy, S. S., Tang, C. Y., and Fann, S. Y. (1997). A nearly isotropic turbulence generated by a pair of vibrating grids. *Experimental Thermal and Fluid Science*, 14(3):251–262.

[Song et al., 2007] Song, I.-S., Chun, H.-Y., Garcia, R. R., and Boville, B. A. (2007). Momentum Flux Spectrum of Convectively Forced Internal Gravity Waves and Its Application to Gravity Wave Drag Parameterization. Part II: Impacts in a GCM (WACCM). *Journal of the Atmospheric Sciences*, 64(7):2286–2308.

[Spiegel and Zahn, 1992] Spiegel, E. A. and Zahn, J.-P. (1992). The solar tachocline. *Astronomy and Astrophysics*, 265:106–114.

[Süring, 2013] Süring, R. (2013). Report by A.Berson about the aerological expedition of the Royal Aeronautic Observatory to East Africa in 1908. *Meteorologische Zeitschrift*, 22(3):343–348.

[Staquet and Sommeria, 2002] Staquet, C. and Sommeria, J. (2002). Internal Gravity Waves: From Instabilities to Turbulence. *Annual Review of Fluid Mechanics*, 34(1):559–593.

[Stern, 1960] Stern, M. E. (1960). The "Salt-Fountain" and Thermohaline Convection. *Tellus*, 12(2):172–175.

[Stevens et al., 2009] Stevens, R. J. A. M., Zhong, J.-Q., Clercx, H. J. H., Ahlers, G., and Lohse, D. (2009). Transitions between Turbulent States in Rotating Rayleigh-B\'enard Convection. *Physical Review Letters*, 103(2):024503. Publisher: American Physical Society.

[Stevenson and Salpeter, 1977] Stevenson, D. J. and Salpeter, E. E. (1977). The phase diagram and transport properties for hydrogen-helium fluid planets. *The Astrophysical Journal Supplement Series*, 35:221–237.

[Stier and Koochesfahani, 1999] Stier, B. and Koochesfahani, M. M. (1999). Molecular Tagging Velocimetry (MTV) measurements in gas phase flows. *Experiments in Fluids*, 26(4):297–304.

[Sutherland, 2010] Sutherland, B. (2010). *Internal gravity waves*. Cambridge University Press, Cambridge New York, NY Port Melbourne New Delhi Singapore. OCLC: 731503476.

[Taguchi, 2010] Taguchi, M. (2010). Observed connection of the stratospheric quasi-biennial oscillation with El Niño–Southern Oscillation in radiosonde data. *Journal of Geophysical Research: Atmospheres*, 115(D18). _eprint: https://agupubs.onlinelibrary.wiley.com/doi/pdf/10.1029/2010JD014325.

[Talon and Charbonnel, 2005] Talon, S. and Charbonnel, C. (2005). Hydrodynamical stellar models including rotation, internal gravity waves, and atomic diffusion - I. Formalism and tests on Pop I dwarfs. *Astronomy & Astrophysics*, 440(3):981–994. Number: 3 Publisher: EDP Sciences.

[Talon et al., 2002] Talon, S., Kumar, P., and Zahn, J.-P. (2002). Angular Momentum Extraction by Gravity Waves in the Sun. *The Astrophysical Journal*, 574(2):L175–L178. Publisher: IOP Publishing.

[Thorpe, 1975] Thorpe, S. A. (1975). The excitation, dissipation, and interaction of internal waves in the deep ocean. *Journal of Geophysical Research (1896-1977)*, 80(3):328–338.

[Townsend, 1964] Townsend, A. A. (1964). Natural convection in water over an ice surface. *Quarterly Journal of the Royal Meteorological Society*, 90(385):248–259.

[Turner, 1974] Turner, J. S. (1974). Double-diffusive phenomena. *Annual Review of Fluid Mechanics*, 6:37–54.

[Vallis, 2017] Vallis, G. K. (2017). *Atmospheric and Oceanic Fluid Dynamics: Fundamentals and Large-Scale Circulation*. Cambridge University Press, 2 edition.

[Wedi and Smolarkiewicz, 2006] Wedi, N. P. and Smolarkiewicz, P. K. (2006). Direct Numerical Simulation of the Plumb–McEwan Laboratory Analog of the QBO. *Journal of the Atmospheric Sciences*, 63(12):3226–3252.

[Wunsch and Ferrari, 2004] Wunsch, C. and Ferrari, R. (2004). Vertical Mixing, Energy, and the General Circulation of the Oceans. *Annual Review of Fluid Mechanics*, 36(1):281–314.

[Xue et al., 2012] Xue, X.-H., Liu, H.-L., and Dou, X.-K. (2012). Parameterization of the inertial gravity waves and generation of the quasi-biennial oscillation. *Journal of Geophysical Research: Atmospheres*, 117(D6):n/a–n/a.

[Yoden and Holton, 1988] Yoden, S. and Holton, J. R. (1988). A new look at equatorial Quasi-Biennial Oscillation models. *Journal of the Atmospheric Sciences*, 45(19):2703–2717.

[Yoo and Son, 2016] Yoo, C. and Son, S.-W. (2016). Modulation of the boreal wintertime Madden-Julian oscillation by the stratospheric quasi-biennial oscillation. *Geophysical Research Letters*, 43(3):1392–1398. _eprint: https://agupubs.onlinelibrary.wiley.com/doi/pdf/10.1002/2016GL067762.

[Yu et al., 2017] Yu, C., Xue, X., Wu, J., Chen, T., and Li, H. (2017). Sensitivity of the quasi-biennial oscillation simulated in WACCM to the phase speed spectrum and the settings in an inertial gravity wave parameterization. *Journal of Advances in Modeling Earth Systems*, 9(1):389–403.

[Zahn et al., 1996] Zahn, J.-P., Talon, S., and Matias, J. (1996). Angular momentum transport by internal waves in the solar interior. *arXiv:astro-ph/9611189*. arXiv: astro-ph/9611189.

[Zarembo, 1971] Zarembo, L. K. (1971). Acoustic Streaming. In Rozenberg, L. D., editor, *High-Intensity Ultrasonic Fields*, Ultrasonic Technology, pages 135–199. Springer US, Boston, MA.

[Zhang, 2005] Zhang, C. (2005). Madden-Julian Oscillation. *Reviews of Geophysics*, 43(2).

Abstract: Coupled dynamics between turbulent and stratified layers are often encountered in geophysical and astrophysical flows, for example in the Earth's atmosphere, oceans and core, but also in stars. Due to the large space- and time-scale difference between the phenomenon involved in the two layers, their interaction is sometimes overlooked. Still, the turbulent motions enhance mixing at the interface and generate internal gravity waves which propagate in the stratified layer. Those waves extract energy from the convective layer and distribute this energy along their propagation path. They also carry chemicals and bio-elements. Therefore, the comprehension of the coupled dynamics of a turbulent layer interacting with a stratification one is essential in order to build reliable models predicting the long-time evolution of those flows. Our first study focuses on the large-scale flow generation by internal gravity waves forcing. A striking example of such flow is the oscillation of equatorial winds in the Earth's stratosphere (Quasi-Biennial Oscillation), with a mean period of 28 months. An analytical model, inspired from previous studies, is derived to explain why the oscillations are almost periodic while the excitation comes from waves with various frequencies and wavenumbers. We find that, in a finite domain, multi-modal forcing favours periodic oscillations. Then, we introduce three different experimental set-ups, focusing on the interaction of a turbulent layer with a stratified one. The internal gravity waves generation is particularly looked at, and we also investigate any large-scale flow emergence. One of these experiments uses salty water to build the stratification and water jets to create the turbulent layer. The two others investigate the dynamics of penetrative convection. The first one uses the non-linear equation of state of water, to allow the study of penetrative convection in a stationary configuration. The second one uses gases as working fluids, in order to lower the Prandtl number, which is interesting for astrophysical and atmospheric applications.

Résumé : L'étude du couplage entre une couche turbulente et une couche stratifiée a un intérêt particulier pour les écoulements géophysiques et astrophysiques, par exemple pour l'atmosphère, les océans et le cœur de notre planète, mais aussi pour les étoiles. L'interaction entre ces deux couches est trop souvent négligée car les échelles de temps et de longueur qui les caractérisent sont très différentes. Pourtant, les mouvements de la couche convective brassent le fluide au niveau de l'interface, provoquant un mélange continu des espèces en présence. De plus, l'agitation créée par ces mouvements génère des ondes internes de gravité. Ces ondes redistribuent une partie de l'énergie de la couche turbulente dans la couche stratifiée, dans laquelle elles se propagent. En outre, ces ondes peuvent aussi transporter température et espèces chimiques. Elles ont donc une grande influence sur la dynamique globale du système. Il paraît naturel de chercher à approfondir notre compréhension des différents phénomènes régissant l'interaction entre couches stratifiée et turbulente, dans le but d'améliorer les modèles numériques prédisant l'évolution des étoiles ou de notre atmosphère. Au début de cette thèse est présenté un modèle numérique étudiant la génération d'écoulements grande échelle par le forçage d'ondes internes de gravité. Un exemple de ce type d'écoulement est l'oscillation, avec une période de 28 mois, des vents équatoriaux dans la stratosphère terrestre. En nous fondant sur d'anciens modèles étudiant le forçage de ce type d'écoulement par une onde monochromatique, nous complétons ces études passées en prenant en compte diverses fréquences dans notre spectre de forçage. Nous trouvons que dans un domaine fini, un forçage contenant un large spectre de fréquences favorise l'apparition d'oscillations périodiques. Le reste de la thèse présente trois dispositifs expérimentaux étudiant l'interaction entre turbulence et stratification. Dans le premier, la stratification est créée par un gradient de concentration en sel dissous dans l'eau, et la turbulence vient de l'interaction de plusieurs jets d'eau. Le second utilise le fait que la densité maximale de l'eau soit atteinte à 4°C. Grâce à cette propriété, le phénomène de convection pénétrante peut être étudiée dans un système stationnaire. La dernière expérience s'intéresse aussi à la convection pénétrante, mais en utilisant des gaz, afin de travailler à des nombres de Prandtl plus bas, ce qui a un intérêt particulier pour les applications atmosphériques et astrophysiques liées à notre étude.